SEARCH FOR AXIONS WITH MICROMEGAS DETECTORS IN THE CERN CAST EXPERIMENT

by

Süleyman Cenk Yıldız

B.S., Physics, Koç University, 2005

M.S., Physics, Boğaziçi University, 2008

Submitted to the Institute for Graduate Studies in
Science and Engineering in partial fulfillment of
the requirements for the degree of
Doctor of Philosophy

Graduate Program in Physics

Boğaziçi University

2013

To the memory of Engin Arık and Berkol Doğan

ACKNOWLEDGEMENTS

Having finished a masters in mathematical physics, I asked guidance of my supervisor Metin Arık on how to continue my studies. I'm thankful to him for encouraging me to join this completely foreign field and always putting great confidence in me.

Serkant Çetin deserves a special thank you, for supporting me all the time and making sure that we work and live in good conditions when we travel to CERN. Without him, it would be much harder.

Martyn Davenport is the person I could call *boss* at CAST. His guidance was always helpful and his perfectionist and professional way of working is something that I will always like to maintain. Konstantin Zioutas was one of the reasons I felt *home* at CAST, his enthusiasm is one of the things that run this experiment.

I would also like to thank to: my dear friends Theodoros, Inaki and Nuno, who made my days more interesting with deeply scientific or not so scientific, but extremely interesting discussions... Biljana, Thomas, Esther, Jaime, Igor and Theopisti for their guidance... Juanan, Javier Garcia, Alfredo and Juan for endless hours of joyful micromegas installations... Jean-Michel, for helping me understand world of vacuum with his amazing knowledge... Javier Galan, my first mentor at CAST, for having introduced me to many interesting things (primarily python and vim, which has contributed greatly to writing of this thesis)... My parents for their unconditional support that always made me feel safe... Maria and Nicole for making this hard time of my life much happier...

It was a great chance to be able to travel to CERN. This has been possible thanks to the funding provided by Turkish Atomic Energy Authority(TEAK).

ABSTRACT

SEARCH FOR AXIONS WITH MICROMEGAS DETECTORS IN THE CERN CAST EXPERIMENT

The CAST experiment is searching for the axion, which is a light, weakly interacting pseudoscalar particle, that is proposed to solve the so called Strong Charge-Parity Problem. The axions CAST is looking for are produced from photons in the solar core and CAST aims to convert them back into photons in a superconducting LHC dipole magnet and detect the photons in the x-ray detectors attached to ends of each magnet bore. CAST uses three micromegas and a CCD detector and can track the Sun during sunset and sunrise. The two of the micromegas take tracking data during the sunset solar tracking, and were used for the first time in 2008. The analysis of the data taken in 2008 with these two detectors show no signal of axions, and new upper limits on the axion mass-coupling constant parameter space are established due to sensitivity of detectors for the axion mass range of 0.38eV to 0.65eV.

ÖZET

CERN CAST DENEYINDE MİKROMEGAS ALGIÇLARI İLE AKSIYON ARAYIŞI

CAST deneyi, Güçlü Yük-Parite sorununa çözüm olarak önerilmiş olan aksiyon denen hafif, zayıf etkileşen sözde-skaler parçacığı aramaktadır. CAST'ın aradığı aksiyonlar güneşin çekirdeğinde fotonlardan dönüşmüş olup, CAST tarafından süperiletken, çift kutuplu bir LHC mıknatısında tekrar fotonlara dönüştürülmeye, ve bu fotonlar mıknatısın uçlarına yerleştirilmiş x-ışını algıçlarıyla tespit edilmeye çalışılmaktadırlar. CAST üç mikromegas, bir de CCD algıçı kullanmakta, ve güneşi gün doğumu ve gün batımı olmak üzere günde iki kez takip edebilmektedir. Mikromegas algıçlarının ikisi gün batımı süresince güneş izleme verisi almakta olup ilk olarak 2008 yılında kullanılmışlardır. Bu algıçlar ile yapılan 2008 yılı veri alımı herhangi bir aksiyon izine rastlanmadığını göstermektedir. Axion kütlesi-etkileşme sabiti parametre uzayında, kütlesi 0.38eV-0.65eV aralığındaki aksiyonlar için, detektörlerin duyarlılığı düzeyinde yeni üst limitler belirlenmiştir.

TABLE OF CONTENTS

ACKNOWLEDGEMENTS iv
ABSTRACT v
ÖZET vi
LIST OF FIGURES xiii
LIST OF TABLES xxvi
LIST OF SYMBOLS xxvii
LIST OF ACRONYMS/ABBREVIATIONS xxviii
1. INTRODUCTION 1
2. THEORY OF AXIONS 4
2.1. CP Violation in Weak Interactions 4
2.2. Theoretical Motivation for Axions 5
2.2.1. The $U(1)_A$ Problem 6
2.2.2. Strong CP Problem 6
2.2.3. Peccei-Quinn Mechanism 8
2.3. Couplings of Axions 9
2.3.1. Coupling to Gluons 9
2.3.2. Coupling to Photons 10
2.3.3. Coupling to Fermions 11
2.4. Axion Models 12
2.4.1. Visible Axion Models 12
2.4.2. Invisible Axion Models 12
2.4.2.1. KSZV Model 13
2.4.2.2. DFSZ Model 13
2.5. Limits on Axion Couplings and Mass 14
2.5.1. Axions and Dark Matter and Cosmological Constraints 14
2.5.2. Solar Model 15
2.5.3. Globular Clusters 16
2.5.4. White Dwarf Cooling 17
2.5.5. Supernova 1987A 18

2.6. Axion Experiments . . . 19
2.6.1. Photon Regeneration and Polarization Experiments . . . 19
2.6.1.1. Photon Regeneration Experiments . . . 20
2.6.1.2. Photon Polarization Experiments . . . 21
2.6.2. Haloscope Experiments . . . 21
2.6.3. Solar Axion Experiments . . . 22
2.6.3.1. Bragg Scattering Experiments . . . 22
2.6.3.2. Helioscope Experiments . . . 22
3. SOLAR AXION DETECTION WITH HELIOSCOPES . . . 24
3.1. Primakoff Effect . . . 24
3.2. Solar Axion Flux . . . 25
3.3. Axion-Photon conversion in Magnetic Field . . . 29
3.3.1. Axion-Photon Transmission Amplitude . . . 29
3.3.2. Axion-Photon Conversion Probability . . . 30
3.3.3. Absorption of Photons . . . 32
3.3.4. Coherence of Conversion . . . 34
3.4. Expected Number of X-rays . . . 35
4. CERN AXION SOLAR TELESCOPE . . . 37
4.1. History . . . 37
4.2. CAST Magnet . . . 39
4.3. Movement and Tracking System . . . 41
4.3.1. Motor Encoders . . . 42
4.3.2. Tracking Program . . . 43
4.3.3. Precision of Solar Tracking . . . 45
4.3.3.1. Yearly Grid Measurement . . . 45
4.3.3.2. Sun Filming . . . 46
4.4. Slow Control System . . . 46
4.5. Gas System . . . 47
4.5.1. Cold Windows . . . 48
4.5.2. Filling System . . . 50
4.5.3. Expansion Volume . . . 51

4.5.4. Programmable Logic Controller 52
4.6. Detectors 52
4.6.1. CCD and the X-ray Telescope 54
4.6.1.1. X-ray Telescope 55
4.6.1.2. The pn-CCD Detector 55
4.6.2. TPC 56
4.6.3. MicroMEGAS 59
4.6.3.1. Sunrise Micromegas 59
4.6.3.2. Sunset Micromegas 60
5. MICROMEGAS DETECTOR 61
5.1. Interactions of Particles in Matter 61
5.1.1. Interaction of Charged Particles 61
5.1.1.1. Energy Loss 62
5.1.1.2. Range of Slow Electrons 63
5.1.2. Interaction of Photons 64
5.1.2.1. Photoelectric Effect 65
5.1.2.2. Compton Scattering 67
5.1.2.3. Pair Production 67
5.2. Detection of Particles in Gaseous Detectors 67
5.2.1. Drift and Diffusion 68
5.2.2. Avalanche Multiplication 69
5.2.3. The Detector Gas 70
5.3. Working Principle of Micromegas 70
5.4. Micromegas Technologies 72
5.4.1. Conventional Micromegas 72
5.4.2. Bulk Micromegas 73
5.4.3. Microbulk Micromegas 73
5.5. CAST Micromegas Detectors 75
5.6. Characterization of CAST Microbulk Detectors 77
5.6.1. Experimental Setup 77
5.6.2. Method 78

5.6.3. Results . . . 79
6. SUNSET MICROMEGAS SYSTEM . . . 81
6.1. The Overview of the System . . . 81
6.2. Gas System . . . 82
6.2.1. Gas Purity Test . . . 83
6.3. Vacuum System . . . 84
6.4. Hardware Efficiency . . . 85
6.5. The Calibration System . . . 86
6.6. Shielding . . . 87
6.7. Data Acquisition System . . . 89
6.7.1. Electronics . . . 89
6.7.2. DAQ software . . . 91
6.8. Upgrades . . . 96
6.8.1. Cable Trays . . . 96
6.8.2. Shielding and Detector Upgrade . . . 97
6.8.3. Muon Veto Counter . . . 98
6.8.4. Calibrators . . . 99
7. ANALYSIS OF MICROMEGAS DETECTORS . . . 101
7.1. Data Reduction . . . 101
7.1.1. Strips . . . 101
7.1.1.1. Pedestal Calculation . . . 101
7.1.1.2. Clustering . . . 103
7.1.2. Mesh Pulse . . . 105
7.1.3. Gain Calculation and ROOT File Creation . . . 106
7.2. Background Selection . . . 107
7.2.1. List of Observables . . . 108
7.2.2. Multivariate Analysis . . . 110
7.2.3. Contour Cut Analysis . . . 113
8. BACKGROUND STUDIES . . . 116
8.1. Multivariate Analysis . . . 116
8.2. Contour Cut Analysis . . . 117

8.3. Comparison of Analysis Methods 119
9. DATA TAKING AND BACKGROUND LEVEL CALCULATION OF 2008 . 123
9.1. Data Taking Overview 123
9.1.1. The Sunset Micromegas Detectors that are used during 2008 . . 123
9.1.2. Incidents in 2008 Data Taking 124
9.1.3. Evolution of Cold Bore Pressure and Leak Problem 126
9.2. Detector Stability 128
9.2.1. Gain and Energy Resolution 128
9.2.2. Pulse and Strip Observables 128
9.2.3. Positional Analysis 129
9.2.3.1. B3 129
9.2.3.2. M6 130
9.2.3.3. M9 131
9.2.4. Electronic Noise Problems 132
9.3. Detector Efficiency 134
9.3.1. Software Efficiency 134
9.3.2. Total Efficiency 134
9.4. Tracking and Background Levels 135
9.4.1. Tracking Definition 136
9.4.2. Background Definition 136
9.4.3. Levels and Spectra 137
9.5. Study of Micromegas Systematics 139
9.5.1. Magnet Position 139
9.5.2. Compatibility with Poisson Distribution 140
10. COUPLING CONSTANT LIMIT FOR 2008 AXION SEARCH 143
10.1. Unbinned Likelihood Method 143
10.2. ^{3}He Dynamics 145
10.2.1. Gas Density 146
10.2.2. Effective Length 146
10.3. Results 148
10.3.1. Expected Number of Photons 148

10.3.2. Search for Axion Signal 149
10.3.3. Coupling Constant Limit and the Exclusion Plot 151
11. CONCLUSION 153
APPENDIX A: UNIT ANALYSIS 155
APPENDIX B: MAXIMUM LIKELIHOOD METHOD 157
B.1. Theory 157
B.2. Binned Likelihood Method 158
APPENDIX C: MICROMEGAS PLOTS 160
REFERENCES 169

LIST OF FIGURES

Figure 2.1. Axion-gluon interaction with a triangle fermion loop. g_{af} is the axion-fermion Yukawa coupling, while g_s is the strong coupling constant. 10

Figure 2.2. (a) The axion-photon interaction due to pion mixing. (b)The axion-photon interaction due to Primakoff effect. 11

Figure 2.3. Axion mass versus the coupling constant, depending on the E/N ratio for most widely accepted axion models. 13

Figure 2.4. The Hertzsprung-Russell diagram for 10637 stars in M3 [27]. The surface brighthess is plotted in y axis and increases towards the top while the surface temperature is plotted in x axis and increases towards left. 17

Figure 2.5. Cooling time vs. axion-nucleon coupling constant. In case of small or large couplings the cooling time would be affected minimally, while in between, axion-nucleon interaction would decrease the time significantly. Image taken from [9]. 18

Figure 2.6. Summary of excluded mass and PQ scale ranges due to different constraints. Image taken from [9]. 19

Figure 2.7. Schematics and different possible setups of photon regeneration experiments. 20

Figure 2.8. (a) Results of first generation haloscopes and ADMX [44]. (b) Recent results from ADMX [47]. 22

Figure 3.1. Primakoff Effect. 25

Figure 3.2. Differential solar axion flux at Earth. Note that the real flux depends on the value of coupling constant. 28

Figure 3.3. He^3 mass attenuation coefficient: Circles show the values taken from NIST database, continous line show the fit function. 33

Figure 3.4. (a) Conversion probability in vacuum for different energies. (b) Conversion probability with 10mbar of pressure for different energies, the vertical line shows effective photon mass for 10mbar, $m_\gamma = 0.33596$. 34

Figure 3.5. (a) Conversion probability for axions with energy 3keV, for pressures between 0-100 mbar, with step of 10mbar. (b) Total expected number of photons per unit area for 2 different densities. 35

Figure 4.1. The CAST magnet. 37

Figure 4.2. The exclusion plot produced from the result of CAST, including all detectors until 2009, and three micromegas detectors between 2009-2012. 38

Figure 4.3. Cross section of LHC dipole magnets. 39

Figure 4.4. Magnet feed box and flexible lines. 40

Figure 4.5. Drawing of the CAST Magnet and movement system. 41

Figure 4.6. Vertical and horizontal driving mechanisms. (a) Driving wheel and horizontal motor encoder. (b) Vertical movement jacks and vertical motor encoder. 42

Figure 4.7. Motor encoders vs. angles. 43

Figure 4.8. Non linearity of the encoder-angle relation. In each plot, a linear fit was done for encoders vs. angles, and this fit were subtracted from the angles. (a) Deviation of horizontal angle. (b) Deviation of vertical angle. 44

Figure 4.9. Horizontal encoder coverage for trackings throughout the year. Each line denotes the coverage of a tracking. Gaps are due to not having trackings in specific parts of the year. 44

Figure 4.10. Labview based tracking software. 45

Figure 4.11. 2008 Sun Filming. (a) The deviation from the center of the Sun in pixels. (b) Analysis software that calculates the position of the center of the Sun. 46

Figure 4.12. Slow Control software. 48

Figure 4.13. The schematics of the gas pipes inside of the cryostat. Green parts denote the cold windows and horizontal red pipes are the cold bores of the magnet. Yellow pipes denote the various vacuum parts of the system. 49

Figure 4.14. (a) Photo of the cold window and its strongback. (b) Schematic drawing of the cold window. 49

Figure 4.15. (a) Photo of the gas system. (b) Filling scheme used during 2008. 51

Figure 4.16. A photo from the installation of the expansion volume. 52

Figure 4.17. User interface of the CAST PLC System. 53

Figure 4.18. (a) The photo of the X-ray telescope and pn-CCD detector. (b) The combined efficiency of the telescope system and the pn-CCD for $1 - 10$keV range. 54

Figure 4.19. (a) The comparison of the aperture of the cold bore and the X-ray telescope. (b) The pn-CCD chip. 55

Figure 4.20. The exploded view of the CAST TPC. 57

Figure 4.21. The schematics of the working principle of the CAST TPC [80]. . 58

Figure 4.22. Different shielding setups of the sunrise micromegas. (a) The detector with the compact shielding. (b) The detector with the additional layers of polyethylene shielding. (c) Latest addition to the shielding. 60

Figure 4.23. Drawing of the sunrise micromegas. 60

Figure 5.1. dE/dx in air for different particles. Plot taken from [83]. At high energies, differential energy loss becomes almost sames for all particles, independent of their mass, until radiative effects become considerable. 63

Figure 5.2. (a)Landau distribution, with a cutoff at maximum energy transfer E_M. The green and red curves show the most probable and average energy transfers. (b)Range of electrons from 1 to 100keV in 1.4 bar Argon in room temperature. 63

Figure 5.3. Cross section of different photon interactions in (a) Lead, (b) Argon. X axis shows the energy of the beam, while y axis shows the cross section, which is proportional to the interaction probability. 65

Figure 5.4. The working principle of the micromegas detector. 71

Figure 5.5. The funnel like shape of the electric field lines around the micromesh. Units are in microns. Plot taken from [86]. 72

Figure 5.6. (a) Pillars in the bulk micromegas are separated 2mm from each other. (b) The woven mesh has a pitch of 80μm. 74

Figure 5.7. (a) The readout pads of the microbulk micromegas. First axis is connected at the pad level, while second axis is connected in an additional layer. (b) Mesh holes, that are grouped by nine are aligned with the readout pads. 74

Figure 5.8. Photo of two sides of a microbulk micromegas detector without the readout cards and plexiglas chamber. 76

Figure 5.9. (a)Photo of the strip plane. (b) Plexiglas chamber and aluminized mylar drift window connected to micromegas detector. 76

Figure 5.10. (a) The experimental setup of the characterization tests. (b) The positioning of the ^{55}Fe source. 78

Figure 5.11. An example spectra from the characterization measurements. The ^{55}Fe peak is at channel 230, where the escape peak can be seen around channel 120. 79

Figure 5.12. (a) Electric field ratio vs. electron transparency. The transparency of the highest gain is normalized to 1. (b) Amplification field vs. energy resolution(continuous lines) and gain(dashed lines). 80

Figure 6.1. Drawing of the sunset micromegas. 81

Figure 6.2. Simplified schematics of sunset micromegas vacuum and gas systems. 82

Figure 6.3. Schematics of the sunset micromegas gas system. 83

Figure 6.4. The results of gas purity tests. (a) The model to fit the data. (b) The PPM of both gases for different flows compared with the energy resolution. There is no significant effect observed even for high impurities. 84

Figure 6.5. The schematics of the sunset micromegas vacuum system. 85

Figure 6.6. The hardware efficiency curve of sunset micromegas. 86

Figure 6.7. The schematic representation of the calibration system, viewed from the back of the detectors. 87

Figure 6.8. (a) Drawing of the shielding. (b) The inner view before the shielding is installed. (c) Inner Faraday cage. (d) Shielding with the lead bricks. 88

Figure 6.9. (a) Gassiplex card: On the bottom, lemo connectors of clear, clock, track and hold, and output signal can be seen. (b) A gassiplex card connected to the micromegas detector. 90

Figure 6.10. (a) Sketch of the important signals in the micromegas DAQ chain. (b) The strips gain of different runs with different delay values. The highest gain was obtained when the delay was set to 900ns. 91

Figure 6.11. An example 12 hour run schedule of Sunset Micromegas. The run starts with a 1 minute pedestal run, common for both detectors, continued with calibrations of each detector, and a common background run. 92

Figure 6.12. (a)RunControlAll.vi: The main panel of the software, that is used to set auto/manual mode, start and stop runs.(b)RunControlMonitor.vi: Displays information about the run. (c) RunEvd.vi: Displays mesh and strip signals. 93

Figure 6.13. The electronics chain of the Sunset Micromegas. 95

Figure 6.14. (a) General view of the cable trays and the electronics. (b) View of the cables inside the cable tray. 96

Figure 6.15. (a) Drawing of sunset micromegas shielding, (b) Exploded view of the inner part of the shielding. 98

Figure 6.16. The different stages of installation of sunset micromegas. 99

Figure 6.17. The muon veto counter. 100

Figure 6.18. (a) The control box of the calibrators. (b) The source manipulator. (c) View of the source inside the vacuum pipe. 100

Figure 7.1. The mean and sigma of pedestals for x and y channels for M9 detector. 103

Figure 7.2. A single cluster event that has multiplicity eight, with two non-hit strips inside. 105

Figure 7.3. A sample mesh pulse from ^{55}Fe calibration with explanation of mesh observables. 105

Figure 7.4. The spectra and Gaussian fits to three gain observables. 107

Figure 7.5. Risetime distribution for 6 and 3keV events. The energy from the escape peak has the same mean, but higher standard deviation. . . 112

Figure 7.6. The distribution of the q value for main and escape peaks during the calibration. (a) Non-corrected q value. (b) Corrected q value, with $a = 1.1$. 113

Figure 7.7. (a) Selection region of the risetime-width cut is indicated in red. (b) The effect of the same cut on the background data, where selected events account for 5% of the all events. 114

Figure 7.8. Risetime - width distribution during a single calibration run. All events are shown in green, while red region shows the selection region. 115

Figure 8.1. The efficiency vs. FOM curves for events in $5 - 7$keV range. . . . 118

Figure 8.2. The efficiency vs. FOM curves for events in $2-5$keV range. The efficiency of the low energy events are fine tuned by varying the energy correction factor. 119

Figure 8.3. Comparison of efficiencies. 120

Figure 8.4. Comparison of background rates. 121

Figure 8.5. Comparison of FOM for different methods. FOM is directly related with the sensitivity of CAST experiment, thus is the most essential parameter in choosing of the discrimination method. 121

Figure 9.1. Increase of the precision value of the tracking software during the evening shift on 14.08.2008. 125

Figure 9.2. (a) Evolution of P_{check} during an evening shift. (b) Evolution of P_{check} throughout the year, using values of the pressure at 15:00 every day. The gaps are due to the incidents explained in Section 9.1.2. 127

Figure 9.3. The time exposure histogram of P_{check}, with bin size as 0.001mbar. From 13.4mbar to 33.7mbar B3 and M6 are operational; for pressures higher than 37.3mbar, only M9 is operational. 128

Figure 9.4. Hitmaps of B3, from the events that form clusters, from the run 10544. (a) Calibration hitmap. (b) Background hitmap. 129

Figure 9.5. Cumulative hitmap of background events in B3 after background selection. Tracking and background counts are shown in different colors. 130

Figure 9.6. Hitmaps of M6, from the events that form clusters, from the run 10544. (a) Calibration hitmap. (b) Background hitmap. 130

Figure 9.7. Cumulative hitmap of background events in M6 after background selection. Tracking and background counts are shown in separate plots. The noisy area in the background can be seen in the left bottom part of the coldbore circle. 131

Figure 9.8. Closeup look at the noisy area in the detector M6. 131

Figure 9.9. Cumulative hitmap of background events in M6 after removal of the noisy area. 132

Figure 9.10. Hitmaps of M9, from the events that form clusters, from the run 11085. (a) Calibration hitmap. (b) Background hitmap. 132

Figure 9.11. Cumulative hitmap of background events in M9 after background selection. Tracking and background counts are shown in separate plots. 133

Figure 9.12. The deadtime as percentage in the sunset micromegas overall the year. 133

Figure 9.13. Software efficiency curves for all three detectors. 135

Figure 9.14. Total efficiency of all three detectors. 135

Figure 9.15. Comparison of tracking and background levels, using 100 hours of background data for each tracking. (a) B3, (b) M6, (c) M9. 137

Figure 9.16. Comparison of tracking and background levels, using the run that includes the tracking data. (a) B3, (b) M6, (c) M9. 138

Figure 9.17. The cumulative background and tracking energy spectrum of 2008 Sunset Detectors. (a) B3, (b) M6, (c) M9. 140

Figure 9.18. The schematics for the time binning for calculation of count rate statistic. In case of gas transfer, the two half trackings are binned separately, not to include the gas transfer time in calculation. . . . 141

Figure 9.19. Compatibility of background and tracking count rates with Poissonian statistics considering a time bin of 0.35 hours. (a) B3, (b) M6, (c) M9. 142

Figure 10.1. (a) Density profile in the magnet for pressure 14mbar. The red lines show the DST while the dashed vertical lines show the length of the gas volume within the DST. (b) Parametrization of effective length for warm(red) and cold(blue) windows. 147

Figure 10.2. Density exposure of all three detectors(dashed lines) and combined exposure(solid line). 149

Figure 10.3. (b) Expected number of photons during 2008 data for all sunset micromegas, depending on the axion mass, assuming coupling constant $g_{a\gamma} = 10^{-10}$. 149

Figure 10.4. Likelihood function for $m_a = 0.451$eV, plotted as a function of g_{10}^4. 150

Figure 10.5. Deviation of maximum likelihood from the null hypothesis for the axion masses CAST was sensitive in 2008. The deviation is in terms of left sigma of the distribution. 151

Figure 10.6. The exclusion plot of 2008 data for all three sunset detectors(dashed lined), and combined(black line) exclusion plot. 152

Figure C.1. The number of observables vs. the background levels, for B3. . . 160

Figure C.2. The number of observables vs. the background levels, for M6. . . 160

Figure C.3. The number of observables vs. the background levels, for M9. . . 160

Figure C.4. The observable pairs vs. FOM for low and high energy events, for B3. 161

Figure C.5. The observable pairs vs. FOM for low and high energy events, for M6. 161

Figure C.6. The observable pairs vs. FOM for low and high energy events, for M9. 162

Figure C.7. The gain of pulse amplitude and strip charge in fADC units during the calibrations for B3 and M9. The period when each detector is used and an unstable period of operation is shown in different background colors. 162

Figure C.8. The gain of pulse amplitude and strip charge in fADC units during the calibrations for M6. 162

Figure C.9. Evolution of the energy resolution for B3 and M9, given in FWHM percentage at 5.96keV. 163

Figure C.10. Evolution of the energy resolution for M6, given in FWHM percentage at 5.96keV. 163

Figure C.11. Evolution of pulse risetime for B3 and M9. Different detectors are indicated by different background colors. 163

Figure C.12. Evolution of pulse risetime for M6. 164

Figure C.13. Evolution of strip multiplicity for B3 and M9. Different detectors are indicated by different background colors. 164

Figure C.14. Evolution of strip multiplicity for M6. 164

Figure C.15. Evolution of the software efficiency for B3. 165

Figure C.16. Evolution of the software efficiency for M6. 165

Figure C.17. Evolution of the software efficiency for M9. 165

Figure C.18. Background rate in counts/hour at different magnet positions for B3.166

Figure C.19. Background rate in counts/hour at different magnet positions for M6. 166

Figure C.20. Background rate in counts/hour at different magnet positions for M9. 167

Figure C.21. Background rate and its standard deviation for each bin for B3. . 167

Figure C.22. Background rate and its standard deviation for each bin for M6. . 167

Figure C.23. Background rate and its standard deviation for each bin for M9. . 168

LIST OF TABLES

Table 4.1. The Run History of CAST. 38

Table 6.1. Data Format of Micromegas Raw Files. 94

Table 8.1. Best Observable Combinations Using Multivariate Analysis: Observables that give the highest FOM for both 6 and 3keV events are chosen. 118

Table 8.2. Selected observable pairs for contour cuts. 120

Table 9.1. Run Statistics of 2008 Sunset Detectors. 124

Table 9.2. The Background and Tracking Levels of Sunset Micromegas Detectors. 139

Table A.1. Conversion to Natural Units. 155

LIST OF SYMBOLS

c	Speed of light
f_a	Peccei-Quinn scale
$g_{a\gamma}$	Axion - 2 Photon coupling constant
g_{ae}	Axion - Electron coupling constant
$\hbar$	Reduced Planck constant
$\mathcal{L}$	Lagrangian
k_B	Boltzmann constan
m_a	Axion mass
m_γ	Effective photon mass
Γ	Inverse absorption length
ω_{pl}	Plasma frequency
θ_C	Cabibbo angle

LIST OF ACRONYMS/ABBREVIATIONS

ABRIXAS	A BRoad band Imaging X-ray All-sky Survey
ADMX	Axion Dark Matter Experiment
AFS	Andrew File System
ALPS	Any Light Particle Search
BFRT	Brookhaven Fermilab Rutherford Trieste
CAST	CERN Axion Solar Telescope
CCD	Charge Coupled Device
CDMS	Cryogenic Dark Matter Search
CDM	Cold Dark Matter
CERN	European Organization for Nuclear Research
CL	Confidence Level
CP	Charge Parity
CRAM	CAEN Readout for Analog Multiplexed Signals
DAQ	Data Acquisition
DELPHI	DEtector with Lepton, Photon and Hadron Identification
DFSZ	Dine Fischler Srednicki and Zhitnitski
DST	Density Stability Threshold
EDMN	Electron Dipole Moment of Neutron
FOM	Figure of Merit
FWHM	Full Width Half Maximum
GammeV	A Gamma to milli-eV Particle Search
HB	Horizontal Branch
HDM	Hot Dark Matter
KSZV	Kim Shiftman Vainshtein and Zakharov
LEP	Large Electron Positron Collider
LHC	Large Hadron Collider
MACHOS	Massive Compact Halo Objects
MFB	Magnet feed box

Micromegas	MICRO MEsh GAseous Structure
MPGD	Micro Pattern Gaseous Detectors
MRB	Magnet return box
MWPC	Multiwire Proportional Chambers
NIM	Nuclear Instrumentation Module
NOVAS	Naval Observatory Vector Astrometry Software
OSQAR	Optical Search of QED Vacuum Magnetic Birefringence, Axion and Photon Regeneration
PDF	Probability Density Function
PLC	Programmable Logic Controller
PPM	Parts Per Million
QCD	Quantum Chromodynamics
RGB	Red Giant Branch
TCP	Time Charge Parity
TPC	Time Projection Chamber
WIMPS	Weakly Interacting Massive Particles
WMAP	Wilkinson Microwave Anisotropy Prob

1. INTRODUCTION

The Standard Model of particle physics explains the elementary particles and their interactions to a great extend with some problems and unanswered questions. One of the problems is the Strong CP problem, which is the non-observation of CP violation in strong interactions. A widely accepted possible solution to this problem is called the Peccei-Quinn mechanism and it gives rise to a hypothetical particle called axion, which is a light, very weakly interacting neutral pseudoscalar boson. The weak interacting nature of axions makes them also a viable dark matter candidate.

Axions, interacting weakly with known forces, have a special interaction with photons, called the Primakoff effect. Via Primakoff conversion, the axions and photons can be converted into each other in transverse magnetic or electric fields, with a probability depending on the coupling constant of the interaction, axion mass, the conversion medium, field strength and the length of the field.

Axions, if they exist, can be created in the laboratories, or are naturally generated during the evolution of the universe. A common axion creation mechanism takes place in the hot plasma in the core of the stars. In particular in the solar core, the blackbody x-ray photons that are emitted in all directions, pass through the high electric field of the atoms and some of them should be converted into axions. The axions travel to the earth and can be detected by specialized systems.

Among several axion detection methods, the one that gives a good sensitivity for a wide range of axion masses is the helioscope technique, which is based on converting the solar axions into photons in magnets, aligning the magnetic field perpendicular to the axion trajectory. Helioscope experiments can be done in vacuum being sensitive to axion masses less than a certain value, or with a buffer gas being sensitive to a very narrow band of axion masses.

CAST experiment is a helioscope based at CERN and aims to convert the axions

coming from the sun back into photons using a superconducting LHC dipole magnet, which has two bores with 14.55cm^2 area, 9.26m length and 8.8T magnetic field. CAST magnet is built on a movement system, that allows it to track the sun for 1.5 hours during sunrise and sunset. On each side of the magnet, there are in total two x-ray detectors, placed to detect the photons converted from axions. The detectors after tracking the sun for 1.5 hours, take background data during the rest of the day. The tracking and background data are compared to observe any excess of detected x-rays during the tracking. The commissioning of CAST started in 2000 and it has been taking data since 2003. The first years of the CAST was dedicated to vacuum run, while the later years utilized ^{3}He and ^{4}He as buffer gas to probe higher mass axions. Since the beginning of CAST experiment, TPC, CCD, Calorimeter and Micromegas detectors have been used, and since 2008 CAST operates with three micromegas and a CCD detector.

The Micromegas is a recent technology, based on ideas of MWPC, and gives better energy and time resolution than conventional MWPC. The CAST micromegas has a two dimensional strip readout, built on an area of 6cm $\times$ 6cm, with addition of a micromesh. The energy of the incoming particles can be given by mesh signal and strip signals separately, and the position of the interaction is given by the signal on the strips. The micromegas detectors at CAST operate at 1.4bar, with mixtures of Argon-Isobutane and can show energy resolutions as good as 12% FWHM at 5.96keV.

In the sunset side of the CAST magnet(where sunset axions are detected), there are two micromegas detectors that were installed for the first time in 2007, replacing the TPC detector. The sunset micromegas detectors had good performance in their first year, however there were periods with excessive electronic noise or instability that lead to loss of data. The micromegas detectors were calibrated twice a day, and each event that is observed in the detectors during the day is accepted or rejected as x-ray by pattern recognition algorithms which define multi dimensional selection regions. Selection method is optimized to have a high software efficiency and low background level.

The 2008 data taking of CAST was carried out between 28.03.2008 to 13.11.2008, and axion masses from 0.38 to 0.65eV were probed by sunset micromegas, by increasing the amount of ^{3}He buffer gas in the magnet bore every day. Due to a leak of ^{3}He in the system, calculated and measured gas densities differed, and CAST needed to rely more strongly on the measured values. The leak also resulted in some gaps in the axion mass range CAST aimed to probe.

To determine if CAST detected axions, unbinned maximum likelihood analysis is used. With no statistical excess observed, limit on the coupling constant have been set. Based on these result, CAST probes deeper into region of axion models that are physically favoured.

2. THEORY OF AXIONS

2.1. CP Violation in Weak Interactions

In physics, some transformations are linked with symmetries. If a system is not invariant under a transformation, symmetry is said to be violated, or broken.

Charge conjugation(C) and parity(P) are two important physical transformations. C transforms a particle into its antiparticle, changing the sign of all its internal quantum numbers, leaving spin, mass, momentum and energy unchanged. We know that electromagnetism, strong interactions and gravity are invariant under C, while weak interactions are not. P is the transformation changing the sign of spatial coordinates of the particle. Similar to C, P is broken under weak interactions. Violation of both symmetries can be observed by looking at neutrinos. While neutrinos are left handed, anti-neutrinos are right handed. But both C and P transformations, create a right handed neutrino or left handed anti-neutrino, which doesn't exist.

After realization of violation of C and P symmetries separately, CP, combination of C and P was thought to be a universal symmetry. However, in 1964 an experiment done by James Cronin and Val Fitch showed evidence of CP violation in decay of K_0 and $\overline{K_0}$.

The weak interactions of quarks brought the idea of Cabibbo angle θ_c. The decay rates of $d \to u + W^-$ and $s \to u + W^-$ are proportional to $\cos\theta_c$ and $\sin\theta_c$, where $\theta_c = 13.15°$. Many interaction rates supported this scheme. Similarly decay rate K_0 was expected to be proportional to $\cos\theta_c \sin\theta_c$, since it included both vertices for $d \to u + W^-$ and $s \to u + W^-$. However it appeared that the rate was much higher than calculated. This lead to the prediction of a new quark "charm", its couplings to d and s quarks being proportional to $\cos\theta_c$ and $-\sin\theta_c$. This shows that interactions conserving quark generation are favored and quark states appear as combinations in

weak interactions as

$$d' = d\cos\theta_c + s\sin\theta_c \quad s' = -d\sin\theta_c + d\cos\theta_c$$

This can be expressed in matrix formulation as

$$\begin{pmatrix} d' \\ s' \end{pmatrix} = \begin{pmatrix} \cos\theta_c & \sin\theta_c \\ \sin\theta_c & \cos\theta_c \end{pmatrix} \begin{pmatrix} d \\ s \end{pmatrix} \quad or \quad \begin{pmatrix} d' \\ s' \end{pmatrix} = \begin{pmatrix} V_{ud} & V_{us} \\ V_{cd} & V_{cs} \end{pmatrix} \begin{pmatrix} d \\ s \end{pmatrix}$$

V_{ij}^2 being proportional to the decay rate of i quark to j quark. However, CP violation can not be incorporated to a model with two quark families. Kobayashi and Maskawa extended the idea to a third quark family, creating the CKM matrix.

$$\begin{pmatrix} d' \\ s' \\ b' \end{pmatrix} = \begin{pmatrix} V_{ud} & V_{us} & V_{ub} \\ V_{cd} & V_{cs} & V_{cb} \\ V_{td} & V_{ts} & V_{tb} \end{pmatrix} \begin{pmatrix} d \\ s \\ b \end{pmatrix}$$

Elements of the matrix can be expressed in terms of three quark mixing angles, and a phase factor, which is the source of CP violation.

2.2. Theoretical Motivation for Axions

CP violation in weak interactions gives rise to this question: "Why is CP conserved in strong interactions?". Quantum Chromodynamics (QCD) is expected to be a CP violating theory, while it has not been observed. Furthermore matter domination in the universe also shows CP must have been violated at some point after big bang to a greater extend. CP violations in weak interactions is quite small to account for the ratio of anti-matter to matter.

2.2.1. The $U(1)_A$ Problem

QCD Lagrangian can be written as follows

$$\mathcal{L}_{QCD} = \sum_f \bar{q}_f \left(\gamma^\mu \frac{1}{i} D_\mu + m_f \right) q_f - \frac{1}{4} G_a^{\mu\nu} G_{a\mu\nu}$$

where f runs in quark flavors. In the Lagrangian, q_f is the quark field, γ^μ is the Dirac matrices, m_f is the quark mass and $G_{a\mu\nu}$ is the gluonic field tensor, analogy of $F^{\mu\nu}$, electromagnetic field tensor. In the limit $m_f \to 0$, chiral rotations of the quark states into each other is a global symmetry: $U(f)_R \times U(f)_L$. However only m_u and m_d are small enough to be approximated to zero in QCD scale (Λ_{QCD}), and one has an approximate chiral $U(2)_R \times U(2)_L$ symmetry. There are two subgroups of this symmetry: vectorial $U(2)_V (V = R + L)$ and axial $U(2)_A (A = R - L)$. Vectorial part is an exact symmetry and implies conservation of baryon number, however axial part is not observed yet. This means $U(2)_A$, thus $U(2)_R \times U(2)_L$ is spontaneously broken and one should observe 4 pseudoscalar Nambu-Goldstone bosons. Three of them are the pion triplet (π^+,π^0 and π^-). There should be a 4th particle with smaller mass, however there exist no such particle. This is called $U(1)_A$ problem, since the unobserved particle is the Nambu-Goldstone boson of $U(1)_A$ broken symmetry [1].

2.2.2. Strong CP Problem

It is pointed out by 't Hooft [2] that the problem arises from a chiral anomaly of $U(1)_A$. $U(1)_A$ is not a quantum symmetry and the 4th Nambu-Goldstone boson doesn't exist. Furthermore an extra CP violating term can be added to QCD Lagrangian,

$$\mathcal{L}_\theta = \bar{\theta} \frac{g^2}{32\pi} G_{a\mu\nu} \tilde{G_a^{\mu\nu}}$$

where θ is the parameter defining the strength of the CP violation and g is strong coupling constant. QCD, being a non-Abelian gauge theory, has a complex vacuum structure. Gauge transformation transforms the vacuum state n into vacuum state

$n+1$. A gauge invariant vacuum state(θ-vacuum) should be an eigenstate of gauge transformation, and is the superposition of all possible states as

$$|\theta\rangle = \sum_n e^{-in\theta}|n\rangle$$

However, θ transforms under $U(1)_A$ as follows,

$$\bar{\theta} = \theta + \mathrm{Arg}(\mathrm{det}M)$$

While the first term represents QCD contribution, second term $\mathrm{Arg}(\mathrm{det}M)$ represents the electroweak source of the CP violation, M being the quark mass matrix.

It is shown that there is indeed a CP violating term in the QCD Lagrangian, that can provide a solution to $U(1)_A$ problem. But this creates a new problem. Why is the CP violation not observed in strong interactions? One of the finest measurements of the value of $\bar{\theta}$ is done by measuring electric dipole moment of neutron(EDMN). EDMN violates P and T symmetries. According to TCP theorem, we expect it to violate CP symmetry. If the parameter $\bar{\theta}$ is not extremely low, one expects to observe a large value for EDMN. However, last measurements show that [3]

$$|d_n| < 2.9 \cdot 10^{-26} e \text{ cm } (90\% \text{ C.L.})$$

This implies that $\bar{\theta} < 10^{-9}$. Puzzling thing is why this parameter is so low, while there is no limiting factor on its value(i.e. it can take any value between 0 and 2π with the same likelihood). Either both QCD and electroweak contributions are in the order of $\bar{\theta}$ or two terms cancel each other resulting in such a small value. This fine tuning is called the Strong CP Problem.

There were several solutions proposed for Strong CP Problem such as unconventional dynamics, spontaneously broken CP, and addition of a chiral symmetry. Among these the third one, also known as Peccei Quinn solution is a widely accepted solu-

tion [4].

2.2.3. Peccei-Quinn Mechanism

Peccei and Quinn proposed a neat solution to the Strong CP Problem. Standard model Lagrangian is invariant under a global chiral $U(1)$ symmetry, and one can add this to the Lagrangian. This additional symmetry is called $U(1)_{PQ}$. It is not an exact symmetry, thus is spontaneously broken at some scale f_a. Breaking of this symmetry gives rise to its pseudo Nambu-Goldstone boson: axion. The effect of Peccei Quinn symmetry is making the CP violating angle θ a dynamical variable(due to interactions of the axion field $a(x)$) instead of a parameter of the model. Upon the breaking of this symmetry, this parameter is set to 0 dynamically. Axion field transforms as

$$a(x) \to a(x) + \alpha f_a$$

where α is the phase parameter. With addition of Peccei-Quinn symmetry, axion terms are added to the standard model Lagrangian.

$$\mathcal{L}_{SM}^{\text{axion}} = +\bar{\theta}\frac{g^2}{32\pi}G_a^{\mu\nu}\tilde{G_{a\mu\nu}} - \frac{1}{2}\partial_\mu a \partial^\mu a + \mathcal{L}_{\text{int}}[\partial^\mu a/f;\psi] + \frac{a}{f}\xi\frac{g^2}{32\pi}G_a^{\mu\nu}\tilde{G_{a\mu\nu}} \tag{2.1}$$

First term is the coupling with gluons, second term accounts for the kinetic energy of axion, third term is for the interactions with a field ψ and last term is the effective potential for the axion field, ξ being model dependent. Minimizing this potential, one can get the expectation value of the axion field $\langle a \rangle$. The minimization of the potential is done as

$$\left\langle \frac{\partial V\text{eff}}{\partial a} \right\rangle = \frac{\xi}{f}\frac{g^2}{32\pi}\langle G_a^{\mu\nu}\tilde{G_{a\mu\nu}}\rangle\Big|_{\langle a\rangle} = 0 \tag{2.2}$$

It was shown by Peccei and Quinn that

$$\langle a \rangle = -\frac{f}{\xi}\bar{\theta} \tag{2.3}$$

Thus first and last terms in the Equation 2.1 cancels out, removing the CP violating term with θ from the Lagrangian. One can see it as follows: Lagrangian can be written in terms of physical axion field $a_{\text{phys}} = a - \langle a \rangle$, and this Lagrangian will not contain a CP violating term. Furthermore one can expand V_{eff} at $\langle a \rangle$ and get the axion mass from the second order term.

$$m_a^2 = \left\langle \frac{\partial^2 V\text{eff}}{\partial a^2} \right\rangle = -\frac{\xi}{f}\frac{g^2}{32\pi}\frac{\partial}{\partial a}\langle G_a^{\mu\nu}\tilde{G_{a\mu\nu}}\rangle\Big|_{\langle a\rangle} \tag{2.4}$$

2.3. Couplings of Axions

2.3.1. Coupling to Gluons

As the physical axion field is introduced, the CP violating terms cancel out in the Equation 2.1 but the following new term remains, according to which axions couple to gluons.

$$\mathcal{L}_{Ga} = \frac{\alpha_s}{8\pi f_a} G_a^{\mu\nu}\tilde{G_{a\mu\nu}} a \tag{2.5}$$

with $\alpha_s = g^2/4\pi$. This coupling gives rise to axion-pion mixing, and axion mass can be estimated as

$$m_a^2 = \frac{f_\pi^2 m_\pi^2}{f_a^2}\frac{z}{(1+z+w)(1+z)} \tag{2.6}$$

where $f_\pi = 93\text{MeV}$ is the pion decay constant, $m_\pi = 135\text{MeV}$ is the pion mass, $z = m_u/m_d$ and $w = m_u/m_s$ are mass rations of quarks. By using $z = 0.55$ and $w = 0.029$ from [5], one gets the following relation between the axion mass and the Peccei-Quinn scale

$$m_a = \frac{1}{f_a} 6\text{eV} \cdot 10^6\text{GeV}$$

The Feynmann diagram of axion-gluon coupling is presented in Figure 2.1.

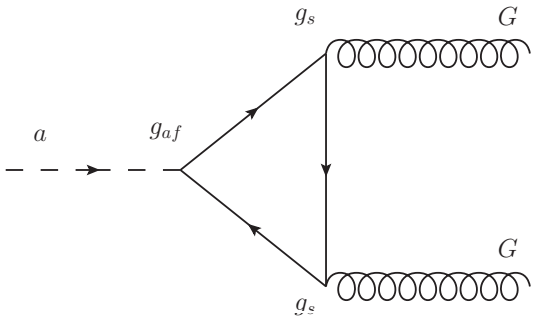


Figure 2.1. Axion-gluon interaction with a triangle fermion loop. g_{af} is the axion-fermion Yukawa coupling, while g_s is the strong coupling constant.

2.3.2. Coupling to Photons

Axions can couple to photons in two ways. First is due to the axion-pion mixing, through the 2γ decay channel of the neutral pions(Figure 2.2a). The second is the Primakoff Effect(See Section 3.1), which occurs with a triangle loop of a fermion carrying PQ charge. The interaction takes place according to the Lagrangian

$$\mathcal{L}_{a\gamma\gamma} = \frac{-1}{4} g_{a\gamma} F_{\mu\nu} \tilde{F}^{\mu\nu} a = g_{a\gamma} \mathbf{E} \cdot \mathbf{B} a \tag{2.7}$$

where $F_{\mu\nu}$ is the electromagnetic field-strength tensor, $\tilde{F}^{\mu\nu}$ its dual, $\mathbf{E}$ and $\mathbf{B}$ are electric and magnetic fields, a is the axion field and $g_{a\gamma}$ is the coupling constant [6]. The Feynmann diagram of this interaction is shown in Figure 2.2b.

The coupling constant of axion-photon interactions can be expressed in terms of f_a, electromagnetic anomaly E, color anomaly N and quark mass ratios as follows [7]

$$g_{a\gamma} = \frac{\alpha}{2\pi f_a} \left(\frac{E}{N} - \frac{2(4+z+w)}{3(1+z+w)} \right) \tag{2.8}$$

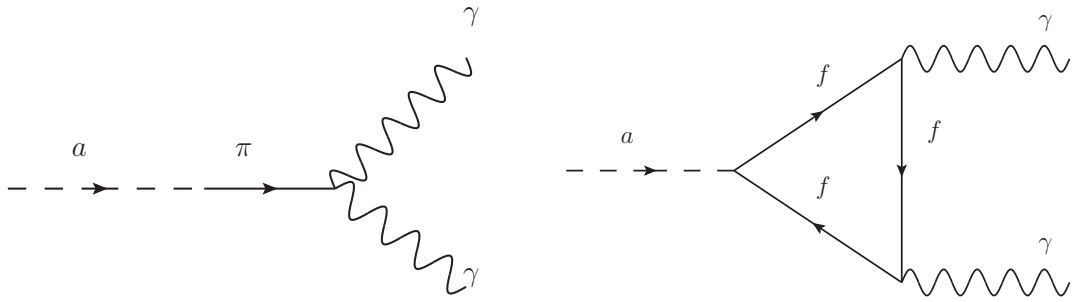


Figure 2.2. (a) The axion-photon interaction due to pion mixing. (b)The axion-photon interaction due to Primakoff effect.

and can be rewritten using the standard values for z and w.

$$g_{a\gamma} = \frac{\alpha}{2\pi f_a}\left(\frac{E}{N} - 1.93 \pm 0.08\right) \tag{2.9}$$

E/N is a model dependent ratio, that determines the strength of axion-photon coupling and defines the relation between m_a and $g_{a\gamma}$, which is also called the "axion line" as seen in Figure 2.3.

2.3.3. Coupling to Fermions

The axions couple to fermions in some models and the Lagrangian term of the interaction is

$$\mathcal{L}_{af} = \frac{g_{af}}{2m_f}\bar{\Psi}_f\gamma^\mu\gamma_5\Psi_f\partial_\mu a \tag{2.10}$$

where m_f is the mass of the fermion in the interaction, Ψ_f is the fermion field, the coupling constant $g_{af} = C_f m_f/f_a$, with C_f being the model-dependent effective PQ charge. One can consider the g_{af} as the Yukawa coupling and $\alpha_{af} = g_{af}^2/4\pi$ as the fine structure constant [8, 9].

Depending on the model, axions can couple to fermions in tree level, furthermore

Peccei-Quinn charge of electrons and nucleons vary according to the model that is used.

2.4. Axion Models

The Peccei-Quinn scale f_a determines the properties of the axion, which is pseudoscalar and very weakly interacting particle. A large f_a results with weakly coupled and light particle. On the other hand if f_a smaller, a heavier axion is expected. The relation of axion mass(m_a) and coupling to other particles(g_a) with f_a can be summarized as: $m_a \propto 1/f_a$ and $g_a \propto 1/f_a$.

2.4.1. Visible Axion Models

The first proposed axion models were *Visible Axion Models* [10, 11], in which the Peccei-Quinn scale f_a is in the order of the electroweak scale $f_{EW} \sim 250GeV$. A requirement for visible models is existence of two independent Higgs fields, which give mass to u and d quarks.

These *standard axion* models were excluded by the following kaon decay

$$K^+ \rightarrow \pi^+ a$$

The experimental limit on this decay is lower than the expected branching ratio resulting from the visible models [12].

2.4.2. Invisible Axion Models

The exclusion of the visible models gave motivation for the models with $f_a \gg f_{EW}$, which are also called *Invisible Axion Models*. The mass and coupling of axions in these models are much lower than visible models. In invisible models, there is a Higgs field with large vacuum expectation value $f_a/2$.

2.4.2.1. KSZV Model. First invisible model was proposed by Kim, Shiftman, Vainshtein and Zakharov [13,14]. This model requires the existence of a new heavy quark Q that carries the Peccei-Quinn charge, and forbids the tree-level coupling with fermions as none of them carry Peccei-Quinn charge. The axion interaction in this model occurs mainly through the new exotic quark, thus axions in this model are considered as "hadronic axion".

In KSZV models, E/N can take different values as in Equation 2.8. While the standard KSZV model has the ratio $E/N = 0$, there are variations such as $E/N = 2$, suppressing the coupling with photons.

2.4.2.2. DFSZ Model. Another model is proposed by Dine, Fischler, Srednicki and Zhitnitski in which the ordinary quarks and leptons carry Peccei-Quinn charge, thus they can interact with axions in tree-level [15]. The advantage of this model is not having a necessity for an additional exotic quark. In DFSZ Model $E/N = 8/3$. The comparison of coupling constant and axion mass for different E/N ratios are plotted in Figure 2.3.

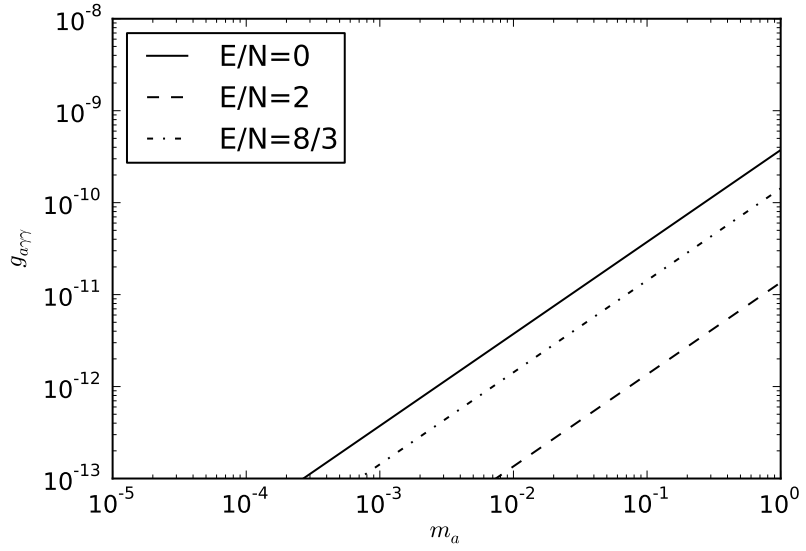


Figure 2.3. Axion mass versus the coupling constant, depending on the E/N ratio for most widely accepted axion models.

2.5. Limits on Axion Couplings and Mass

Since axion is a weakly interacting particle, it has remained undetected till the day. Especially looking at astronomical objects one can determine rough limits on properties of axion. The ability to impose limits come from the fact that if axion coupling was high enough, the predicted energy loss in astronomical objects would be higher than measured, causing incompatibility with the expectations.

In this section cosmological constraints and four different astrophysical observations that let one to set limits on axion properties will be explained.

2.5.1. Axions and Dark Matter and Cosmological Constraints

Dark matter is kind of matter that does not interact with other matter to produce radiation, but can be predicted to exist via gravitational effects, such as rotation curves of the galaxies and gravitational lensing [16]. According to recent WMAP results, it forms 84% of the matter content in the universe [17] and 23% of the mass-energy content.

The weakly interacting nature of axions make them an important candidate for the dark matter. Other popular non-baryonic candidates are exotic or standard model neutrinos, supersymmetric particles, Weakly Interacting Massive Particles(WIMPS) and Massive Compact Halo Objects(MACHOS).

Dark matter can be Hot Dark Matter(HDM), particles that are very light and travel with relativistic speeds, or Cold Dark Matter(CDM), which are result of particles that are heavier and that travel with non-relativistic speeds, and are more favored by cosmological observations. Axion is a candidate for both, with certain limits imposed on its mass to be a candidate for HDM or CDM.

Axions with masses in eV range can account for HDM together with neutrinos. For HDM axions, after the QCD phase transition they should have been created via

the thermalization process $\pi + \pi \rightarrow \pi + a$ and the results of WMAP impose the limit for HDM axion mass as: $m_a < 1.02\text{eV}$ [18].

More favorable axions are CDM axions, which are created before or during the QCD phase transition via following effects: vacuum realignment [19], axion string decay [20] and axion domain wall decay [21, 22].

Depending on the cosmological scenarios, axion mass can have upper or lower limits. If the PQ symmetry was broken before the inflation, one can set an upper limit to axion mass as $m_a < 10^{-3}\text{eV}$ [23]. On the other hand, if the inflation did not happen at all or happened before PQ symmetry breaking, axions become non-relativistic after the QCD phase transition, and form the CDM content of the universe. Although it is dependent on the considered axion production mechanisms, one can set a lower limit on axion mass based on its density and the total dark matter content of the universe as: $m_a > 10^{-4}\text{eV}$ [24].

2.5.2. Solar Model

The Sun and solar model itself can give important hints about the coupling strength of axions.

The x-ray flux due to blackbody radiation and the high electric fields in the core of the sun, give rise to creation of axions in the sun via Primakoff effect. These axions can escape from the sun, while x-rays can't. If the axion production rate was too high, it would make the sun lose its mass and its lifetime would be shorter. The helioseismological observations provide a limit on the axion-two photon coupling constant($g_{a\gamma}$) [25] as

$$g_{a\gamma} \lesssim 1 \cdot 10^{-9}\text{GeV}^{-1}$$

which also implies $L_a \lesssim 0.2 L_\odot$, where L_a and $L_\odot$ are axion and photon luminosity of the sun. A more strict limit comes from the neutrino flux measurements. To account

for the energy loss in form of axions, the temperature of the sun should be higher, and so the neutrino flux. The neutrino flux measurements give $4.94 \times 10^6 \mathrm{cm}^{-2}\mathrm{s}^{-1}$, with an uncertainty of 8.8% [26]. This uncertainty implies the following upper limit on the coupling constant [9] as

$$g_{a\gamma} \lesssim 5 \cdot 10^{-10}\mathrm{GeV}^{-1}$$

which implies $L_a \lesssim 0.04 L_\odot$. The limit due to neutrino fluxes can be improved with a more accurate solar model that has less uncertainty.

The details of the solar axion production and detection will be explained in Chapter 3.

2.5.3. Globular Clusters

The globular cluster stars are groups of stars, that are approximately in the same stage of evolution and that orbit the galaxies being gravitationally bound to each other. They only differ in mass, and differences in their evolutionary phase can be determined by comparing their surface temperature with their surface brightness(Figure 2.4). The horizontal branch(HB) stars are in stage of burning helium to create carbon and oxygen. From the density and temperature of these stars, one can predict the energy loss due to Primakoff conversion, and decrease in the lifetime of the star. On the other hand, the lifetime can be measured by comparing number of HB stars to brighter Red Giant Branch(RGB) stars and it is in agreement with theoretical predictions in case of no Primakoff conversion, within 10% [27]. This can imply a limit on the $g_{a\gamma}$ as

$$g_{a\gamma} < 10^{-10}\mathrm{GeV}^{-1}$$

An additional limit for the axion-electron coupling constant g_{ae} comes from the RGB stars, which do not have a high Primakoff conversion rate, but have a higher bremmsstrahlung rate to contribute to energy loss in form of axions ($e + Ze \rightarrow Ze + e + a$). The observed

mass of the core of the stars are in agreement with theoretical predictions within 10%, and this implies the following limit.

$$g_{ae} < 3 \cdot 10^{-13}\text{GeV}^{-1}$$

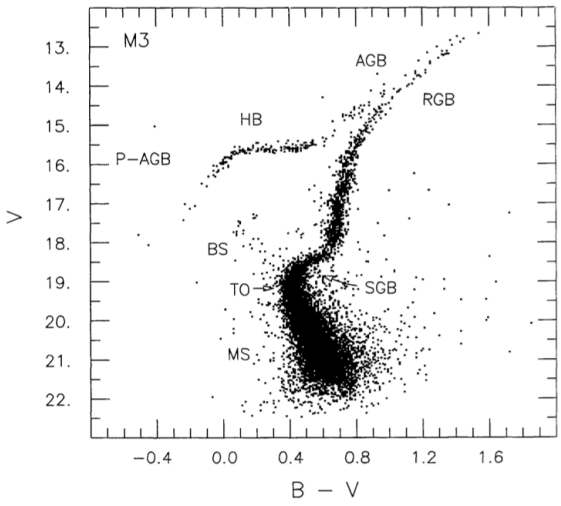


Figure 2.4. The Hertzsprung-Russell diagram for 10637 stars in M3 [27]. The surface brighthess is plotted in y axis and increases towards the top while the surface temperature is plotted in x axis and increases towards left.

2.5.4. White Dwarf Cooling

White dwarfs are a later stage in stellar evolution. Red giants have an oxygen-carbon core, and helium burning takes place in the shell, which creates the plenatery nebula, and the center becomes a white-dwarf. These stars lose energy in form of neutrinos and photons. The axion-electron coupling would create another channel of energy loss and increase the speed of cooling. This speed is estimated and is within predictions [28], imposing a stricter limit on axion-electron coupling [29] such as

$$g_{ae} < 1.3 \cdot 10^{-13}\text{GeV}^{-1}$$

2.5.5. Supernova 1987A

A limit on axion-nucleon coupling can be implied by Supernova 1987A, which was detected in 1987 by the burst of visible light and neutrinos in a short time [30]. The supernova happens as a massive star collapses and a very dense and hot protoneutron star is formed, creating a burst of neutrinos during few seconds due to neutrinos being trapped in the resulting star. The dominant axion process would be axion-nucleon bremmsstrahlung $N + N \rightarrow N + N + a$. An axion-nucleon coupling constant g_{aN} in a certain range would increase energy loss and decrease the neutrino burst duration. Small coupling constant would not affect the burst duration. Large coupling constant would have a similar consequence since axions would be trapped due to too many nucleon interactions, and neutrinos would still be the main energy loss and cooling mechanism. In case the coupling constant was in a certain range, then the cooling time could decrease dramatically as shown in Figure 2.5.

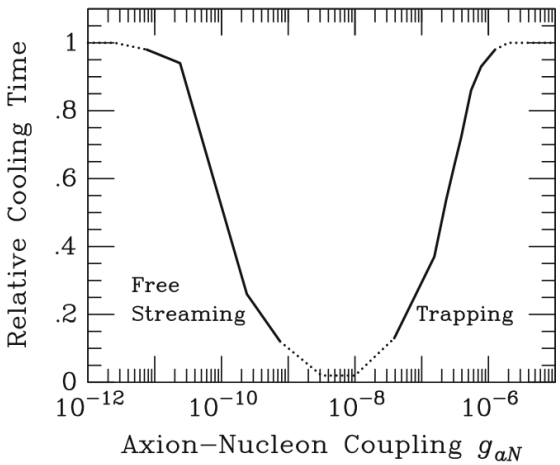


Figure 2.5. Cooling time vs. axion-nucleon coupling constant. In case of small or large couplings the cooling time would be affected minimally, while in between, axion-nucleon interaction would decrease the time significantly. Image taken from [9].

The observed burst duration was in agreement with the theoretically expected duration and this is used to obtain the limit [9] as

$$m_a < 16meV$$

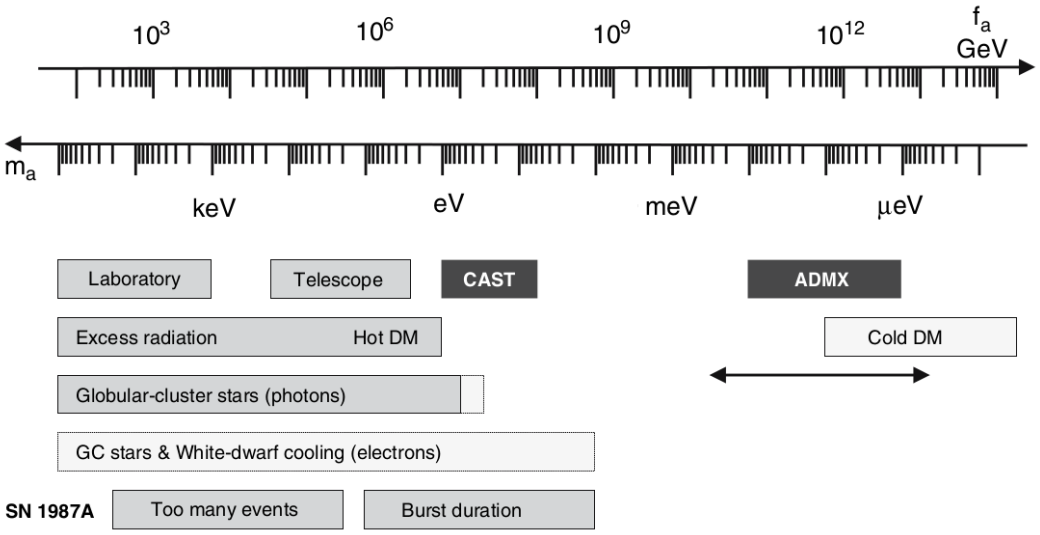


Figure 2.6. Summary of excluded mass and PQ scale ranges due to different constraints. Image taken from [9].

2.6. Axion Experiments

Axions that are coming from different sources or created in the lab can be probed through different experimental setups. The detection mechanism also depends on the axion model and the coupling of the axions that are implied in the model. The most highly favored models are hadronic axion models, which are defined by the lines in Figure 2.3 and most experiments are designed to use Primakoff inversion, which is the most common coupling of axion in different models.

2.6.1. Photon Regeneration and Polarization Experiments

There are two groups of experiments that are conducted using lasers, and converting them into axions in strong transverse magnetic fields. They are also called laser experiments and are considered as laboratory searches, since no external source is needed. These experiments have advantage of not having to depend on solar or cosmological models as haloscope or helioscope experiments do.

2.6.1.1. Photon Regeneration Experiments. axions by passing them from a secondary magnet. By placing a shield between two magnets, it is guaranteed that only axions will pass from the second magnet, and the photons that are detected after the second magnet will be the ones that are regenerated via inverse-Primakoff effect as in Figure 2.7, implying an axion signal [31].

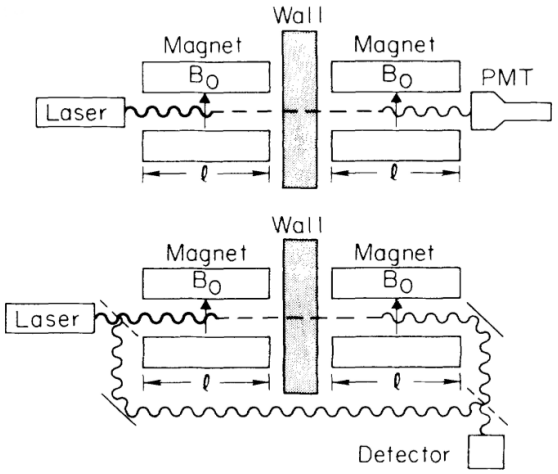


Figure 2.7. Schematics and different possible setups of photon regeneration experiments.

The first experiment that used this technique was Brookhaven-Fermilab-Rutherford-Trieste(BFRT) in the beginning of 1990's and provided limit $g_{a\gamma} < 6.7 \cdot 10^{-7}\text{GeV}^{-1}$ for axion masses $m_a < 10^{-3}\text{eV}$ [32, 33]. Next generation experiments are still running. A gamma to milli-eV Particle Search (GammeV), which is situated at Fermilab has published its first results in 2008, excluding the meV mass range with the limit $g_{a\gamma} < 3.1 \cdot 10^{-7}\text{GeV}^{-1}$ [34]. Any Light Particle Search(ALPS) is running at DESY and looking for Axion like particles [35]. Optical Search of QED vacuum magnetic birefringence, Axion and photon Regeneration(OSQAR) experiment is running at CERN, probing axions and measuring Quantum Electrodynamics magnetic Vacuum Birefringence at the same time [36].

Next step for laser experiments is using Fabry-Perot optical cavities, enhancing the photon regeneration [37]. This technique can bring the coupling constant limit

down to 10^{-10} for axion masses $10^{-6} < m_a < 10^{-4}$.

2.6.1.2. Photon Polarization Experiments. Another way to detect axions is to pass a linearly polarized laser beam from a magnet, and measure the change in the polarization of the initial beam [38]. If the field is strong enough, the photons with electric field parallel to the external magnetic field will be converted into axions, and the linearly polarized light will rotate(dichroism) or the polarization will become elliptical(birefringence). These effects can be tested with similar instruments used in regeneration experiments, and BFRT collaboration provided limits due to rotation such as $g_{a\gamma} < 3.6 \cdot 10^{-7}\text{GeV}^{-1}$ for $m_a < 5 \cdot 10^{-4}\text{eV}$ [39].

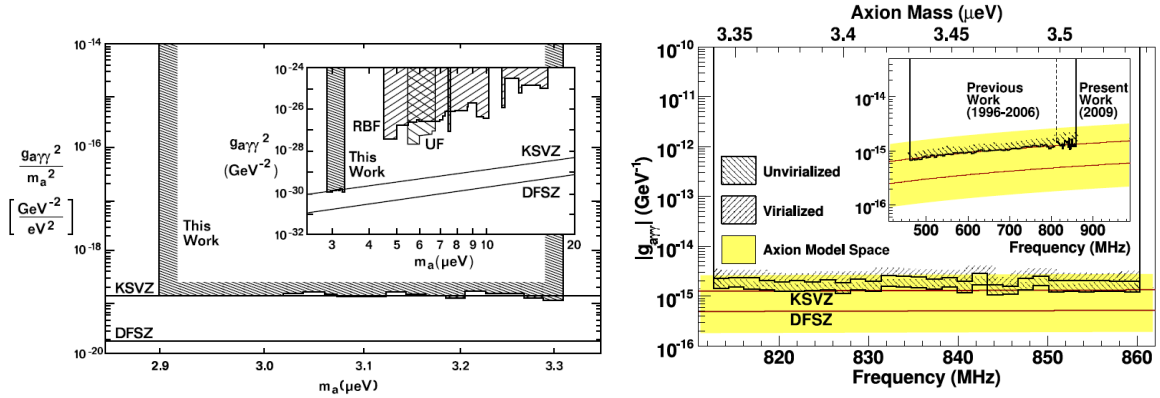
The Polarizzazione del Vuoto con LASer(PVLAS) experiment has claimed to see a signal due to dichroism but further searches showed that the signal was due to an error in the experiment, and not a real signal due to the existence of axions [40].

2.6.2. Haloscope Experiments

Haloscope experiments search for μm mass range CDM axions, which are gravitationally bound in galactic halo. These axions have a speed $v = 10^{-3}c$ and their energy have a spread from axion mass in order of 10^{-6}. By using microwave cavities, one can apply static magnetic field, and resonantly convert axions to photons via Primakoff conversion in the cavity [41]. The resulting microwave photons are detected by sensitive microwave receivers, and the excess of photons would imply an axion signal. These experiments are sensitive to a narrow band of axion masses that is defined by the angular frequency of the cavity modes such that $2\pi f = m_a$.

The first experiments that searched for galactic halo axions were conducted before 1990 by Rochester-Brookhaven-Fermilab collaboration [42] and University of Florida [43]. After 1990, experiments with more sensitive microwave receivers were built and provided much better limits than first experiments. Most notable of these experiments is Axion Dark Matter Experiment(ADMX) [44–47]. ADMX has successfully probed

the theoretical axion models and excluded an important part in mass range $2.9\mu\text{eV} < m_a < 3.5\mu\text{eV}$ (Figure 2.8)



(a) (b)

Figure 2.8. (a) Results of first generation haloscopes and ADMX [44]. (b) Recent results from ADMX [47].

2.6.3. Solar Axion Experiments

Another possible axion source is the Sun, due to Primakoff conversion of photons in the high electric fields in the solar core. There are two types of solar axion search, Brag scattering experiments and helioscopes.

2.6.3.1. Bragg Scattering Experiments. These experiments utilize crystals such as Ge,Si or NaI and aim at converting axions into photons using the high electric field due to atomic nuclei. From the experiments COSME [48], SOLAX [49], DAMA [50] and CDMS [51, 52], the strictest limit on the axion coupling is the result of DAMA experiment, which is: $g_{a\gamma} < 1.7 \cdot 10^{-9}\text{GeV}^{-1}$.

2.6.3.2. Helioscope Experiments. The more sensitive solar axion searches are done by helioscopes, aiming to convert the solar axions to photons in strong magnets. The first experiment of this type was done at Brookhaven National Laboratory and with a fixed magnet it provided a limit $g_{a\gamma} < 3.6 \cdot 10^{-9}\text{GeV}^{-1}$ and $g_{a\gamma} < 7.7 \cdot 10^{-9}\text{GeV}^{-1}$ for mass ranges $m_a < 0.03\text{eV}$ and $0.03 < m_a < 0.11\text{eV}$ [53]. Next experiment the

Tokyo Helioscope has been built on a movable system with ability to track the sun and pushed the limits down to $g_{a\gamma} < 6 \cdot 10^{-10}\text{GeV}^{-1}$ for $m_a < 0.03\text{eV}$ [54].

Last and the most sensitive helioscope is CAST. Details of solar axion detection and CAST will be given in the following chapters.

3. SOLAR AXION DETECTION WITH HELIOSCOPES

In this section, the dynamics of solar axion detection will be explained in detail. The detection mechanism consist of few steps: Creation of axions in the sun and conversion to photons on earth. By calculating the theoretical axion flux and conversion probabilities, one can get the total number of photons that will be seen in detectors.

3.1. Primakoff Effect

The known decay of π^0 into two photons implies the interaction of π^0 field, pseudoscalar field φ and electric and magnetic fields $\mathbf{E}$ and $\mathbf{H}$. Lagrangian density of the interaction is: $\eta(\hbar/m_\pi c)(\hbar c)^{-1/2}\varphi\mathbf{E}\cdot\mathbf{H}$, with η being a dimensionless constant depending on decay mecanism [6]. This implies coupling of pseudoscalar particles to two photons, and is known as Primakoff Effect. Primakoff conversion can occur in both directions, photons to pseudoscalar, or pseudoscalar to photons. It is known that for particles with two photon vertex, one of the photons can be a virtual photon of an electromagnetic field. Thus a photon can be converted into the pseudoscalar particle, upon entering to an electromagnetic field. In our studies, this kind of conversion is of interest.

Since axion is also a pseudoscalar, it is subject to Primakoff Effect. Lagrangian density of axion - two photon interaction is

$$\mathcal{L}_{a\gamma\gamma} = \frac{-1}{4} g_{a\gamma} F_{\mu\nu} \tilde{F}^{\mu\nu} a = g_{a\gamma} \mathbf{E}\cdot\mathbf{B} a \tag{3.1}$$

where $F_{\mu\nu}$ is the electromagnetic field-strength tensor, $\tilde{F}^{\mu\nu}$ its dual, $\mathbf{E}$ and $\mathbf{B}$ are electric and magnetic fields, a is the axion field and $g_{a\gamma}$ is the coupling constant. A representation of Primakoff effect is shown in Figure 3.1.

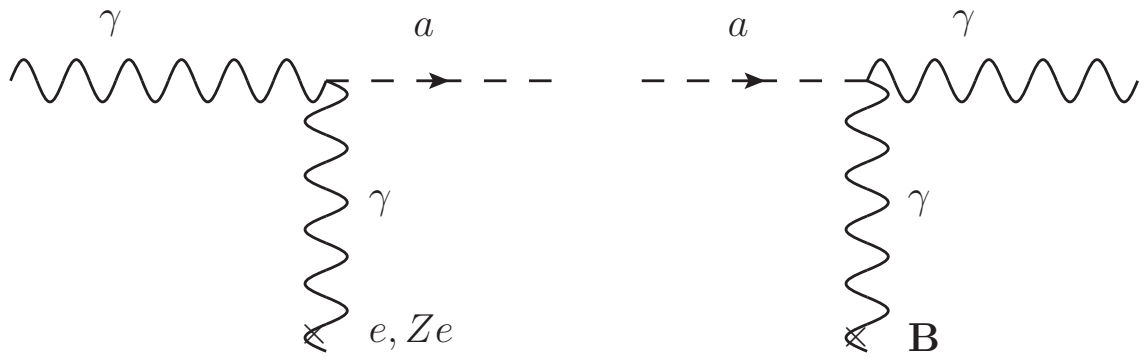


Figure 3.1. Primakoff Effect.

3.2. Solar Axion Flux

To create axions from photons one needs a luminous photon source and a high electric or magnetic field. Stars are best candidate for this process. In the hot and dense core of the stars, blackbody photons are created in x-ray energies, and these are subject to high electric fields of stellar plasma, which are created by nuclei and electrons. Primakoff conversion in the stars can be expressed as

$$\gamma + (e^-, Ze) \rightarrow (e^-, Ze) + a \tag{3.2}$$

This process occurs via the field $\mathbf{E}(\mathbf{r})$, which is the result of the charge distribution $\rho(\mathbf{r})$. Since the incident photon energies are much less than electron mass($\omega \ll m_e$), the field can be thought as "external", meaning that Primakoff conversion will not affect the field. Similarly recoil effects can be neglected, which implies that photon and axion energies will be equal, but there will be a mismatch in their momentum, due to mass of the axion and the plasma frequency, which gives photon an effective mass. The conversion is favoured in a way that axion will be emmited in the direction of photon motion. As the angle increases, interaction becomes suppressed.

Differential cross section of this process is [55]

$$\frac{d\sigma_{\gamma\rightarrow a}}{d\Omega} = \frac{g_{a\gamma}^2 \alpha}{8\pi} \frac{|\mathbf{k}\times\mathbf{p}|^2}{|\mathbf{q}|^4} |F(\mathbf{q})|^2 \tag{3.3}$$

where $\mathbf{k}$ is the photon momentum, $\mathbf{p}$ is the axion momentum and $\mathbf{q}$ is the momentum transfer ($\mathbf{q} = \mathbf{k} - \mathbf{q}$). F is the form factor that describes the charge distribution, and is defined as

$$F(\mathbf{q}) \equiv \int d^3\mathbf{r}\rho(\mathbf{r})e^{-i\mathbf{q}\cdot\mathbf{r}} \tag{3.4}$$

For a point charge with magnitude Ze, form factor is simply $F^2 = Z^2$. However in the more realistic picture, particles in the plasma interact, screening effects come into scene, and form factor changes depending on momentum transfer. This affects the cross section of the process in a negative way. This can be seen as follows. In the plasma a particle with charge Ze, attracts oppositely charged particles around itself and on average its coulomb potential is modified to Yukawa Potential.

$$\frac{Ze}{4\pi}\frac{1}{r} \rightarrow \frac{Ze}{4\pi}\frac{e^{-\kappa r}}{r} \tag{3.5}$$

where κ is called the inverse Debye-Huckel radius or Debye-Huckel scale. This has an important physical meaning. The charges that are much farther than κ^{-1} are screened, and their coulomb field has no effect. Debye-Huckel scale is given by

$$\kappa = \frac{4\pi\alpha}{T}\left(n_e + \sum_j Z_j^2 n_j\right) \tag{3.6}$$

where T is the plasma temperature, n_e is the electron density and n_j is the number density of particles with charge $Z_j e$. $\kappa \approx 9$keV in the core of the Sun, and its ratio to temperature is constant in the whole sun ($\kappa/T \approx \sqrt{12}$) [9].

Including the screening effect, each particle can be assigned an effective form factor, which is less than the case in which screening is not taken into account.

$$|F_{eff}(\mathbf{q})|^2 = Z^2\frac{|\mathbf{q}|^2}{|\mathbf{q}|^2 + \kappa^2} \tag{3.7}$$

Integrating the differential flux, transition rate for photon to axion conversion in the

sun is given by [56]

$$\Gamma_{\gamma\to a} = \frac{g_{a\gamma}^2 T\kappa}{32\pi}\left[\left(1+\frac{\kappa^2}{4E^2}\right)\ln\left(1+\frac{4E^2}{\kappa^2}\right)-1\right] \tag{3.8}$$

where T is the temperature of the plasma and E is the incident photon energy.

To get the total flux, one has to combine transition rate with photon luminosity and blackbody spectrum throughout the sun for all energies. The most current Solar model that is calculated by Bachall and Pinsonneault in 2004 [57] is used. Integrating over the solar model, one obtains the axion flux on earth [58, 59].

$$\Phi_a = \frac{R_\odot^3}{4\pi D_\odot^2}\int_0^1 \mathrm{d}r 4\pi r^2 \int_{\omega_{pl}}^\infty \mathrm{d}E \frac{4\pi k^2}{(2\pi)^3}\frac{\mathrm{d}k}{\mathrm{d}E}\frac{2\Gamma_{\gamma\to a}}{(e^{E/T}-1)} \tag{3.9}$$

where $R_\odot = 6.910^{10}$cm is the solar radius, $D_\odot = 1.510^{13}$cm is the earth-sun distance, $(e^{E/T}-1)^{-1}$ is the Bose-Einstein distribution of the photons and ω_{pl} is the plasma frequency which can be expressed as

$$\omega_{pl} = \sqrt{\frac{4\pi\alpha n_e}{m_e}} \tag{3.10}$$

Note that ω_{pl}, $\Gamma_{\gamma\to a}$ and T are all dependent on the position on the Sun. The lower limit of the integration over photon energy is the plasma frequency ω_{pl}, because photons have the dispersion relation $E^2 = k^2 + \omega_{pl}^2$ and the transition rate calculation includes the assumption that plasma frequency is less than photon energy(for instance in the solar core, $\omega_{pl} = 0.3$keV). Dispersion relation is similar to relativistic energy-momentum relation $E^2 = p^2 + m^2$ and it is said that photon gets an effective mass, equivalent to the plasma frequency ω_{pl}. Thus its momentum is no more equal to its energy.

One can get normalized flux at earth and axion luminosity as

$$\Phi_a = g_{10}^2 3.75\cdot 10^{11}\mathrm{cm}^{-2}\mathrm{s}^{-1} \tag{3.11}$$

$$L_a = g_{10}^2 1.85\cdot 10^{-3} L_\odot \tag{3.12}$$

where $g_{10} = g_{a\gamma}/10^{-10}\mathrm{GeV}^{-1}$, which is a commonly used parameter and $L_\odot = 3.8418\mathrm{ergs}^{-1}$ is the photon luminosity of the sun from the recent model [57]. Since coupling constant is unknown, we chose to express fluxes in terms of g_{10}^2.

The differential flux $d\Phi/dE$ can be seen at figure 3.2, and is parametrized up to a very good precision with the formula

$$\frac{\mathrm{d}\Phi_a}{\mathrm{d}E_a} = 6.02 \cdot 10^{10}\mathrm{cm}^{-2}\mathrm{s}^{-1}\mathrm{keV}^{-1} g_{10}^2 E^{2.481}\mathrm{e}^{-E/1.205} \tag{3.13}$$

This formula is a good enough approximation for the x-ray energies in the interest of CAST(1-7keV). The mean of the distribution is $\langle E_a \rangle = 4.2\mathrm{keV}$, while the most expected energy is 3keV.

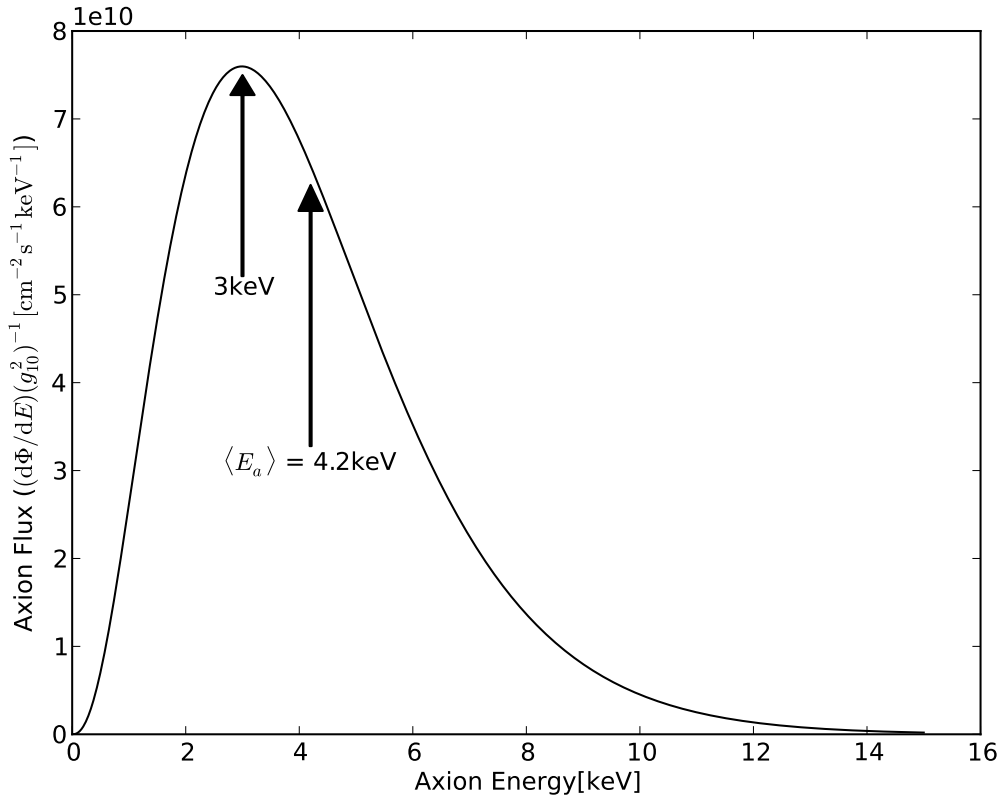


Figure 3.2. Differential solar axion flux at Earth. Note that the real flux depends on the value of coupling constant.

3.3. Axion-Photon conversion in Magnetic Field

Having the axion flux at our magnet, one can go a step further and calculate the conversion probability in the magnet. The magnet has magnetic field B and length L. And for now it will be assumed that there is a buffer gas with constant density in the conversion region.

3.3.1. Axion-Photon Transmission Amplitude

Raffelt and Stodolsky [60] showed that only photons, that are polarized in the direction of magnetic field mixes with axions. That means, for an axion to convert into a photon, electric field of the photon should be parallel to the external magnetic field, therefore direction of motion should be perpendicular to the external magnetic field.

If A is the component of photon that is parallel to the direction of motion, a is the axion field, B is the transverse component of magnetic field, Γ is the inverse absorption length(see Section 3.3.3), m_γ is the effective photon mass due to density in the magnetic field region and z the direction of motion, wave equation can be written as [61]

$$i\partial_z \begin{pmatrix} A \\ a \end{pmatrix} = \begin{pmatrix} E_a - \frac{m_\gamma^2}{2E_a} - \frac{i\Gamma}{2} & \frac{g_{a\gamma}B}{2} \\ \frac{g_{a\gamma}B}{2} & E_a - \frac{m_a^2}{2E_a} \end{pmatrix} \begin{pmatrix} A \\ a \end{pmatrix} \tag{3.14}$$

Since axions interact very weakly with the buffer gas, only (1,1) term of the matrix contains the absorption term. One can calculate q, the momentum transfer from one particle to other. Since the axion mass and effective photon mass are considered small compared to energy range we are working in, the system can be treated as if the whole energy is transfered, but not the momentum. The mismatch in the momentum is caused by the mass difference of two particles.

$$q = |\mathbf{p_a} - \mathbf{k}| = \left| \sqrt{E_a^2 - m_a^2} - \sqrt{E_a^2 - m_\gamma^2} \right| \tag{3.15}$$

Expanding both terms for $m_\gamma \ll E_a$ and $m_a \ll E_a$,

$$q = |(m_\gamma^2 - m_a^2)/2E_a| \tag{3.16}$$

Effective mass of the photons is calculated as in Equation 3.10 and electron density n_e is given by

$$n_e = Z\frac{N_A}{W_A}\rho \tag{3.17}$$

where Z is the atomic number of the gas, N_A is the avagadro number, W_A is the atomic weight in g/mol and ρ is the density in g/cm^3.

Using definition of n_e, Equation 3.10 can be rewritten as

$$m_\gamma = \sqrt{\frac{4\pi\alpha N_A}{m_e}\frac{Z}{W_A}\rho} \tag{3.18}$$

Solving Eq 3.14 in the first order perturbation theory, one gets the transition amplitude as

$$\langle A(z)|a(0)\rangle = \frac{g_{a\gamma}}{2}\mathrm{e}^{-\left(\int_0^z dz'\Gamma/2\right)} \times \int_0^z dz' B\mathrm{e}^{i\left(\int_0^{z'} dz''[q-i\Gamma/2]\right)} \tag{3.19}$$

3.3.2. Axion-Photon Conversion Probability

Since the magnetic field and buffer gas density are assumed constant throughout the length, B, m_γ and Γ act are also constants and all integrals in Equation 3.19 can be trivially calculated. First and second integrals give

$$\mathrm{e}^{-\left(\int_0^z dz'\Gamma/2\right)} = \mathrm{e}^{-z\Gamma/2} \tag{3.20}$$

$$\int_0^z dz' B\mathrm{e}^{i\left(\int_0^{z'} dz''[q-i\Gamma/2]\right)} = \frac{B}{i(q-i\Gamma/2)}\left(\mathrm{e}^{iz[q-i\Gamma/2]} - 1\right) \tag{3.21}$$

Evaluating the result at L, hermitian square of the transition amplitude: $|\langle A(L)|a(0)\rangle|^2$ is the probability to see a photon at distance L,

$$P_{a\to\gamma}(z=L) = \left(\frac{g_{a\gamma}B}{2}\right)^2 \frac{1}{q^2+\Gamma^2/4}[1+\mathrm{e}^{-\Gamma L} - 2\mathrm{e}^{-\Gamma L/2}\cos(qL)] \tag{3.22}$$

In case of vacuum, there would be no absorption, therefore to get the conversion probability in vacuum, one can simply set $\Gamma = 0$ and $m_\gamma = 0$

$$\begin{aligned} P_{a\to\gamma}^{vac} &= \left(\frac{g_{a\gamma}B}{2q}\right)^2 2(1-\cos(qL)) && (3.23)\\ &= \left(\frac{g_{a\gamma}B}{q}\right)^2 \sin^2\left(\frac{qL}{2}\right) && (3.24)\end{aligned}$$

where this time

$$q = \frac{m_a^2}{2E_a} \tag{3.25}$$

One can rewrite the Equation 3.22 in terms of g_{10}, qL and ΓL and a common factor $\mathcal{M}$

$$P_{a\to\gamma} = (10^{-10}\mathrm{g}_{10})^2(BL/2)^2\mathcal{M} \tag{3.26}$$

where $\mathcal{M}$ is

$$\mathcal{M} = \frac{1}{(qL)^2+(\Gamma L)^2/4}[1+\mathrm{e}^{-\Gamma L} - 2\mathrm{e}^{-\Gamma L/2}\cos(qL)] \tag{3.27}$$

for general case with buffer gas, and

$$\mathcal{M} = \frac{2}{(qL)^2}[1-\cos(qL)] \tag{3.28}$$

for vacuum.

3.3.3. Absorption of Photons

When photons travel in a medium, they may get absorbed due to properties of the medium. In the buffer gas of the axion helioscope, photons will similarly be absorbed. This effect is already included in the conversion probability (Equation 3.27) by the factor Γ, which is the inverse absorption length and depends on gas type, gas pressure and energy of the photons.

The absorption phenomenon takes place as follows. If a monoenergetic photon beam with intensity I_0 is passing through a medium with thickness L and inverse absorption lenght Γ, its density decreases to I with the following equation

$$\frac{I}{I_0} = \mathrm{e}^{-\Gamma L} \tag{3.29}$$

Γ can be written in terms of mass attenuation coefficient μ/ρ, and the buffer gas density ρ_{gas} as

$$\Gamma = (\mu/\rho)\rho_{\mathrm{gas}} \tag{3.30}$$

Although it may seem redundant to use this notation, there is a good reason to use (μ/ρ) as a parameter instead of μ itself. While μ is both density and energy dependent, μ/ρ is only energy dependent, and experimental values in NIST database [62] are given for μ/ρ. Also instead of thickness, mass thickness $x = \rho_{\mathrm{gas}}L$ is more commonly used to express absorption,

$$\frac{I}{I_0} = \mathrm{e}^{-(\mu/\rho)x} \tag{3.31}$$

The absorption measurements are done for different energies and mass thicknesses to get parametrization of mass attenuation coefficient. By using values for $\mu/\rho(\mathrm{g/cm^3})$ from NIST database, one can get a good fit for He^3, parametrized in photon en-

ergy(keV), for 1-15 keV.

$$\mu/\rho = \exp\left[-1.5832 + 5.9195 \cdot \mathrm{e}^{-0.353808E} + 4.03598 \cdot \mathrm{e}^{-0.970557E}\right] \tag{3.32}$$

The agreement of the fit and measurements from NIST database can be seen in Figure 3.3.

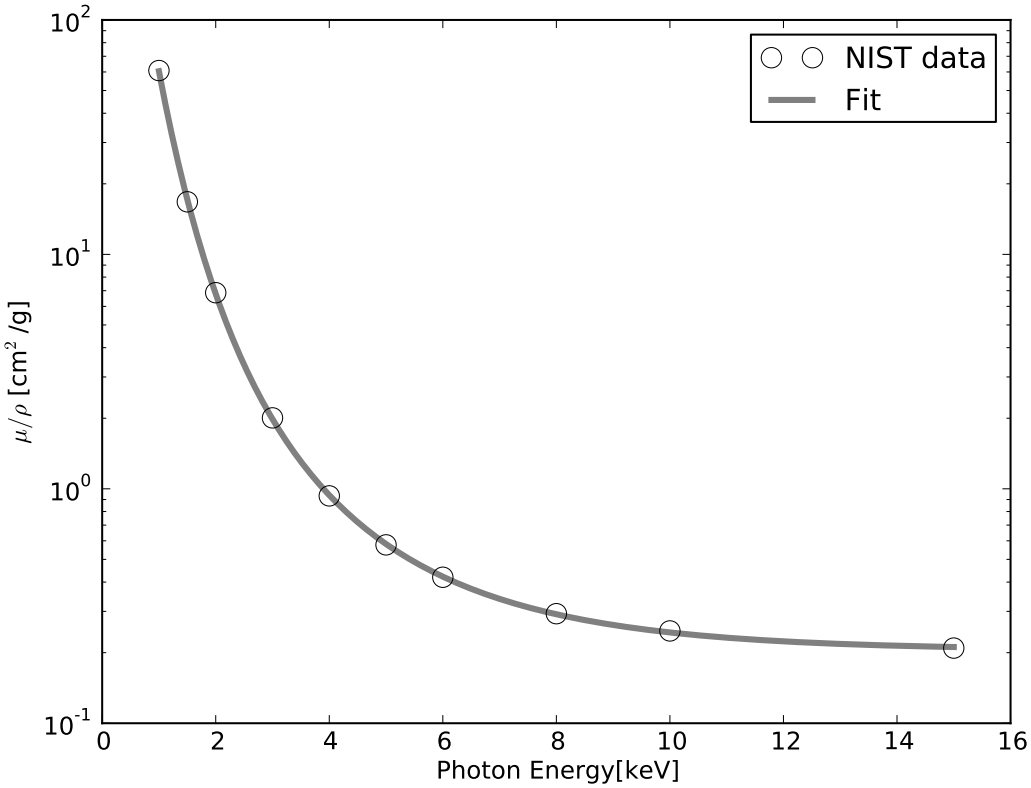


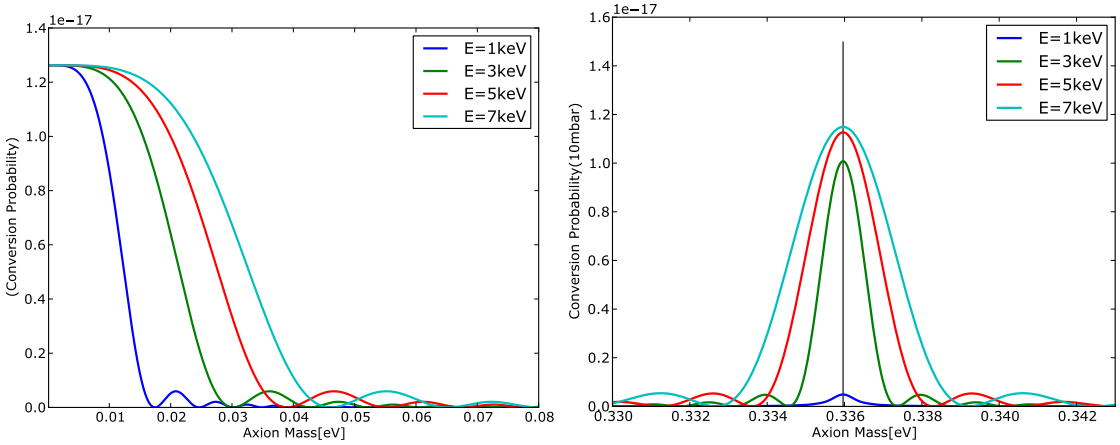
Figure 3.3. He^3 mass attenuation coefficient: Circles show the values taken from NIST database, continous line show the fit function.

Using Equation 3.30, Γ as a function of energy E and gas pressure ρ can be obtained in cm^{-1}

$$\Gamma(E,\rho) = \rho \cdot \exp\left[-1.5832 + 5.9195 \cdot \mathrm{e}^{-0.353808E} + 4.03598 \cdot \mathrm{e}^{-0.970557E}\right] \tag{3.33}$$

3.3.4. Coherence of Conversion

In both cases, with or without a buffer gas, conversion is coherent in a specific mass range. Plotting conversion probability for different axion energies in vacuum and presence of 10mbar of ^{3}He, one gets Figure 3.4.

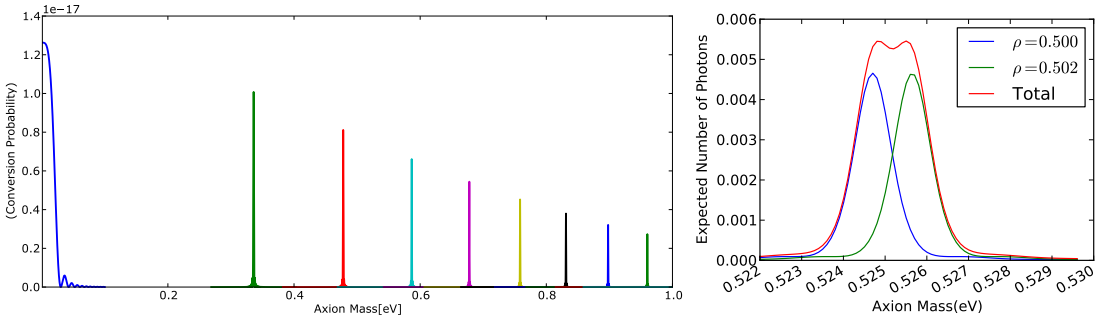


(a) (b)

Figure 3.4. (a) Conversion probability in vacuum for different energies. (b) Conversion probability with 10mbar of pressure for different energies, the vertical line shows effective photon mass for 10mbar, $m_\gamma = 0.33596$.

One can see that, in the vacuum experiment is sensitive to low masses($m_a < 0.02eV$). As the pressure is increased, experiment becomes sensitive to a mass band around effective photon mass, as given in Equation 3.18. Conversion probability 3keV axions for range of pressures from 0 to 100mbar is shown in Figure 3.5a, as the pressure increase conversions becomes coherent only for a narrow band of higher axion masses. Also due to absorption, maximum probability is decreasing at higher pressures. Total number of expected photons for neighboring densities assuming coupling constant as 10^{-10}GeV^{-1} and using exposure time of 30 minutes are shown in Figure 3.5b. The red curve shows the combined number of photons expected for each mass.

This behaviour of the conversion probability shows that, for a helioscope experiment to be sensitive to all axion masses, all pressures with a narrow step size should



(a) (b)

Figure 3.5. (a) Conversion probability for axions with energy 3keV, for pressures between 0-100 mbar, with step of 10mbar. (b) Total expected number of photons per unit area for 2 different densities.

be scanned, in the end obtaining a flat probability distribution for all masses.

3.4. Expected Number of X-rays

Knowing the flux and conversion probability of axions, one should calculate expected number of x-rays theoretically. To do this, following will be used

- $\frac{\mathrm{d}\Phi_a}{\mathrm{d}E_a}$: Theoretical differential axion flux at earth, normalized in energy, time and area, depending on coupling constant.
- $P_{a\to\gamma}$: Probability of axion to photon conversion, depending on coupling constant, buffer gas properties(density and gas type), magnet properties(effective lenght and field strength), axion energy and axion mass.
- ϵ : Detector efficiency, depending on energy.
- A : Cross sectional area of the conversion region.
- Δt : Exposure time for a certain gas density.

Expected number of photons can be ideally calculated for a specific gas density(or photon mass), axion mass, energy and coupling constant. In the following formula

dependence on all parameters are explicitly showed.

$$N_\gamma(g_{a\gamma}, E, m_\gamma, m_a) = \frac{\mathrm{d}\Phi_a}{\mathrm{d}E_a}(g_{a\gamma}, E) \cdot P_{a\to\gamma}(g_{a\gamma}, E, m_\gamma, m_a, g_{a\gamma}) \cdot \epsilon(E) \cdot \Delta t \cdot A \quad (3.34)$$

Note that in both in $(\mathrm{d}\Phi_a/\mathrm{d}E_a)$ and $P_{a\to\gamma}$ there are factors $g^2_{a\gamma}$, giving N_γ dependence $g^4_{a\gamma}$

$$N_\gamma \propto g^4_{a\gamma} \quad (3.35)$$

To get the total expected number of photons for a fixed axion mass, N_γ should be integrated over energy, and exposure for each photon mass. The method for calculating gas density, effective length and pressure will be explained in Chapter 10.

4. CERN AXION SOLAR TELESCOPE

The CERN Axion Solar Telescope(CAST) is an experiment looking for Solar axions at European Organization for Nuclear Research(CERN). CAST uses one of the prototype dipole magnets of the Large Hadron Collider(LHC). It aims to convert axions to photons via Primakoff effect, and detect them using X-ray detectors that are coupled to both sides of the magnet to detect the x-rays. A picture of the whole system that tracks the sun is seen in Figure 4.1.

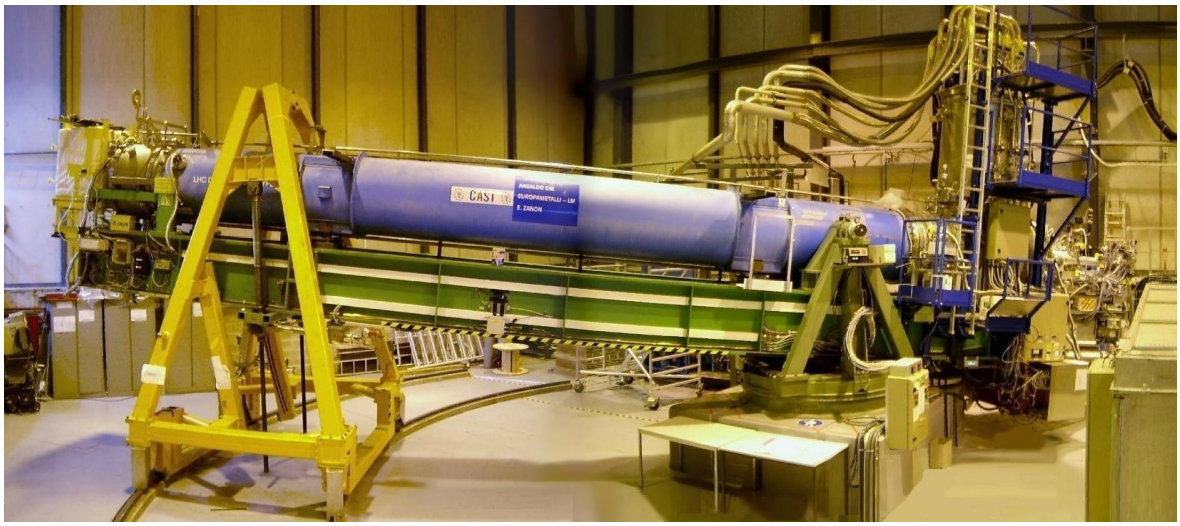


Figure 4.1. The CAST magnet.

4.1. History

CAST was proposed in 1999 [63], commissioned between 2000-2003 and started to run in 2003. Until 2013, it has run in vacuum(Phase I) and with addition of buffer gas into cold bore (Phase II). Phase II can also be separated into two, ^{4}He and ^{3}He phases (Table 4.1). During the vacuum phase, CAST was sensitive to axion masses up to 0.02eV [59]. With ^{4}He as buffer gas, masses between 0.02eV - 0.4eV were scanned [64] and with ^{3}He the scanned mass range was extended to 0.4eV - 1.15eV [65]. In 2012, the gas system was reverted back to operate with ^{4}He, to revisit some part of the low mass range with newer detectors [66]. The results of experiment until end of 2012 are

Table 4.1. The Run History of CAST.

Year	Phase	Sensitivity Range
2000-2003	Commissioning	
2003-2004	Phase I(Vacuum)	<0.02eV
2006-2007	Phase II(^{4}He)	0.02eV - 0.4eV
2008-2011	Phase II(^{3}He)	0.4eV - 1.15 eV
2012	Phase II(^{4}He)-Revisit	0.02eV - 0.4eV

presented in the Figure 4.2.

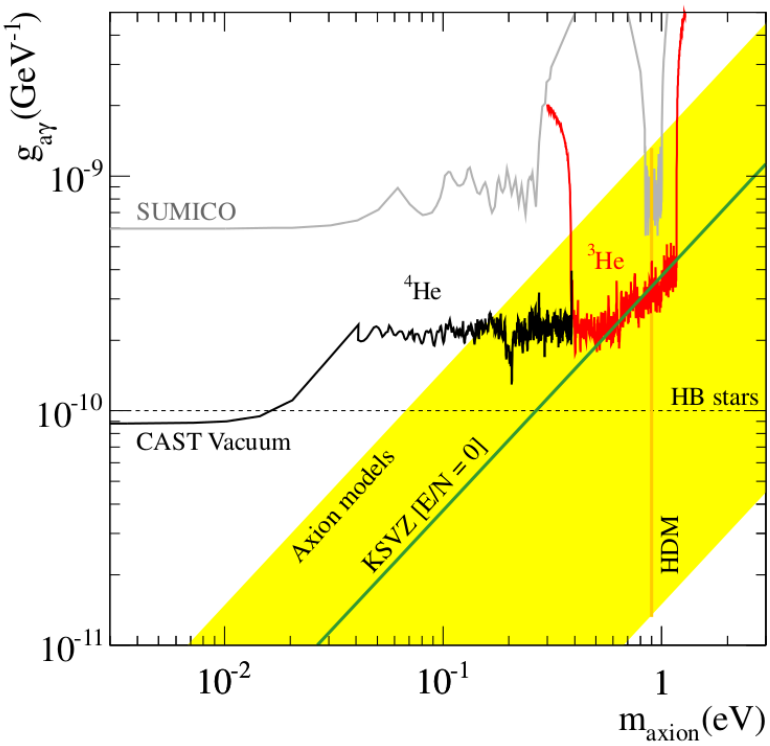


Figure 4.2. The exclusion plot produced from the result of CAST, including all detectors until 2009, and three micromegas detectors between 2009-2012.

4.2. CAST Magnet

CAST magnet is a decommissioned prototype LHC dipole magnet. It was used in tests before the LHC magnets took their final shape. It has two bores, each of which has 2.15cm radius and 14.52cm^2 cross-sectional area. The magnet becomes superconductive at temperatures lower than 4.5K thanks to current carrying wires being Niobium-Titanium. It can be loaded up to 13kA current, providing a magnetic field of 8.8T over a length of 9.26m, which is aligned in the direction of gravitation. Magnet cross section can be seen in Figure 4.3. The operation of superconducting magnets require cryogenic

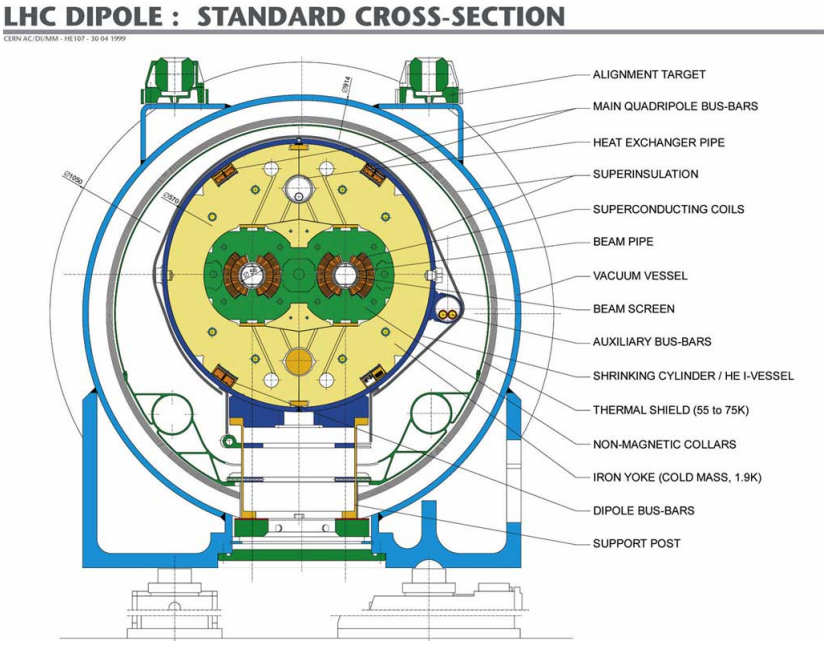


Figure 4.3. Cross section of LHC dipole magnets.

cooling. CAST magnet has been using a cryogenic infrastructure built from different parts of two different structures, some from the Large Electron–Positron Collider(LEP) and some from the Detector with Lepton, Photon and Hadron Identification(DELPHI). To support the recovered system, a new Roots pumping unit is installed. The magnet feed box(MFB) is placed near the rotation point of the mechanical system, and its connected to rest of the system via flexible lines(Figure 4.4), to allow magnet to move freely without disturbing operation of cryogenics. Cooling of the magnet is done in three phases, finally decreasing the temperature of the magnet down to 1.8K. At the

final stage, helium becomes superfluid after passing the lambda point and circulates all over the cold mass from MFB to magnet return box(MRB). The cooling is done via injecting cold liquid Helium periodically, and pumping the gaseous helium continuously. Magnet is isolated from the outside by the isolation vacuum to prevent heat exchange [67]. Under normal conditions, CAST magnet stays at temperatures lower than 1.8K.



Figure 4.4. Magnet feed box and flexible lines.

However due to rate of change of the field, or the extreme magnitude of the field, magnet can lose its superconductivity and go into a resistive state. This phenomenon is called *quench*. During a quench, the current carrying wires turn resistive at a point, and the resistivity propagates through the wire. This would create a big local stress, and damage the magnet. To prevent this, *quench heaters* are activated and magnet temperature is increased in a controlled manner, in all parts of the magnet. This

way, the stress due to resistivity is distributed over the magnet. Activation of quench heaters, cause magnet temperature to increase by a factor 20 in two minutes. To avoid any breakdown in the system by overpressure, helium is purged from he system. The extra measures taken to protect gas system during quench is explained in Section 6.2.

4.3. Movement and Tracking System

The CAST magnet is mounted on a structure, that allows it to rotate from -7.2° to +7.95° [59] vertically(inclination), and a from 46.7° to 133.3° horizontally(azimuth). The main rotation point is in the MFB side of the magnet. This assures the stability of the cryogenics structure while the magnet is moving. The vertical movement is done by a motor that rotates the lifting jacks, which are 7m distant from the pivot. Near the jacks, four wheels of the magnet is sitting on top of a pair of rails. One of the outer wheels is connected to another motor that drives the wheel, and makes the magnet move azimuthally(Figures 4.5 and 4.6). The motors can be controlled such that the direction and frequencies can be set. While horizontal motor frequencies range from 1 to 150Hz, vertical frequencies range from 0.1 to 70Hz. Every day, CAST

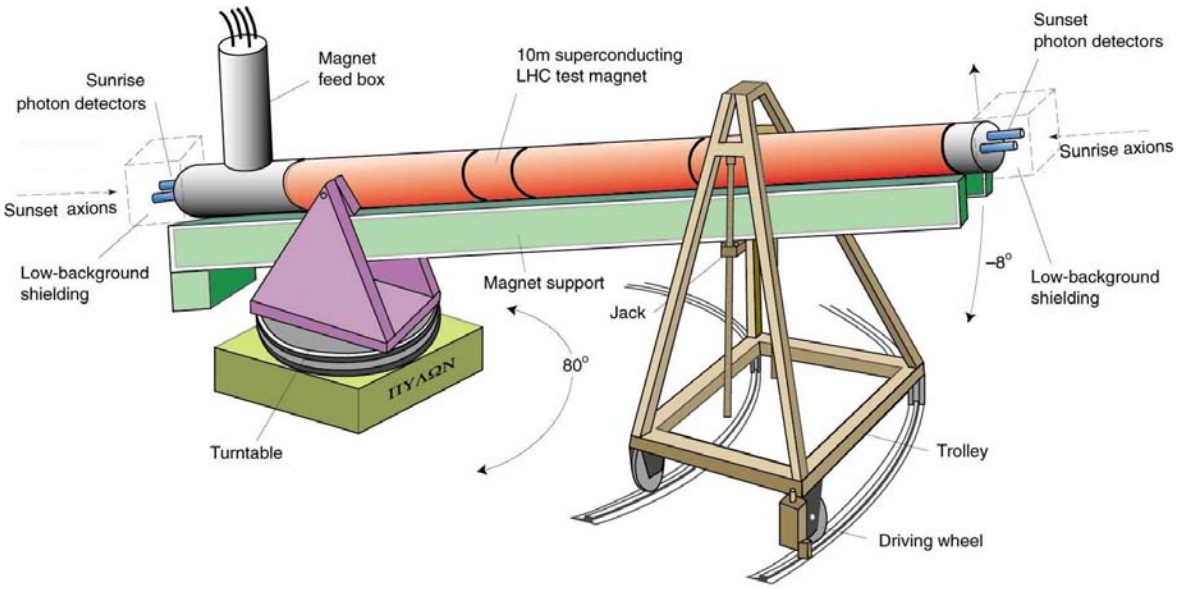
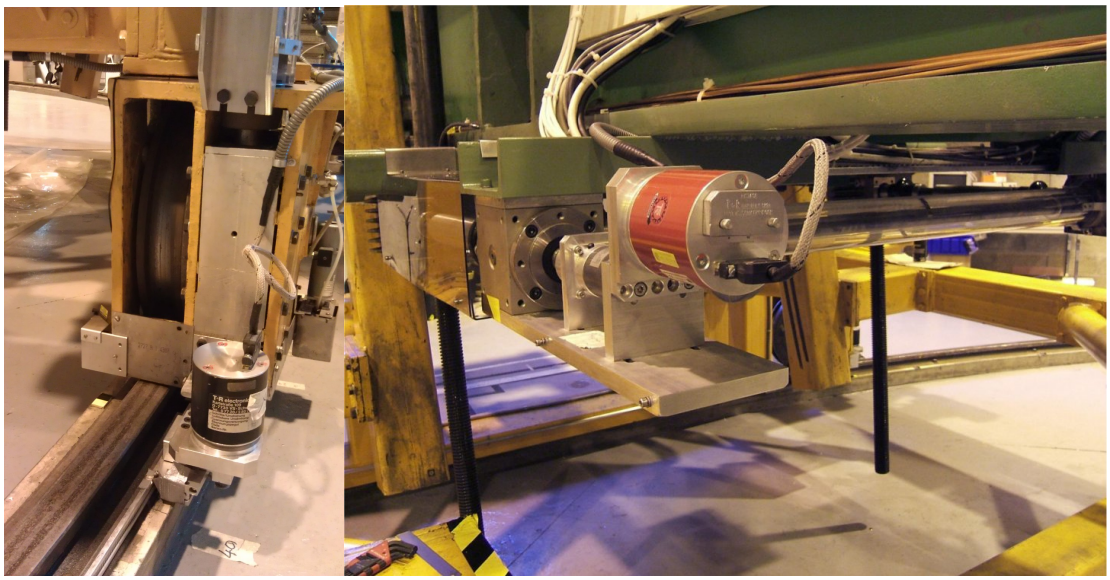


Figure 4.5. Drawing of the CAST Magnet and movement system.

is capable of doing morning and evening tracking, each of which lasts 1.5 hours. In



(a) (b)

Figure 4.6. Vertical and horizontal driving mechanisms. (a) Driving wheel and horizontal motor encoder. (b) Vertical movement jacks and vertical motor encoder.

the morning tracking, axions come from the MRB side(also denoted sunset side), and detectors in the MFB side(also denoted sunrise side) are used to detect signal. In the evening tracking the opposite happens. The whole vertical range(15°) is covered in all trackings, while only 16° of azimuthal angles are scanned.

4.3.1. Motor Encoders

To know the position of the CAST magnet in spherical coordinates, two motor encoders are used, one coupled to jacks, and one coupled to the drive wheel(Figure 4.6). The vertical encoder ranges from 0 to 53000 while horizontal encoder ranges from 0 to 33000. Encoder units are discreet, and the relation of the encoder units to angles can be seen in Figure 4.7. However, this is a rough conversion and it is not sufficient to calculate the exact angle of the magnet. Inclination and azimuthal angles depend not only on the corresponding encoder, but on both encoders. To have a correct estimate of the position, an initial reference *grid measurement* was done in 2002, in which inclination and azimuthal angles of the magnet were measured precisely for a grid of encoder values. These values are used to make a 2-dimensional interpolation to

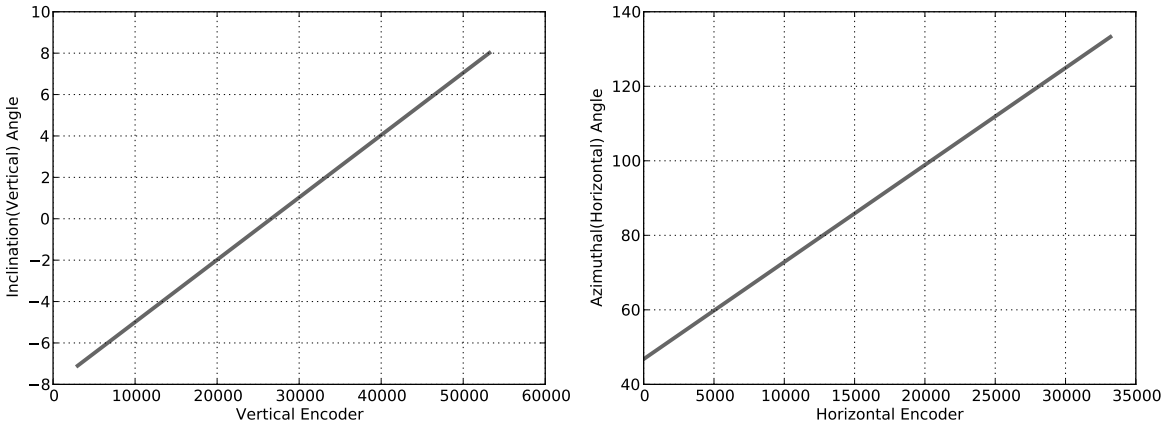
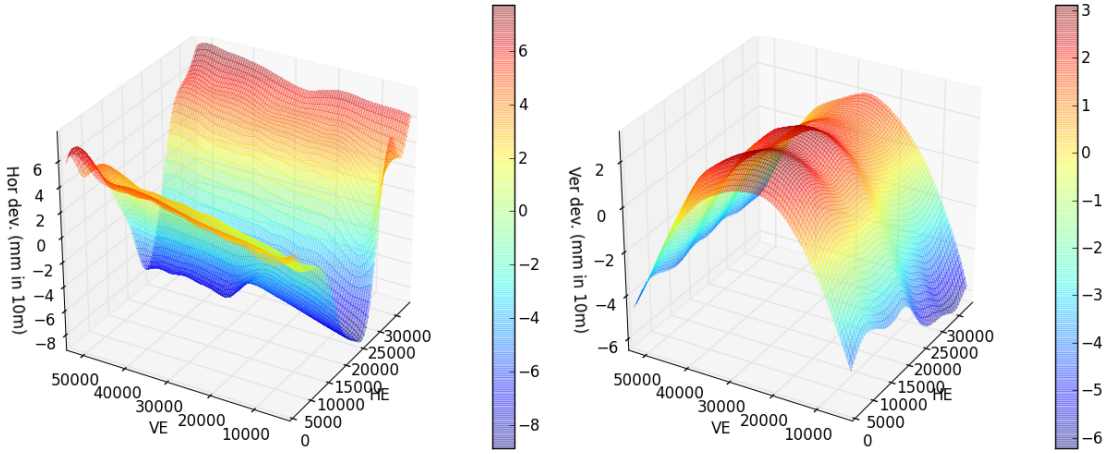


Figure 4.7. Motor encoders vs. angles.

the whole encoder space using Hardy's Multiquadrics method [68], such that for each motor encoder pair (HE, VE), there is a corresponding angle pair (θ, ϕ) and vice versa. From the grid data, it is obvious that the relationship between angles and encoders are not perfectly linear [69]. The deviations from the linear behaviour can be seen in Figure 4.8. The azimuthal angle for beginning of sunrise and sunset vary depending on the time of the year. Thus, in every tracking different range of horizontal encoders are covered, while the full range vertical angles are scanned. Cumulative data of all years from 2005 to 2011, that shows the range of horizontal encoders in different parts of the year is presented in Figure 4.9.

4.3.2. Tracking Program

To track the Sun with CAST magnet, a Labview based program is being used(Figure 4.10). To calculate the position of the Sun, it uses Naval Observatory Vector Astrometry Software (NOVAS). The program can communicate with motor encoders and motors to get the current position of the magnet, read the motor frequency and set the motor frequency. In the manual mode, program aims to direct the motors to the encoder values entered by user. In the tracking mode, it continuously aligns magnet to the Sun, only if it is close to the reachable limits. The program works on a loop with period of one minute. In a single cycle, it calculates what the angular position of the



(a) (b)

Figure 4.8. Non linearity of the encoder-angle relation. In each plot, a linear fit was done for encoders vs. angles, and this fit were subtracted from the angles. (a) Deviation of horizontal angle. (b) Deviation of vertical angle.

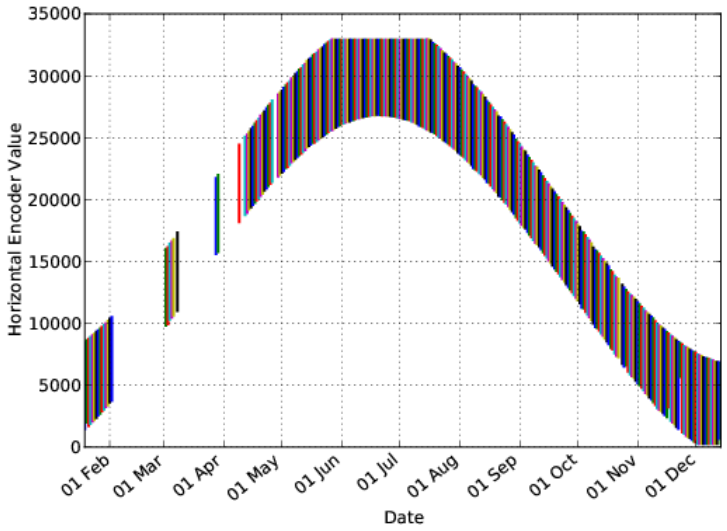


Figure 4.9. Horizontal encoder coverage for trackings throughout the year. Each line denotes the coverage of a tracking. Gaps are due to not having trackings in specific parts of the year.

Sun will be at the start of next minute, and uses the information deduced from the reference grid measurement to convert the angle into encoder units. It then sets the

motor frequencies to go to the exact calculated position.

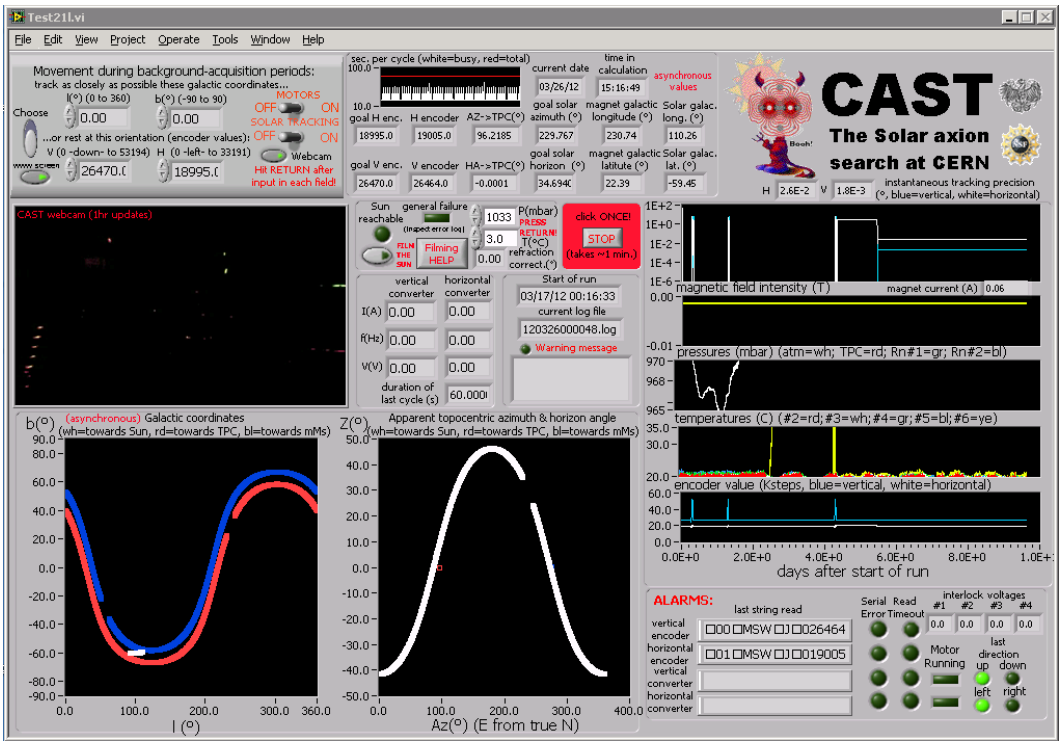
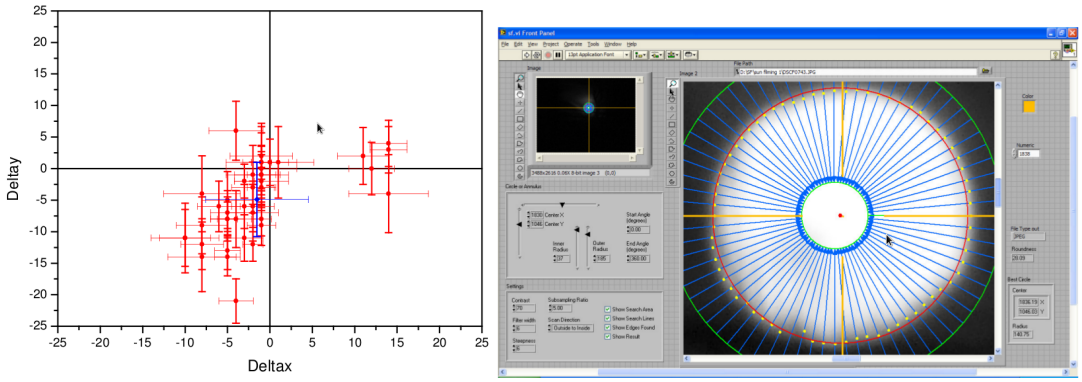


Figure 4.10. Labview based tracking software.

4.3.3. Precision of Solar Tracking

For CAST, precision of the tracking is crucial. One should not be farther than one arcmin(9.2mrad) from the center of the Sun. Otherwise, the calculated axion flux would decrease, and sensitivity of the experimental results would be less reliable. To ensure the alignment precision, independent methods are used.

4.3.3.1. Yearly Grid Measurement. Every year, grid measurements are repeated and compared with the reference grid. This indicates the changes that the system may have undergone throughout the years. The new grids are implemented in the software to create a new interpolation that takes all changes into account.



(a) (b)

Figure 4.11. 2008 Sun Filming. (a) The deviation from the center of the Sun in pixels. (b) Analysis software that calculates the position of the center of the Sun.

4.3.3.2. Sun Filming. During trackings, CAST magnet tracks the sun behind the walls of experimental hall. Only during March and September, CAST has chances to observe the visible light emitted from the sun, through a window in the experimental area. During the tracking, an optical camera that is aligned with the magnet takes photos of the sun. The optical analysis is done on the images to calculate the position of the center of the sun on the CCD of the camera. The position in pixels is compared with the calibration that shows where the center of the sun should fall on the CCD. The analysis software and deviation in pixels from 2008 sun filming can be seen in Figure 4.11.

4.4. Slow Control System

Slow Control System is a Labview based data acquisition, logging and plotting system(Figure 4.12). In the CAST experiment, there are numerous sensors to measure important parameters such as

- pressures of detector gas, buffer gas, environment and vacuum systems
- temperatures
- loads on the jacks that lift the magnet
- position of the magnet

- inclination of the magnet.

All of these parameters are measured real time and most are already displayed in digital displays in various parts of the experimental area. For periodic logging and merging of the data, all data is transfered to the Slow Control System. Data is taken in form of analog and digital signals to the Slow Control rack, connected into national instruments cards, and read by the PC via Labview. Slow Control performs three important tasks with the data:

(i) Plot the data real-time. All parameters that are fed into Slow Control can be viewed remotely.

(ii) Log the data periodically. During normal conditions, period is 60 seconds. However if one of the sensors see a large relative change, or if it is initiated manually, the program starts logging with different period. The logged data is periodically transfered to Andrew File System(AFS) for easy access from Linux and Windows machines.

(iii) Send SMS alarms to warn the people responsible of the systems. Especially if some pressures exceed specific values, there is a danger of some parts of the vacuum system being damaged. When running with ^{3}He as a buffer gas, these warnings become more essential, since any loss of ^{3}He will cause serious problems in the running of CAST.

4.5. Gas System

As explained in Chapter 3, axion helioscopes can make use of a low-absorption buffer gas to detect axions of a specific mass. CAST experiment have used ^{4}He in the first part of Phase II, and filled the magnet bores with amount of gas that accounts for pressures from 0 to 16.4mbar at the magnet temperature of 1.8K. At such low temperatures, ^{4}He liquefies at 16.405 mbar and the pressure can no longer be increased. For this reason, to probe axions with higher masses, ^{3}He was used. In contrast to ^{4}He, ^{3}He has its saturation pressure for 1.8K at 135.6mbar, thus it allows CAST to increase the pressure to scan for higher mass axions. With both gases, to ensure the sensitivity

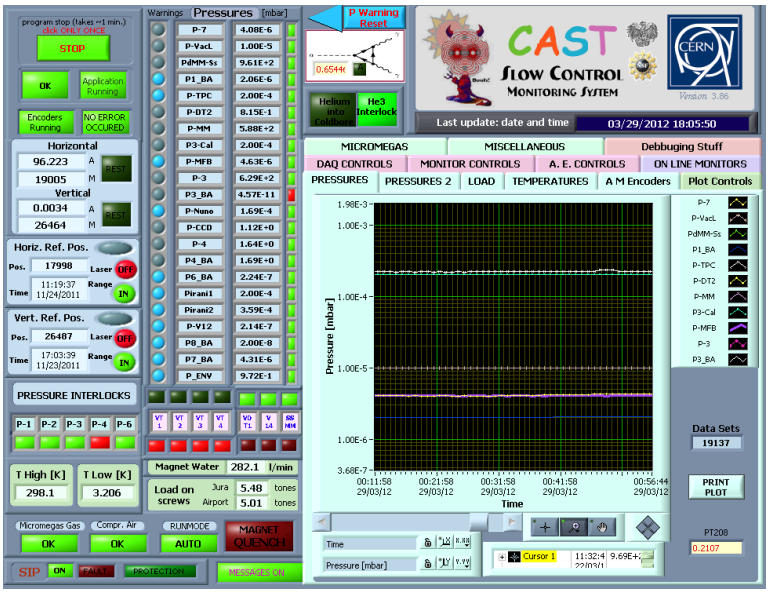


Figure 4.12. Slow Control software.

of axion scanning, one has to be able to insert the gas in precise amounts. CAST gas system was developed to serve this purpose. For the operation with ^{3}He, a general upgrade had to be done. Pressures reached by ^{3}He would be much higher than ^{4}He, and ^{3}He is an extremely expensive gas. Thus extra protective measures were taken to prevent leakage of ^{3}He outside the system and protect the cold windows. The elements of gas system will be explained in this section. For further details, [70] can be used as a reference.

4.5.1. Cold Windows

Operation with ^{3}He require a good isolation of the buffer gas region from the vacuum regions as seen in Figure 4.13. At CAST it is done by *cold windows* that are installed in the ends of cold bores. The windows used in CAST are developed by CERN Central Cryogenics Laboratory(Cryolab) [71] to have the following properties:

- High X-ray transmission for $2 - 10$keV range.
- Low leak rate of Helium from cold bore to vacuum side.
- Stability under rapid pressure changes, for instance during a quench.

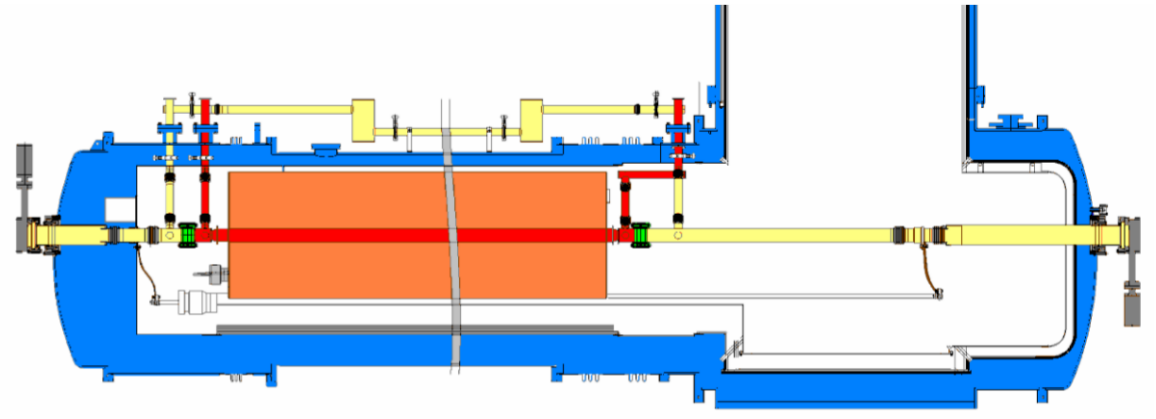
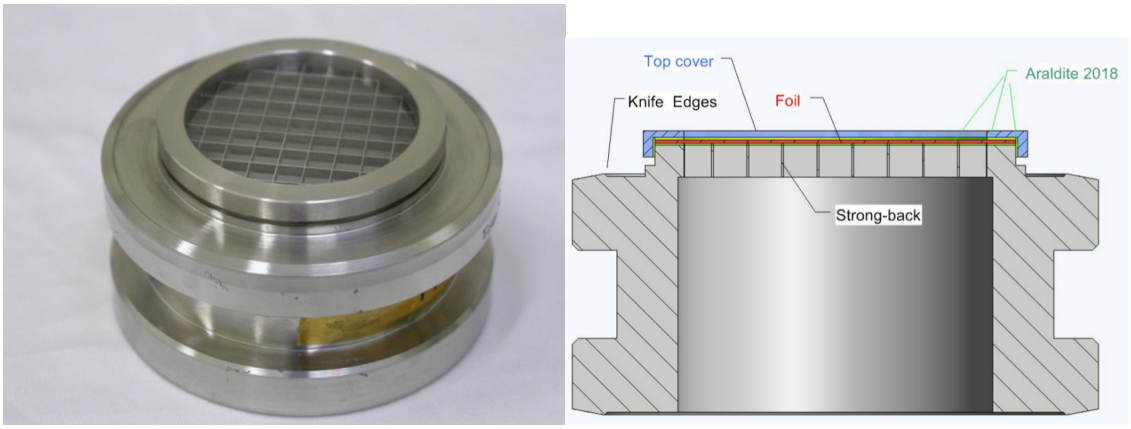


Figure 4.13. The schematics of the gas pipes inside of the cryostat. Green parts denote the cold windows and horizontal red pipes are the cold bores of the magnet. Yellow pipes denote the various vacuum parts of the system.

Cold windows are made from 15μm thick polypropylene attached to stainless steel grid structure, which is called *strongback*(Figure 4.14). The polypropylene provides 70% to 90% transmission for two to 10keV X-rays, and good hermeticity to prevent leaks. In 2008, the windows were heated to 80K to prevent some gasses condensing on their surface.



(a) (b)

Figure 4.14. (a) Photo of the cold window and its strongback. (b) Schematic drawing of the cold window.

4.5.2. Filling System

The density inside the cold bore is increased in small steps, and in each step one becomes sensitive to a narrow range of axion masses. The details of this discussion can be found in Section 3.3.4. For 2008, the first year of the ^{3}He phase, step size was chosen to be 0.08mbar to provide equal coverage for all axion masses. In the middle of each shift density is increased one step during 3-4 minutes. This way, detectors on both side have chance to scan the same setting for half a shift.

The filling system consist of the following elements(Figure 4.15a):

- Storage volume: All gas that is used to fill the magnet bores is stored here.
- Purging system: Purging system consists of two charcoal traps, first to capture water and oil, and second to purify the gas up to a higher degree. While the first trap operates at room temperature, second trap is at 77K.
- Metering volumes: There are two metering volumes, MV2 and MV10, consecutively with capacities 1.63 litres and 8.58 litres. MV10 is used to fill the magnet up to 10 pressure steps at once and MV2 is used to fill the magnet up to two steps.
- Thermal bath: The metering volumes are placed in a temperature bath, that is regulated at constant temperature of 36.0°C. It provides a precise measurement of the amount of gas in the metering volumes and the gas sent into the magnet bores.

The gas is primarily sent from the storage volume to metering volume via purging system, then from metering volume to the magnet. A full filling cycle during 2008 was as follows(Figure 4.15b):

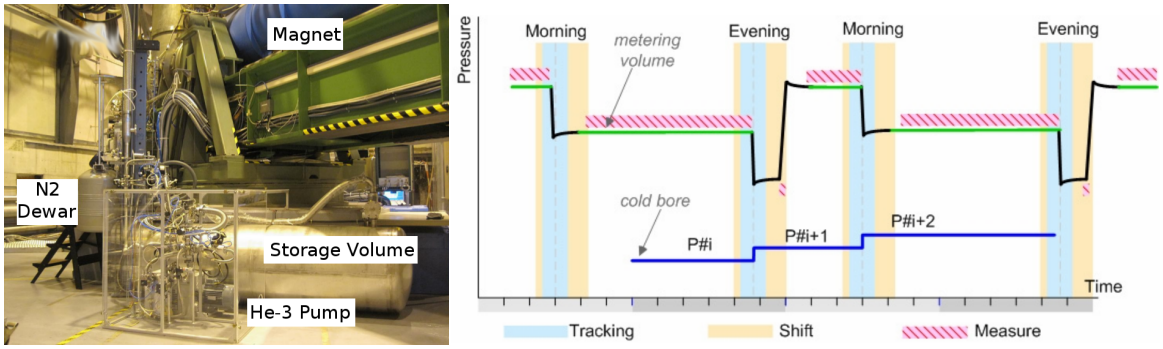
(i) After morning shifts MV2 is filled up to 900mbar, getting the system ready for filling the cold bore.

(ii) In the middle of the evening shift, MV2 is emptied into the magnet down to a calculated value, so that magnet bores are filled with amount of gas accounting

for one pressure step.

(iii) In the morning shift, magnet is filled one more step, emptying the MV2 down to 200mbar.

During the data taking, there may be quenches, bake outs(heating of cold windows to release the gases that has condensed on the surface) or cryogenics maintenances that require CAST to empty the cold bore to the storage volume. In such occasions, magnet is filled from zero to a certain pressure using MV10, shortening the filling time significantly.



(a) (b)

Figure 4.15. (a) Photo of the gas system. (b) Filling scheme used during 2008.

4.5.3. Expansion Volume

With the ^{3}He upgrade, the robustness and security of the gas system was increased against higher pressure differences. During a quench, due to increase in the temperature, the pressure in the coldbore can increase up to 2.7bar. Although cold windows are tested at high pressures, it is highly risky to expose the windows to such pressures. To prevent this, a 500 lt expansion volume was installed on the top of the magnet. In case of a quench or a rapid increase of cold bore pressure, a digital signal is sent from PLC to open the pneumatic valves between the cold bore and the expansion volume, letting ^{3}He flow to expansion volume. Later, recovery procedure is applied to transfer the gas from expansion volume to storage volume. Installation process of the expansion volume to CAST magnet is shown in Figure 4.16.

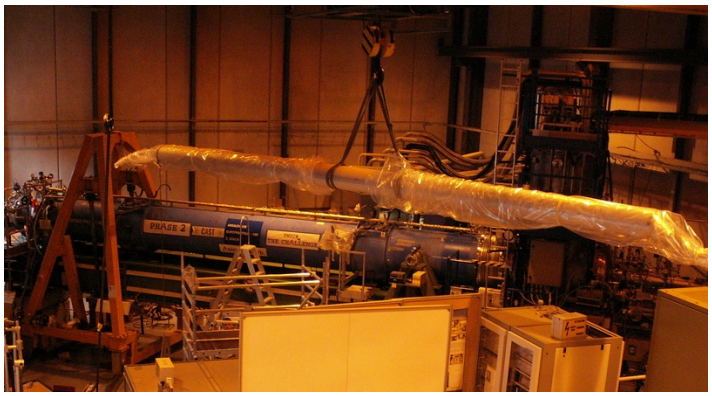


Figure 4.16. A photo from the installation of the expansion volume.

4.5.4. Programmable Logic Controller

The operation of the gas system is done via Programmable Logic Controller(PLC) system. PLC is integrated with PVSS II [72], which provides a GUI and data logging capabilities. The PLC can communicate with the pneumatic valves and pumps in the system. Furthermore interlocks can be defined inside the PLC to perform automatic operations in special cases. The CAST PLC can be operated in different modes, with different permission and access levels. The regular filling cycle is done in *operator mode*, in which the user is allowed to run pre-defined procedures such as filling the metering volume or transferring a certain amount of gas into the magnet bore. In *expert mode*, user has more access, and can manipulate valves and pumps manually to run more complex operations. The user interface of CAST PLC is displayed in Figure 4.17.

4.6. Detectors

At CAST, X-ray detectors are mounted at both ends of two magnet bores to detect photons converted from axions. During the sunrise, axions come from the MRB side of the magnet and enter the magnet without interacting with sunset detectors and their shielding. In the magnetic field of the magnet, some of them can be converted into photons and be detected by the sunrise detectors. During the sunset the opposite occurs. Axion to photon conversion probability is expected to be quite small and

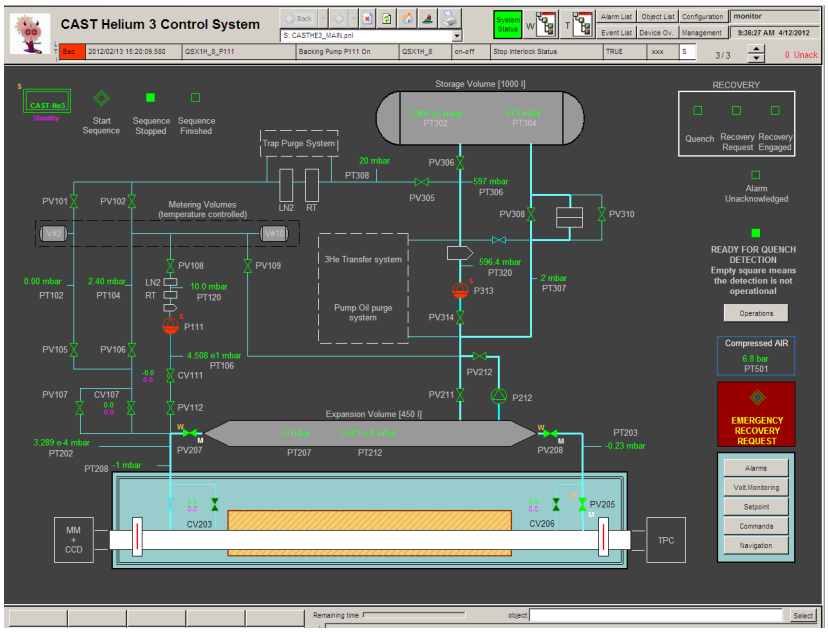


Figure 4.17. User interface of the CAST PLC System.

asuming a coupling constant of 10^{-10}GeV^{-1}, mean number of photons that are expected each tracking is less than one. To be able to detect excess of photons during tracking, CAST X-ray detectors need to have low intrinsic background levels. To achieve this, few methods have been used at CAST:

- Passive shielding to block external gammas and X-rays.
- Active shielding to create an active veto for incoming muons.
- Using radiopure materials in and around the detector.
- Using pattern recognition algorithms to distinguish X-rays from other particles.
- Focusing expected incoming X-rays into a smaller plane, to increase signal to noise ratio.

Since the beginning of CAST three types of detectors were used to detect X-rays, X-ray telescope with Charge Coupled Device (CCD) as the focal plane, Time Projection Chamber (TPC) and MICROMEsh GAseous Structure (MICROMEGAS).

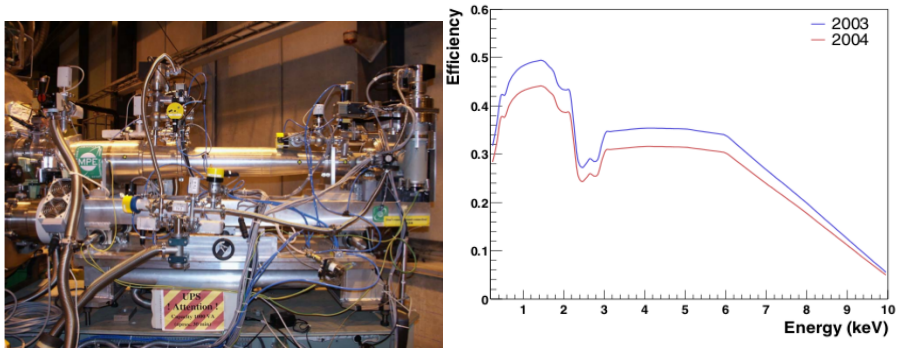
4.6.1. CCD and the X-ray Telescope

On the MFB side of the CAST, one of the magnet bores are coupled to an X-ray telescope(Figure 4.18a), which focuses all X-rays that come parallel to its axes to a small spot of 9mm^2 on pn-CCD detector. CAST CCD is the only detector at CAST that utilizes an X-ray telescope. Focusing the incoming signal has two advantages:

(i) The expected signal is in a area much smaller than the cold bore. Thus the background rejection is increased by a factor 150, furthermore signal and background can be measured at the same time, such that all events outside the spot is considered as background.

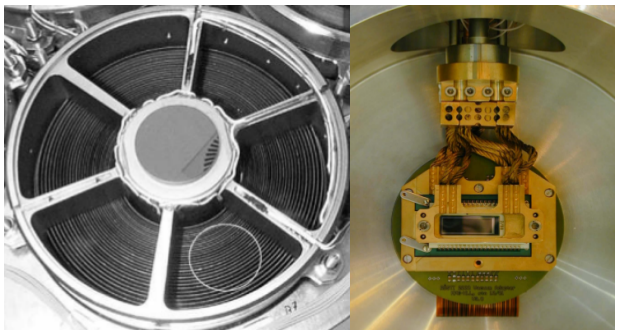
(ii) Sun's axion emission image can be seen in the CCD chip, thanks to imaging capability provided by the telescope.

X-ray telescope and the pn-CCD have lower hardware efficiency than gaseous detectors at CAST, but since the signal to noise ratio is better, it has bigger discovery potential. The efficiency curve of the X-ray telescope and pn-CCD is shown in Figure 4.18b.



(a) (b)

Figure 4.18. (a) The photo of the X-ray telescope and pn-CCD detector. (b) The combined efficiency of the telescope system and the pn-CCD for $1 - 10$keV range.



(a) (b)

Figure 4.19. (a) The comparison of the aperture of the cold bore and the X-ray telescope. (b) The pn-CCD chip.

4.6.1.1. X-ray Telescope. In contrary to visible light telescopes, X-ray telescopes can only utilize reflections from X-ray mirrors at small angles, which is called *grazing incidence*. CAST X-ray telescope is a Wolter I type [73] and was built for the A BRoad band Imaging X-ray All-sky Survey(ABRIXAS) mission [74].

The telescope is made of 27 gold coated concentric nickel shells, each of which are parabolic or hyperbolic. The diameters of the shells are between 76mm to 163mm and telescope has a focal length of 1600mm. The telescope is azimuthally divided into six sectors, and a single sector is enough to cover whole aperture of coldbore, which has a diameter of 43mm. The comparison of the entrance of the telescope and the cold bore aperture is presented in Figure 4.19a.

4.6.1.2. The pn-CCD Detector. pn-CCD is type of a silicon detector that works with the following principle. The incoming radiation creates electrons and holes in the silicon, and with the help of the electric field, electrons and holes move to opposite sides of the detector. Electrons get captured in the potential wells below the pixels, and are transferred from one well to another as the potential of each cell changes consecutively.

The pn-CCD at CAST is developed for XMM-Newton [75], it is fully depleted and 280μm thick. It has an area of 2.88 cm^2 consisting of 200×64 pixels, each of which

is $150 \times 150\mu m^2$. The X-rays coming parallel from the cold bore aperture fall on a spot with an area of $9mm^2$ on the detector. The detector has no trigger and takes data continuously. All pixels are read in 6.1msec and the resulting charge is integrated during 65.7msec creating a 71.9msec cycle. It is running at temperature of -130°C and pressure of 10^{-5}mbar.

The detector is illuminated daily by an ^{55}Fe source for calibration, which provides the monitoring of the performance and stability of the detector.

4.6.2. TPC

The TPC takes its roots from drift chambers [76] and multiwire proportional chambers(MWPC) [77]. In both, there is a gas filled volume, readout wires and there are different voltage levels on opposite sides, to guide electrons to move toward the wires.

MWPC is an older technology compared to drift chamber. In MWPC there is a gaseous volume and planes of parallel wires. In the gaseous volume incident charged particles or photons can ionize gas atoms and the free electrons move towards the wires with the help of the electric field, ionizing more atoms on their way. A signal is induced in the wires. The position of the interaction and the energy of the particle can be calculated from the wires in which a charge is accumulated. On the other hand the drift chamber is a particle detector, that utilizes the signal on the wires, with addition of the arrival time of the electrons to the wires. An additional information, the position of the interaction in the drift direction can be calculated from the drift time.

Blum [78] categorizes drift chambers in three categories and puts TPC in the 3rd one. This type consists of a wire free drift volume, and one or more layers of wires. The wires are loaded with different voltage levels to provide cathode and anode planes. The CAST TPC works on the same principle. It has a rectangular drift volume of 10cm × 15cm × 30cm(Figure 4.20), filled with 95%Ar+5%CH_4 mixture, the drift direction being aligned to 10cm length [79]. On one side of drift volume, there is

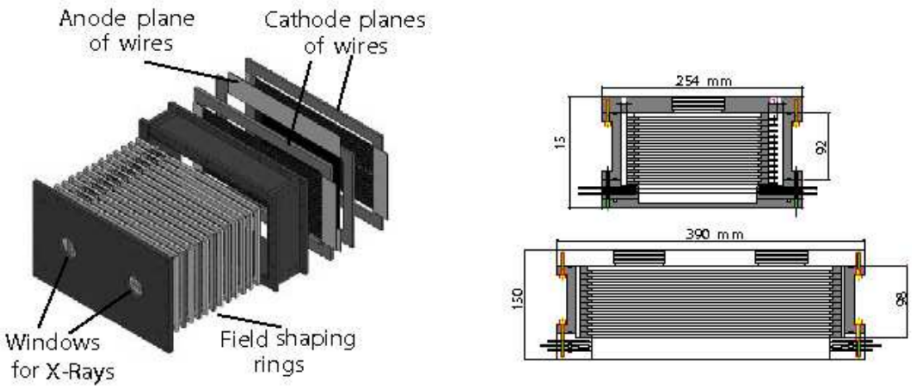


Figure 4.20. The exploded view of the CAST TPC.

a plane loaded with -7kV. On the other side, there are 3 wire planes: cathode wires(at ground), anode wires(at +1.85kV) and dead cathodes(at ground). The cathode and anode wires are aligned perpendicular to each other. All the wire planes are separated by 3mm from the adjacent one and wires in the same plane are separated by 3mm. The region between the cathode wire planes is called the amplification region. The drift volume has an electric field of 700V/cm, while in the amplification region the field increases to 5kV/cm(Figure 4.21). In the CAST TPC, free electrons that are created in the gas mixture drift to the cathode wires. In the high field of the amplification region, they are multiplied with an avalanche effect and create a bigger signal on the anode wires. The position of the event can be obtained from the fired anode and cathode wires [1] and the drift time.

The cross section of the TPC is large enough to cover both bores of the magnet. On the magnet side, its closed by a plane that has two circular openings that are aligned with the magnet bores. The connection of the gas chamber and vacuum is done by drift windows: 3μm aluminized mylar, stretched on a strongback. In the vacuum sides, there are two vacuum regions, separated by a differential window. The bad vacuum region is between drift window and the differential window, and the good vacuum region is between the differential window and the cold bore. The separation

[1]When the charge on a wire is higher than the mean charge on it with excess of few standard deviations, the wire is said to be fired.

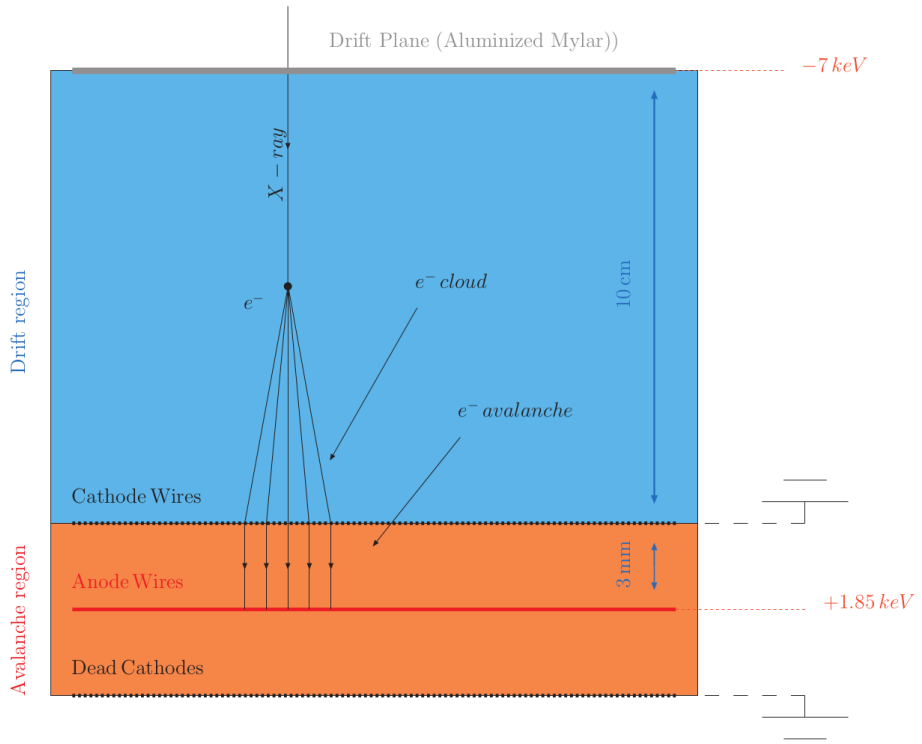


Figure 4.21. The schematics of the working principle of the CAST TPC [80].

is necessary, because there is a diffusion of detector gas through the drift window to vacuum side, and the differential window prevents the gas molecules from reaching the cold bore and sticking to the cold windows.

To build the right shielding for the TPC, a comprehensive background study, consisting of simulation and experimental measurements has been done [81]. The test show that the big contribution to the background comes from the environmental gamma radiation, which is mostly due to the radioactivity of the walls in the experimental area. The CAST TPC shielding consist of 5mm copper, 2.5cm lead, 1mm cadmium and 22.5cm polyethylene. This set up allowed the CAST TPC to have lower background level by a factor of 4. Although increasing the thickness of the shielding would result in a lower background, it is not feasible due to the mechanical restrictions of the magnet movement system.

Time Projection Chamber has been operated on the MRB side of CAST, from

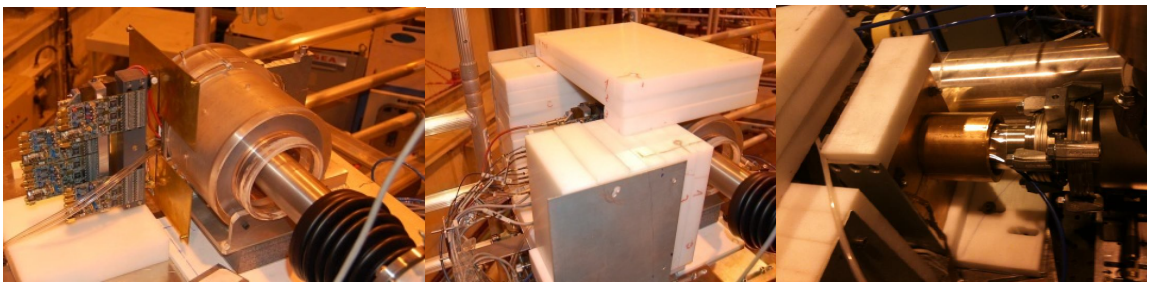
the beginning of the experiment until 2007, and took data in vacuum and ^{4}He phases. In the start of ^{3}He phase in 2008, TPC is replaced with two micromegas detectors. This choice is primarily favored by the lower background level and better stability of the micromegas detectors.

4.6.3. MicroMEGAS

Micromegas has been developed in 1996 to provide better characteristics for particle detection than MWPC technology [82]. It is also a gaseous drift detector, in which wire planes of MWPC are replaced with micromesh and strips. Further details and working principle will be explained in the Chapter 5.

Micromegas detectors have been used in CAST in three of the four magnet bores. On the sunrise side one micromegas is installed, whereas in the sunset side two micromegas are installed.

4.6.3.1. Sunrise Micromegas. Sunrise Micromegas is installed in the MFB side of the magnet. It is in the end of a 2m long vacuum line after the magnet. (Figure 4.23). Many detectors with different micromegas technologies(Chapter 5) have operated in the sunrise line since 2003. Currently a latest technology microbulk detector is installed and operates with a gas mixture of 97.7% Argon, 2.3% Isobutane, at a pressure of 1.4 bar. It has a compact shielding composed of lead, copper, cadmium and polyethylene. In 2011, the shielding is extended with an extra piece installed to cover the pipe near the detector. (Figure 4.22). The detector is calibrated once a day using a radioactive ^{55}Fe source, that is attached to an automatic calibrator system. The information that is obtained from the calibration is used to select or reject the counts in the detectors as X-rays. The drift window of the sunrise micromegas is connected to the vacuum pipe. Similar to TPC, sunrise micromegas vacuum line has a differential window with high X-ray transparency. The purpose is to stop any gas molecules from reaching the cold windows. The vacuum in detector side of the window are in the range of 10^{-4}mbar, while in the magnet side it is 10^{-7}mbar.



(a) (b) (c)

Figure 4.22. Different shielding setups of the sunrise micromegas. (a) The detector with the compact shielding. (b) The detector with the additional layers of polyethylene shielding. (c) Latest addition to the shielding.

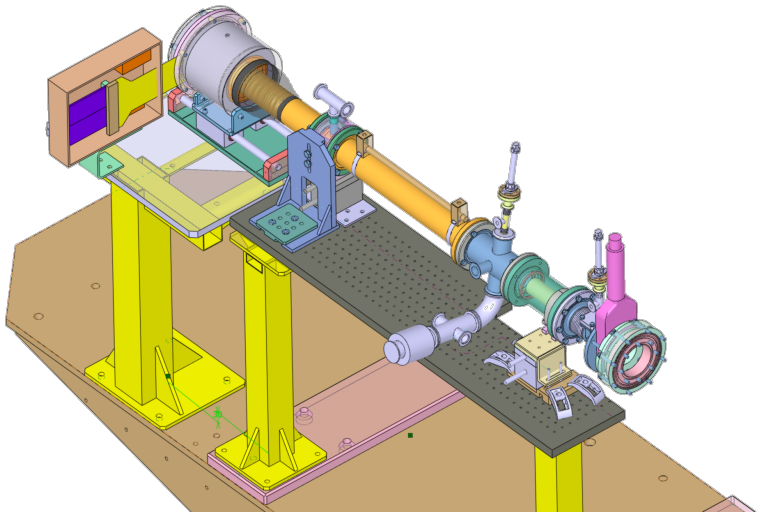


Figure 4.23. Drawing of the sunrise micromegas.

4.6.3.2. Sunset Micromegas. In the sunset(MRB) side of the magnet, there are two micromegas detectors, each one covering a magnet bore. These have been installed in 2007, after the removal of the TPC detector. The detailed explanation of the sunset micromegas system will be given in the Chapter 5.

5. MICROMEGAS DETECTOR

Micromegas detector has been derived from the ideas of MWPC, and aims to provide better characteristics such as energy resolution, spatial resolution, response time and as a result of these factors, a better rejection capability. In this chapter, firstly the interactions of photons and charged particles in matter, secondly the detection of particles in gaseous detectors, then the working principle of the micromegas will be explained. Next, the different types of micromegas that are used in CAST will be introduced, and finally a detector characterization study will be described.

5.1. Interactions of Particles in Matter

To understand the micromegas detector, one has to understand the basic interactions of the particles with the gas. For both charged particles and photons, interaction with the gas atoms can result in:

(i) Ionization: The incoming particle directly ionizes the gas atom, creating free electron and a gas ion. These electrons are called primary electrons.

(ii) Excitation: Interaction of the incoming radiation causes the atom to go in an excited state. It can emit a photon and go back to its ground state, or if there is another gas in the environment, it can interact with molecules of these gases to cause ionization.

5.1.1. Interaction of Charged Particles

Charged particles mainly interact with gas atoms through electromagnetic processes[2] like coulomb interactions, Cerenkov radiation, transition radiation and bremsstrahlung. The most dominant process for gaseous detectors is the coulomb interaction, where the incoming particles interact with the electromagnetic field of the gas atoms. Depending

[2]The strong and weak interactions are orders of magnitude less likely than electromagnetic, thus can be ignored in the context of gaseous detectors.

on their energy, charged particles deposit some of their energy to the gas atoms at each interaction, ionizing or exciting the atoms. It is common to talk about energy loss per unit length, instead of the energy transfer in each interaction.

5.1.1.1. Energy Loss. The energy loss per unit length, dE/dX is given by the Bethe-Bloch formula as

$$-\frac{dE}{dX} = \frac{2\pi N_A z^2 e^4 Z\rho}{A\beta^2 m_e c^2}\left[\ln\frac{2m_e c^2\beta^2 E_M}{I^2(1-\beta^2)} - 2\beta^2 - \delta - 2\frac{C}{Z}\right] \tag{5.1}$$

where N_A is the Avogadro number, z and β are the charge(in units of e) and velocity(in units of c) of the incoming particle, Z and A is the atomic number and weight, ρ is the density of the medium, m_e and e are the electron mass and charge, E_M is the maximum energy transfer in a single collision and is derived from kinematics of head-on collisions, I is the average ionization potential, δ and C are the density and shell corrections for particles with low and high energies.

The Bethe-Bloch has a shape as seen in Figure 5.1. The energy loss is maximum for lower energies, and almost constant after a certain energy. It can be said in general that after 1GeV, all particles deposit the same amount of energy per unit length. This is called the minimum ionization. For each gas, there is an ionization and excitation potential, which is the minimum energy needed to ionize or excite an atom. However, the average energy that is deposited by the incoming particle to ionize the atom in each collision is higher than the ionization potential. This is due to the fact that the incoming particle normally ionize and excite the gas atoms at the same time. For instance for Argon, excitation potential is 11.6eV, and the ionization potential is 15.8eV, but the average ionization potential per collision is 26eV [84]. The energy loss distribution for collisions is given by landau distribution (Figure 5.2a), which has a tail on the higher values and a cut off at E_M, the maximum energy transfer. The tail causes the average ionization energy to be higher than the most probable ionization energy.

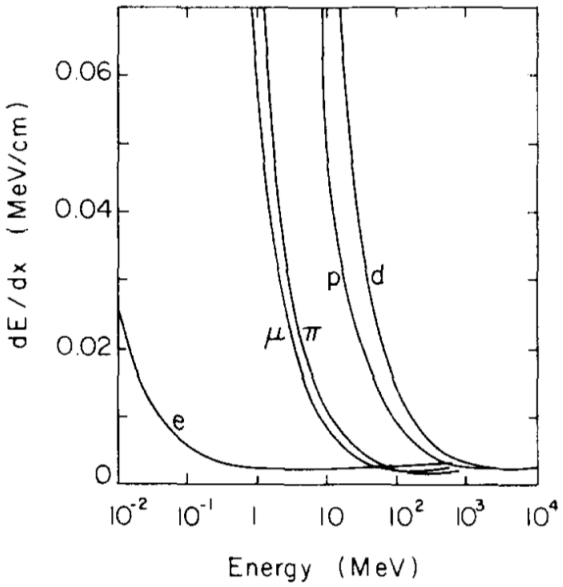
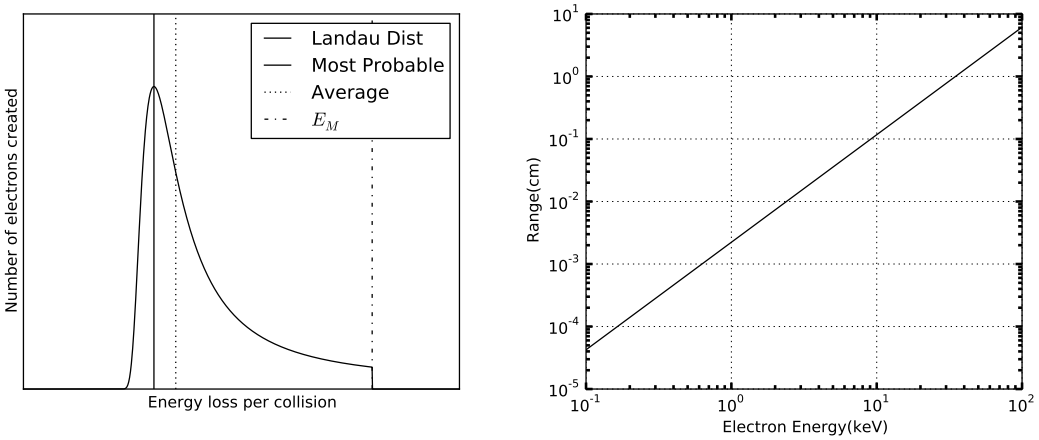


Figure 5.1. dE/dx in air for different particles. Plot taken from [83]. At high energies, differential energy loss becomes almost sames for all particles, independent of their mass, until radiative effects become considerable.



(a) (b)

Figure 5.2. (a)Landau distribution, with a cutoff at maximum energy transfer E_M. The dashed curves show the most probable and average energy transfers. (b)Range of electrons from 1 to 100keV in 1.4 bar Argon in room temperature.

5.1.1.2. Range of Slow Electrons. At ionizing collisions, electron ion pairs are created. Although most electrons are created with low energies(less than 100eV) and are immediately absorbed, landau distribution shows that electrons can gain energy up to

E_M. This relatively faster electrons can traverse an amount of material. An empirical formula up to few hundred keV is given by [83]

$$R = 0.71E^{1.72} \tag{5.2}$$

where R is the range of electron(in length×density→ $\mathrm{g \cdot cm^{-2}}$), and E is the energy of the electron in MeV. For instance in micromegas chamber conditions(1.4bar of Argon gas in room temperature), a 3keV electron has range 140μm while a 100keV electron has range 6.3cm (Figure 5.2b).

The range of slow electrons are important in the following sense: If the electrons are energetic enough, they can escape the detection volume, and this would decrease the energy deposited in the chamber.

5.1.2. Interaction of Photons

Photons can interact with matter via three processes:

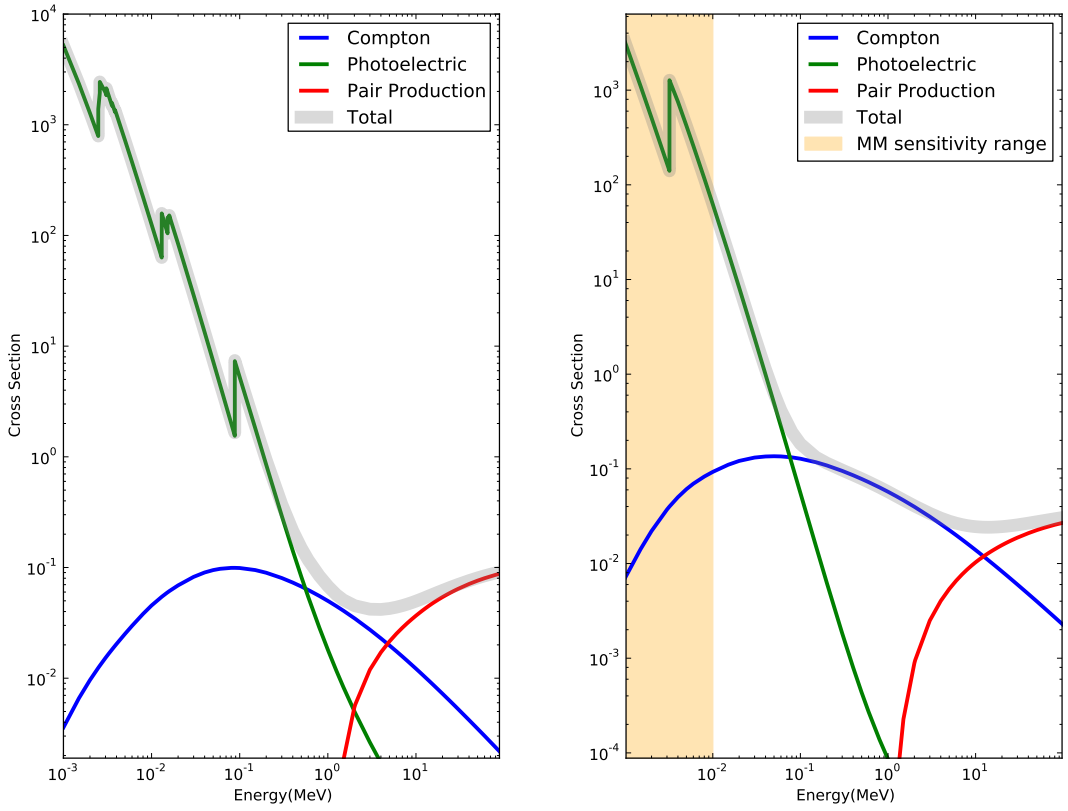
- Photoelectric effect
- Compton scattering
- Pair production

Contrary to the interaction of charged particles, photons deposit nearly all of their energy in single interaction. Thus instead of energy loss per unit length, one can work on the attenuation of the photon beam after a distance x.

$$I(x) = I_0 \exp\left(\frac{\mu}{\rho}x\right) \tag{5.3}$$

where x is the mass thickness of the material(length×density), $I(x)$ is the intensity of the photon beam after a thickness x, I_0 is the intensity of the initial beam, $\frac{\mu}{\rho}$ is the absorption coefficient. The absorption coefficient is proportional to the cross section of the different interaction processes and has units $\mathrm{cm^2/g}$. Cross section of each process

depends on the energy of the photon, and total cross section is simply sum of all possible processes. As the photon energy goes from low to high, photoelectric effect, Compton scattering and pair production has highest cross sections respectively. Cross section of these three processes for Lead and Argon can be seen in Figure 5.3. In Argon, the range of energies to which micromegas detector is sensitive, is indicated with orange. For x-rays in this energy range, photoelectric effect dominates with orders of magnitude. Data obtained from [62].



(a) (b)

Figure 5.3. Cross section of different photon interactions in (a) Lead, (b) Argon. X axis shows the energy of the beam, while y axis shows the cross section, which is proportional to the interaction probability.

5.1.2.1. Photoelectric Effect. The lowest energy process is the photoelectric effect, where incident photon interacts with the bound electrons of gas atoms. An atom has different shells with different binding energies. The cross section of interaction with

the electrons in a shell depends on the energy of the photon and the total cross section is sum of the cross sections for all shells. For instance if the incoming photon with energy E_γ interacts with a certain shell i with binding energy E_i, an electron will be emitted with energy $E_e = E_\gamma - E_i$. It is clear that the cross section is zero for a specific shell if the photon energy is less than the binding energy of the shell. This cause sharp increases in the cross section at binding energies of the shells, and is called *absorption edge*. For instance in the 5.3b, it is seen that at 3.2keV, there is the K-edge for Argon, which cause a sharp increases in the Argon photoelectric cross section. It should also be noted that, for x-rays with energy higher than K-edge, the most probable interaction is with the K-shell electrons.

After the emission of electron, the atom rearranges its electrons to go to its ground state via two processes:

- Fluorescence: If the photon has interacted with the i^{th} shell, an electron from j^{th} shell with lower binding energy fills the gap in the i^{th} shell, and a photon with energy $E_i - E_j$ is emitted.
- Auger effect: An electron from a higher shell fills the gap in the shell in which interaction took place and the remaining energy is released by emitting and electron, which is called and *Auger electron*. The arrangement of the inner electrons may continue and low energy photons may be released to complete the arrangement.

The fraction of the fluorescence photon emission to total emissions is an important quantity in gaseous detectors. It is called *fluorescence yield* and it increases with the atomic number of the gas. In argon, it is 0.15 and the emitted photons have energy lower than the K-edge binding energy, thus the probability of them interacting again with the gas atoms is much lower. These photons can easily traverse and leave the detection volume. On the other hand, the auger electrons that are emitted have much shorter mean free path, and will most likely be absorbed immediately. This is responsible for the *escape peak* phenomenon. When the fluorescence photons which has lower energy than the K absorption edge escape the volume, the total energy that is deposited in

the detector will be the energy of the first emitted electron. The accumulation of this type of events create a secondary peak with lower count in the calibration spectrum of the gaseous detectors(See Section 5.6).

5.1.2.2. Compton Scattering. Compton scattering occurs for energies above the highest binding energy of the shells. In Compton processes, the photon is not fully absorbed, but scattered with a lower energy, at the same time detaching an electron from the atom.

5.1.2.3. Pair Production. Pair production, the high energy phenomenon is creation of a particle-anti particle pair from the incoming photon, and only occurs if the incident photon energy is higher than two times the particle mass. The most common one is production of an electron-positron pair.

5.2. Detection of Particles in Gaseous Detectors

Historically roots of gaseous detectors go back to proportional counters, which is simply a cylindrical gas filled metallic volume, that has a wire at the center aligned with the axis. The wire is loaded with a voltage V, so that when incident particles ionize gas atoms, electrons are attracted to the wire and ions are attracted to the outer shell. As the electrons and ions drift, they do collide with gas atoms, frequency depending on their mean free path. Since the field is proportional to V/r, the acceleration of electrons increase as they approach to the wire, and they start gaining enough speed to ionize new gas atoms, creating an avalanche effect. This phenomenon is called *amplification* or *multiplication*.

With time, gaseous detectors evolved into MWPC and drift chambers, where the drift region and the amplification region is separated, and one or two dimensional spatial reading can be provided with planes of wires, where the 3rd dimension can be measured by using the drift time. An important property is that the electric field in the drift region is constant, so that the drift time can be used to extract the position

of interaction, by using the constant drift velocity. The detection occurs in three steps: ionization, drift and amplification. Ionization phenomenon is already explained in the previous section, this section will explain rest of the phenomena and the gas choice.

5.2.1. Drift and Diffusion

After the ionization, electrons will move to the anode, while the ions move to cathode. As electrons gain speed, they do more collision where they may ionize more atoms. At each collision, the primary electron is scattered in random directions, but the electric field makes them accelerate again in the direction of the field. In average, electrons and ions can be considered to be moving with a constant velocity in the direction of the field. This is called the drift velocity and is much higher for electrons compared to ions. The drift velocity depends on the field E and the gas pressure P, and specially for ions, it is proportional to ratio E/P. A widely used parameter is *mobility*, which is defined as

$$\mu = \frac{u}{E}$$

where μ is the mobility and u is the drift velocity. It is obvious that at constant pressure mobility is constant, therefore is a better quantity to measure experimentally compared to the drift velocity. The mobility is related to the diffusion coefficient D as

$$\frac{D}{\mu} = \frac{\mathrm{kT}}{e}$$

For electrons, mobility is not constant and the drift velocity can be expressed by using mean time between collisions τ, which depends on the interaction cross section of the electron with gas atoms as

$$u = \frac{e}{2m} E\tau$$

While electrons drift, diffusion takes place which cause the dispersion of the electrons in all directions. The space diffusion in a single direction after a time t is given by

$$\sigma_x = \sqrt{2Dt}$$

where the diffusion coefficient D also depends on the electric field, since it changes the energy distribution of the electrons. The spatial resolution gets worse with higher diffusion, and can be improved by choosing a gas with lower diffusion coefficient.

5.2.2. Avalanche Multiplication

As the field becomes higher in the amplification region, electrons easily gain energy to ionize more atoms. In each mean free path, the number of electrons will be multiplied by 2. If we denote the mean free path by α^{-1} and the current number of electrons by n, after a distance dx, the number of electrons will increase by

$$dn = n\alpha dx$$

and integrating, $n(x)$ becomes

$$n(x) = n_0 \mathrm{e}^{\alpha x}$$

The multiplication factor, or gain denoted M can be expressed as

$$M = n/n_0 = \mathrm{e}^{\alpha x}$$

Although there is no theoretical limit in the equations, in operation of gaseous detectors Raether limit applies, $M < 10^8$. As one gets close to this limit, the spark breakdown occurs due to secondary processes and to keep the operation stable, detectors are run well below this limit [83].

5.2.3. The Detector Gas

The gaseous detectors can be operated with almost any gas, however to obtain high gain, good energy resolution and stable operation, there are guidelines for the choice of gas. One has to use a noble gas, because only processes noble gasses interact with particles are excitation and ionization. On the contrary complex molecules have more modes of interaction, and less ionization occurs compared to noble gases with the same voltages. The most common choice is Argon, for being cheaper. The maximum gain one can reach with argon is in the order of 10^4, after which the spark limit is reached. The sparks occur when the emitted photons ionize the atoms of cathode and secondary avalanches are created. To prevent this, it is a common practice to mix the noble gas with another gas, called the quencher. Polyatomic quenchers have transitionless excitations, thus they capture these photons without radiating, and prevent the discharges. Addition of quencher cause gain to drop with the same voltage, but lets higher operation voltages to be used and they can increase the gain of an Argon filled detector up to 10^6. Some commonly used quenchers are CO_2, CH_4, C_4H_{10} and BF_3. Electronegative gases like O_2 cause a worse gain by capturing drifting electrons, so they should be generally avoided [83].

An important property of gaseous detectors is ion exchange. The ions after some number of collisions transfer their charge to the molecule with the lowest ionization potential, causing all ions except this molecule to be neutralized.

In CAST, the micromegas detectors have been operated with Argon + Isobutane mixtures. Although the Isobutane concentration of 5%-7% gives the best energy resolution [85], due to Isobutane being flammable, CERN regulations let CAST to use 2% or 2.3% Isobutane. Effects on the quencher concentration can be seen in Section 5.6.

5.3. Working Principle of Micromegas

In micromegas detector, there are two regions, three voltage levels and two readout layers. First layer is the drift electrode, which is a window made of aluminized

mylar, and supported by a aluminium or copper strongback. Drift window is the first voltage level(set between -500V to -1000V). Second voltage level and the first read-out level is the transparent conducting mesh: micromesh. It has a voltage set between -250V to -300V. The region between the drift window and the micromesh that is filled with the detector gas is the drift region, and it has length of 3cm in CAST prototypes. The third voltage level is the anode strip layer, set at the ground level. The anode strips are separated from the mesh by a distance 50-150μm, and the region in between is called the amplification gap [82, 86].

As explained in previous section, electrons drift to the micromesh, and pass from the mesh to the amplification field, where they are multiplied with an avalanche effect in the higher electric field. As they are multiplied, they ionize more gas atoms. The ions move to the mesh and create a signal there, while the electrons create a signal in the strips. The mesh information can be used to estimate the energy of the incoming particle, while the strip information is used to estimate both energy and the position of the incoming particle. (Figure 5.4) The drift and amplification regions respectively

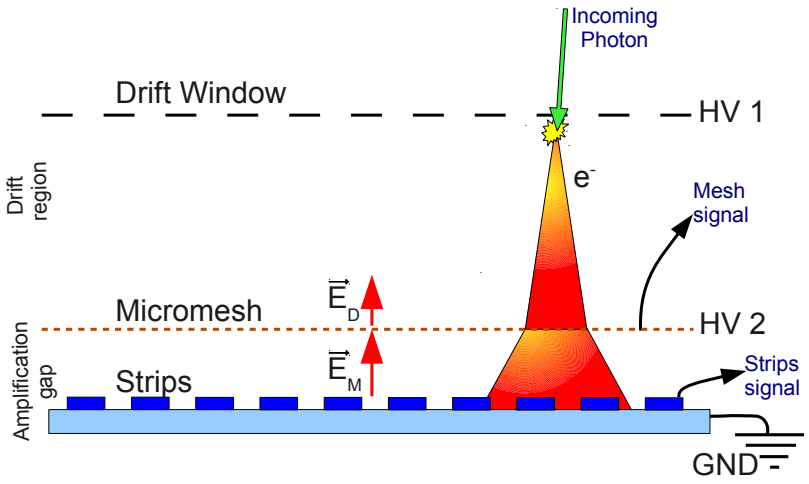


Figure 5.4. The working principle of the micromegas detector.

have around 60V/cm and 3kV/cm electric fields, which are homogeneous throughout both regions. Near the micromesh the field have funnel shape, due to change of the magnitude. This field orientation provide a high *electron transparency*, which is defined

similar to optical transparency: fraction of free electrons that pass from mesh to the amplification region. Furthermore the ions are collected in the mesh due to this shape of the field. The field lines are shown in Figure 5.5.

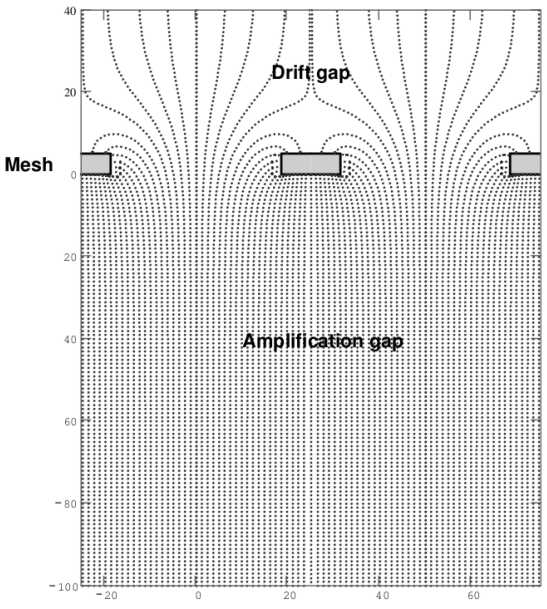


Figure 5.5. The funnel like shape of the electric field lines around the micromesh. Units are in microns. Plot taken from [86].

5.4. Micromegas Technologies

In the CAST experiment, three types of Micromegas detectors have been used since the beginning.

5.4.1. Conventional Micromegas

The first prototypes that were used in CAST were conventional micromegas, in which strip planes and mesh were built separately, and attached to each other by mechanical means. The metallic mesh and strips were separated by insulating kapton pillars, which are printed on the strips by lithography technique. The mesh was stretched and glued to a frame, then placed on the pillars. With the application

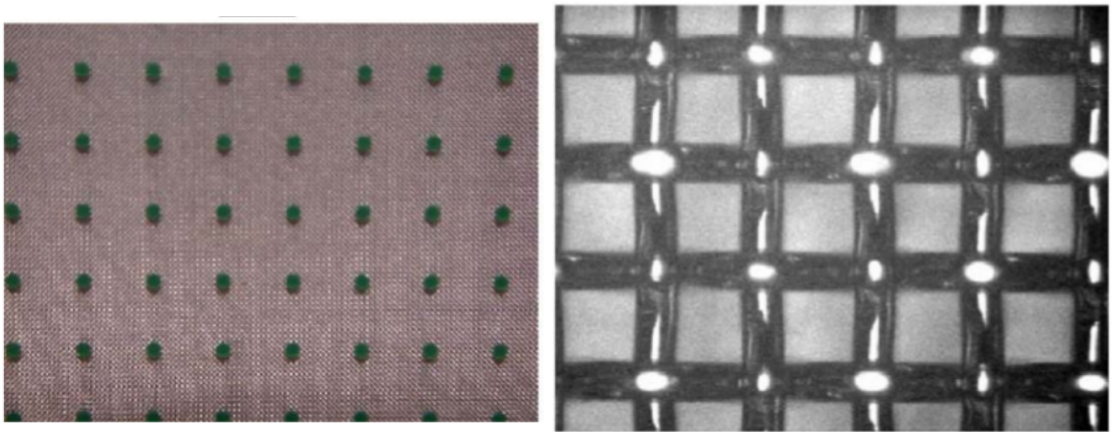
of high voltages, two would be pulled to each other and the pillars would provide a constant distance between the two readouts with an accuracy of 10μm. However this way of manufacturing technique needed human intervention and was prone to errors. Furthermore the resolution and sharpness of x-ray distributions was limited and new techniques had to be adopted.

5.4.2. Bulk Micromegas

The bulk micromegas technology was developed in 2005 by CEA/Saclay and CERN [87]. Instead of mechanical connection, a more sophisticated technique was used to combine the mesh and the strips. A base material like FR-4 was used, on which the strips were printed. A photoresistive film and the mesh was laminated together with the base. Then etching technique was used to create pillars in the photoresistive material. The cylindrical pillars had thickness of 300μm and pitch of 2mm. The desired distance of the mesh and strips could be defined by the thickness of the photoresistive film. A 30μm thick stainless steel woven mesh that can be found commercially was chosen in production of bulk micromegas. With bulk micromegas technique, one can build relatively large area detectors. One can obtain gains up to 2×10^4 and energy resolutions as good as 18%(FWHM at 5.96keV). Moreover, bulk detectors are quite robust and have stable operation. The photos of pillars and mesh is presented in Figure 5.6.

5.4.3. Microbulk Micromegas

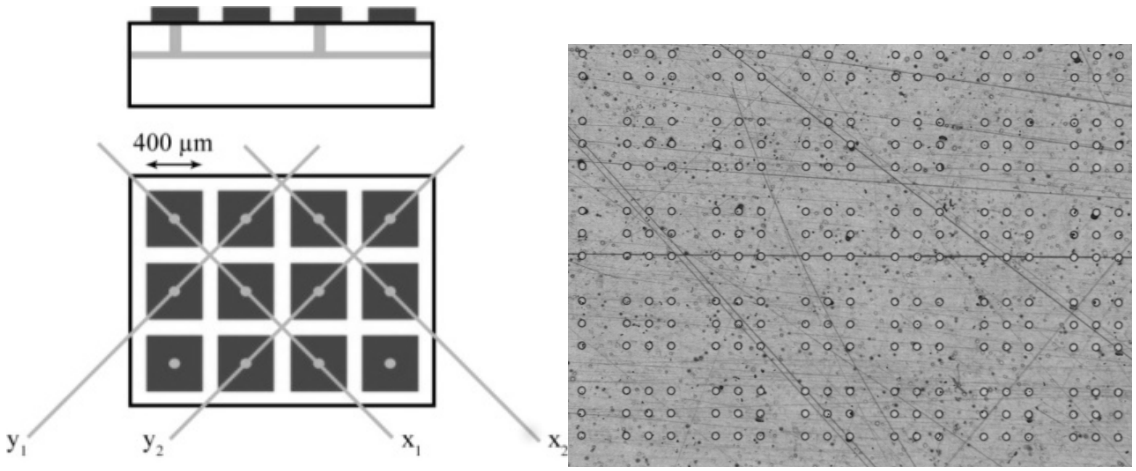
Microbulk technique was developed in 2008 to improve the bulk production technique. Similar to bulk micromegas, strips are produced together with the mesh as a single structure. However, instead of using a commercially available one, the mesh was produced during the fabrication. Several fabrication techniques were used to build microbulk micromegas. In the CAST microbulk detectors, fabrication started from a 50μm kapton foil, coated with 5μm copper on both sides. By photolithography technique, readout pads were formed in one side. A 25μm thick kapton foil, with copper coating on one side was attached to the strips side of the previous foil, and readout



(a) (b)

Figure 5.6. (a) Pillars in the bulk micromegas are separated 2mm from each other. (b) The woven mesh has a pitch of 80μm.

lines were constructed and connected to half of the readout pads diagonally. Another copper coated kapton was attached to the previously attached foil to create the readout lines in the other axis and connecting them to the other half of the pads(Figure 5.7a. Finally the mesh holes were formed on the pads using a photochemical process, and kapton etching was used to remove material between the mesh holes and the pads [88]. Unlike the bulk production technique, the mesh holes are grouped by 9, and are aligned with the readout pads(Figure 5.7b). The amplification gap is smaller in microbulk de-



(a) (b)

Figure 5.7. (a) The readout pads of the microbulk micromegas. First axis is connected at the pad level, while second axis is connected in an additional layer. (b) Mesh holes, that are grouped by nine are aligned with the readout pads.

tectors, and alignment of mesh holes with readout pads provide better characteristics for the detector. The resolutions that are achieved with microbulk detectors are as good as 12%(FWHM at 5.96keV).

5.5. CAST Micromegas Detectors

The micromegas detectors can be produced in many sizes and properties depending on the application. The CAST micromegas has a circular base, on which strips and mesh lies. Strips provide two dimensional anode readout plane as seen in Figure 5.9a. While the first CAST micromegas had 192 strips, in microbulk and bulk micromegas, there are 106 strips in each direction with a pitch of 550μm, which makes an active area of 33.9cm^2. The micromesh on the other hand has radius 8cm, and covers the whole active area. The connection of strips are extended to readout planes through the neck of the detector and welded to connectors in the racket of the detector, in groups of 96 (Figure 5.8). Since the bulk and microbulk detectors has only 106 strips, second connector in each axis is connected to only 10 strips. The gassiplex cards [89] are used for readout and each card is connected to the 96 pin connectors. Detail of gassiplex cards will be given in Chapter 6.

Drift window is made of 5μm aluminized mylar, with an aluminium strongback and is attached to a plexiglas cylindrical chamber which has two holes for the gas input and output (Figure 5.9b). The chamber is also bolted to the neck of the detector. In newer detectors, copper strongback was used for being more radiopure.

The connections of mesh and drift window are done via flat connectors, and custom made cables, which uses classical SHV connectors on the other side. The drift connector goes to high voltage power supply through a filter, whereas the mesh connector goes to the preamplifier. The signal output and high voltage input of mesh is connected to the readout electronics through the preamplifier. An important aspect of CAST micromegas readouts is their radiopurity. It is extremely important in rare event searches like CAST, where background level is one of the parameters that can improve the final coupling constant limit and discovery potential. The choice of

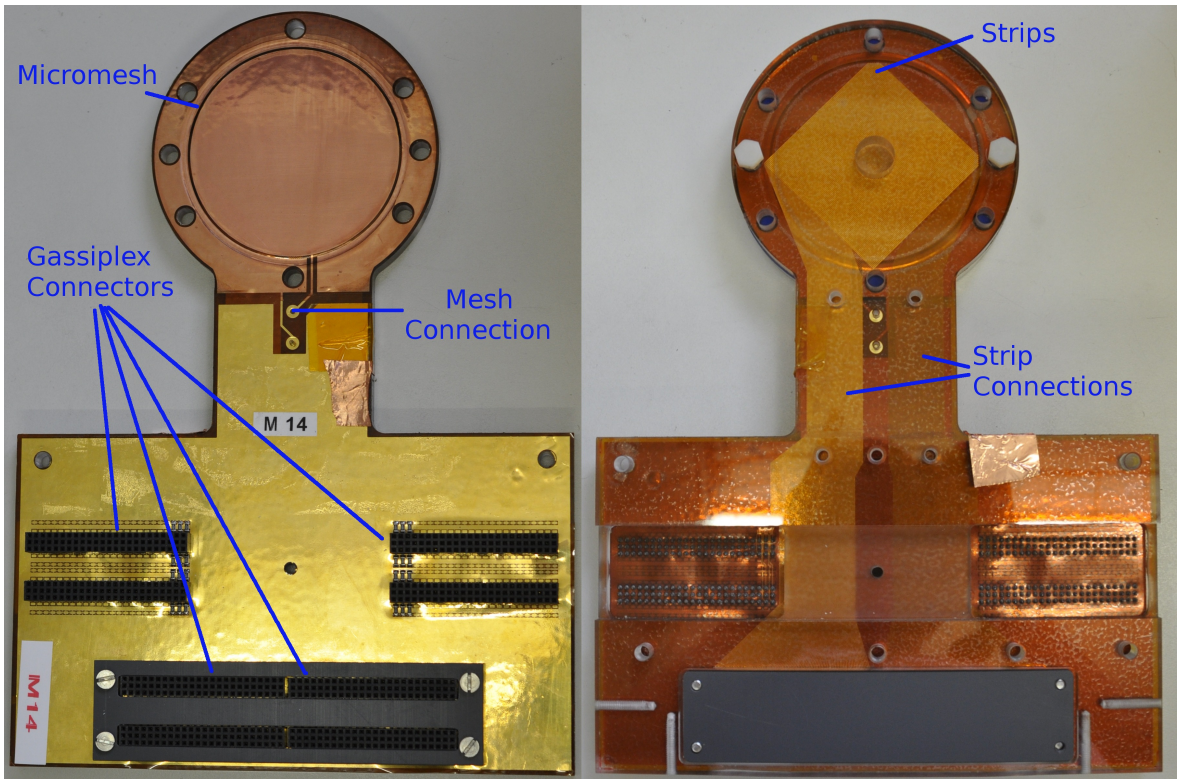
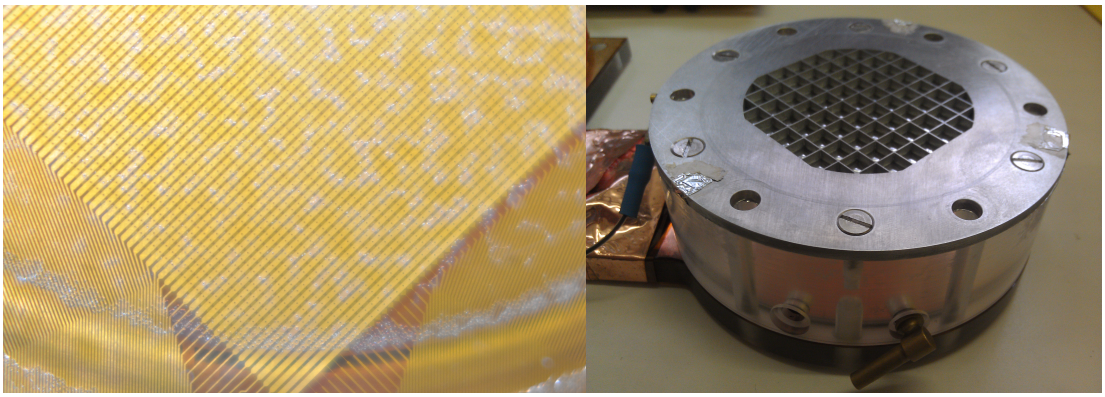


Figure 5.8. Photo of two sides of a microbulk micromegas detector without the readout cards and plexiglas chamber.



(a) (b)

Figure 5.9. (a)Photo of the strip plane. (b) Plexiglas chamber and aluminized mylar drift window connected to micromegas detector.

material in the detector brings intrinsic radiopurity to a really low level. The tests that has been done in University of Zaragoza with germanium detector prove that the

radiopurity level indeed is really low in the sensitivity range of the CAST micromegas detectors [90]. The highest contamination is coming from contamination of ^{40}K at the level $57.3 \pm 24.8 \mu\text{Bq/cm}^2$, and it is mostly due to materials used in the fabrication of the readout, and not the readout itself.

5.6. Characterization of CAST Microbulk Detectors

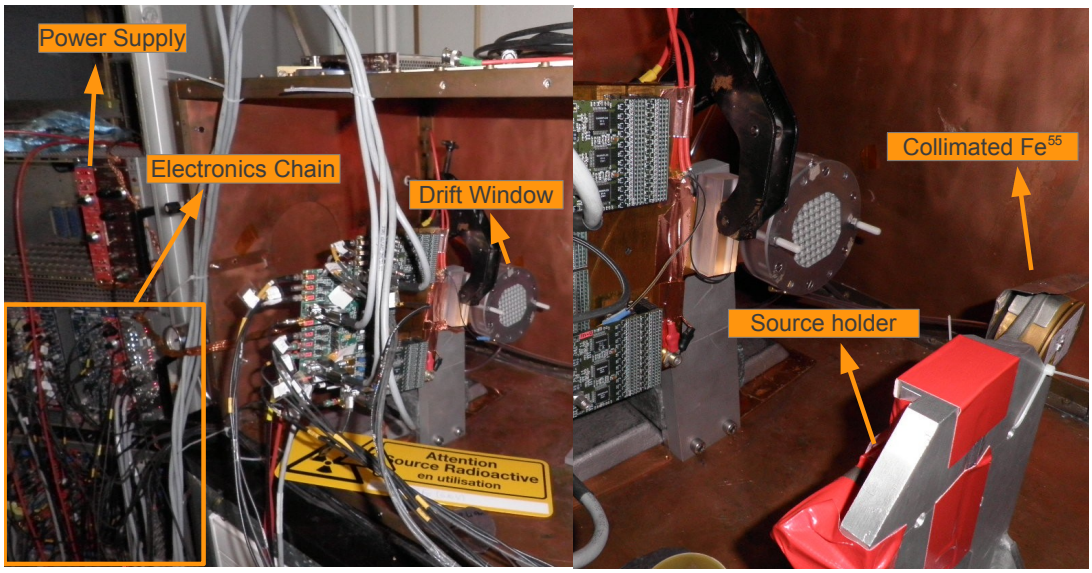
Micromegas detectors at CAST are built at CERN in the micromegas lab, and characterized before being used at CAST. Even though all detectors are produced with the same technique, each detector is unique. The characterization is mainly done to understand:

- The response of the detector to different drift and mesh voltages.
- The response of the detector to different gas mixtures.
- Intrinsic gain of the detector.
- Achievable energy resolution.

In this section results of characterization of the detector M16, which was performed in June 2010 in CEA/Saclay will be given.

5.6.1. Experimental Setup

The detector is connected an electronic chain made from NIM modules. The output of the mesh signal is is connected to a preamplifier, output of which is inputted to a bipolar amplifier. The final output is connected to Amptek brand Multi Channel Analyser(MCA), which has capability of reading and histograming the pulse amplitudes with a high rate. The voltages are set through a NIM high voltage power supply. A radioactive ^{55}Fe source is placed 20cm from the drift window of the detector to send x-rays of 5.96keV. The setup is presented in Figure 5.10.



(a) (b)

Figure 5.10. (a) The experimental setup of the characterization tests. (b) The positioning of the ^{55}Fe source.

5.6.2. Method

One measurement is taken with MCA for each voltage setting and spectrum is written into a file. The spectrum for each setting is fitted to a Gaussian to estimate the gain and resolution. Gain is the MCA channel where the peak appears, and the resolution is the FWHM of the Gaussian around the peak. An example spectra and the fit can be seen in Figure 5.11. In the first step of the tests, the mesh voltage is kept constant while increasing the drift voltage. The aim is to determine the optimal E_D/E_M, the ratio of electric fields of drift and amplification regions. This ratio is related to the electron transparency of the mesh and the magnitude of the fields can be calculated as

$$E_D = \frac{V_D - V_M}{d_{drift}} \quad and \quad E_M = \frac{V_M}{d_{amp}}$$

where V_D and V_M are the drift and the mesh voltages, d_{drift} and d_{amp} are the lengths of drift and amplification gaps.

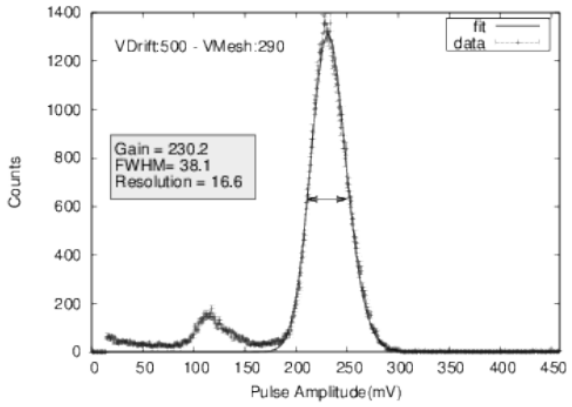


Figure 5.11. An example spectra from the characterization measurements. The ^{55}Fe peak is at channel 230, where the escape peak can be seen around channel 120.

The ratio, where one has the best amplification(highest gain), thus the highest transparency is chosen from the first set of measurements. The second set of measurements are done by increasing both drift and mesh voltages while keeping this ratio fixed. This helps to find the best voltages, that give highest gain and lowest resolution. Furthermore it gives an idea of operational limits of the detector. At excessively high voltages, discharges called *sparks* can occur and damage the detector.

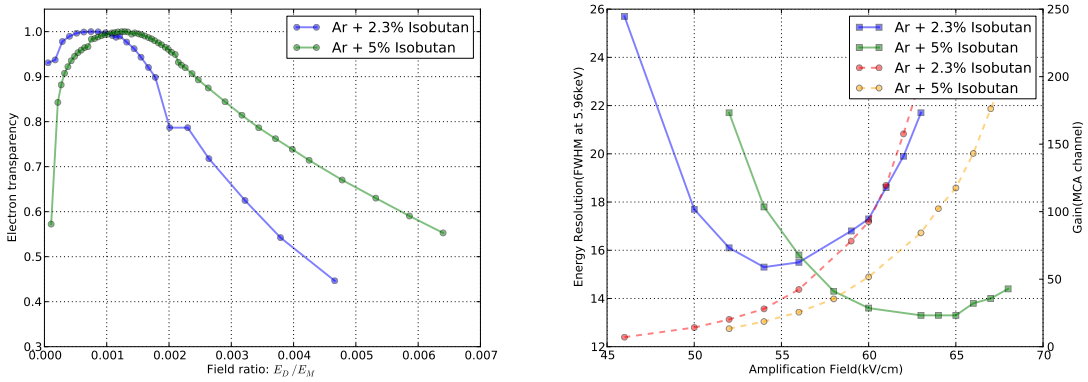
The whole procedure can be repeated for different gas mixtures. For M16, two Argon-Isobutane mixtures are used, with respectively 2.3% and 5% Isobutane concentration.

5.6.3. Results

For 2.3% Isobutane concentration, mesh voltage was fixed to 289V and calibration spectra was taken for different drift voltages. The optimal ratio was found to be $0.76 \cdot 10^{-3}$, reached with voltages $V_D = 440$V and $V_M = 289$V. For 5% concentration, reference mesh voltage was 310V, the optimal ratio was $1.24 \cdot 10^{-3}$, with $V_D = 560$V and $V_M = 310$V (Figure 5.12a). For both cases, electron transparency reaches a plateau with a sharp increase, then decrease almost linearly. For higher Isobutane concentration, plateau becomes wider, but the maximum transparency is achieved at a higher

ratio.

Keeping the ratios fixed and increasing the both voltages, the second set of measurement are done. The dependence of gain and resolution on amplification field can be seen in Figure 5.12b. While the gain is increasing exponentially with the amplification field, resolution is getting worse for low and high fields. For the low amplification fields, the reason for the bad energy resolution is the noise effects becoming more significant, while for the high fields, it is the higher gain fluctuations. The achievable energy resolution with M16 is respectively 15.5 and 13.3 for 2.3% and 5% Isobutane. The quencher(Isobutane) has lower ionization potential, thus higher quencher concentration cause better energy resolution, due to absorption of bigger amount of UV photons. A detailed study on characterization of micromegas detectors in different gas mixtures can be found in [85].



(a) (b)

Figure 5.12. (a) Electric field ratio vs. electron transparency. The transparency of the highest gain is normalized to 1. (b) Amplification field vs. energy resolution(continuous lines) and gain(dashed lines).

6. SUNSET MICROMEGAS SYSTEM

Since 2007, there are two micromegas detectors in the sunset line, which were installed after removal of the TPC detector. In this chapter the sunset micromegas system will be described in detail. The main emphasis will be given on the system as it was in 2008, and finally a section will be dedicated to the upgrades that has been done up to recently.

6.1. The Overview of the System

Bulk and microbulk type of micromegas detectors have been used in the sunset side since 2008, with properties explained in Section 5.5. Two detectors are placed, each of them being centered with the axes of each cold bore, and with their rackets oriented towards outside the axes. The drawing of the system can be seen in Figure 6.1, while the schematics of the detector line is shown in Figure 6.2.

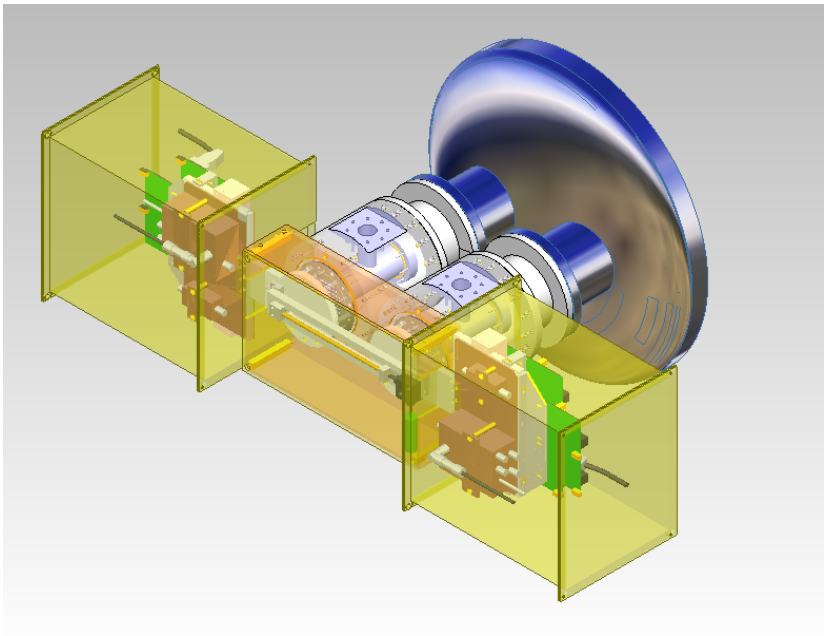


Figure 6.1. Drawing of the sunset micromegas.

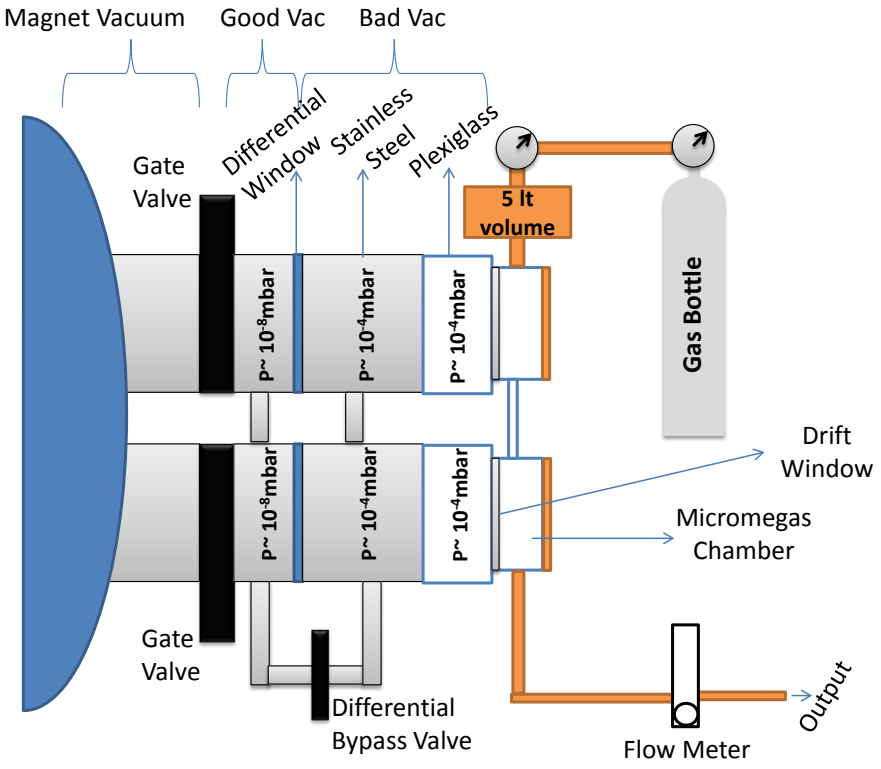


Figure 6.2. Simplified schematics of sunset micromegas vacuum and gas systems.

6.2. Gas System

The gas line from the TPC detector was migrated to sunset micromegas system. The gas for the detectors is Argon + 2% Isobutane mixture. As shown in Section 5.6, higher isobutane concentration can provide a better energy resolution. However the size of the total flammable gas volume in the experimental hall limits the allowed concentration to 2% according to CERN regulations.

The gas line starts from a premixed bottle. The 100bar pressure in the bottle is regulated to 1.4 bar in 3 steps. After the final regulation, a 5L volume is installed before the detectors. The gas is connected to both detectors in series, and output of the line is connected to a flowmeter, that can let 1-10lt/h flow. The regular flow in sunset micromegas is 2-5lt/h. In the gas system, mainly copper pipes are used, only in the input and output of the detectors plastic pipes are preferred for flexibility. The schematics of the system can be seen in Figures 6.3 and 6.2. Although the constant

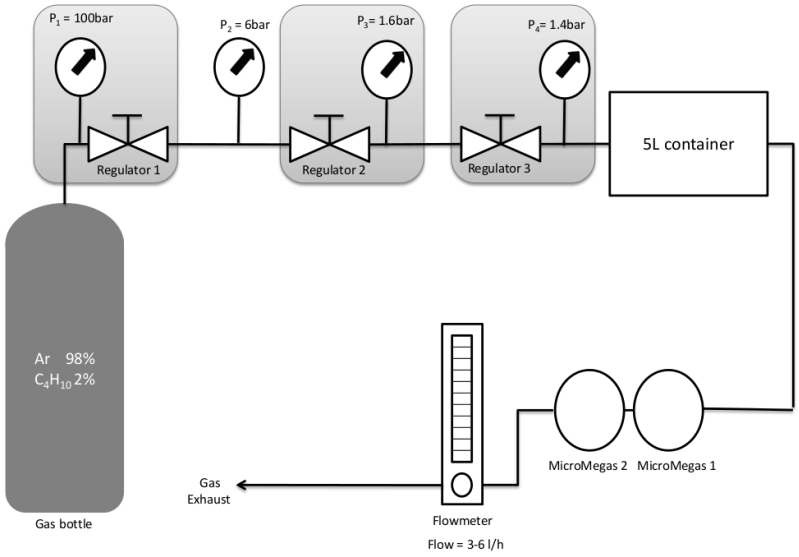


Figure 6.3. Schematics of the sunset micromegas gas system.

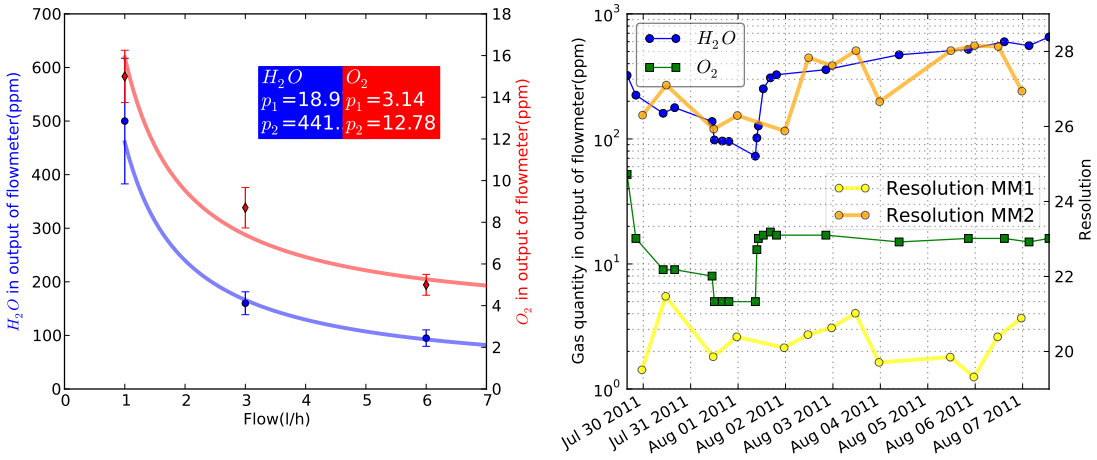
gas flow is to prevent impurities, such as H_2O,O_2 and radon contamination, these gases can diffuse through plastic pipes and the plexiglas detector chamber. To prevent contamination around the detector, nitrogen is being circulated inside the shielding, aiming the purify the area from all unwanted molecules.

6.2.1. Gas Purity Test

In 2011, the purity of the sunset micromegas gas has been measured for different flow rates by using H_2O and O_2 monitors that are installed between the flowmeter and the exhaust of the gas line. The results show that, higher the flow, lower the percentage of the impurities as percentage. A simple model was constructed to fit the data taking into account the impurity of the bottle, which is a constant percentage and the diffusion into the system, which is constant per unit time, thus decreasing with the flow. The fit function was chosen as

$$G(f) = c_1 + \frac{c_2}{f}$$

where $G(f)$ is the amount of the gas(in PPM) that is measured by the monitor for a fixed flow of f, c_1 is the impurity of the bottle and c_2 is the contribution of the diffusion into the system. It was seen bigger contribution to the gas impurity is due to diffusion, but the detector operation is stable enough and the impurities do not affect the resolution or gain significantly [91] (Figure 6.4).



(a) (b)

Figure 6.4. The results of gas purity tests. (a) The model to fit the data. (b) The PPM of both gases for different flows compared with the energy resolution. There is no significant effect observed even for high impurities.

6.3. Vacuum System

Similar to the gas system, vacuum system was derived from the TPC vacuum line. The drift window of the sunset micromegas is bolted to a cylindrical plexiglas piece with o-rings on both side, which is then bolted to the vacuum pipe. There are two vacuum regions separated by a differential window. The vacuum between the drift window and the differential window is pumped by a diaphragm and a turbo pump, and the pressure is between 10^{-4}mbar and 10^{-3}mbar. The vacuum line between the differential window and the magnet bore is pumped by more powerful pumps(2 turbos and a primary) and the pressure is between 10^{-8}mbar and 10^{-7}mbar. The differential window that separates the two vacuums are made from 4μm polypropylene and it's

main purpose is to prevent gas molecules that diffuse through the detector window from condensing on the cold windows. This window is quite fragile, and is protected by *differential bypass valve* which opens in case one of the vacuums go higher than a set-point. Between the magnet bore and the differential windows, there are *gate valves* and they are normally opened during the data taking conditions. The gate valves can be closed to separate the detector vacuum system from the magnet vacuum system. The schematics of the vacuum system is shown at Figures 6.2 and 6.5.

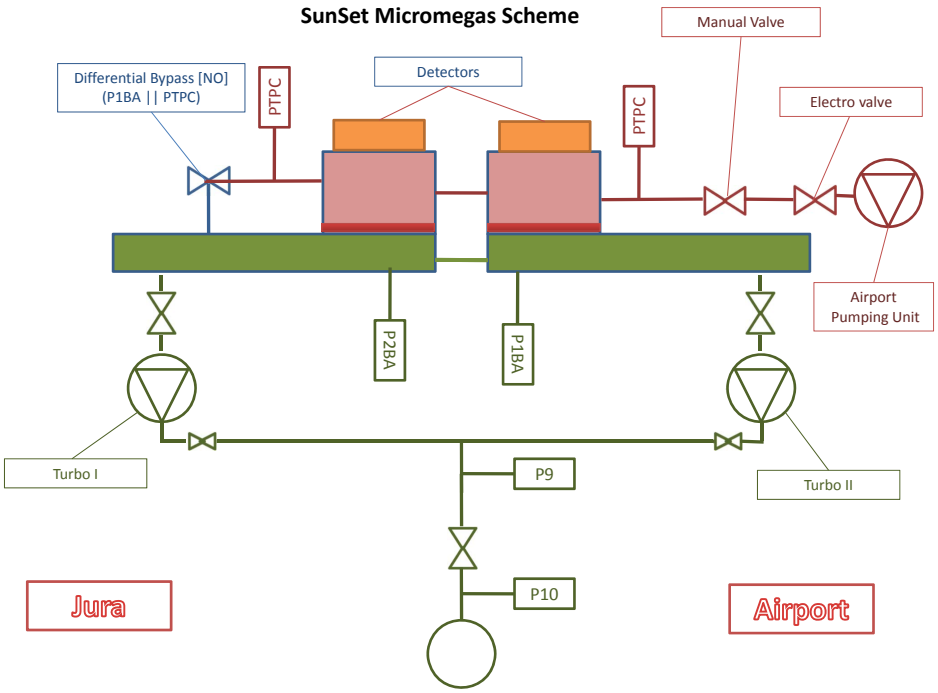


Figure 6.5. The schematics of the sunset micromegas vacuum system.

6.4. Hardware Efficiency

The hardware efficiency of the micromegas detectors at CAST are simulated in GEANT4 software package [92], taking into account all the windows in the pipeline and detector gas [93]. The detector line is presented in Figure 6.2. X-rays that are converted from axions in the coldbore are attenuated in the following windows:

- Cold window: 15μm polypropylene, with 17.5% strongback.
- Differential window: 4μm polypropylene.
- Drift window: 5μm Aluminized mylar, with 5% strongback.

Combining the attenuation from all windows with the absorption of x-rays in the Ar + 2% Isobutane mixture, one obtains the efficiency curve in Figure 6.6.

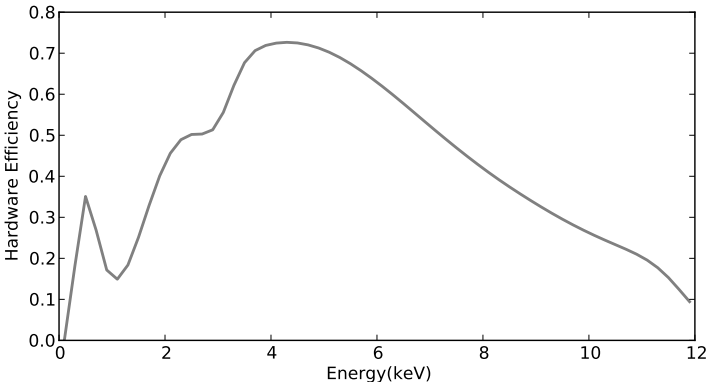


Figure 6.6. The hardware efficiency curve of sunset micromegas.

The total efficiency of the detector is combination of the hardware and software efficiencies, which will be given in Chapter 9.

6.5. The Calibration System

The detectors are calibrated with a ^{55}Fe source through an automated calibrator system. The source is placed in the back of the detectors, in the center of the two beam axis and can be moved to right-left to be centered with both detectors by the data acquisition software, via the VME module. While the source is in the garage position, it is shielded and the x-rays can't penetrate to the chambers. The calibration is done on a schedule that can be set in the software(see Section 6.7), and normally both detectors are calibrated for 30 minutes, twice a day. The schema of the calibration system in shown in Figure 6.7. The calibrators were upgraded in 2010 (see Section 6.8)

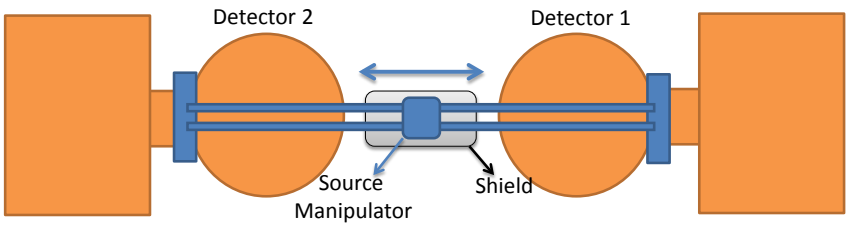


Figure 6.7. The schematic representation of the calibration system, viewed from the back of the detectors.

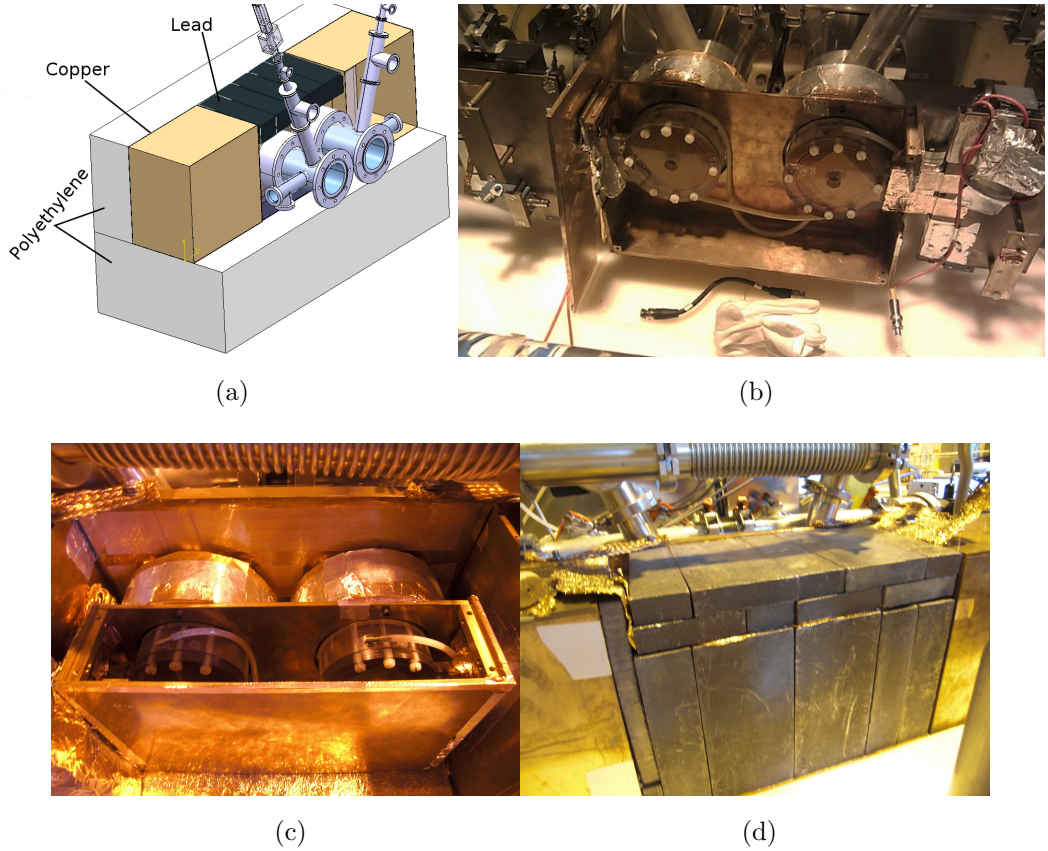
6.6. Shielding

The shielding of sunset micromegas is built from copper, lead, cadmium and polyethylene. The gas chambers of the detectors until the drift window are together placed in a rectangular copper Faraday cage. This Faraday cage itself is bolted to the plexiglas connection part that connects detector to the vacuum line. The necks of the detectors pass from a opening in the cage and extend to the sides, where they go into a higher and wider Faraday cage, which cover the racket, readout cards, preamplifier and drift filter. On the sides of these Faraday cages there are rectangular openings to provide space for connecting signal and power cables into detector electronics, preamplifier and the drift filter. Lead bricks are placed on top and back of the smaller Faraday cage, cover the distance between Faraday cages of electronics horizontally and reach the same height with these cages. This layers of lead create a lead filled volume of $20\text{cm} \times 35\text{cm} \times 5\text{cm}$ on the top and on the back of the detectors. On the bottom of the detectors, there is another lead layer, making up a volume of $20\text{cm} \times 30\text{cm} \times 5\text{cm}$. The lead layers on the top and the bottom extend till the top of the plexiglas connection part to provide better coverage against external photons. The whole shielding is sitting on top of 40cm thick polyethylene. On the back of the shielding there is another 15cm thick layer of lead. Photos and drawings from different parts of the shielding is shown in Figure 6.8.

The lead that is used in the shielding is archaeological Roman lead, whose ra-

dioactivity has decreased significantly. It blocks most of the environmental gammas. This amount of lead is not able to stop cosmic muons, however most of the muons can be rejected by the offline analysis, and thus doesn't have a serious impact on background for the levels the sunset micromegas had in 2008. Purpose of the copper around the detector is stopping fluorescence x-rays that can be emitted from lead. Finally the polyethylene is used to stop the thermal neutrons.

The shielding, although providing an important factor in background reduction, had some weaknesses and was upgraded in 2012 with a more advanced design(See Section 6.8.2)



(a) (b)

(c) (d)

Figure 6.8. (a) Drawing of the shielding. (b) The inner view before the shielding is installed. (c) Inner Faraday cage. (d) Shielding with the lead bricks.

6.7. Data Acquisition System

The signals that are induced in mesh and strips are written into files for the offline analysis. The whole process is done by the data acquisition(DAQ) system and two sunset detectors utilize a single DAQ.

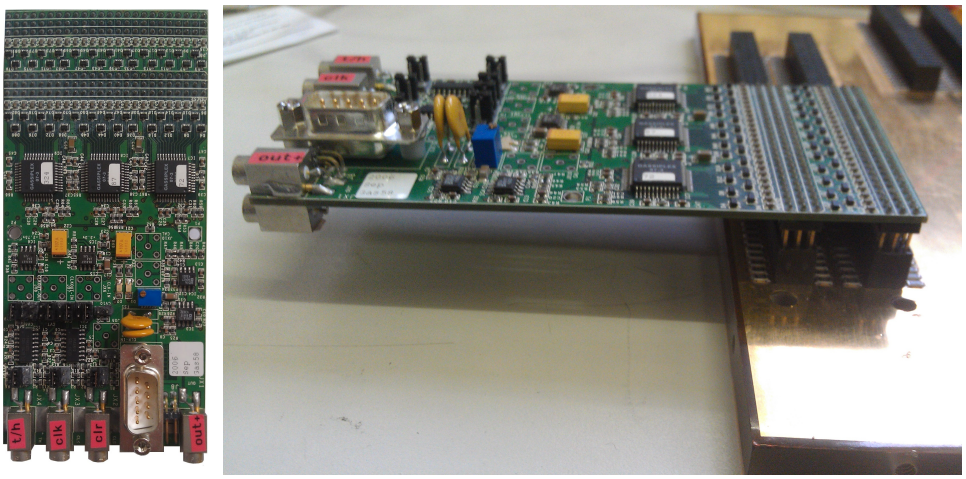
6.7.1. Electronics

In the electronics of the sunset micromegas there are 2 NIM crates and one VME crate. The NIM modules can not communicate between each other from the back panel of the crate, and can only communicate via cables passed between them. NIM crates are used for signal processing like duplicating, amplifying or delaying signals, opening gates, discriminate signals by their magnitude; and for powering the instruments. On the other hand, the VME modules in the same crate can communicate without external cabling, VME can be programmed to perform specific tasks and communicate with another computer to do tasks like file input/output operations.

In the sunset micromegas, the mesh signals are passed through ORTEC 124B preamplifiers to NIM timing amplifiers, then duplicated via a Fan In-Fan Out module. One of the signals from each detector is sent to a quad discriminator for trigger, and both resulting signals are passed to a OR module. The trigger mechanism depends solely on the mesh signals, such that if the mesh signal of one of both detectors has higher amplitude than a set threshold(normally set to a channel corresponding to less than 2keV), 2 NIM signal is send to VME crate to start recording the mesh and strips information. The other duplicates of the mesh signal are send to MATACQ module [94] in the VME crate. In the MATACQ chip the signal is sampled and recorded with a duration of 2500ns, and sampling rate of 1GHz.

The strips are read via the front end gassiplex cards, CAEN Sequencer and CRAMS(CAEN Readout for Analog Multiplexed Signals) [95]. A CAST micromegas can host up 4 gassiplex cars, each of which is connected to 96 strips. Gassiplex has 3 digital inputs(Track and Hold, Clock and Clear) and one output (Figure 6.9). The

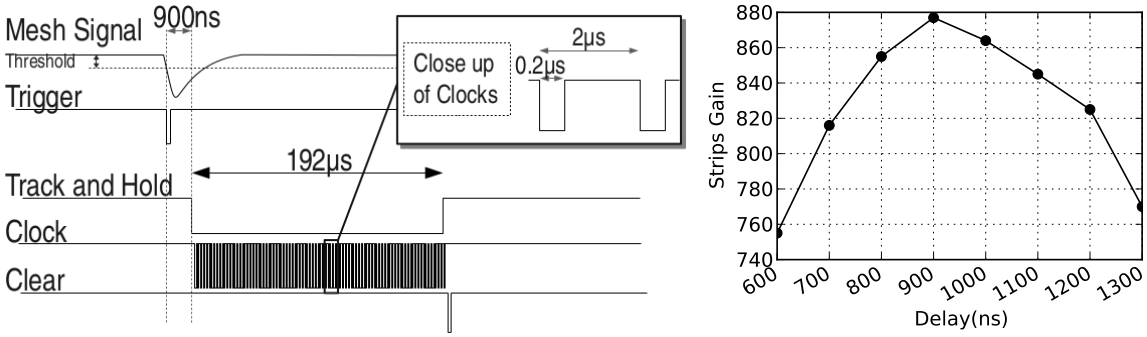
charge is integrated in the card, and is frozen when the track and hold signal starts. During the track and hold, clock signals are sent from CRAM sequencer to gassiplex. Clocks have a period of 2μs and during each clock signal a strip is read and multiplexed signal is sent to CRAMS. When all 96 clocks finish, Track and Hold signal stops and Clear signal is sent to gassiplex to reset the memory. The mesh pulse, trigger signal and gassiplex input signals are shown in Figure 6.10a. The strip readout does not



(a) (b)

Figure 6.9. (a) Gassiplex card: On the bottom, lemo connectors of clear, clock, track and hold, and output signal can be seen. (b) A gassiplex card connected to the micromegas detector.

include pulse sampling, the reading is done at a fixed time during the evolution of the charge. To record the strips when they have the maximum charge, one has to provide a delay in the gassiplex signals (Track and Hold, Clear, Clock). It was observed that optimum value for this delay is 900ns(see Figure 6.10b). When there is a trigger, the detectors must reject new triggers until the event is recorded, for this, VME sends a busy signal to block incoming triggers during the readout. When the recording of the event is finished, the busy is removed. Normally time to fully acquire an event is between 10-20ms. A detailed sketch of the electronics chain is shown in Figure 6.13, and a photo can be seen in Figure 6.14a.



(a) (b)

Figure 6.10. (a) Sketch of the important signals in the micromegas DAQ chain. (b) The strips gain of different runs with different delay values. The highest gain was obtained when the delay was set to 900ns.

6.7.2. DAQ software

A Labview based software was developed for CAST type micromegas and was used in sunrise micromegas since the beginning of CAST. The sunset DAQ software is forked from the original sunrise micromegas DAQ extended to operate with 2 detectors. It connects to the VME controller via a fiber optic cable, and it is able to do input/output operations on the VME. The software can work in autopilot and manual modes. In autopilot mode, the DAQ can carry out an pre-defined schedule, which defines when to start what kind of run without need of human intervention, an example of which can be seen in Figure 6.11. In the manual mode, user can start a specific type of run. The run types are as follows:

(i) Pedestal run. External triggers with frequency of 100Hz is sent to DAQ, and the strip signals are recorded to have a estimate of the electronic noise level in each strip. Mesh pulse is not recorded during pedestal runs. For explanation of pedestals, see Chapter 7.

(ii) Background run. During the data taking, this run is chosen. The naming *background run* may be confusing, although having this name, these files contain the data of both background, and tracking.

(iii) Calibration of detector 1. The source is moved to detector 1.

(iv) Calibration of detector 2. The source is moved to detector 2.

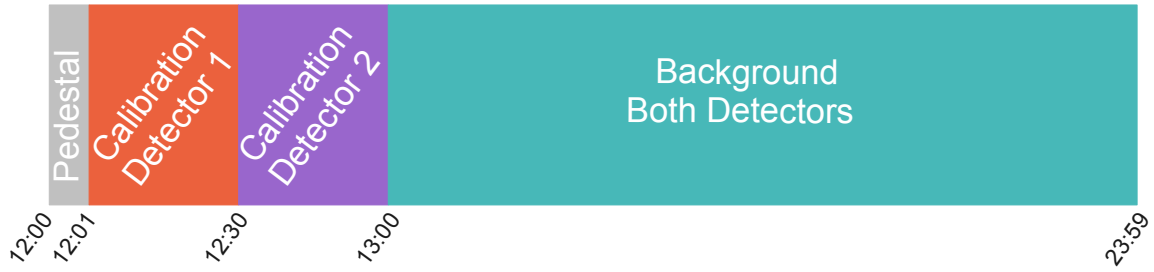
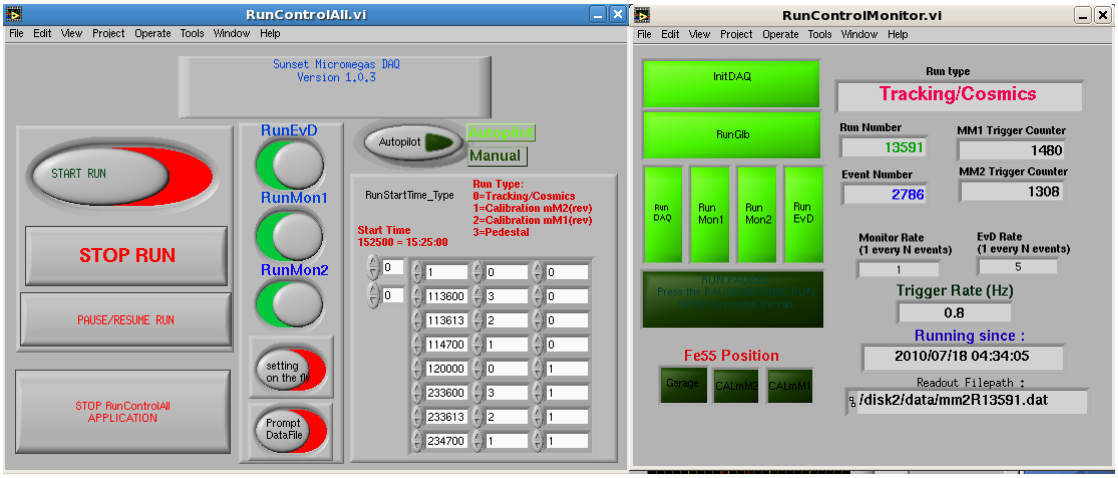


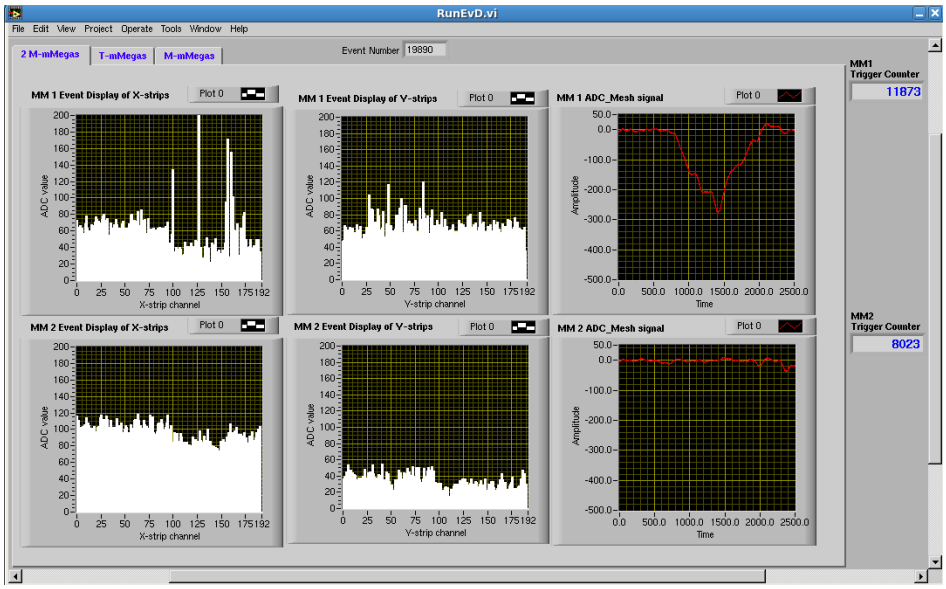
Figure 6.11. An example 12 hour run schedule of Sunset Micromegas. The run starts with a 1 minute pedestal run, common for both detectors, continued with calibrations of each detector, and a common background run.

During the background runs, trigger rate is around 1Hz, and most of the triggers are due to cosmic muons which traverse one of the chambers. During the calibration runs, the trigger rate can rise up to 100Hz and is limited to the activity of the source, and readout time of the detector. Screenshots from the DAQ is showed in Figure 6.12. The DAQ is designed in a way that whenever there is a trigger in a detector, both detectors data is written into file. Raw files are binary files, made of 4 byte(32bit) words. It starts with run header, which contains information about the start of the run. After the header, individual events are written. Events start with event header. In a event, firstly the pulse information of both detectors is written. Secondly strip information are written from both channels of each CRAM. Finally event finishes with an event end label. In the end of the run, run footer is written, which contains the number of total events and run end time. The trigger information in each event is used to find the detector that triggered the recording of the event. The event that is in the non-triggered detector is either ignored, or used as pedestal.

The header, footer and each event in raw files have the data format seen in Table ??.



(a) (b)



(c)

Figure 6.12. (a)RunControlAll.vi: The main panel of the software, that is used to set auto/manual mode, start and stop runs.(b)RunControlMonitor.vi: Displays information about the run. (c) RunEvd.vi: Displays mesh and strip signals.

Table 6.1. Data Format of Micromegas Raw Files.

Run Header		Event Body	
Word	Data	Word	Data
1	Header start label: 0x90000000	1	Event start label: 0x80000000
2	Run Number	2	Event ID
3	Date	3	Event time (Labview timestamp)
4	Date offset	4	Event type
5	Start time	5	Trigger 1
6	Run Type	6	Trigger 2
7-10	Unused words	7	Counter
10	Magnetic Field	8	N_{ADC1}(Number of ADC data of detector 1)
11	High Voltages	$\times N_{ADC1}$	Bits 0-16: ADC data Bits 0-16: ADC data
12-19	Unused words	$8 + N_{ADC1}$	N_{ADC2}(Number of ADC data of detector 2)
19	Header End label : 0x9FFFF000	$\times N_{ADC2}$	Bits 0-16: ADC data Bits 16-32: ADC data
Run Footer		$\times N_{strips}$	Bits 0-12: Strip charge Bits 12-23: Strip ID Bits 23-30: Unused Bit 30: Validity Bit 31: Overflow
Word	Data		
1	Footer start label: 0x90000000		
2	Number of events		
3	Run end time	...	Event end label

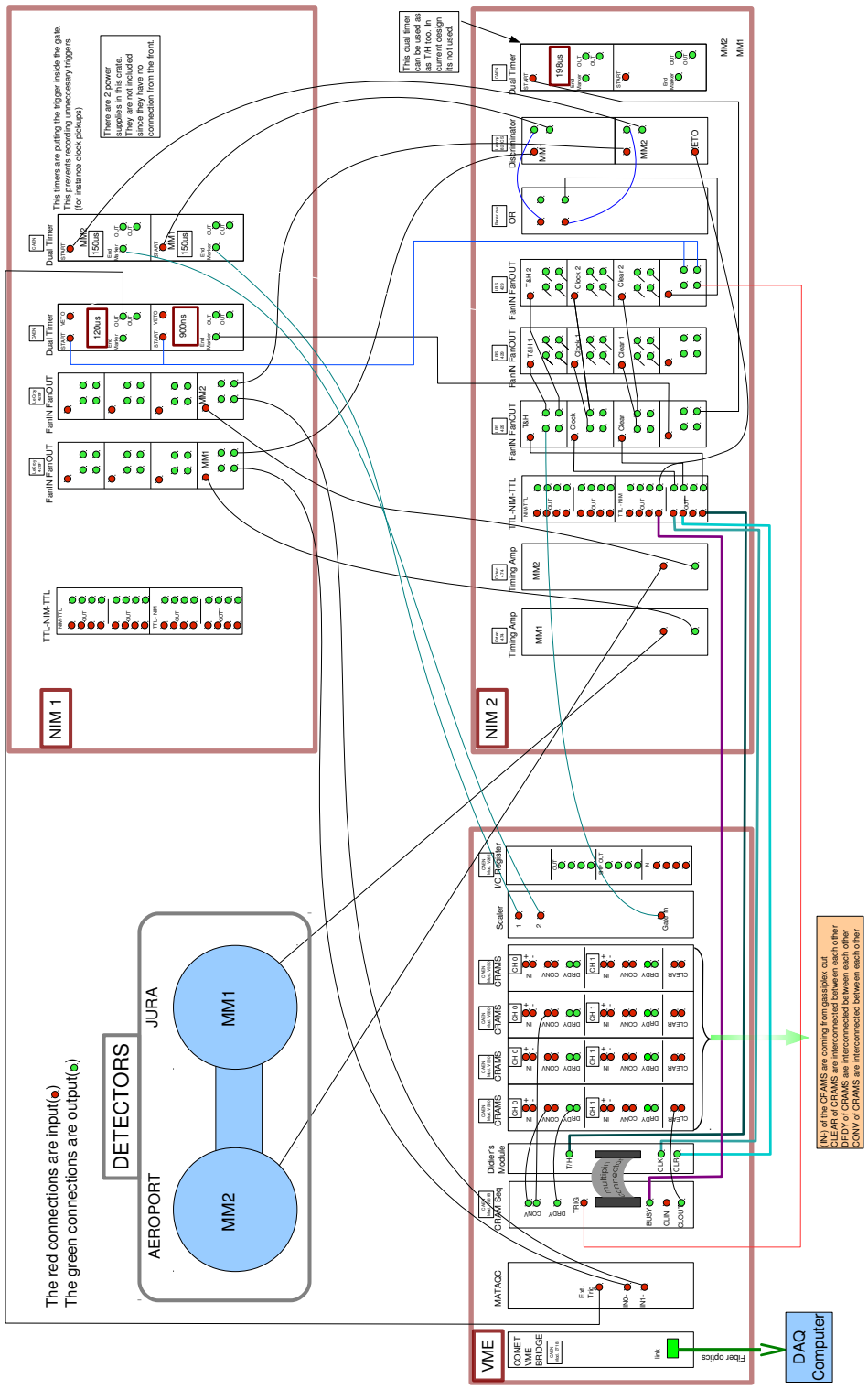


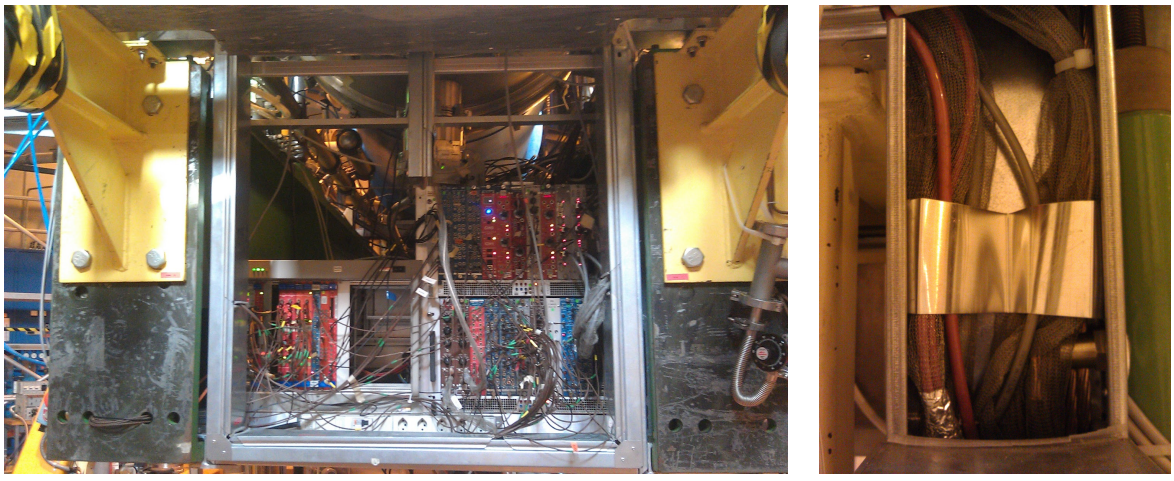
Figure 6.13. The electronics chain of the Sunset Micromegas.

6.8. Upgrades

In this section the upgrades since 2008, until end of 2012 will be presented.

6.8.1. Cable Trays

In the years 2008-2009, sunset micromegas has suffered from electronic noise on several occasions(See Chapter 7). The negative effect of the noise is the increase in the trigger rate and thus dead time of the detector. The main reason of the noise in CAST experiment is the electronic instruments that is connected to the magnet that are powered in various frequencies. Especially it was observed that when the magnet motors are turned on electronic noise in the sunset micromegas would increase. Furthermore, when the power cables that power the detector and gassiplex are too close to signal cables, it would introduce an additional noise. The solution to the noise problem was found as installation of metal cable trays, in which voltage and signal cables could be separated, and a common ground line was along(Figure 6.14).



(a) (b)

Figure 6.14. (a) General view of the cable trays and the electronics. (b) View of the cables inside the cable tray.

6.8.2. Shielding and Detector Upgrade

In 2012, the sunset micromegas has gone through a major upgrade with a complete new shielding design, and new detectors. The new detectors M18 and M19 was tested and characterized in CEA Saclay, and the new shielding has been designed and built by University of Zaragoza.

The motivation for the new shielding and detectors was the background laboratory tests conducted in Canfranc Underground Laboratory and GEANT4 background simulations [96, 97]. The simulations has shown that the majority of the events that are accepted are x-rays are resulting from the interaction of environmental gamma's with the vacuum pipes and drift window. Such interactions can produce fluorescence photons that can penetrate the detector without further obstacle. On the other hand underground tests have proved that shielding the detector by 10cm thick lead, covering 4π solid angle decrease the background level of the detector maximally. After 10cm, addition of lead has an insignificant contribution. Another drop in the background level comes when copper drift windows is used instead of aluminium.

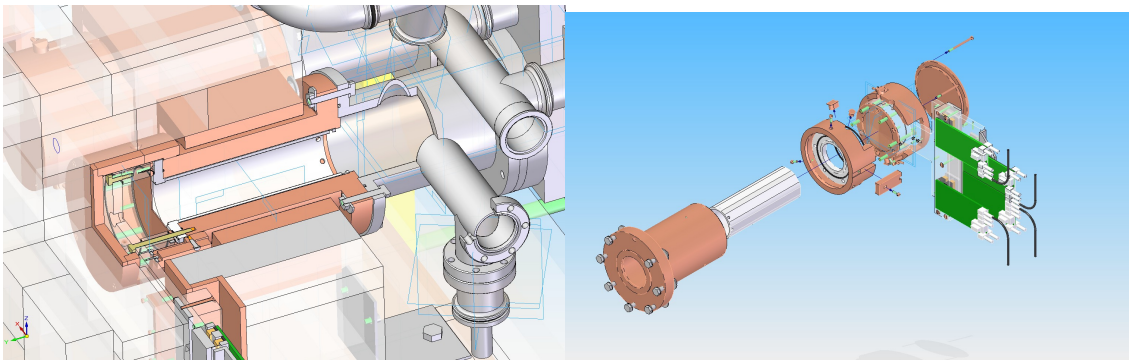
The weakness of the old shielding was the front side. Due to space constraints, the stainless steel pipe in front of the detector was not shielded, and there was a big opening angle for incoming gamma rays.

The design principles of the new shielding are the following:

- Copper drift windows are used in the detectors.
- Plexiglas connection to the drift window is replaced with a thinner teflon part, due to teflon being a more radiopure material.
- The detectors were moved away from the magnet, adding a 20cm long, 1.5cm thick copper pipe.
- A teflon pipe is installed inside the copper, to stop fluorescence photons of copper.
- The chamber is shielded with a 1.5cm thick cylindrical copper Faraday cage.
- The whole shielding is covered by 10cm thick lead.

- A steel cage is installed around the whole shielding to prevent it from moving.

After the installation of the shielding, the background level has been $1.6{\cdot}10^{-6}\mathrm{keV}^{-1}\mathrm{cm}^{-2}\mathrm{s}^{-1}$ compared to previous years $7 \cdot 10^{-6}\mathrm{keV}^{-1}\mathrm{cm}^{-2}\mathrm{s}^{-1}$. Although the detectors were not the same, this was the lowest stable background levels that are obtained by the micromegas detectors at CAST until then. Drawing and exploded view of the shielding can be seen in Figure 6.15 and various photos taken during the installation can be seen in Figure 6.16.



(a) (b)

Figure 6.15. (a) Drawing of sunset micromegas shielding, (b) Exploded view of the inner part of the shielding.

6.8.3. Muon Veto Counter

The tests that has been done in Zaragoza University [98] showed that cosmic muons are correlated with a percentage of the events that are accepted as x-rays after the background selection in micromegas detectors. This encouraged the installation of a muon veto system to sunset micromegas in May 2012. The muon veto is build from 120cm $\times$40cm scintillator coupled to a photomultiplier, powered by 1kV and giving an output signal which is amplified with a NIM amplifier. Due to topological constraints of the system, the scintillator is installed with and angle of 45°) and placed on top of detectors covering both(Figure 6.17).

When a muon pass through the scintillator, the output signals that are higher

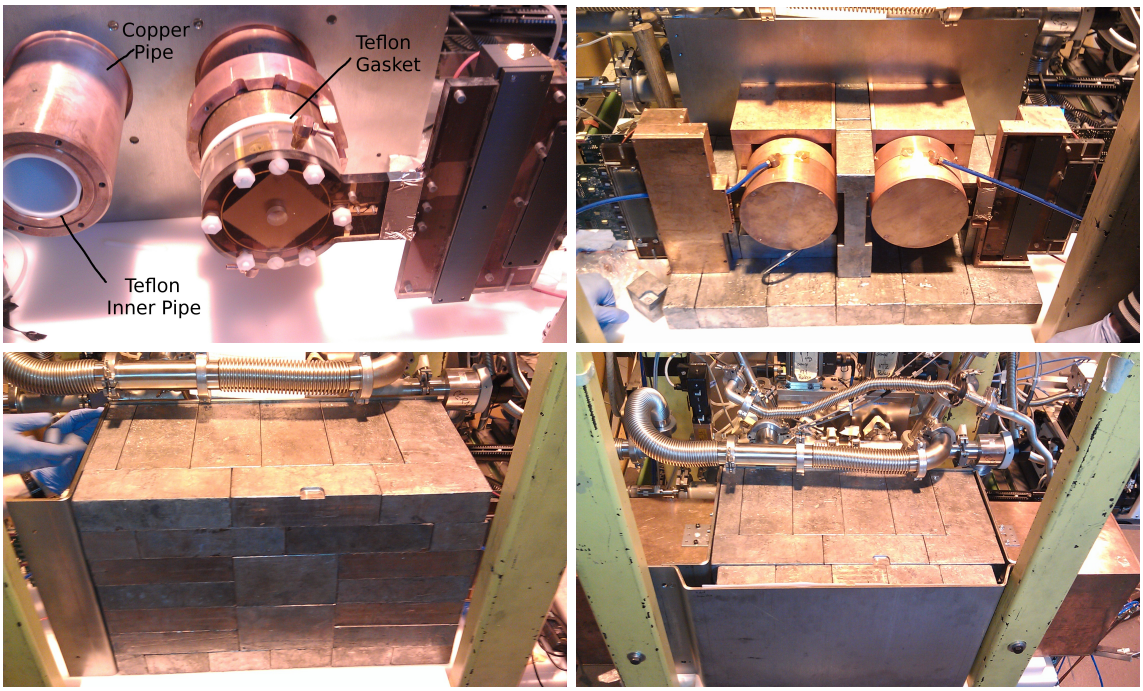
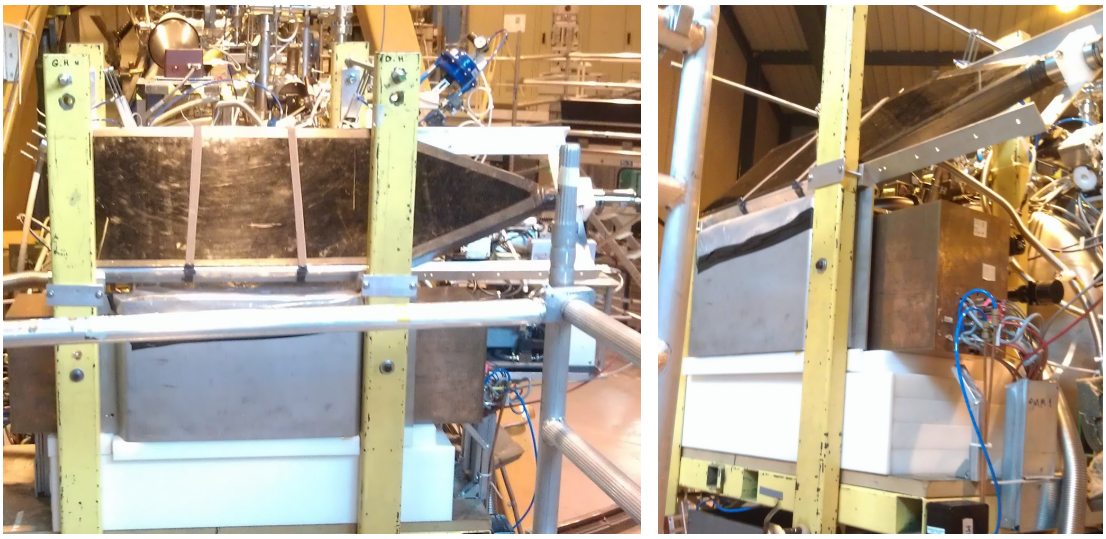


Figure 6.16. The different stages of installation of sunset micromegas.

than a certain threshold (determined before by measuring the energy muon spectrum of the muons) trigger a counter that counts the time until the micromegas trigger. Since muon signal arrives faster, the time between trigger of an event in the micromegas and the last muon trigger is recorded. If the time between two triggers is lower than a threshold, it is concluded that event is correlated to passage of a muon, and is rejected. The implementation of the muon veto has decreased the background level from $1.6 \cdot 10^{-6}\mathrm{keV}^{-1}\mathrm{cm}^{-2}\mathrm{s}^{-1}$ to $1.2 \cdot 10^{-6}\mathrm{keV}^{-1}\mathrm{cm}^{-2}\mathrm{s}^{-1}$.

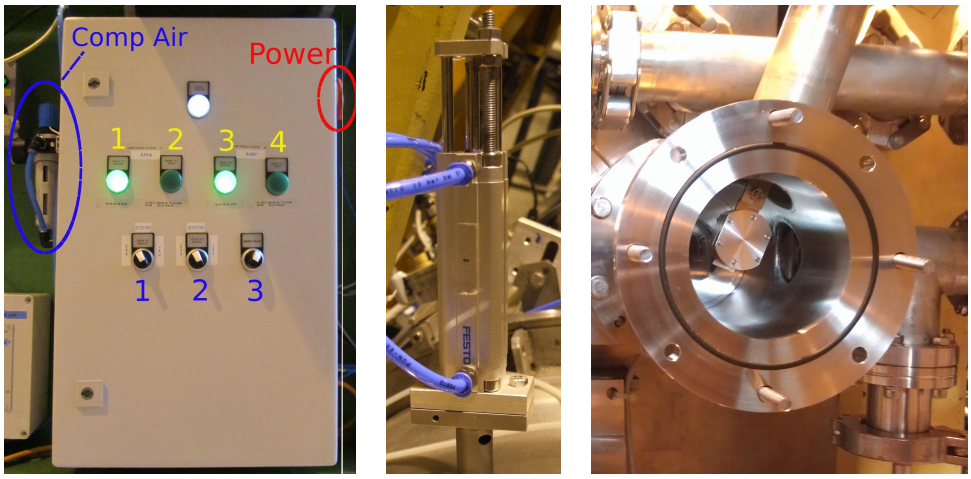
6.8.4. Calibrators

In 2010 the calibration system is upgraded with 2 pneumatic calibrators that are installed in the bad vacuum side of the line. The new calibrators are moved with compressed air through a calibrator box and the sunset micromegas DAQ has been modified to control them. The calibrators can be moved 8cm up and down, facing the detector when sent into calibration position, and being shielded by the pipe when they are moved up to garage.



(a) (b)

Figure 6.17. The muon veto counter.



(a) (b) (c)

Figure 6.18. (a) The control box of the calibrators. (b) The source manipulator. (c) View of the source inside the vacuum pipe.

7. ANALYSIS OF MICROMEGAS DETECTORS

The raw data files of the sunset micromegas detectors have the format in Table **??** and each event in the files contains the information of the mesh and the strips for each detector. To have a common interface with the analysis of the sunrise micromegas files, the raw files of sunset micromegas is processed and separated into subfiles for each detector, and for each run type. For instance a raw file that includes calibration, pedestal and background data, is separated into three files for each detector. This way, analysis of both detectors can also be done separately and more efficiently in terms of computing time.

The offline analysis is applied in order to remove the non x-ray events from the data, and estimate the energy and the position of the x-ray events. Former is done from strip information, while the latter can be done both from strips or mesh. There are two main steps in the detector analysis: data reduction and background discrimination.

7.1. Data Reduction

Each event in the raw files includes information of 106 strips, and the time evolution of the pulse with 2500 samples. Both data can be reduced to few observables that represent it without big loss of information. After the reduction, the gain is calculated for the selected parameters and reduced number of observables are written into ROOT [99] files, by applying a preliminary selection criteria. To analyse a single background run, one needs to use the closest calibration and a pedestal run that are taken in the similar conditions such as voltage levels and gas pressure.

7.1.1. Strips

7.1.1.1. Pedestal Calculation. The strips have and intrinsic electronic noise level, called pedestals. Even when there is no charge deposited on the strips, this noise remains. Thus level of a strip in any event is evaluated together with the mean and standard

deviation(σ) of its pedestal level, such that a strip is considered to be *hit* if its value is three σs higher than the pedestal mean.

Pedestal runs are taken in the beginning of each run cycle. In a pedestal run, automatic triggers are sent to VME (with a frequency of approximately 200Hz), and strip charges are recorded in each trigger. Since the charges recorded in the pedestal run are due to fake triggers, there are no real charge deposition in the strips in majority of these events. This provides an estimate for the electronic noise level(pedestal level) of each strip.

Pedestals can be read from pedestal runs, or background runs. Although there are real events in background runs that cause strips to have charge higher than noise level, a three step method is used to overcome this problem.

Pedestal calculation is done in the following steps. In the first step, charge in each strip for the first 15000 events are read. From these, preliminary means(μ_0) and standard deviations(σ_0) are calculated. In the second step, the strips are read again, but only the ones with charge c, deviating less than a σ_0's from the mean are accepted. (i.e. a pedestal is accepted only if: $|c - \mu_0| < \sigma_0$.). Secondary means and sigmas are calculated from accepted data. In the last step, second step is repeated using the new mean and sigma. It should be noted that, when pedestals are calculated from backgrounds, only events with charge c, deviating less than $0.5\sigma_0$ are accepted. This is due to background runs having higher sigma than pedestal runs.

This three step reading method is essential when background run is used as pedestal. For each strip, it helps to eliminate the events, in which the particular strip is hit. Otherwise, the final sigma of the each strip's pedestal value would be higher than the real sigma. The pedestal means and standard deviations of a 2008 run for M9 detector are shown in Figure 7.1.

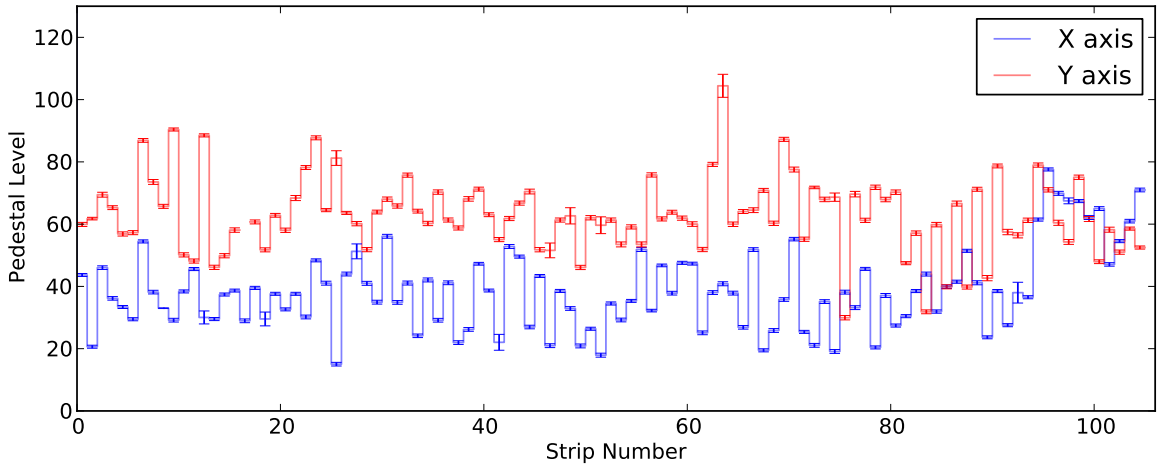


Figure 7.1. The mean and sigma of pedestals for x and y channels for M9 detector.

7.1.1.2. Clustering. After calculating pedestal levels in each strip, events can be evaluated one by one. For the k^{th} event, the effective charge on strip i on one of the axis is calculated as

$$c_{ik} = c'_{ik} - \mu_i^{(p)} - \eta_k \tag{7.1}$$

where c'_{ik} is the charge that is registered by the CRAM, $\mu_i^{(p)}$ is the mean pedestal level of the strip i, calculated from 15000 events and η_k is the momentary noise level of the whole gassiplex card, calculated from the whole strips connected to the same card for the event k.

According to value of c_{ik}, the strip is considered *hit* or *not hit*. For analysis of the 2008 sunset micromegas data, the hit condition is selected as $c_{ik} > 3\sigma_i^{(p)}$, where $\sigma_i^{(p)}$ is the standard deviation of the pedestal for the strip i.

When two or more strips are hit consecutively, they are said to form clusters, and in an event there maybe more than one cluster with different multiplicities. In some cases, strips losing their connection with a readout card, or being removed due to noise problems, may cause the interruption in the clusters. To prevent this, within a cluster up to two non-hit strips are allowed, and are still counted in the current cluster.

A 3rd non-hit strip marks the end of the cluster. Initially clusters are formed in one dimension, and then combined to build the cluster in two dimensions. One dimensional clusters for the k^{th} event have the following properties and a single cluster event can be seen in Figure 7.2.

- *Cluster Multiplicity:* The number of strips hit in a cluster, m_k
- *Cluster Charge:* The total charge in a cluster

$$c_k = \sum_i c_{ik}$$

- *Cluster Position:* Position of the cluster in strip space

$$p_k = 1/c \sum_i^{m_k} i \cdot c_{ik}$$

- *Cluster Sigma/Size:* The standard deviation of the charge distribution in a cluster. It gives a measure of the width of the cluster shape.

$$\sigma_k^2 = 1/c \sum_i^{m_k} c_{ik} \cdot (i - p_k)^2$$

- *Cluster Skew:* The asymmetry of the charge distribution in a cluster.

$$\gamma_k = 1/c \sum_i^{m_k} c_{ik} \cdot \left(\frac{i - p_k}{\sigma} \right)^3$$

Since x-rays produce single clusters in the micromegas detector, the events which have a single cluster, or a cluster that contains more than 70% of the total charge are accepted and written into ROOT files, while the rest are rejected. The cluster charge gives a measure of the energy of the incoming x-rays by using the calibration information.

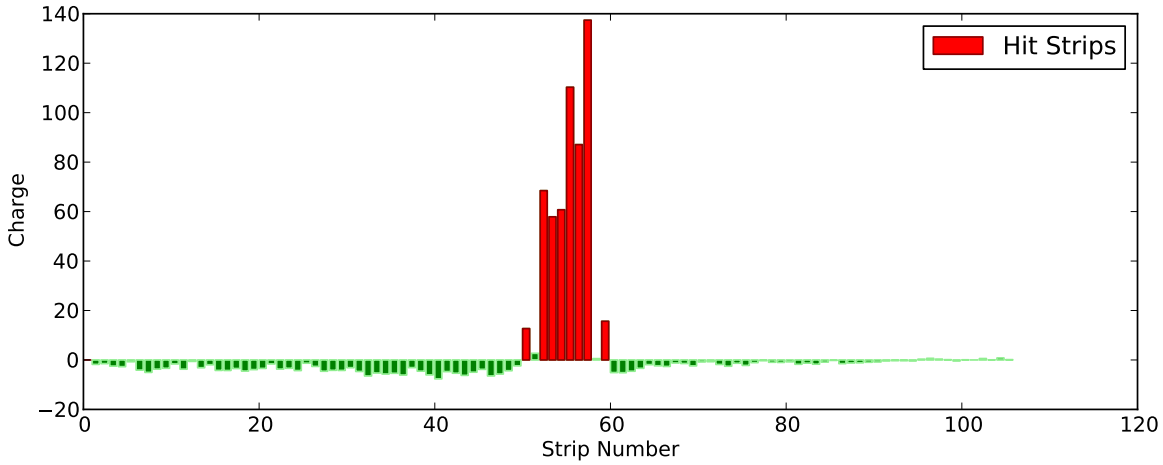


Figure 7.2. A single cluster event that has multiplicity eight, with two non-hit strips inside.

7.1.2. Mesh Pulse

The mesh pulse, which is recorded with 1GHz, and has total of 2500 samples, is read from raw files and analysed to extract the following observables, which can also be seen in Figure 7.3.

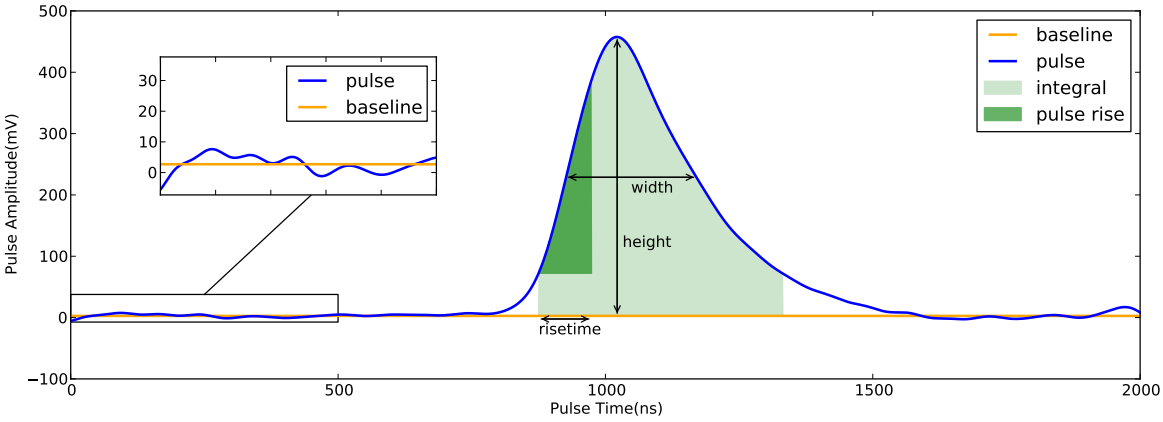


Figure 7.3. A sample mesh pulse from ^{55}Fe calibration with explanation of mesh observables.

- *Baseline:* The level of the pulse baseline, calculated from first 500 samples.

- *Amplitude* or *Height*: The amplitude of the pulse.
- *Risetime*: The time that takes pulse to rise from 15% to 85%.
- *Width*: The width of the pulse at half amplitude.
- *Integral*: The integral of the pulse from the time it reaches to 15% of the amplitude, until the time it drops to 15%.

7.1.3. Gain Calculation and ROOT File Creation

The gain is calculated before creating the root files, to get the calibration peak position in the units they are read and recorded by the electronics. This allows one to determine energy of the background events. The gain is calculated again only from events that satisfy the single cluster condition as explained in Section 7.1.1.2. The three gain observables are:

(i) Amplitude/Height(E_h): The pulse height.
(ii) Integral(E_i): The pulse integral.
(iii) Charge(E_c): Sum of the charges in the main clusters in x and y axes.

A sample spectra from 2008 data for all three observables is presented in Figure 7.4. In the Sunset Micromegas, calibration is done with a ^{55}Fe source, where the main peak has energy 5.96keV, and the escape peak for the detector gas is around 3keV. In the calibration spectra, there is also contribution of fluorescence X-rays of aluminium at 1.5keV that are emitted from the drift window, however this is quite low in percentage. After the analysis of the gain, the strip and pulse variables and normalized energies are written to ROOT files, along with the experimental variables, read from Slow Control and tracking system log files. These variables are used to have the tracking start-end times, gas pressure in the cold bore, state of gate valves that are in between detectors and the magnet, detector gas pressure and the environmental temperature. Two root files are created, one that has the calibration data, and the other that has the background data.

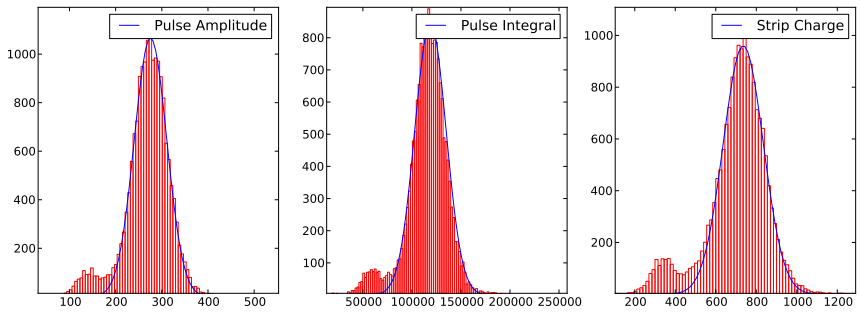


Figure 7.4. The spectra and Gaussian fits to three gain observables.

7.2. Background Selection

After the formation of the root files, the background selection algorithms are applied, to select the events that show the most similar characteristics to the calibration runs, i.e. the ones that most likely are x-rays. To identify x-ray characteristics, distribution of the selected observables during the calibration are constructed. The whole calibration, or just the events with energies in the vicinity of 5.96keV peak can be used. The second approach is preferred more often, because most 6keV events are from the incoming x-rays, while the 3keV events are due to the interactions in which fluorescence photon have escaped the detection volume.

The general idea behind the event selection is building the statistical distributions of the calibration, and accepting the background events that are close to the peak of the distribution, by applying particular *cuts*. The same cuts are applied to calibration data to estimate the software efficiency(i.e. percentage of events that are accepted by the cuts) and to background data to estimate the level of background. The cuts are supposed to accept as many calibrations events as possible, while rejecting as many background, since finally the sensitivity of the CAST experiment depend on the factor

$$\frac{\epsilon}{\sqrt{b}} \tag{7.2}$$

being as high as possible, where b is the background level and ϵ is the total detector

efficiency. This factor is called the Figure of Merit(FOM) and defines the discovery potential and capability of better exclusion in case of no axion signal.

For the Sunset Micromegas detector in 2008, two types of analysis are used: multivariate analysis and contour cut analysis. In both cases, there are two preliminary cuts that are applied to data after selection:

(i) Fiducial Cut: Everything out of the projection of cold bore area is rejected. Since photons converted from the axions are supposed to come parallel to the magnet bore, all photons should fall onto this area. Furthermore, the edges of the gaseous detectors are known to have different characteristics, such as lower gain or worse energy resolution [78].
(ii) Energy Cut: All photons with energy lower than 2keV or higher than 7keV is rejected.

In this section the list of discriminant observables and different methods will be explained. Next chapter is dedicated to comparison of the background selection methods.

7.2.1. List of Observables

For both types of analysis the same set of observables are used.

() *Risetime*: Pulse risetime.
(i) *Width*: Pulse width.
(ii) *Charge balance*: Balance of charge in x and y clusters.

$$\frac{c_x - c_y}{c_x + c_y}$$

(iii) *Risetime/Width*: Fraction of risetime and with.

(iv) *Height vs. Integral Energy balance*: Balance of pulse height and pulse integral energies.

$$\frac{E_h - E_i}{E_h + E_i}$$

(v) *Height vs. Charge Energy balance*: Balance of pulse height and cluster charge energies.

$$\frac{E_h - E_c}{E_h + E_c}$$

(vi) *Integral vs. Charge Energy balance*: Balance of pulse integral and cluster charge energies.

$$\frac{E_c - Ei}{E_c + E_i}$$

(vii) *Cluster Size Balance*: Balance of x and y cluster sizes.

$$\frac{\sigma_x - \sigma_y}{\sigma_x + \sigma_y}$$

(viii) *Multiplicity Balance*: Balance of x and y cluster multiplicities.

$$\frac{m_x - m_y}{m_x + m_y}$$

(ix) *Skew*: 2-dimensional cluster skew.

$$\gamma_x \cdot \gamma_y$$

(x) *Multiplicity*: 2-dimensional cluster multiplicity.

$$m_x \cdot \mathrm{m}_y$$

(xi) *Size*: 2-dimensional cluster size.

$$\sigma_x \cdot \sigma_y$$

(xii) *Center*: Pulse center

For both type of analysis, the observables are numbered from 0 to 13 to build unique ID for observable combinations.

7.2.2. Multivariate Analysis

Multivariate methods are preferred in cases where the variables have correlation with each other, and provide better pattern recognition capabilities compared to sequential cuts [100]. Historically it has been used in CAST micromegas analysis for many years, and proved good rejection capabilities. The method that will be explained is developed by Kostas Kousouris [101, 102] and Javier Galan [103].

One can chose a group of N observables from the ones that are described in the previous section. Denoting the observables as $\{x_1, x_2, \ldots, x_N\}$, their means and standard deviations as $\{\mu_1, \mu_2, \ldots, \mu_N\}$, $\{\sigma_1, \sigma_2, \ldots, \sigma_N\}$ and assuming the observables follow Gaussian distribution, the covariance matrix is expressed as

$$V =< X_i X_j > \tag{7.3}$$

where $X_i = x_i - \mu_i$ is the distance of the variable from its mean. Converting the covariant matrix Using these, one can create the joint probability density functions as

$$f(\vec{x}) = \frac{1}{(2\pi)^{N/2}|V|^{1/2}} \exp\left(-\frac{1}{2}X^\top V^{-1} X\right) \tag{7.4}$$

By using the correlation matrix instead of covariance matrix, whose elements are $\rho_{ij} = \frac{1}{\sigma_i \sigma_j} V_{ij}$ and scaling the observables by their standard deviation as $\tilde{X} = X_i/\sigma_i$, one can

rewrite Equation 7.4 as

$$f(\vec{\tilde{X}}) = \frac{1}{(2\pi)^{N/2}|\rho|^{1/2}} \exp\left(-\frac{1}{2}\tilde{X}^{\top}\rho^{-1}\tilde{X}\right) \tag{7.5}$$

One can diagonalize ρ^{-1} choosing an orthogonal transformation such that

$$\Lambda = U^{\top}\rho^{-1}U \tag{7.6}$$

and rewrite the term in exponential as

$$\begin{aligned} q &= \tilde{X}^{\top}\rho^{-1}\tilde{X} && (7.7)\\ &= \tilde{X}^{\top}U\Lambda U^{\top}\tilde{X} && (7.8)\\ &= (U^{\top}\tilde{X})^{\top}\Lambda(U^{\top}\tilde{X}) && (7.9)\\ &= Y^{\top}\Lambda Y && (7.10) \end{aligned}$$

where $Y = U^{\top}\tilde{X}$. Since Λ is a diagonal matrix, with diagonal terms as λ_i, the final equation can be rewritten as

$$q = Y^{\top}\Lambda Y = \sum_{i}^{N} \lambda_i Y_i^2 \Rightarrow \sum_{i}^{N} \frac{Y_i^2}{q/\lambda_i} = 1 \tag{7.11}$$

This is equation of a N dimensional ellipsoid, whose axis half lengths are $\sqrt{q/\lambda_i}$. The quantity q has the distribution

$$f_q(q) = \frac{1}{2^{N/2}\Gamma(N/2)} q^{N/2-1}\mathrm{e}^{-q/2} \tag{7.12}$$

which is χ^2 distribution with N degrees of freedom. Using this variable q allows one to combine all the observables into one single value, and perform the rejection or acceptance based on this new variable. The event selection with multivariate analysis is done by building distribution of q for the calibration events with energies close to 6keV, then setting an upper limit Q. The limit is determined by the required calibration efficiency, such as to have N% efficiency, the Q is set such that integral of the left side

of the value Q accounts for $N\%$ of the whole integral. Then selection of background events is done by calculating q value of each event, and rejecting the event if it is less than Q.

However, applying the multivariate cut in this way gives a poor efficiency for the 3keV peak. Although most of the observable means of the 3keV events in the calibration are the around the same values as 6keV, their standard deviation is higher. For some observables like multiplicity, also the means of low energy events are smaller than 6keV events. This causes smaller fraction of them to be able to pass the cut which is set from 6keV events. To increase the efficiency in the lower energies, q is modified

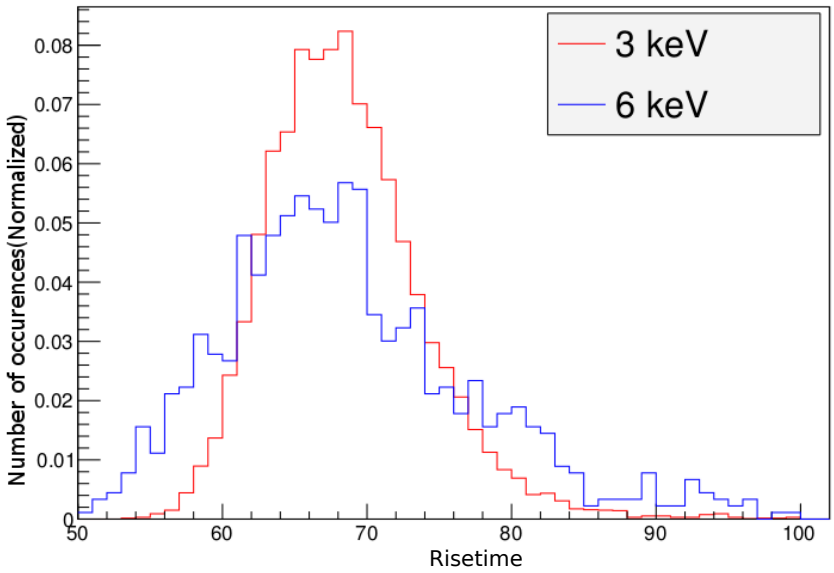


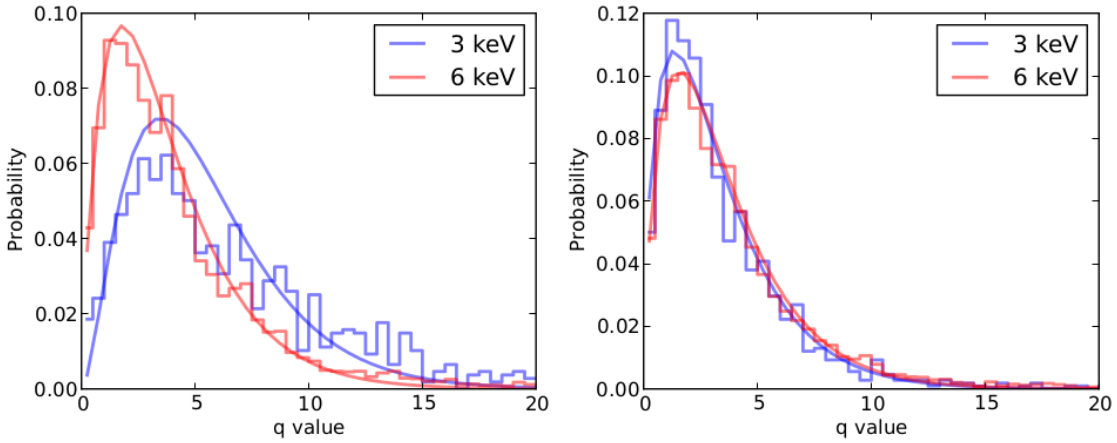
Figure 7.5. Risetime distribution for 6 and 3keV events. The energy from the escape peak has the same mean, but higher standard deviation.

with a multiplicative factor, called *a factor* such as

$$q'(E) = (\frac{E}{E_0})^a q(E)$$

where a effects the efficiency and rejection power in lower energies and can be selected dynamically to tune the efficiency. By using the corrected q value, one gets a similar

distribution for both 3 and 6 keV events as in Figure 7.6.



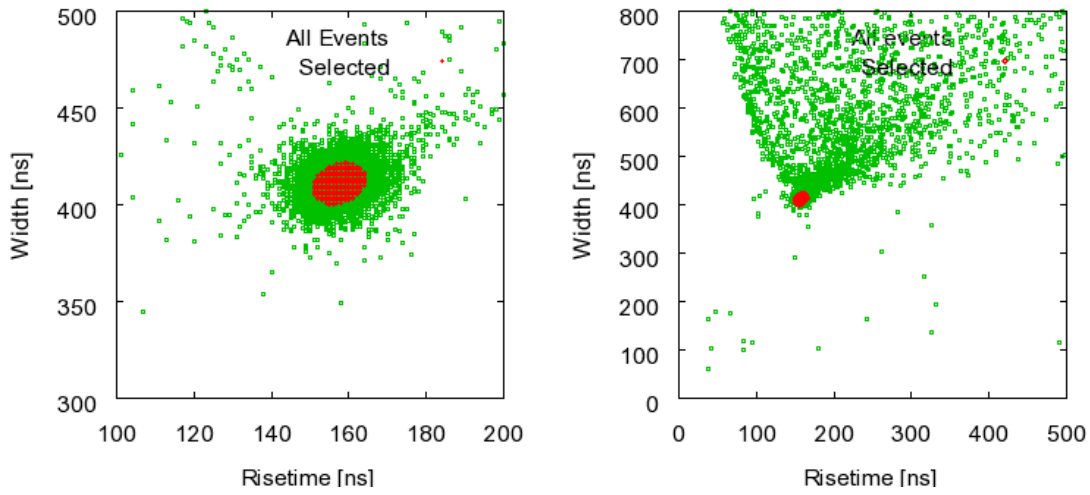
(a) (b)

Figure 7.6. The distribution of the q value for main and escape peaks during the calibration. (a) Non-corrected q value. (b) Corrected q value, with $a = 1.1$.

For instance applying multivariate cut using the risetime and width variables, and setting software efficiency at 75%, one can reject the 95% of the background events. Figure 7.7 shows the ellipsoid selection region in calibration data and the selected background events.

7.2.3. Contour Cut Analysis

Contour cut analysis is implemented by building 2-dimensional distributions of the observable pairs. The 2-dimensional histogram is binned and divided into 100 contours, and selection is done based on the level of contour, which is normally chosen from two to ten. The contour level selection accepts the most populated bins, which are closer to the peak of the distribution, while the less populated bins that are far from the maximum are eliminated. A new two dimensional histogram is built, with the same binning of the original histogram and filled with the information of the bins that are above the selected contour level. During the event selection this histogram is used to apply the cut on background events. If the background event lies in a selected bin in two dimensional parameter space it is accepted, otherwise it is rejected. Selecting



(a) (b)

Figure 7.7. (a) Selection region of the risetime-width cut is indicated in red. (b) The effect of the same cut on the background data, where selected events account for 5% of the all events.

the contour level as 0 corresponds to rejecting all events, while selecting the level as 100 means accepting all. More generally, higher levels implies higher efficiency and background levels. To have good rejection-efficiency balance, more than one cuts are applied sequentially.

Applying the discrimination criteria over the risetime and width variables, using the contour level as 15, lead up to rejection of the 95% of the background events, and calibration events pass the cut with an efficiency of 73%. Figure 7.8 shows the 2-dimensional risetime-width distribution for the calibration data and the selection region. If one uses only 6keV peak for building two dimensional distributions, the problem with having low software efficiency in the escape peak is persistent in contour cut analysis too. To overcome this, two different methods are used.

(i) *Weighted method*: The events with energies $2-5keV$ are also used to build the calibration distributions, and their number is weighted by a factor 20 so that their number becomes comparable to the one of 6keV peak.

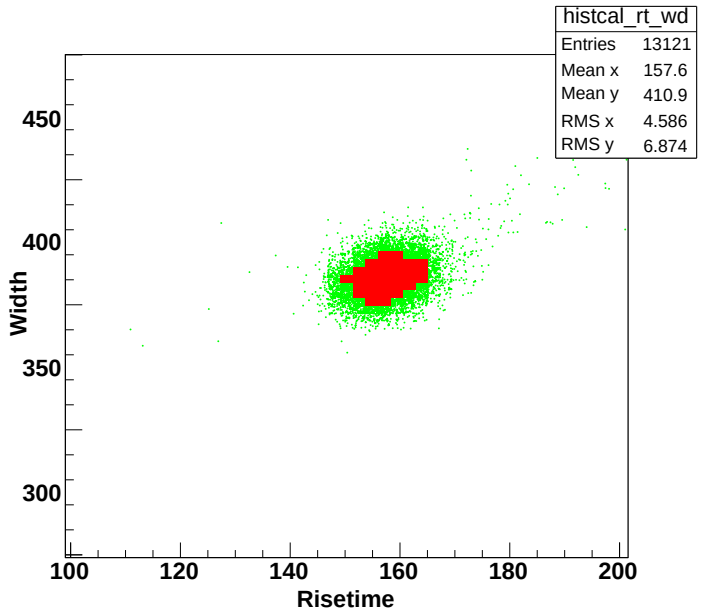


Figure 7.8. Risetime - width distribution during a single calibration run. All events are shown in green, while red region shows the selection region.

(ii) *Energy sensitive method*: Two distributions are created, one from $2-5$keV events and the other from $5-7$keV, and the selection on background event is done with the selection region of the corresponding energy range. The problem with this method is that in case of calibrations with low statistics, the number of events in the 3keV peak will be too low to create distributions.

The contour cuts can be advantageous when the distributions are not Gaussian, and their correlations are not linear. On the other hand, multivariate analysis is only sensitive to linear correlation of variables. The comparison of the methods will be discussed in next chapter.

8. BACKGROUND STUDIES

Different discrimination methods were tested to find the most optimized one, i.e. the one that gives the best sensitivity(highest FOM). The comparison is done between the following methods:

- Multivariate Analysis
  - (i) No energy correction($a = 0$)
  - (ii) Energy correction ($a \neq 0$)
- Contour Cut Analysis
  - (i) Standard method
  - (ii) Weighted method
  - (iii) Energy sensitive method

For each method, best observable combinations should be selected to increase the discrimination power and maintain high efficiency, maximizing

$$FOM = \frac{\epsilon}{\sqrt{b}}$$

During 2008, three different detectors were used in the sunset side(B3, M6 and M9), all of which have different characteristics. Each of them are studied separately to get the best observables.

Following sections will explain how observable selection is done and how the methods compare in terms of figure of merit.

8.1. Multivariate Analysis

In the multivariate analysis, any subset of 13 observables can be used to build the covariant matrix, *i.e.* there are 8178 possible observable combinations. Each

combination is assigned a unique ID, which is formed as

$$I_m = \sum_{i}^{n} 2^{o_i}$$

where I_m is the unique ID for the multivariate method, n is the total number of observables used in the combination and o_i represent the ID of the observable, ranging from 0 to 13. All these combinations are tested for a selection of runs, with no energy correction and with fixed software efficiency at 75% to find the observables that give the best sensitivity for low and high energy events.

The observable combinations are plotted according to number of observables in the combination in Figures C.1, C.2 and C.3. The blue squares show the best observables for that number of observables, while green show the worst, and red dots show all the remaining combinations. e observables that are selected for each detector are as shown in the table 8.1.

Having selected the best combinations, efficiency is fine tuned to get the maximum FOM value. Efficiency for 6keV peak is varied from 0.5 to 9.5 with step of 0.05, keeping the energy correction factor 0. Getting the optimum efficiency for the 6keV events(Figure 8.1), and fixing these efficiencies, 3keV efficiency is varied by tuning the energy correction factor a. Similarly the optimal efficiency for the events in around 3keV are obtained(Figure 8.2). Analysis of all three detectors were performed using multivariate analysis with and without energy correction. In both cases efficiency of 6keV peak was fixed at the same value. In the analysis that is not using energy correction, the efficiency of 3keV events are calculated; in the analysis with energy correction, the 3keV efficiency was fixed at the values obtained from Figure 8.2.

8.2. Contour Cut Analysis

In contour cut method, series of cuts are applied sequentially. To find the best pairs, background level b and efficiency ϵ for all 78 observable pairs are calculated using

Table 8.1. Best Observable Combinations Using Multivariate Analysis: Observables that give the highest FOM for both 6 and 3keV events are chosen.

Detector	Observables
B3	Risetime Charge balance Energy balance(height vs. integral) Energy balance(height vs. charge) Multiplicity Balance Multiplicity Size
M6	Energy balance(height vs. charge) Energy balance(integral vs. charge) Multiplicity Balance Size Center
M9	Charge balance Energy balance (height vs. integral) Multiplicity Balance Size

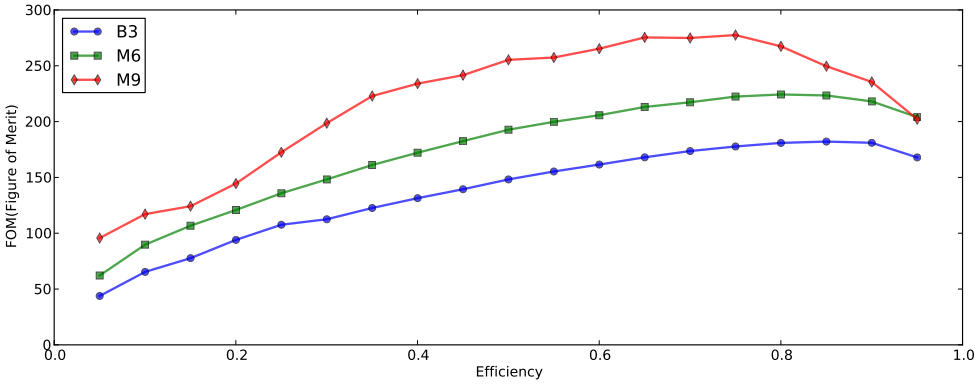


Figure 8.1. The efficiency vs. FOM curves for events in $5-7$keV range.

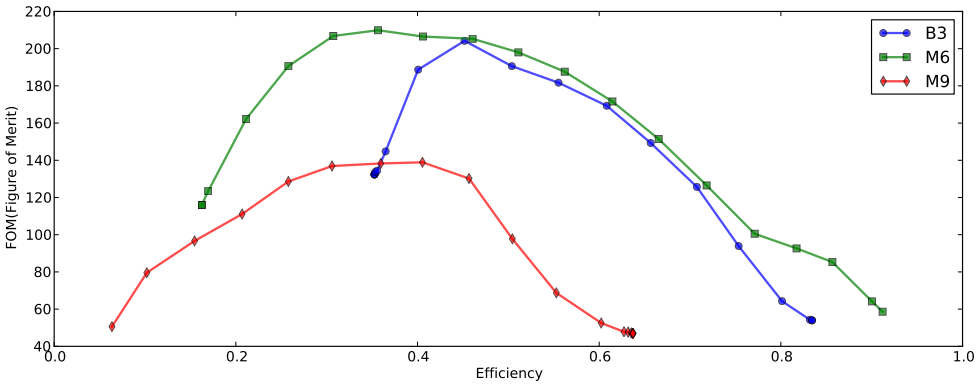


Figure 8.2. The efficiency vs. FOM curves for events in $2-5$keV range. The efficiency of the low energy events are fine tuned by varying the energy correction factor.

threshold contour as 3, and the cuts with highest FOM are selected. The plot of all observable combinations and their FOM is presented in Figures C.4, C.5 and C.6. For each observable pair, a unique ID is created as

$$I_c = 10 \cdot o_1 + o_2$$

where I_c is the unique ID for the contour cut method, o_1 and o_2 are the ID of first and second observables. The observables and contour levels that are selected for each detector are as seen in Table 8.2. The contour thresholds for the cuts are selected empirically, by evaluating the FOM for each level, and tuning to match the 6keV efficiencies close to the ones of the multivariate cuts. The analysis is repeated with weighted and energy sensitive methods.

8.3. Comparison of Analysis Methods

For all three detectors, both methods, and their variants are compared in terms of background rate, efficiency and FOM as seen in Figures 8.3-5.

In the following plots, analysis methods are plotted in x-axis, with the axis tick labels meaning:

Table 8.2. Selected observable pairs for contour cuts.

Detector	Cut	Observable 1	Observable 2
B3	1	Risetime	Width
	2	Balance (height vs. charge)	Balance(charge vs. integral)
	3	Balance (height vs. integral)	Size
M6	1	Risetime	Balance(charge vs. integral)
	2	Balance(charge vs. integral)	Size
	3	Balance (height vs. charge)	Balance(height vs. integral)
M9	1	Width	Size
	2	Balance (height vs. integral)	Multiplicity
	3	Balance (height vs. charge)	Balance(charge vs. integral)

- mv_cor: Multivariate analysis with energy correction
- mv_nocor: Multivariate analysis without energy correction
- cont: Contour cut analysis
- cont_weight: Weighted contour cut analysis
- cont_sens: Energy sensitive contour cut analysis

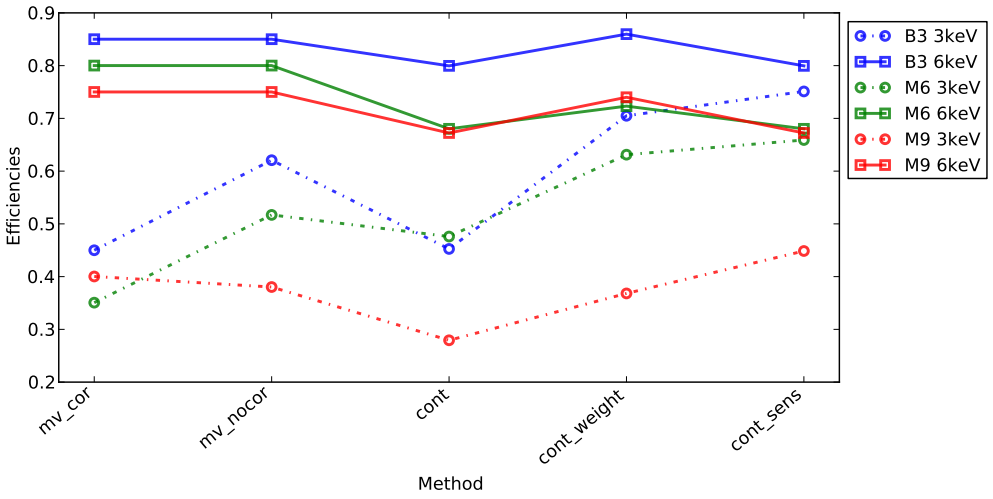


Figure 8.3. Comparison of efficiencies.

The best cut is the one that gives the best overall sensitivity, which is quantified by the

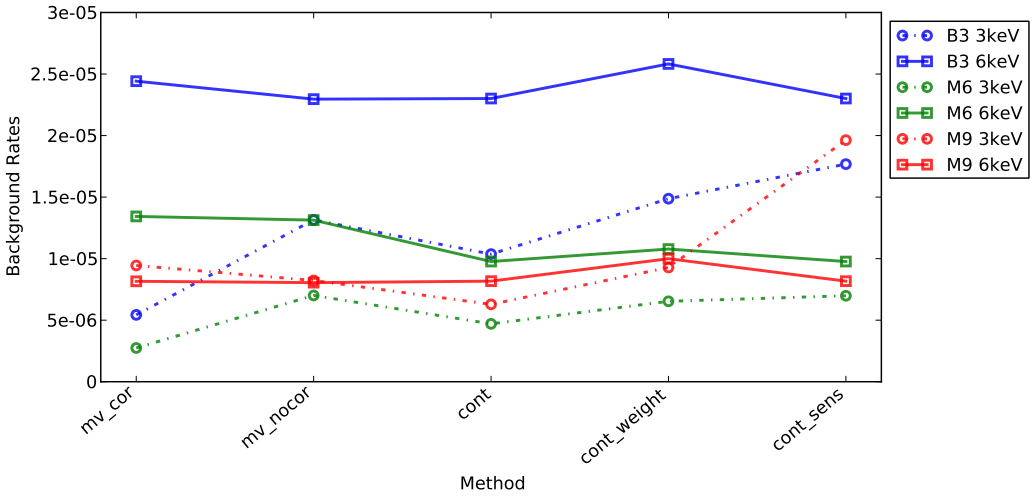


Figure 8.4. Comparison of background rates.

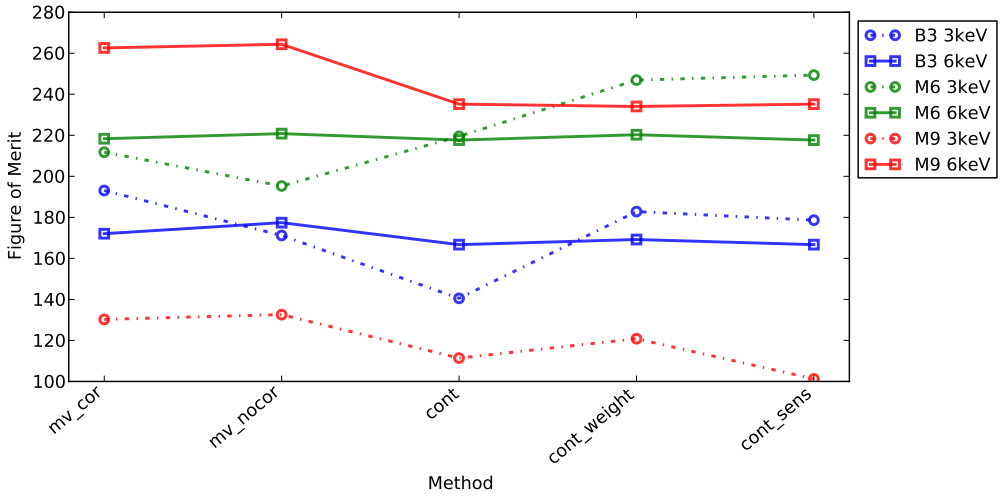


Figure 8.5. Comparison of FOM for different methods. FOM is directly related with the sensitivity of CAST experiment, thus is the most essential parameter in choosing of the discrimination method.

parameter FOM. It is obvious that, for 6keV events, the FOM is almost method independent. On the other hand 3keV events have bigger differences in different methods. It is observed that for each detector a different method may be performing the optimal event discrimination. M9 performs better with multivariate cuts; M6 has better FOM

especially with weighted and energy sensitive contour cuts and B3 has almost the same FOM with multivariate and contour cuts. One thing that is worth mentioning is the difference in the event rejection power of microbulk and bulk detectors. Both microbulk detectors, M6 and M9 has better FOM at 6keV, compared to the bulk detector B3. However, the detector M9 has a low 3keV efficiency and thus FOM.

Finally, the weighted contour cut method is selected to be used for 2008 data, for good rejection capability and better control over cuts. The calculated final background levels and efficiencies will be given in Chapter 9.

9. DATA TAKING AND BACKGROUND LEVEL CALCULATION OF 2008

After one year long shutdown in 2007, CAST has started ^{3}He Phase, to probe axions with mass higher than 0.4eV. The two important upgrades that CAST has done in 2007 are:

(i) Upgrade of the ^{4}He gas system to be able to function with ^{3}He. There were extra security measures that protect the system from higher pressures, and prevent any loss of expensive ^{3}He gas.
(ii) Replacement of TPC with Sunset Micromegas detectors, whose properties are explained in Chapter 6.

In this chapter, the data taking of 2008, performance and results of the first year of sunset micromegas data taking will be presented.

9.1. Data Taking Overview

The data taking of 2008 was carried on from 28.03.2008 to 13.11.2008 with many technical stops in between. The main reasons of the stops were quenches, problems in the mechanical system of the magnet, and vacuum systems.

9.1.1. The Sunset Micromegas Detectors that are used during 2008

Total of three detectors are used in the sunset side during 2008, two of them being microbulk detectors(M6 and M9), while one being a bulk detector(B3). The data taking statistics of each detector is presented in Table 9.1. The detectors labeled 1 are coupled to the magnet bore in the control room side of the CAST experiment, also known as the Jura side, whereas the ones labeled 2 are installed on the other side, known as the Airport side. The run started with a bulk detector in the Jura and a

microbulk detector on the Airport side. In September, CAST went into a shutdown until mid October and the Airport side detector was removed due to a leak in the gate valve. After October, CAST ran with a new microbulk micromegas detector on the Jura side.

Table 9.1. Run Statistics of 2008 Sunset Detectors.

	Before Oct 2008		After Oct 2008
	1 - B3	2 - M6	1 - M9
Number of Trackings	118	118	21
Background Hours	11914	12019	2189
Tracking Hours	178.27	178.43	31.12
Pressure Step Coverage	159 - 374		375 - 412
Pressure Coverage(mbar)	13.45 - 33.73		34.32 - 37.31
Density Coverage(kg/m^3)	0.302 - 0.696		0.707 - 0.773
Axion Mass Coverage(eV)	0.385 - 0.620		0.622 - 0.652

9.1.2. Incidents in 2008 Data Taking

The data taking have stopped on several occasions.

- *30.03.2008 Magnet Quench:* Data taking stopped for nine days due to magnet quench.
- *12.04.2008 Sunset Micromegas DAQ problem:* Raw file for the run 10160 is corrupted and can not be analysed.
- *22.04.2008 Sunset Micromegas DAQ problem:* Raw file for the run 10244 is corrupted and can not be analysed.
- *26.04.2008 Mechanical Problem:* Due to a metal piece getting stuck during magnet movement, data taking was stopped. The tracking system was re-aligned after the repair.
- *22.04.2008 Sunset Micromegas DAQ problem:* Raw file is corrupted and is not written to disk.

- *07.07.2008 Sunset Micromegas DAQ problem:* Raw file is corrupted and is not written to disk.
- *14.08.2008 Tracking PC problems:* During tracking of the magnet, tracking PC logs the tracking precision. When magnet is not tracking the sun, precision is 0. During tracking, precision is defined as difference of the measured angle, and the expected angle, and optimum value is around 10^{-3}. Especially during some morning trackings, there were times that magnet stopped following the sun, and precision value increased above the limit. During the evening trackings, magnet was more stable and there was no significant increase in tracking precision. Analysing with a threshold of 10^{-2}, 22 of the trackings had instant increases in precision values, each of which did not last more than one minute. Furthermore, during these increases, precision always stayed below 10^{-1}. Only on 14/08/2008, precision went above 10^{-2} for a longer time, from 20:56 until end of tracking at 21:22, tracking precision gradually increased from 10^{-2} to 10^{-1} (See Figure 9.1).

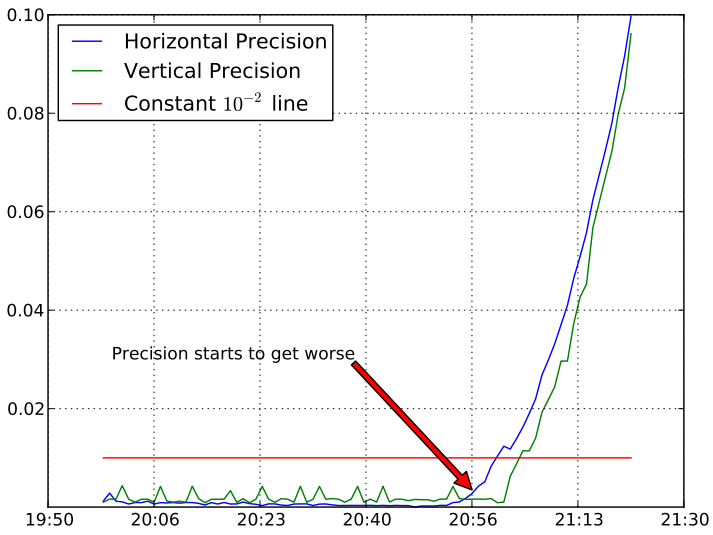


Figure 9.1. Increase of the precision value of the tracking software during the evening shift on 14.08.2008.

- *09.09.2008 Leak in the Gate Valve:* During the cryogenics maintenance, it was realized that the gate valve VT1 on the airport,MRB side of the magnet was

leaking with a rate of $2 \cdot 10^{-2}$mbar. The Sunset detector on this side of the magnet is not operated until the end of the year.

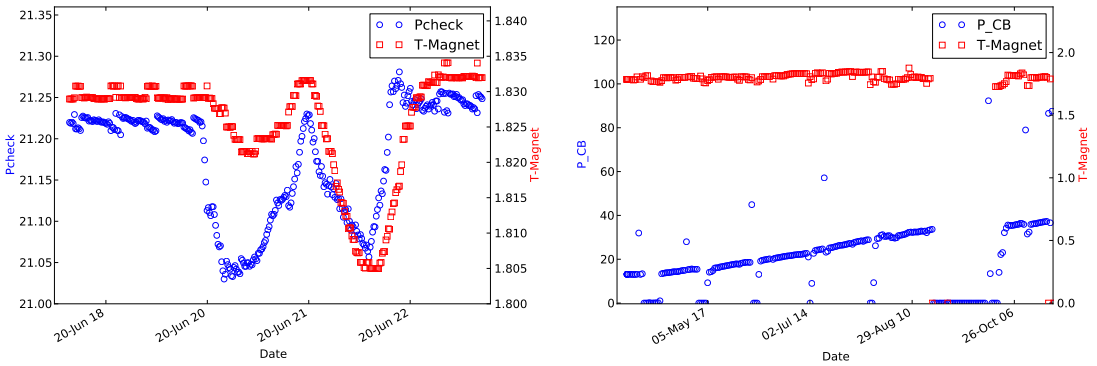
- *22.09.2008 Degradation of resolution of B3:* Due to sparks, B3 started showing worse resolution, and was stopped.
- *07.10.2008 Sparks in M6:* M6 detector was damaged by sparks, and was stopped.
- *14.11.2008 Leak in the ^{3}He System:* It was realized that there was a leak in the gas system and data taking was stopped to investigate it.
- In 2013 it was realized that magnet temperature readout has been calibrated wrongly during 2008. The temperature is recalibrated and corrected. The temperature correction is important since the density of the gas, thus the effective photon mass is calculated using pressure and temperature of the magnet.

9.1.3. Evolution of Cold Bore Pressure and Leak Problem

The axion mass that CAST is sensitive to strictly depends on the density in the cold bore, thus to pressure profile and the temperature. During 2008, the gas density in the coldbore was increased in the middle of each shift, so that the same detectors were sensitive to different axion masses during first and second half of the trackings (as explained in the Section 4.5.2). The pressure and temperature of the magnet is monitored real time and logged with 1Hz frequency.

The precision of the filling system is provided by the well defined filling procedure, in which the number of moles of gas that is transfered to the coldbore is measured, and this allows CAST to predict the pressure in the coldbore as P_{calc}. An independent measurement is done with a Baratron type pressure sensor P_{cb}, not directly in the coldbore, but in the pipework one meter away from the bore. Another pressure variable, P_{check} is used to remove temperature effects. P_{check} is the pressure of the cold bore as if the temperature was 1.8K, such that $P_{check} = 1.8 \cdot P_{cb}/T_{mag}$. P_{check} follows the evolution of the temperature with the movements of the magnet(Figure 9.2a), while P^{calc} is constant between successive fillings. Occasionally, due to quenches, bake outs or other reasons the cold bore was emptied and refilled to the same pressure. In November 2008, it was realized that the difference between the pressure before emptying the cold

bore and pressure after filling it to the same calculated pressure P_{calc} was increased to a significant extend(Figure 9.2b). The suspicion was pursued; several tests were done to probe a possible leak of the buffer gas ^{3}He, and a leak was found in a joint at the MFB side of the magnet. The leak rate was estimated to be $3 \cdot 10^{-3} \frac{\text{mbar·lt}}{\text{s}}$ and it increased with the pressure in the cold bore [103, 104]. It is revealed that the system had the leak since the ^{3}He system upgrade, There are two negative effects of the leak



(a) (b)

Figure 9.2. (a) Evolution of P_{check} during an evening shift. (b) Evolution of P_{check} throughout the year, using values of the pressure at 15:00 every day. The gaps are due to the incidents explained in Section 9.1.2.

to the CAST physics program:

- Due to the leak, the pressure steps that were used in the analysis does not match with the real pressure inside the coldbore.
- Whenever the coldbore was emptied and refilled, it was filled up to a higher pressure, creating gaps in between(Figure 9.3). These gaps were identified and completed in 2010 [105].

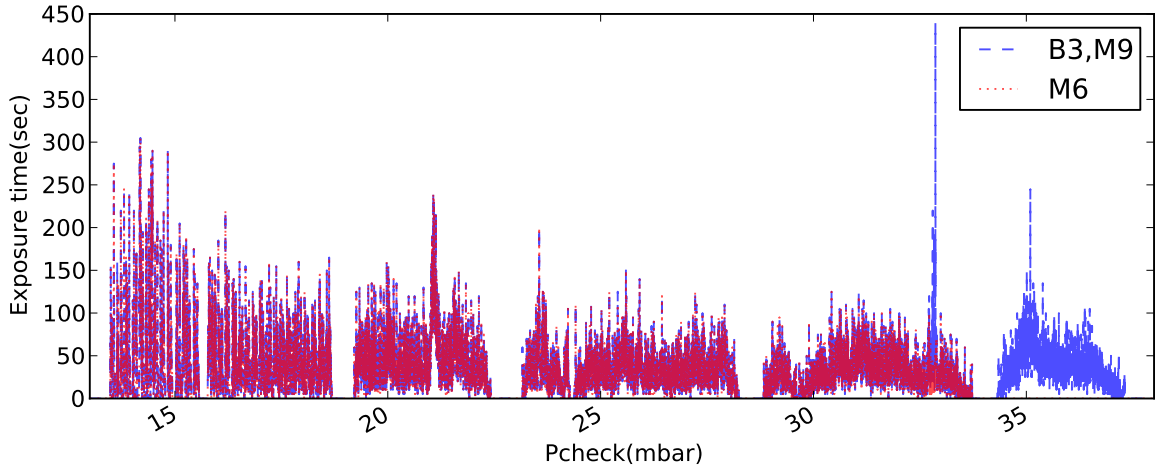


Figure 9.3. The time exposure histogram of P_{check}, with bin size as 0.001mbar. From 13.4mbar to 33.7mbar B3 and M6 are operational; for pressures higher than 37.3mbar, only M9 is operational.

9.2. Detector Stability

9.2.1. Gain and Energy Resolution

A stable gain is one of the first conditions for the stable operation. Each background file is analysed using the closest calibration file, to minimize the effect of changing conditions. The Figures C.7, C.8 show the evolution of gain and Figures C.9 and C.10 show the resolution for the three detectors of 2008. The detectors that were mounted on the same side of the magnet (B3 and M9) are shown in the same plots, while detector M6 is shown separately. The operation during the year was mostly stable. There were relatively unstable periods in the beginning of the year, and a short period after 15^{th} September. The data presented here is selected from the data that is used to calibrate background files.

9.2.2. Pulse and Strip Observables

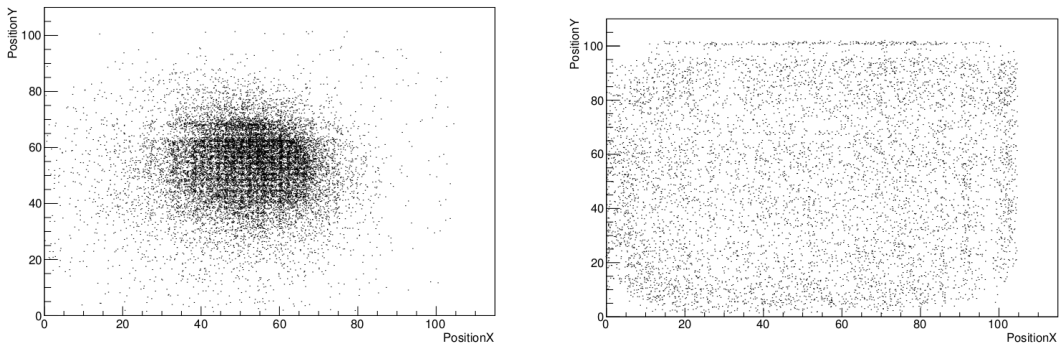
The pulse and strip characteristics are extracted from their statistical distribution, and used in background selection. Risetime is shown in Figures C.11 and C.12,

while strip multiplicity is shown in Figures C.13 and C.14. It is seen that pulse parameters have similar means for both energy range, while strip parameters have slight difference.

9.2.3. Positional Analysis

In micromegas detectors there may be noisy areas, or dead areas, due to electronic failures in the strips. The detectors in 2008 have the following hitmaps during the calibration, where all the events that formed a cluster is plotted. The calibration hitmaps does not show the real active area of the detector, since they also depend on the position of the source, and the system in 2008 was illuminating the detector from the back. It is known that the manipulator system was sometimes not perfectly aligning the source with the center of the detectors. On the other hand, background hitmaps are more homogeneous since background is mostly photons that are induced by interactions of environmental gammas.

9.2.3.1. B3. The calibration and background hitmaps of B3, with all events that formed clusters are shown in Figure 9.4, and with only selected events in Figure 9.5.



(a) (b)

Figure 9.4. Hitmaps of B3, from the events that form clusters, from the run 10544. (a) Calibration hitmap. (b) Background hitmap.

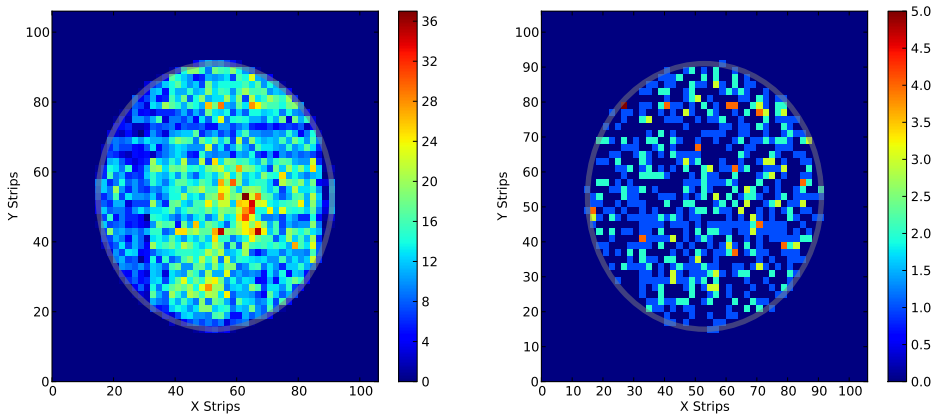
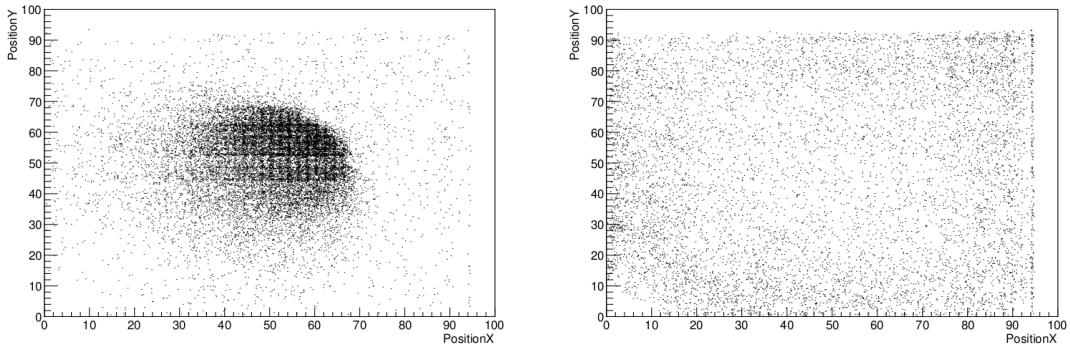


Figure 9.5. Cumulative hitmap of background events in B3 after background selection. Tracking and background counts are shown in different colors.

9.2.3.2. M6. The calibration and background hitmaps of M6, with all events that formed clusters are shown in Figure 9.6, and with only selected events in Figure 9.7. The hitmaps after the background selection show a noisy area, where many events are selected, between x strips 16-17 and y strips 44-45. This area was removed in the background selection process, since it effects the level, but the change in effective area is negligible. The closeup of the noisy area is shown in 9.8 and hitmap after removal of the noisy area is shown in 9.9.



(a) (b)

Figure 9.6. Hitmaps of M6, from the events that form clusters, from the run 10544. (a) Calibration hitmap. (b) Background hitmap.

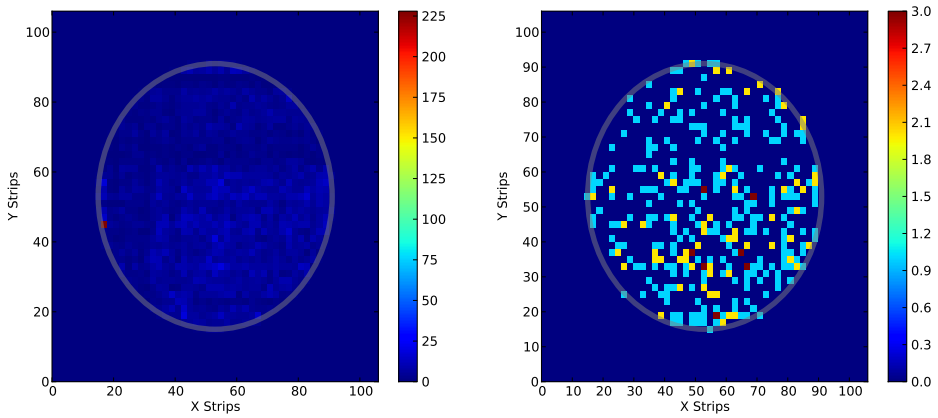


Figure 9.7. Cumulative hitmap of background events in M6 after background selection. Tracking and background counts are shown in separate plots. The noisy area in the background can be seen in the left bottom part of the coldbore circle.

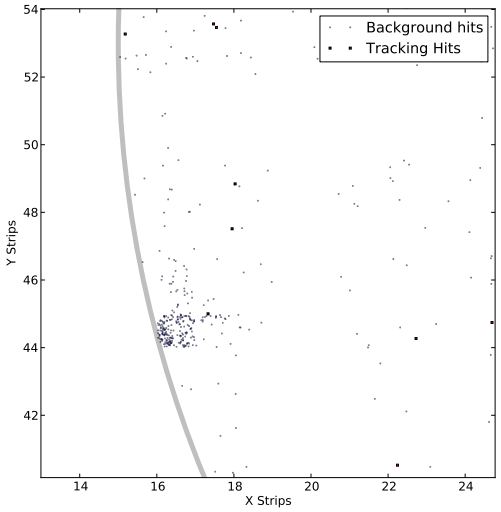


Figure 9.8. Closeup look at the noisy area in the detector M6.

9.2.3.3. M9. The calibration and background hitmaps of B3, with all events that formed clusters are shown in Figure 9.10, and with only selected events in Figure 9.11. In the plots with selected events, it is seen that the area of with y axis between strips 64 and 66 have less events(in both plots), due to dead strips.

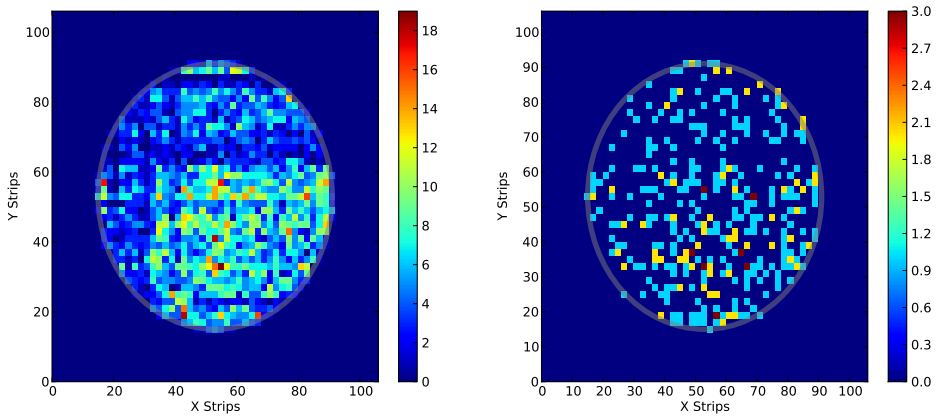
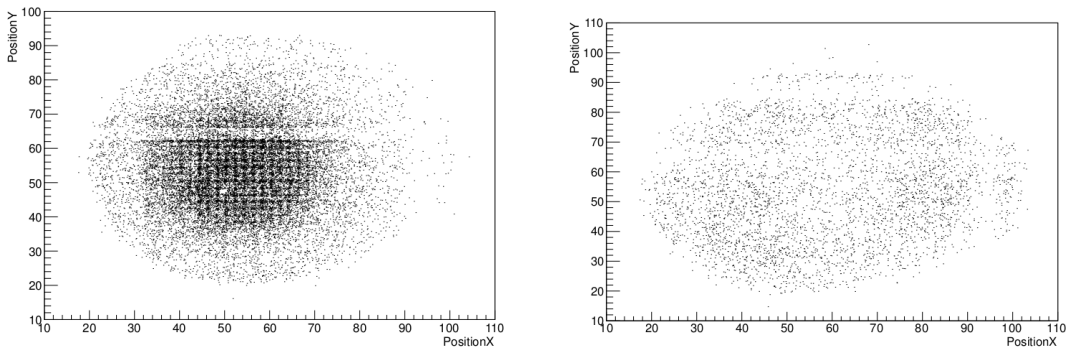


Figure 9.9. Cumulative hitmap of background events in M6 after removal of the noisy area.



(a) (b)

Figure 9.10. Hitmaps of M9, from the events that form clusters, from the run 11085. (a) Calibration hitmap. (b) Background hitmap.

9.2.4. Electronic Noise Problems

The micromegas detectors suffered from electronics noise in many occasions, especially when the magnet was moving. The electronic frequencies that run the instruments on the magnet propagate through the magnet mass and are transfered to the micromegas detectors. Since the noisy events are already far from peak of calibration distributions, they are rejected easily. But they still can increase the deadtime of the detector. One particular problem of the sunset micromegas is that when one of the detectors have high trigger rate, deadtime of both detectors increase due to shared

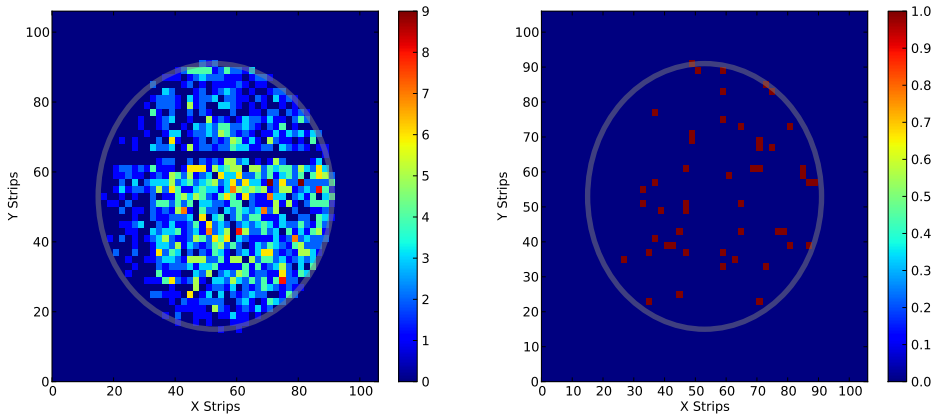


Figure 9.11. Cumulative hitmap of background events in M9 after background selection. Tracking and background counts are shown in separate plots.

DAQ system. The deadtime of micromegas readout for a single event is around 10ms. If the trigger rate is around its nominal value, 1Hz, deadtime is 1% of the total run time, thus negligible. When the trigger rate is higher deadtime can rise, affecting the background time and should be taken into account. For all the runs of 2008, it was observed that, total deadtime never exceeded 10% of the total run time(Figure 9.12).

To see the correlation of the selected event rate with trigger rate, all the runs with high trigger rate was studied, and it was seen that during high trigger rate times of the data, there is no increase of decrease in the event rate.

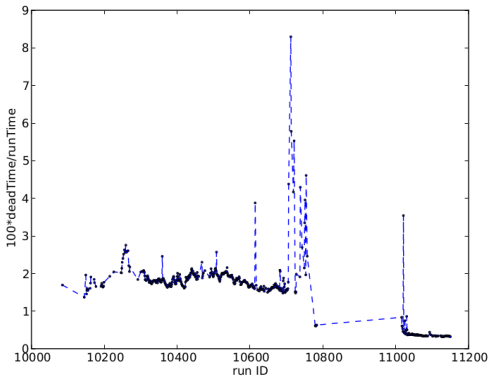


Figure 9.12. The deadtime as percentage in the sunset micromegas overall the year.

9.3. Detector Efficiency

9.3.1. Software Efficiency

The contour cut method doesn't guarantee a fixed efficiency as the multivariate method, however applying the same cuts to same detector overall the year give similar efficiency. The efficiency evolution of 2008 is shown in Figure2 C.15, C.16 and C.17. The efficiency calculation of $6keV$ and $3keV$ peaks show that low energy x-rays have lower efficiency with the same cuts, due to slight shift of observable means, and higher standard deviation. For the analysis of axion signal, one needs the efficiency at all energies.

CAST Detector Laboratory, which is equipped with an x-ray generator [105] is used to understand the efficiency of detectors at energies other than 6keV. Characteristic fluorescence X-rays of elements Al, Ti, Mo, Au are created from 1keV to 9keV are sent to detectors using appropriate filters. A regular calibration was done with a ^{55}Fe source, with which the selection criteria is defined. Using this selection criteria efficiency for all fluorescence peaks is calculated. It is observed that the efficiency decreases for energies lower than 6keV and stays almost same for higher energies.

For detectors used in 2008, mean efficiencies of the main and escape peaks during ^{55}Fe calibrations were used to calculate the efficiency at various energies. For energies less than 6keV, a linear interpolation was done using these peaks, while for energies higher than 6keV, efficiency was kept same as 6keV efficiency. The resulting software efficiencies are seen in Figure 9.13.

9.3.2. Total Efficiency

The total detector efficiency is multiplication of the software efficiency and hardware efficiency from Section 6.4, as seen in Figure 9.14.

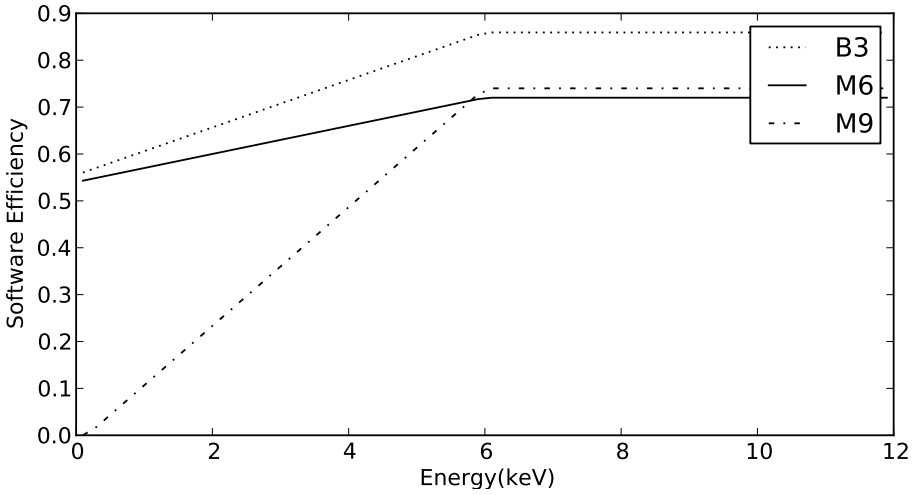


Figure 9.13. Software efficiency curves for all three detectors.

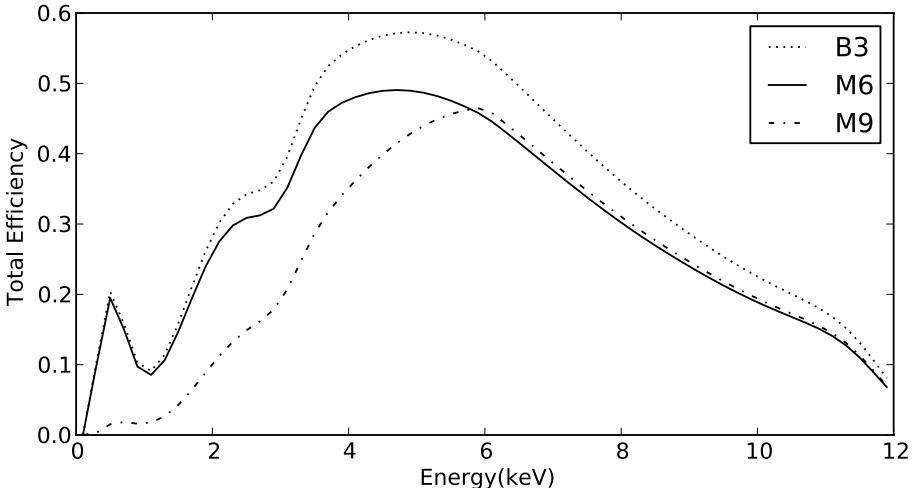


Figure 9.14. Total efficiency of all three detectors.

9.4. Tracking and Background Levels

The selection of background and tracking counts in three detectors were done with weighted contour cut method, using the observable pairs introduced in the Chapter 8.

9.4.1. Tracking Definition

In terms of detector data, Tracking is defined by combination of the following conditions.

- Tracking PC is set to solar Tracking mode, and sun is in the range of the magnet.
- Magnet is following the sun with the error in angle less than 10^{-2}.
- Corresponding gate valve open(VT1 or VT2).
- Magnetic field is on.

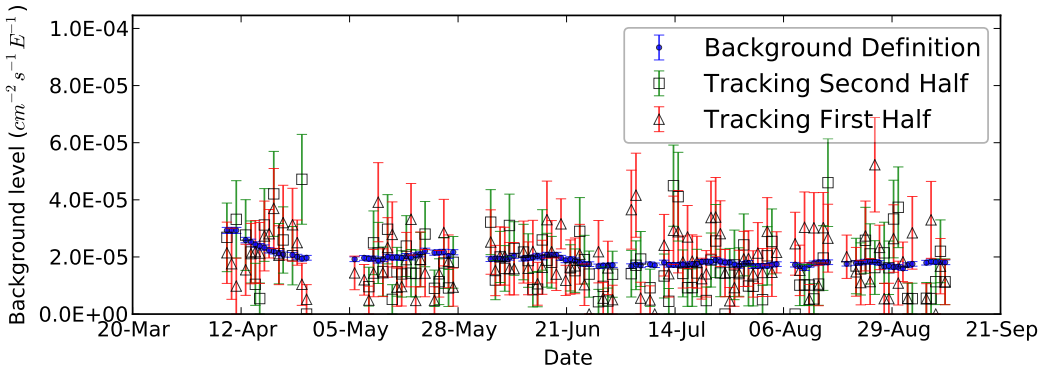
All the data that satisfies these conditions are considered as tracking data, and the counts during the tracking time are called tracking counts. In case of a signal, CAST should observe excess of tracking count rate compared to background rate.

9.4.2. Background Definition

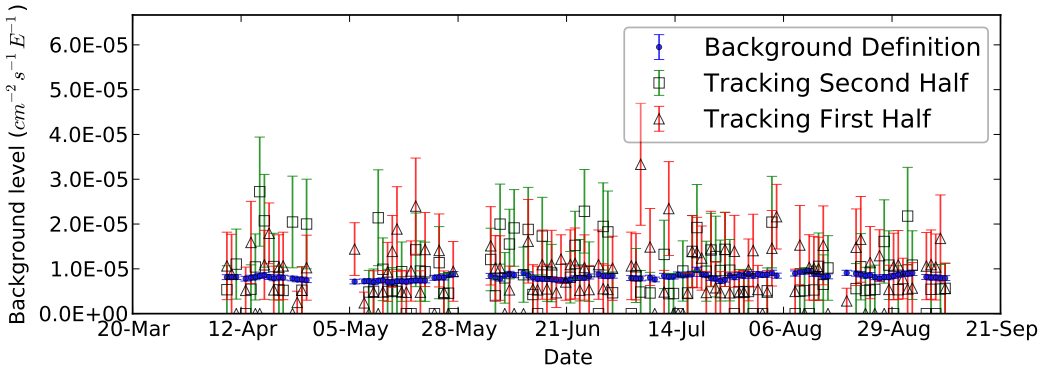
Background is defined as any time other than the tracking time, and ideally, a separate background definition is used for each tracking. The background should be defined to contain enough statistics, and to have similar environmental conditions with the corresponding tracking data. For 2008, two background definitions are used.

(i) Cumulative background of 100 hours, placing the tracking data in the middle.
(ii) Background of the run, that includes the tracking data. The background file length can vary from 6 to 12 hours.

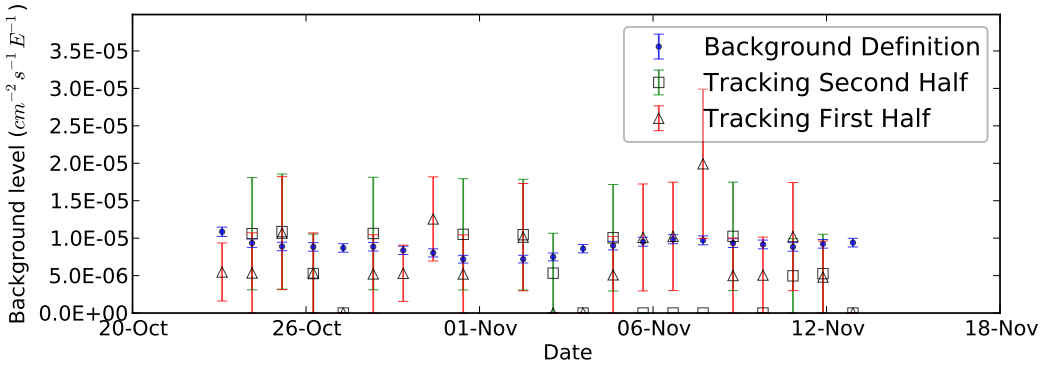
The evolution of background vs. trackings for both definitions are as presented in Figures 9.15 and 9.16. The first and second halves are plotted separately, since the pressure, thus the axion mass that CAST is sensitive to is different in each half. The use of longer tracking smooth out the evolution of the background level. In the second background definition the fluctuations in background level is more obvious, and the errors are bigger compared to other definition.Finally for the background levels are calculated from the first definition, for the better stability due to high statistics.



(a)



(b)

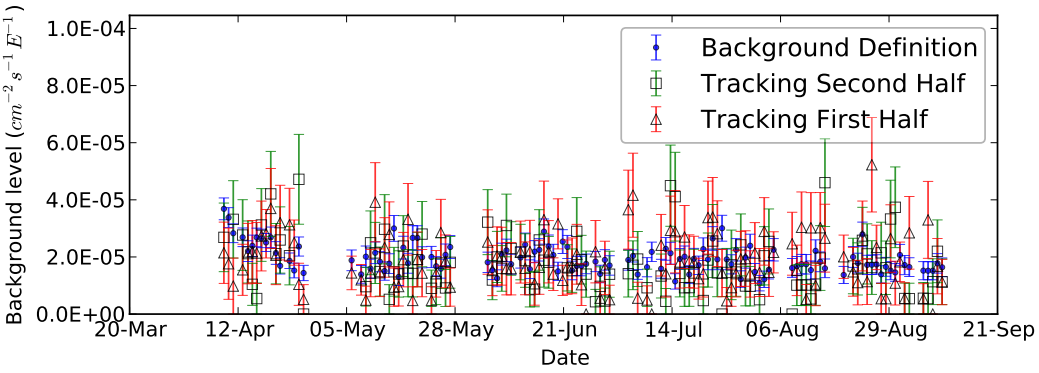


(c)

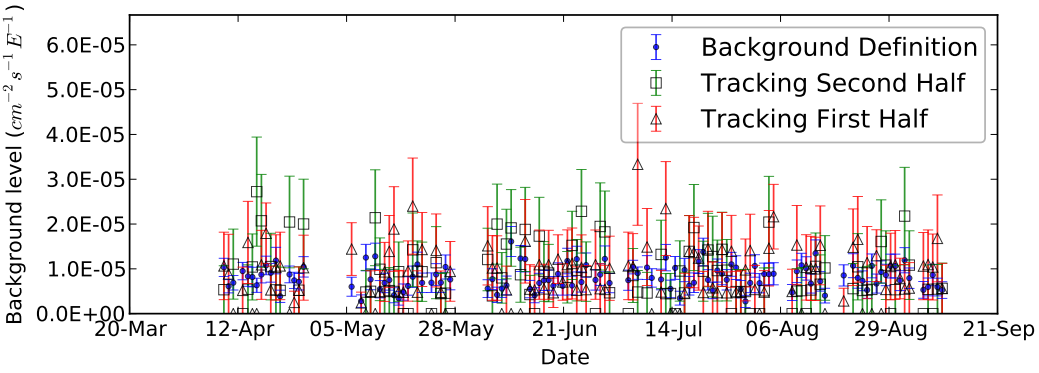
Figure 9.15. Comparison of tracking and background levels, using 100 hours of background data for each tracking. (a) B3, (b) M6, (c) M9.

9.4.3. Levels and Spectra

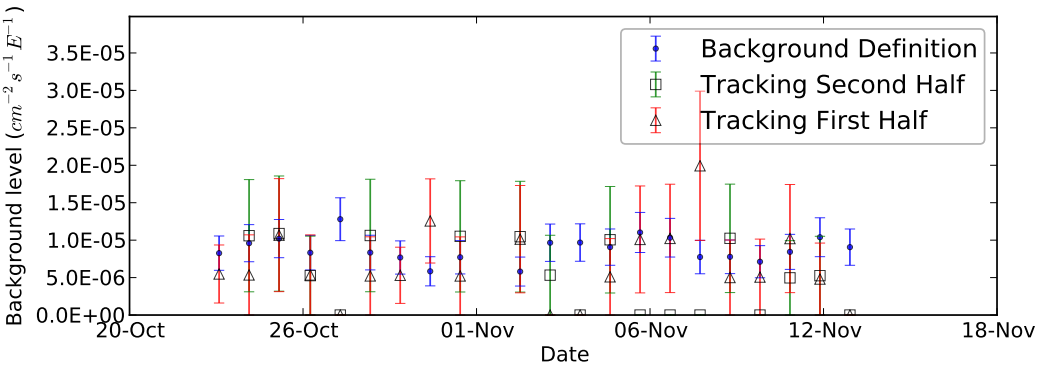
The tracking and background rates in normalized units($\mathrm{keV}^{-1}\mathrm{cm}^{-2}\mathrm{s}^{-1}$) are shown in Table 9.2.



(a)



(b)



(c)

Figure 9.16. Comparison of tracking and background levels, using the run that includes the tracking data. (a) B3, (b) M6, (c) M9.

Energy spectrum of each detector after the event selection, in the range of $1-10$keV is shown in Figure 9.17. For detectors B3 and M9, the copper fluorescence peak at 8keV is dominant, M6 have a more homogeneous spectrum. The high 8keV

Table 9.2. The Background and Tracking Levels of Sunset Micromegas Detectors.

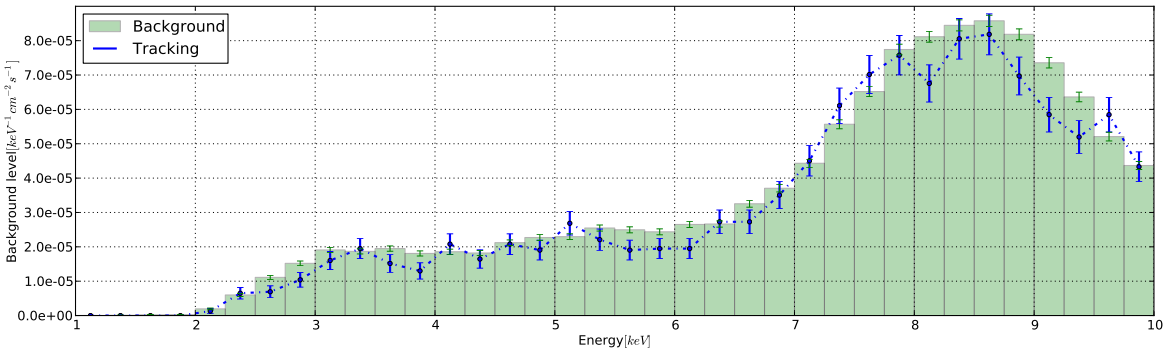
	B3	M6	M9
Background Level ($keV^{-1}cm^{-2}s^{-1}$)	$1.897 \cdot 10^{-05} \pm 7.800 \cdot 10^{-08}$	$8.175 \cdot 10^{-06} \pm 5.097 \cdot 10^{-08}$	$8.880 \cdot 10^{-06} \pm 1.245 \cdot 10^{-07}$
Tracking Level ($keV^{-1}cm^{-2}s^{-1}$)	$1.812 \cdot 10^{-05} \pm 6.263 \cdot 10^{-07}$	$8.577 \cdot 10^{-06} \pm 4.310 \cdot 10^{-07}$	$6.042 \cdot 10^{-06} \pm 8.630 \cdot 10^{-07}$
Efficiency at 6keV	0.85918	0.72322	0.74003
Efficiency at 3keV	0.70725	0.63117	0.36813

peak is caused by the copper around and inside the detector. When external particles hit copper, fluorescence x-rays are emitted and since they are real x-rays, are mostly accepted by the discrimination method.

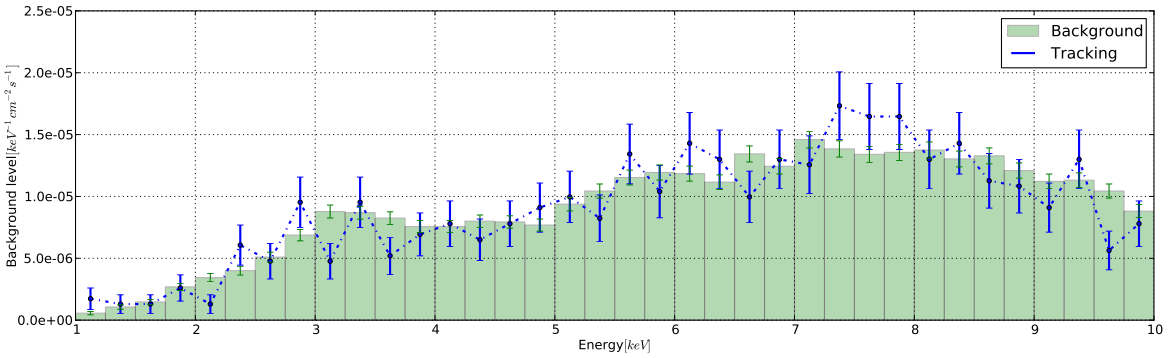
9.5. Study of Micromegas Systematics

9.5.1. Magnet Position

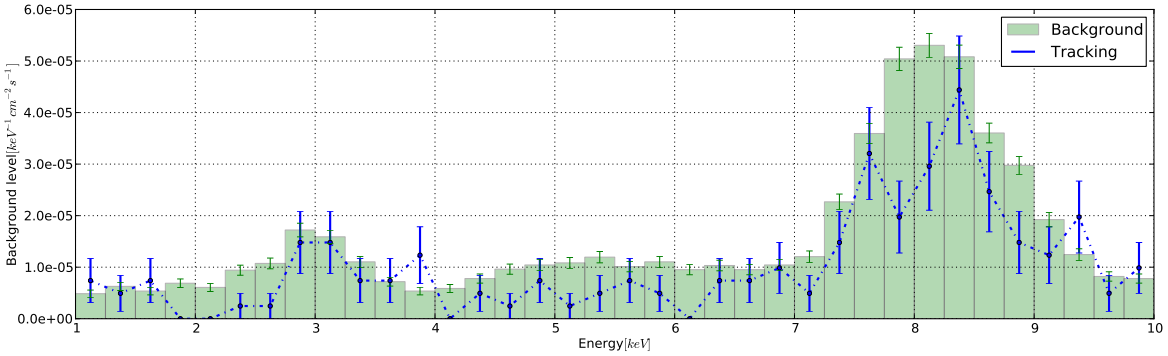
During each shift, CAST magnet moves around 50000 vertical encoders, and 6200 horizontal encoders. Other than shifts the magnet is moved to prepare for the next shift, for grid measurements or to have better access to some parts of the area. During these movements there may be changes in background level due to radioactivity of the concrete walls. The background rate in each magnet position is calculated by dividing the both encoder ranges in 20 bins. The rate and elapsed time hitmap is seen in Figures C.18, C.19 and C.20. Plots on the right shows the time elapsed in hours at each bin. It is seen that the bins with high rate have very small exposure time, thus has big error. Rates and standard deviations in 1-dimensional plots are shown in Figures C.21, C.22 and C.23. X-axis shows the bin number, while the horizontal line shows the mean level.



(a)



(b)



(c)

Figure 9.17. The cumulative background and tracking energy spectrum of 2008 Sunset Detectors. (a) B3, (b) M6, (c) M9.

9.5.2. Compatibility with Poisson Distribution

During the background and tracking conditions, x-ray like events are rare enough in micromegas detectors; the number of events in a fixed period of time should follow Poisson distribution. The compatibility with Poisson statistics were checked with a

time bin of 0.35 hours, both for background and tracking. The time scheme of the calculation is shown in Figure 9.18, while the statistics is shown in Figure 9.19.

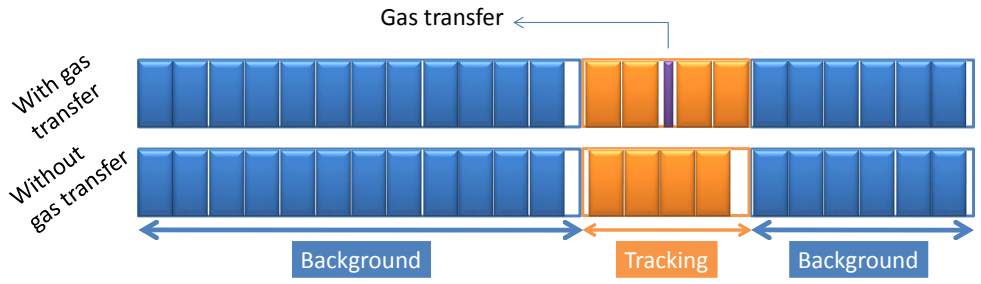
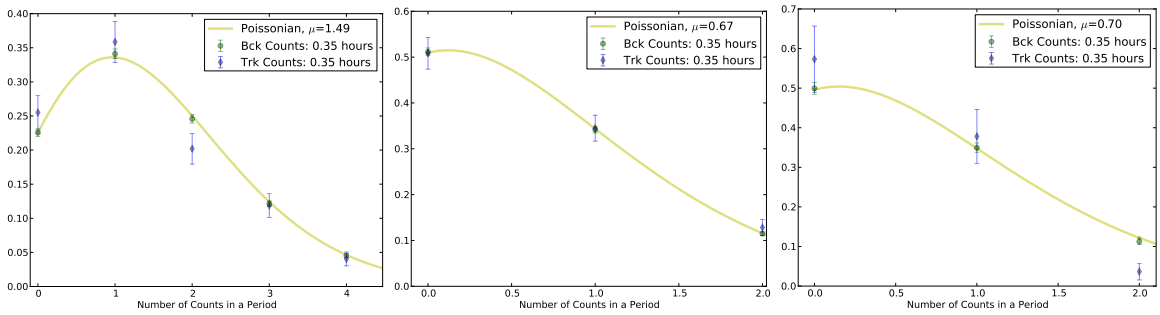


Figure 9.18. The schematics for the time binning for calculation of count rate statistic. In case of gas transfer, the two half trackings are binned separately, not to include the gas transfer time in calculation.



(a) (b) (c)

Figure 9.19. Compatibility of background and tracking count rates with Poissonian statistics considering a time bin of 0.35 hours. (a) B3, (b) M6, (c) M9.

10. COUPLING CONSTANT LIMIT FOR 2008 AXION SEARCH

In the absence of axion signal, CAST results can imply a limit on the $m_a - g_{a\gamma}$ parameter space.

To test the null hypothesis(absence of signal) and determining the limit on coupling constant, the method of maximum likelihood [106] has been used in analysis of all phases of CAST, which in based on building likelihood of detecting the observed number of counts, leaving coupling constant as a free parameter, and maximizing the likelihood function.

The analysis of 2008 data is based on the method used for ^{4}He data, and is modified to take into account the fluctuations of the coldbore pressure during a single tracking. In this chapter the analysis method ^{3}He phase will be derived using binned likelihood method explained in Appendix B.2. The gas dynamics that affect the calculations will be explained and finally results for 2008 data for sunset micromegas detectors will be presented.

10.1. Unbinned Likelihood Method

For the data of 2008, the pressure variation and leak problem makes it impossible to use a single pressure step for the whole half tracking. The correspondence of the steps and pressures diverges as the amount of gas is decreased by the leak. Instead of binned likelihood method, unbinned method can take into account the variation of the pressure in the cold bore during the tracking more accurately as long as one relies on the measured pressure and temperature.

In the unbinned likelihood method, instead of calculating the likelihood for pressure steps, it is calculated for infinitesimal time bins, which converts the discrete bin-

ning into a continuous distribution. Recalling the global likelihood definition, Equation B.9 for a single detector becomes

$$\mathcal{L}_{m_a}(g_{a\gamma}) = \prod_{k'} L^{(k')}_{m_a}(g_{a\gamma}) = \prod_{k(n=0)} L^{(k)}_{m_a}(g_{a\gamma}) \prod_{l(n=1)} L^{(l)}_{m_a}(g_{a\gamma}) \tag{10.1}$$

where k' is an index over the whole time bins during the trackings. The term can be separated into multiplication of two different terms, a term with all time bins in which there was 0 count(index k) and the term with all time bins during which there was 1 count(index l). Using Equation B.6, and calculating Poissonian probability for 0 and 1 counts, these terms can be expressed as

$$\prod_k L^{(k)}_{m_a}(g_{a\gamma}) = \prod_k \prod_i \mathrm{e}^{-\mu_{ik}} \qquad \& \qquad \prod_l L^{(l)}_{m_a}(g_{a\gamma}) = \prod_l \frac{\prod_i \mathrm{e}^{-\mu_{il}} \mu_{il}}{\prod_i \mathrm{e}^{-1}} \tag{10.2}$$

From here one can advance to calculate $-\frac{1}{2}\chi^2$ as

$$\begin{aligned} -\frac{1}{2}\chi^2_{m_a} &= \ln\left(\prod_k \prod_i \mathrm{e}^{-\mu_{ik}}\right) + \ln\left(\prod_l \frac{\prod_i \mathrm{e}^{-\mu_{il}} \mu_{il}}{\prod_i \mathrm{e}^{-1}}\right) && (10.3)\\ &= -\sum_k \sum_i \mu_{ik} + \sum_l \sum_i (-\mu_{il} + \ln \mu_{il} - 1) && (10.4)\\ &= -\sum_k \sum_i \mu_{ik} - \sum_l \sum_i \mu_{il} + \sum_l \sum_i \ln \mu_{il} - \sum_l \sum_i 1 && (10.5) \end{aligned}$$

The first two terms can be combined to a common term that sums over all time bins such as $I_1 = \sum_{k'} \sum_i -\mu_{ik'} = -\sum_k \sum_i \mu_{ik} - \sum_l \sum_i \mu_{il}$, and last term can be written as a constant C_1. Calculating the first term as some of background and signal contributions

$$\begin{aligned} I_1 &= -\sum_{k'} \sum_i b_{ik'} - \sum_{k'} \sum_i g^4_{a\gamma} \int_{E_i}^{E_i + \mathrm{d}E} \frac{\mathrm{d}n_{a\gamma}}{\mathrm{d}E} \mathrm{d}E && (10.6)\\ &= -\sum_{k'} \sum_i b_{ik'} - g^4_{a\gamma} \sum_{k'} \sum_i \int_{E_i}^{E_i + \mathrm{d}E} \frac{\mathrm{d}n_{a\gamma}}{\mathrm{d}E \cdot \Delta t_k} \mathrm{d}E \cdot \Delta t_k && (10.7)\\ & && (10.8) \end{aligned}$$

The sum over energy ranges can be converted into an integral over the whole energy range of the analysis, while time sum can be converted into an integral over the whole

tracking times, as $\Delta t_k \to 0$. Furthermore since first term doesn't depend on $g_{a\gamma}$, it can be considered as another constant C_2, resulting

$$I_1 = C_2 - g_{a\gamma}^4 \int_t \int_E \frac{d^2 n_{a\gamma}}{\mathrm{d}t \cdot \mathrm{d}E} \mathrm{d}t \cdot \mathrm{d}E \tag{10.9}$$

The third term $I_2 = \sum_l \sum_i \ln \mu_{il}$ in 10.5 can be rewritten as

$$\begin{aligned} I_2 &= \sum_l \ln \left(b_{il} + \int_{E_i}^{E_i+\Delta E} \frac{\mathrm{d}n_{a\gamma}}{\mathrm{d}E} g_{a\gamma}^4 \mathrm{d}E \right) && (10.10) \\ &= \sum_l \left\{ \ln \left[\left(b_{il} + \int_{E_i}^{E_i+\Delta E} \frac{\mathrm{d}n_{a\gamma}}{\mathrm{d}E} g_{a\gamma}^4 \mathrm{d}E \right) \frac{1}{\Delta t_l} \right] + \ln \Delta t_l \right\} && (10.11) \end{aligned}$$

Again as $\Delta t_k \to 0$, we can rewrite the Equation 10.11 as

$$I_2 = \sum_l \ln \left(\frac{db_{il}}{\mathrm{d}t_l} + g_{a\gamma}^4 \int_{E_i}^{E_i+\Delta E} \frac{d^2 n_{a\gamma}}{\mathrm{d}E \cdot \mathrm{d}t_l} \mathrm{d}E \right) + C_3 \tag{10.12}$$

where $C_3 = \sum_l \ln \Delta t_l$ is independent of $g_{a\gamma}$. Combining all terms, Equation 10.5 becomes

$$\begin{aligned} -\frac{1}{2}\chi_{m_a}^2 = & - g_{a\gamma}^4 \int_t \int_E \frac{d^2 n_{a\gamma}}{\mathrm{d}t \cdot \mathrm{d}E} \mathrm{d}t \cdot \mathrm{d}E \\ & + \sum_l \ln \left(\frac{db_{il}}{\mathrm{d}t_l} + g_{a\gamma}^4 \int_{E_i}^{E_i+\Delta E} \frac{d^2 n_{a\gamma}}{\mathrm{d}E \cdot \mathrm{d}t_l} \mathrm{d}E \right) + C_1 + C_2 + C_3 \end{aligned} \tag{10.13}$$

The first term is summed over the whole trackings and energy ranges, and gives the total number of expected photons that are converted from axions and is denoted by $n_{a\gamma}$. The second term gives the contribution of each count at energy bin i and time t_l. While calculating the limit with 95% confidence level, the constant terms C_i can be disregarded, since they will be eliminated in the division in Equation B.11.

10.2. ^{3}He Dynamics

The conversion probability in the magnet depends on the length of the conversion region, while the axion mass that CAST is sensitive to depends on the buffer gas density.

10.2.1. Gas Density

The magnet temperature and cold bore pressure are measured and logged every five seconds. The measured temperature is same all through the magnet thanks to good conductance of superfluid helium. The pressure on the other hand is measured in the MRB side of the magnet, while for all calculations, the pressure is taken as the pressure in the center of the cold bore. When the magnet is in horizontal position(vertical angle is 0°), the pressure should be same everywhere inside the cold bore. However during the solar tracking magnet is moved from $-8°$ to $+8°$, and tilting creates a pressure difference between higher and lower parts of the gas volume. To calculate the pressure in the center during the tracking, hydrostatic effect is calculated as

$$P_{hydro} = h \cdot g \cdot \rho_0$$

where h is the height difference between the center of the cold bore, g is the gravitational acceleration and ρ_0 is the density of the gas before the tracking in stable conditions. Stable conditions are defined as:

- Magnet is stationary and is in horizontal position(no inclination).
- Magnet current is stable, there is no ramping up or ramping down.
- Magnet temperature is stable.
- There is no gas transfer.

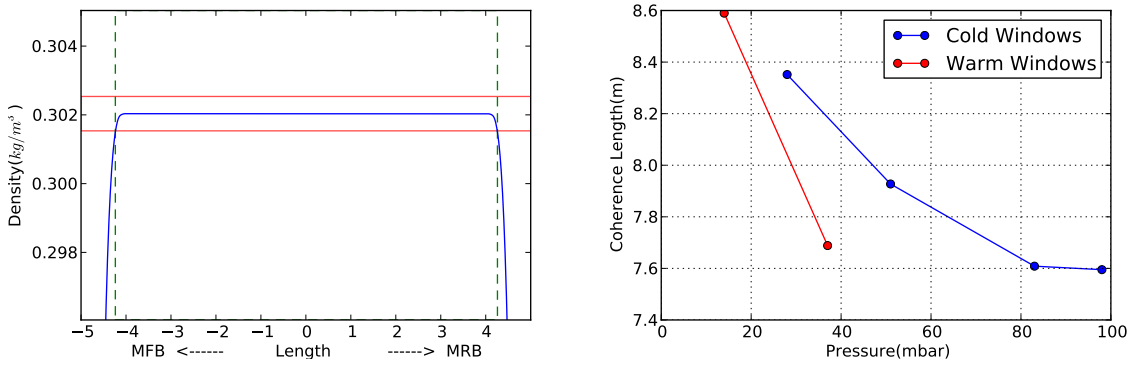
The density ρ of the buffer gas at any time is calculated from the pressure in the center of the coldbore(calculated using the pressure readout and hydrostatic pressure) and the corrected temperature using the equation of state of ^{3}He from NIST database.

10.2.2. Effective Length

In the ideal case the gas density is uniform throughout the cold bore length, thus the whole region with magnetic field, 9.2m can be used as L in conversion probability calculation: Equation 3.22. However this is not the case. In a large portion of the

cold bore length temperature is equal due to superfluid cooling helium, but in the edges of cold bore, windows that separate the buffer gas and the vacuum regions are not at the same temperature with the gas in the cold bore. They are hotter and this create a non-uniform density profile over the coldbore. Furthermore when the magnet is tilted during the tracking, the hot gas is moving to the higher parts due to convection, creating turbulent behaviour. To probe this problem, Computational Fluid Dynamics(CFD) simulations are done, and the density profile of the magnet is calculated for various pressures [110].

During 2008, the windows of the cold bore were heated up to temperatures around 60K, while in later years CAST operated at colder windows with temperatures around 15K. To understand each case separately, two set of simulations are done, one for warm windows, and one for cold windows. The *density stability threshold*(DST) defines the



(a) (b)

Figure 10.1. (a) Density profile in the magnet for pressure 14mbar. The red lines show the DST while the dashed vertical lines show the length of the gas volume within the DST. (b) Parametrization of effective length for warm(red) and cold(blue) windows.

maximum allowed density variation along the cold bore at any moment. One wants to assure that the density variations are within the DST, so that sensitivity is maintained for a certain axion mass. The effective length is calculated as the length of the gas volume along the cold bore axis, within the DST.

Traditionally DST is used as $d\rho = 0.001\text{kg/m}^3$ [108]. The work done by Elias,Vafeiadis

and Lakic [109] shows that this threshold is rather strict and especially at higher pressures, for photons with energies higher than 2keV, a looser threshold can be used depending on the energy of the photon and the magnet length. However, the simulations are still ongoing, and full parametrization of the effective length with energy and pressure is not complete. Due to this fact, for this work to avoid any overestimation, DST is used as the rather strict value, $d\rho = 0.001\text{kg/m}^3$. Profile of 14 mbar case in 2008 is shown in Figure 10.1a, with this DST condition.

For warm windows, CFD simulations are conducted at two pressures, 14 and 37 mbar. Effective length is calculated using common DST condition and a line is fit to obtain effective length L for any pressure P as

$$L = 9.223 - 0.048 \cdot P \tag{10.14}$$

A density profile example together with the parametrization points of the effective length are presented in Figure 10.1b.

10.3. Results

The results for 2008 are obtained by unbinned likelihood method, as explained in Section 10.1.

10.3.1. Expected Number of Photons

For each axion mass, the expected number of photons $n_{a\gamma}$ are calculated as a function of $g_{a\gamma}$ using the density exposure and the effective magnet length as parametrized in previous section, as in the first term of the Equation 10.13. The density exposure is presented in Figure 10.2, while the expected number of photons for each axions mass is shown in Figure 10.3. In both plots the gaps are visible due to the ^{3}He leak in 2008. These gaps are covered later in 2010.

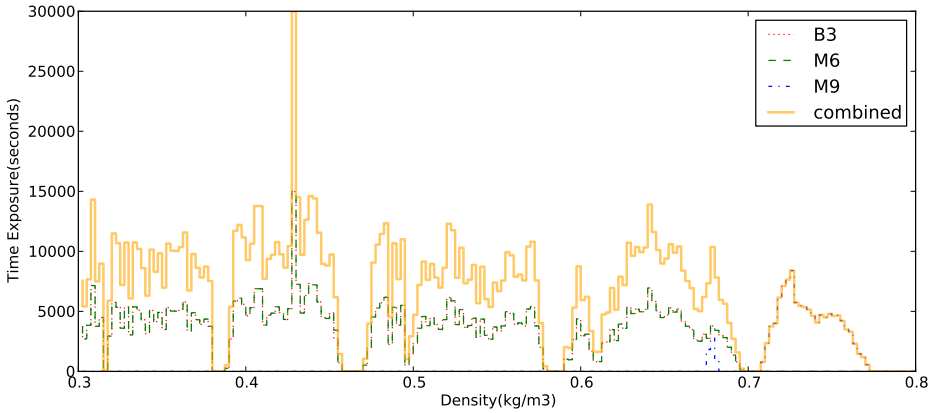


Figure 10.2. Density exposure of all three detectors(dashed lines) and combined exposure(solid line).

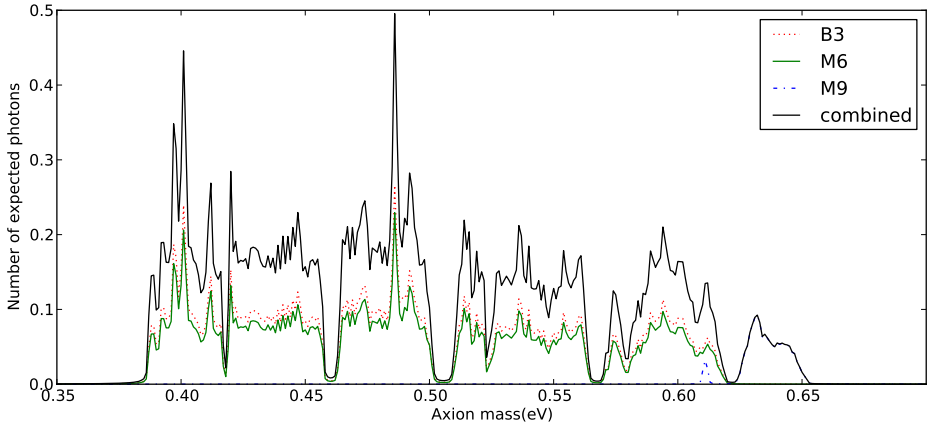


Figure 10.3. (b) Expected number of photons during 2008 data for all sunset micromegas, depending on the axion mass, assuming coupling constant $g_{a\gamma} = 10^{-10}$.

10.3.2. Search for Axion Signal

In Chapter 9, it was shown the tracking count rates are compatible with the background definition, showing no significant excess during trackings. However this alone is not enough to reject the existence of an axion signal.

For each axion mass, it should be checked if the most likely value of $g^4_{a\gamma}$ is within a small-enough statistical deviation from $g^4_{a\gamma} = 0$, which is the null hypothesis. For this, the value of $g^4_{a\gamma_{max}}$, where the likelihood function $\mathcal{L}$, or its natural logarithm $-\frac{1}{2}\chi^2$ has its maximum is calculated. Its standard deviation is calculated from values, where the

likelihood function drops to 1/2 less than the maximum value such as

$$\mathcal{L}_{1/2} = \mathcal{L}_{max} - \frac{1}{2}$$

Note that there are two values, $g_{a\gamma}^{4(left)}$ and $g_{a\gamma}^{4(right)}$ where $\mathcal{L}$ drops to $\mathcal{L}_{1/2}$ on the left and right sides of the maximum. For the axion masses that has a positive maximum such as $g_{a\gamma_{max}}^4 > 0$, the left sigma is used.

The likelihood for $m_a = 0.451$eV is shown in Figure 10.4. The dashed lines show the left and right deviations from the maximum of the distribution, while the filled area shows the 95% of integral of physically acceptable g_{10}^4 values. The exclusion limit is in the right end of the filled area. For this mass, maximum of likelihood distribution is at $g_{10}^4 = 8.4005$ while the exclusion limit is at $g_{10}^4 = 63.87$. The deviation of $g_{a\gamma_{max}}^4$ from $g_{a\gamma}^4 = 0$ in terms of number of sigmas for all axion mass range is shown in Figure 10.5. Considering the axion masses for which there were exposure, 11% of data is more than 1σ away from the expected value $g_{a\gamma}^4 = 0$.

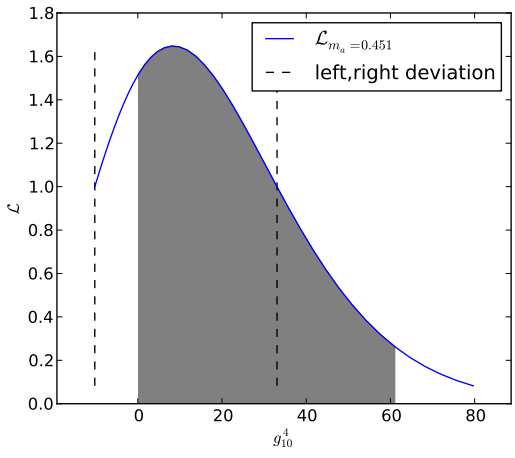


Figure 10.4. Likelihood function for $m_a = 0.451$eV, plotted as a function of g_{10}^4.

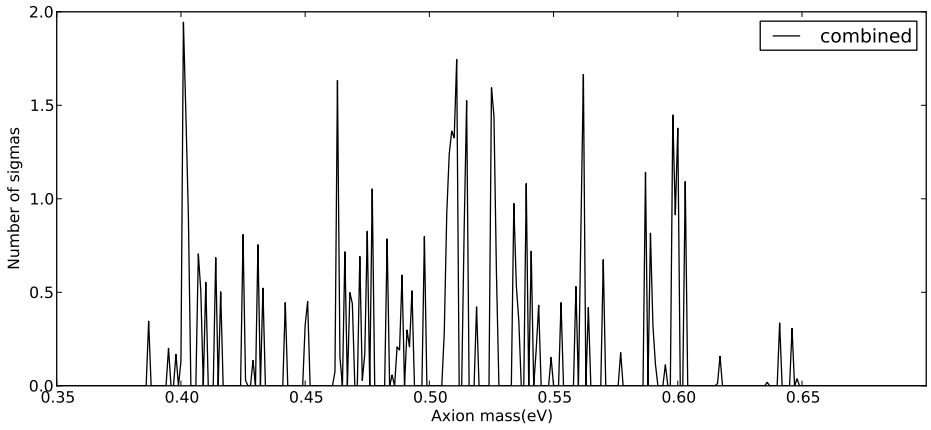


Figure 10.5. Deviation of maximum likelihood from the null hypothesis for the axion masses CAST was sensitive in 2008. The deviation is in terms of left sigma of the distribution.

10.3.3. Coupling Constant Limit and the Exclusion Plot

Showing that there is no potential signal for any axion mass, one should proceed to calculate the coupling constant with 95% confidence level, by integrating over all physically possible $g_{a\gamma}^4$ values as in Equation B.11. The exclusion plot for the three micromegas detectors that was used in 2008 is presented in Figure 10.6. For most of the mass range, the limit is less than the value $3 \cdot 10^{-10}$. For the mass ranges $m_a < 0.39$eV, $m_a > 0.65$eV, and for gaps within the mass range the limit imposed by CAST shows an increase. This is due to low or no exposure at densities corresponding to those axion masses, also verified by Figure 10.3.

Removing the mass ranges with no exposure, the mean limit imposed by CAST sunset micromegas detectors, for axion masses in range $0.385\text{eV} < m_a < 0.652\text{eV}$ is

$$g_{a\gamma} < 2.756 \cdot 10^{-10}\text{GeV}^{-1} \quad at \quad 95\% \ CL$$

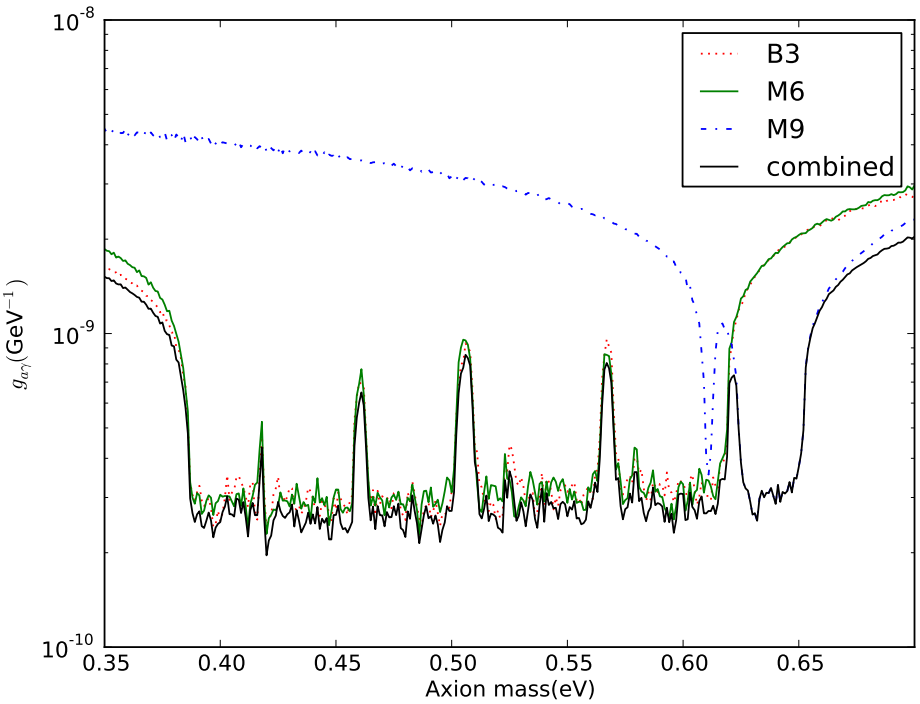


Figure 10.6. The exclusion plot of 2008 data for all three sunset detectors(dashed lined), and combined(black line) exclusion plot.

11. CONCLUSION

The CAST Experiment has been running since 2003, searching for solar axions that will be converted into photons via Primakoff effect in magnetic field of a prototype LHC magnet. The conversion depends strongly on the coupling constant of the interaction, magnetic field strength and length. The density of the conversion medium also affects the conversion, such that for each density there is a narrow axion mass neighborhood for which the conversion is favored. In CAST, ^{4}He and ^{3}He have been used as buffer gas to probe all axion masses that are theoretically favored.

The CAST magnet tracks the sun 1.5 hours each in the morning and evening, reserving the remaining time for detector calibrations and background measurements. Statistical excess of photons during the solar tracking compared to background data taking would be the expected signal, showing that during tracking solar axions are converted into photons and are detected in the detectors. The energy range that the CAST experiment is sensitive to is 2 to 7keV, out of which the solar axion flux diminishes rapidly. The data taking strategy of CAST requires increasing the buffer gas density in the magnet every day to probe all axion masses.

There are four detectors that are installed to CAST magnet, two in each side. Three of them are micromegas and the other is a CCD coupled to an x-ray telescope. The two of the micromegas detectors are installed in the sunset side of the magnet in 2007 and replaced the TPC detector that has operated since the beginning of CAST. The new micromegas detectors showed better performance than the TPC. Furthermore they were improved and upgraded significantly over the years.

The sunset micromegas detectors took data for axion physics for the first time in 2008, and throughout the year 3 different detectors were used in the sunset side. The detectors in general showed good performance, with periods of unstable operation. The analysis of events in the detectors were done by two different methods, multivariate analysis and contour cut analysis. Both methods compare each event with the

calibration events, creating a selection region and decide if it shows characteristics of x-rays. For 2008 data, extensive comparison shows that both methods result in similar sensitivity for axion search, and contour cut method is selected for the final analysis of 2008 data.

The data taking of 2008 started on 28.03.2008 and due to a leak of ^{3}He, it was stopped on 13.11.2008. The leak had directed CAST to re-evaluate the data, and correct the gas density in the magnet using the pressure and temperature measurements. Another effect of the leak is the gaps in the axion mass search, where sensitivity for some mass ranges were reduced. These gaps were closed in 2010 and extensive CFD simulations were carried out to determine the distribution of gas and calculate the length of the region in the magnet, where gas has uniform density.

In this study, the 2008 sunset micromegas data are analysed with the unbinned likelihood method. Axion signal is not observed for any mass, and thus a limit on coupling constant is calculated with 95% CL. For the axions with mass between 0.385eV and 0.652eV, limit is calculated with mean of

$$g_{a\gamma} < 2.756 \cdot 10^{-10}\mathrm{GeV}^{-1}$$

This result lets CAST limits enter into the QCD favored axion models parameter space. The data taking between the years 2008-2013 lets CAST to probe deeper in this region, providing the best experimental coupling constant limit for a wide range of axion masses.

APPENDIX A: UNIT ANALYSIS

One should be careful in the units of the formulas that are used to calculate the limits on the coupling constant. In this work, everything has been written in natural units convention, meaning all units: length, time, mass, charge and temperature are expressed either in powers of eV or without unit. In natural units system used by particle phycisits, $\hbar = c = k_B = \epsilon_0 = \mu_0 = 1$. Conversion of the units used in this thesis in natural units can be summarized in Table A.1. Understanding natural units become important in expressions like $\sin(qL/2)$, or $(g_{a\gamma}B/q)$, where there are hidden physical constants set to unity. To calculate qL one should use both in natural units. Converting meters to eV

$$q[\text{eV}] \cdot 5067730.93 \cdot L[\text{m}] = q[\text{eV}] \cdot L[\text{eV}^{-1}] \tag{A.1}$$

Similarly for BL experimental values are measured in units Tesla meters. This term should be written in terms of eV, since there is the term $(BLg_{a\gamma})^2$ in the conversion probability of axions to photons.

$$\begin{aligned} 195.322 \cdot B[\text{T}] \cdot 5067730.93 \cdot L[\text{m}] &= B[\text{eV}^2] \cdot L[\text{eV}^{-1}] && \text{(A.2)} \\ \Rightarrow 989842342.144 \cdot B[T] \cdot L[m] &= B[\text{eV}^2] \cdot L[\text{eV}^{-1}] && \text{(A.3)} \\ \Rightarrow 0.989842342144 \cdot B[T] \cdot L[m] &= B[\text{GeV}^2] \cdot L[\text{GeV}^{-1}] && \text{(A.4)} \end{aligned}$$

Table A.1. Conversion to Natural Units.

Unit	Metric	Natural
Length	$1.9732697178 \cdot 10^{-7}$m	1eV^{-1}
Mass	$1.78266173154 \cdot 10^{-36}$kg	1eV
Time	$6.58211928 \cdot 10^{-16}$s	1eV^{-1}
Charge	$5.29 \cdot 10^{-19}$C	1
Temperature	$1.1604505 \cdot 10^{4}$K	1eV^{-1}
Magnetic Field	$5.11973546 \cdot 10^{-4}\text{T}\left(\frac{\text{kg}}{\text{C}\cdot\text{s}}\right)$	1eV^2

Photon mass in another quantity that should be calculated in eV's, since it is used to calculate momentum transfer, which will again be given in eV. Recalling Equation 3.18,

$$m_\gamma = \sqrt{\frac{4\pi\alpha}{m_e} Z \frac{N_A}{W_A} \rho} \tag{A.5}$$

Using $m_e = 0.510998928 \cdot 10^{-6} eV$, $\alpha = 1/137.35999074$, $N_A = 6.0221412910^{23}$, where ρ is given in g/cm^3 and W_A is given in grams, one only needs to convert cm^3 into eV^{-3} as

$$\rho \left[\frac{\mathrm{g}}{\mathrm{cm}^3}\right] (1.97 \cdot 10^{-5})^3 = \rho \left[\mathrm{g} \cdot \mathrm{eV}^3\right] \tag{A.6}$$

Combining all constants and conversion, one gets

$$m_\gamma = \sqrt{\frac{4\pi\alpha N_A}{m_e[\mathrm{eV}]} \frac{Z}{W_A[\mathrm{g}]} \rho \left[\frac{g}{cm^3}\right] (1.97 \cdot 10^{-5})^3} = 28.8 \sqrt{\frac{Z}{W_A[\mathrm{g}]} \rho \left[\frac{g}{cm^3}\right]} \tag{A.7}$$

For the special case of He^3, $Z = 2$ and $W_A = 3$. Photon mass in eV is

$$m_\gamma = 23.5 \sqrt{\rho \left[\frac{g}{cm^3}\right]} \tag{A.8}$$

APPENDIX B: MAXIMUM LIKELIHOOD METHOD

Methods of Maximum likelihood can be used for parameter estimation and is especially useful for experiments with small number of events.

B.1. Theory

To understand maximum likelihood method, lets assume a simple model with a fixed unknown parameter θ and observable x. Lets have N observations of the observable x, with results $x_1, x_2, \ldots, x_N$. Probability density function(PDF) for any observation is

$$p = P(x|\theta) \tag{B.1}$$

where $P(x|\theta)$ is normalized

$$\int_{-\infty}^{\infty} P(x|\theta)\mathrm{d}x = 1 \tag{B.2}$$

This probability should be converted into a likelihood by exchanging fixed and variable terms. PDF essentially remains the same, only our point of view changes.

$$P(x_i|\theta) \rightarrow \mathcal{L}_i(\theta|x_i) \tag{B.3}$$

While in reality θ is fixed, it is left as a free parameter in $\mathcal{L}$ and can be varied to obtain the highest probability for a fixed x_i. To combine all observations, individual likelihoods are multiplied and global likelihood is formed as

$$\mathcal{L}(\theta|x_i, \ldots, x_N) = \prod_{i=0}^{N} \mathcal{L}_i(\theta|x_i) \tag{B.4}$$

Finally, maximization of $\mathcal{L}$ will give the maximum likelihood estimator(MLE) of θ. It is a common practice to maximize the natural logarithm of the likelihood, since the maximization will occur for the same θ.

$$\ln \mathcal{L} = \ln \left(\prod_{i=0}^{N} \mathcal{L}_i \right) = \sum_{i=0}^{N} \ln \mathcal{L}_i \tag{B.5}$$

B.2. Binned Likelihood Method

In the ^{4}He phase, in each tracking the gas pressure in the cold bore was increased in the middle of the shift. This created a density profile in each shift. Each half of the shift was considered stable for the calculation of the expected number of photons and a single density was used for each shift, denoted by a pressure step. This method is used throughout the ^{4}He phase and is explained in detail in [107].

For each pressure step k, and for a fixed axion mass m_a, the individual likelihood of having n counts while expecting μ is built, based on the assumption that the count rate follows Poissonian distribution.

$$L_{m_a}^{(k)}(g_{a\gamma}) = \frac{\prod_i \mathrm{e}^{-\mu_{ik}} \frac{\mu_{ik}^{-n_{ik}}}{-n_{ik}}}{\prod_i \mathrm{e}^{-n_{ik}} \frac{n_{ik}^{-n_{ik}}}{-n_{ik}}} \tag{B.6}$$

where i is the energy bin, k is the pressure step, n_{ik} is the observed number of photons during the tracking with pressure step k for the energy bin i and μ_{ik} is the expected number of counts for the same energy and pressure. μ_{ik} consists of two terms such as: $\mu_{ik} = s_{ik} + b_{ik}$, where b_{ik} is the measured background level for the energy bin i and pressure step k, and s_{ik} is the expected signal, which depends on the pressure step k, axion mass m_a, energy bin i, and the coupling constant $g_{a\gamma}$. Recalling Equation 3.34,

$$s_{ik}(g_{a\gamma}, m_a, \rho_k) = \int_E^{E+\Delta E} \frac{d\Phi_A}{\mathrm{d}E} \cdot P_{a\to\gamma}(g_{a\gamma}, m_a, \rho_k) \cdot \epsilon \cdot A \cdot \Delta t_k \cdot \mathrm{d}E \tag{B.7}$$

$$= g_{a\gamma}^4 \int_E^{E+\Delta E} \frac{\mathrm{d}n_{a\gamma}}{\mathrm{d}E} \cdot \Delta_{tk} \cdot \mathrm{d}E \tag{B.8}$$

$L_{m_a}^{(k)}$ represents the likelihood of a single pressure step, for a single detector. The multiplication of all likelihoods for each pressure step and each detector are used to create the global likelihood.

$$\mathcal{L}_{m_a}(g_{a\gamma}) = \prod_{detector} \prod_{k} L_{m_a}^{(k)}(g_{a\gamma}) \tag{B.9}$$

The χ^2 is formed by

$$-\frac{1}{2}\chi^2_{m_a} = \ln(\mathcal{L}_{m_a}(g_{a\gamma})) \tag{B.10}$$

To find the best estimate for the $g_{a\gamma}$, $-\frac{1}{2}\chi^2_{m_a}$ can be maximized. However in case of no signal, one can obtain a limit with 95% confidence level by integrating the exponential of $-\frac{1}{2}\chi^2_{m_a}$ up to 95% of the integral in the physical limits of $g^4_{a\gamma}$.

$$\frac{\int_0^{g^4_{95}} \exp(-\frac{1}{2}\chi^2_{m_a})\mathrm{d}g^4_{a\gamma}}{\int_0^{\infty} \exp(-\frac{1}{2}\chi^2_{m_a})\mathrm{d}g^4_{a\gamma}} = 0.95 \tag{B.11}$$

The result of ^{4}He phase can be summarized as $g_{a\gamma} \lesssim 2.2{\cdot}10^{-10}\mathrm{GeV}^{-1}$ at 95% confidence level for $m_a \lesssim 0.4\mathrm{eV}$

APPENDIX C: MICROMEGAS PLOTS

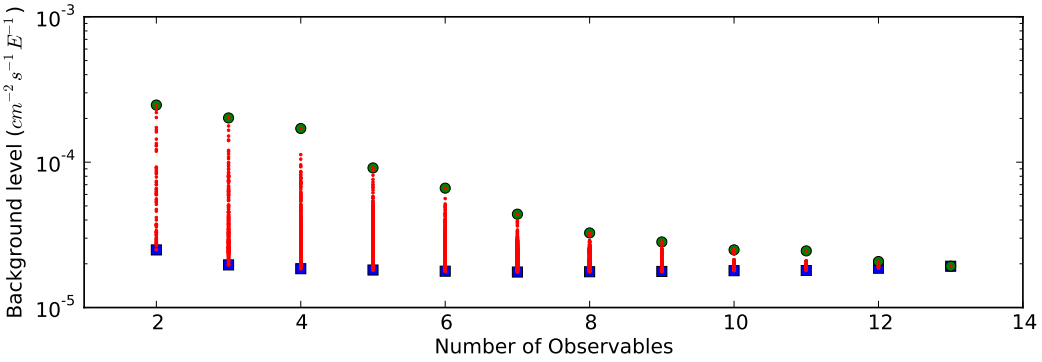


Figure C.1. The number of observables vs. the background levels, for B3.

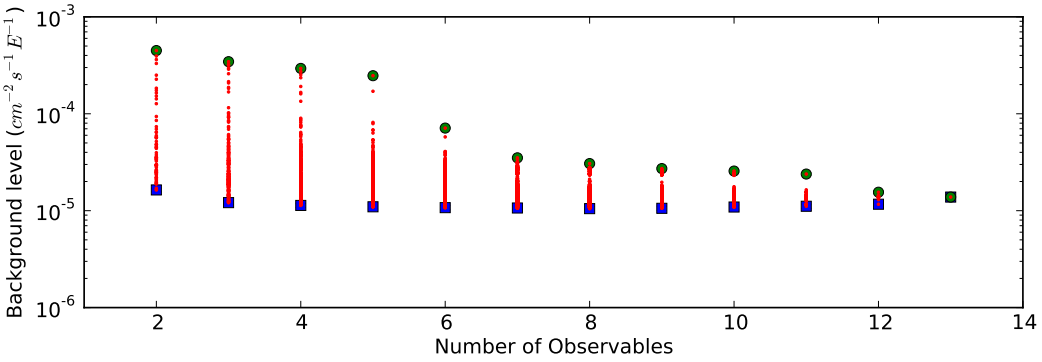


Figure C.2. The number of observables vs. the background levels, for M6.

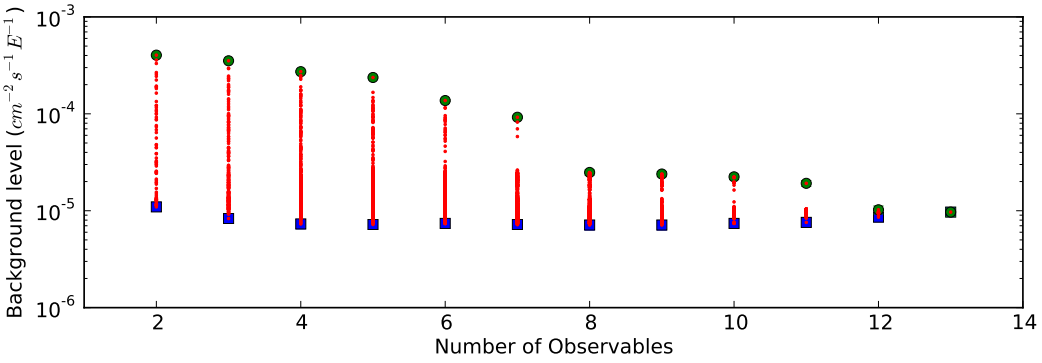


Figure C.3. The number of observables vs. the background levels, for M9.

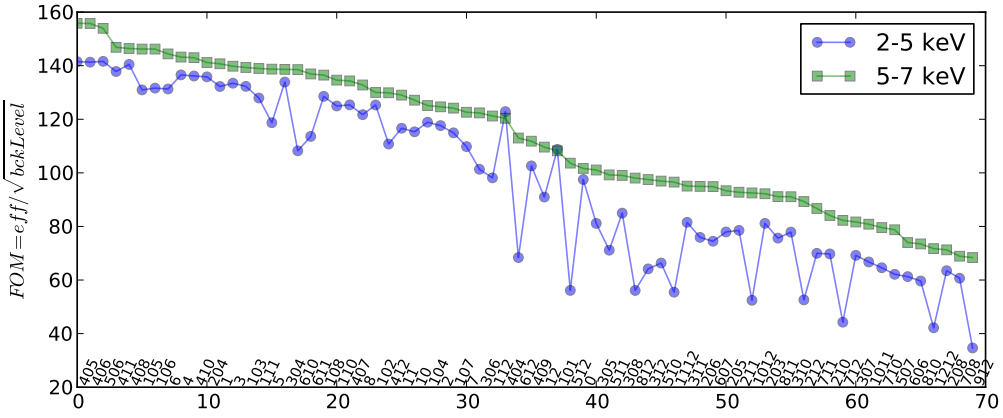


Figure C.4. The observable pairs vs. FOM for low and high energy events, for B3.

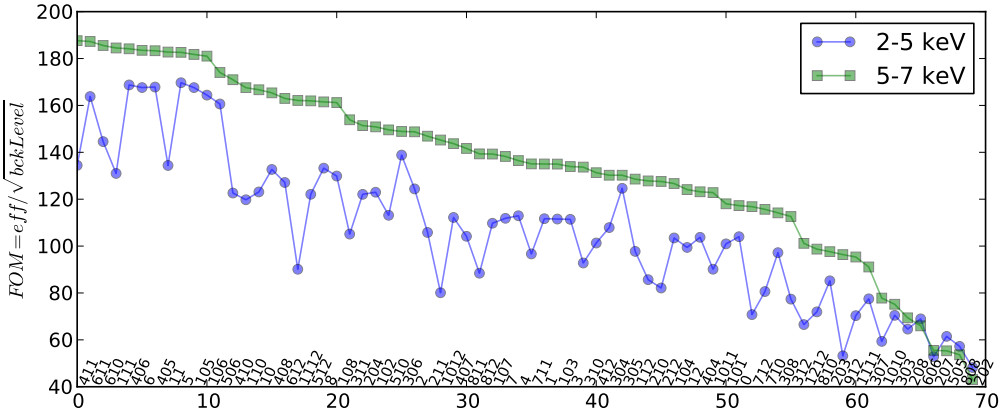


Figure C.5. The observable pairs vs. FOM for low and high energy events, for M6.

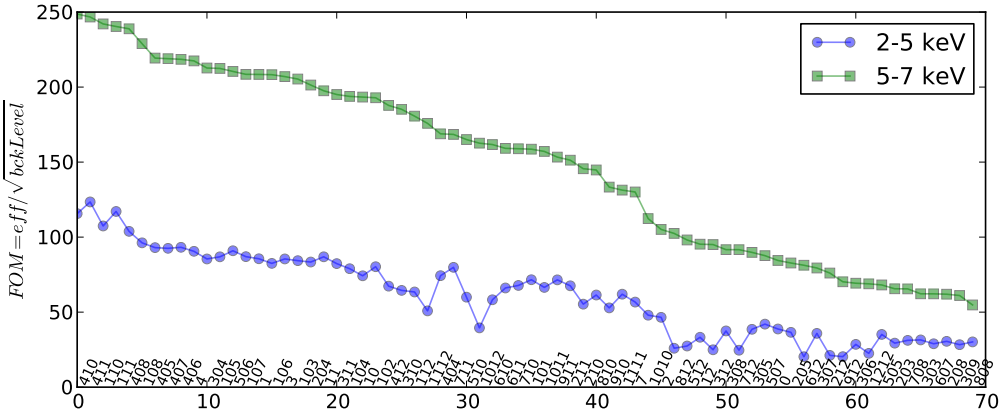


Figure C.6. The observable pairs vs. FOM for low and high energy events, for M9.

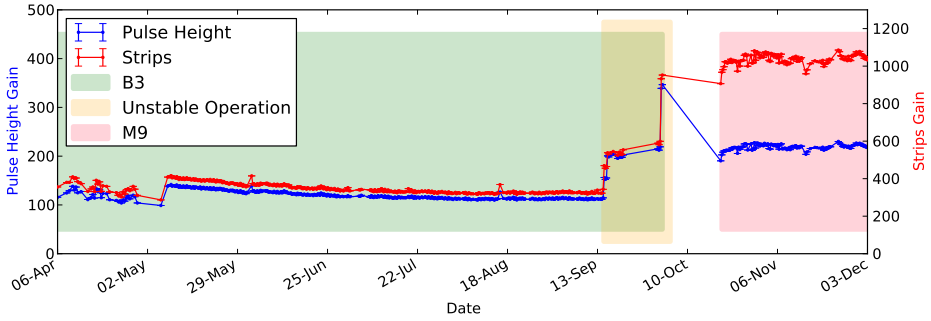


Figure C.7. The gain of pulse amplitude and strip charge in fADC units during the calibrations for B3 and M9. The period when each detector is used and an unstable period of operation is shown in different background colors.

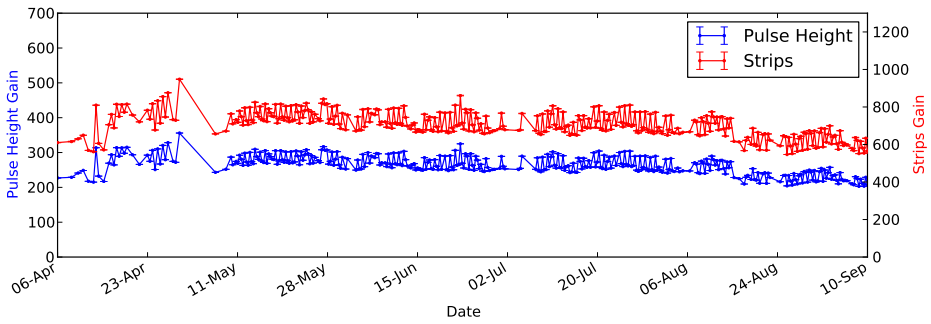


Figure C.8. The gain of pulse amplitude and strip charge in fADC units during the calibrations for M6.

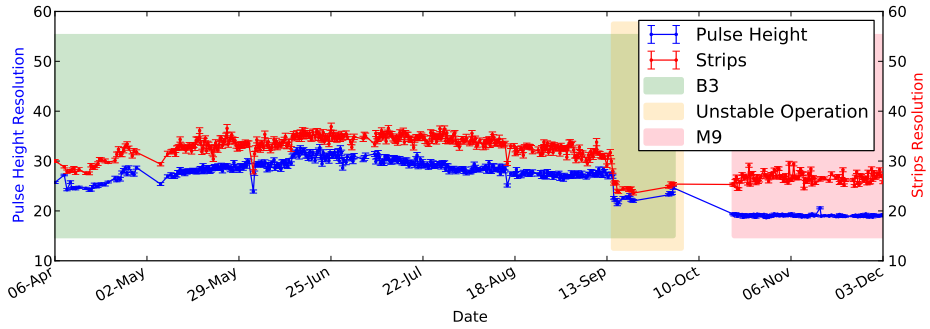


Figure C.9. Evolution of the energy resolution for B3 and M9, given in FWHM percentage at 5.96keV.

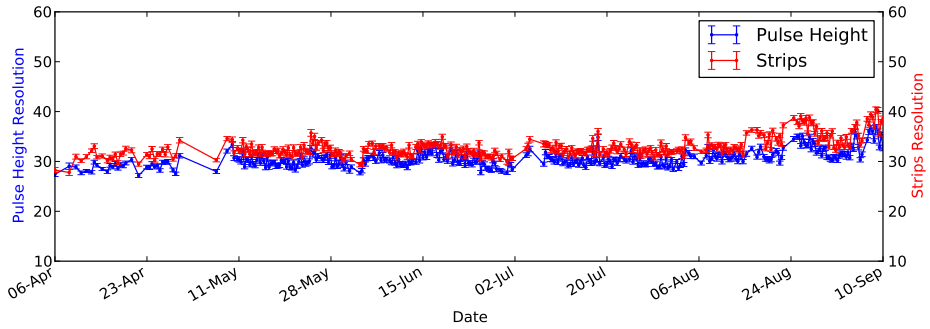


Figure C.10. Evolution of the energy resolution for M6, given in FWHM percentage at 5.96keV.

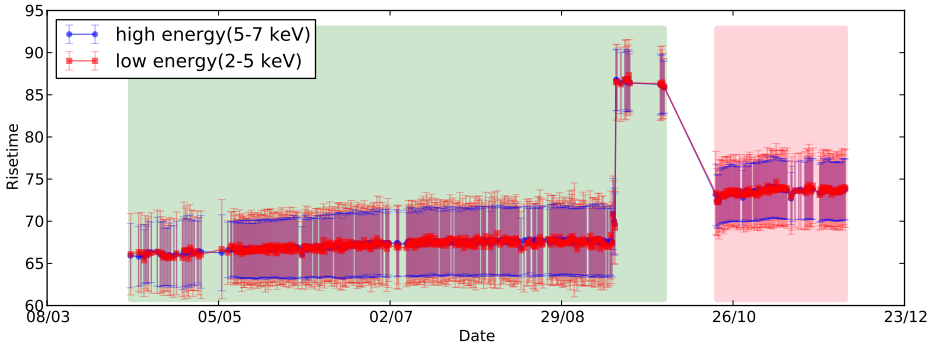


Figure C.11. Evolution of pulse risetime for B3 and M9. Different detectors are indicated by different background colors.

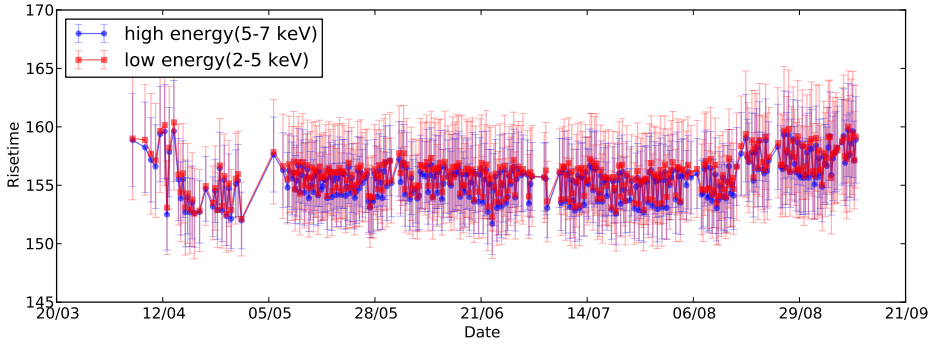


Figure C.12. Evolution of pulse risetime for M6.

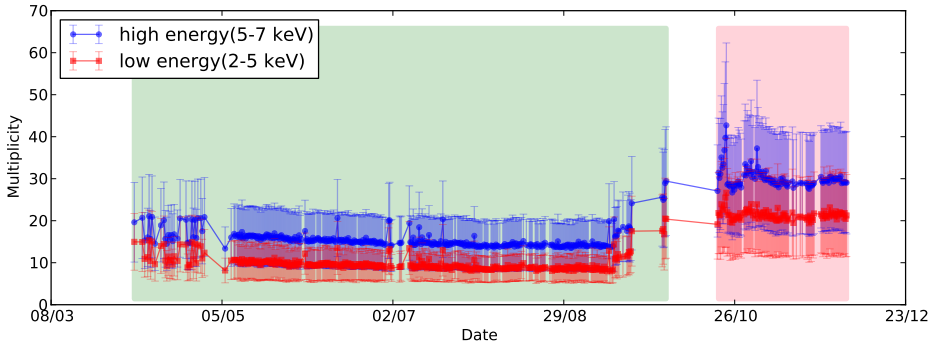


Figure C.13. Evolution of strip multiplicity for B3 and M9. Different detectors are indicated by different background colors.

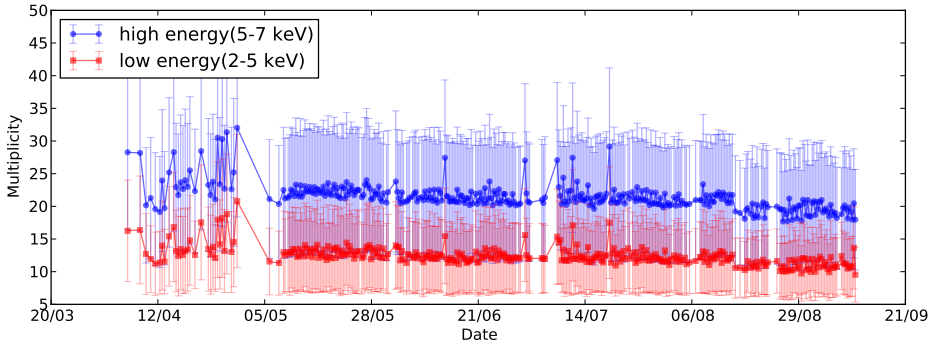


Figure C.14. Evolution of strip multiplicity for M6.

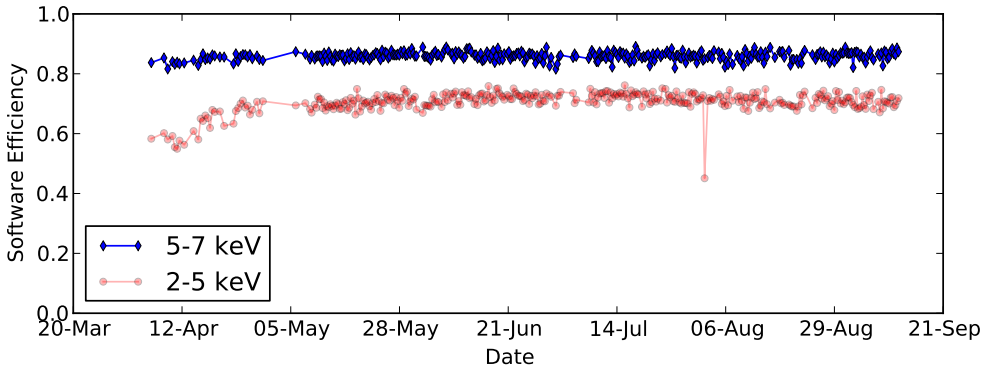


Figure C.15. Evolution of the software efficiency for B3.

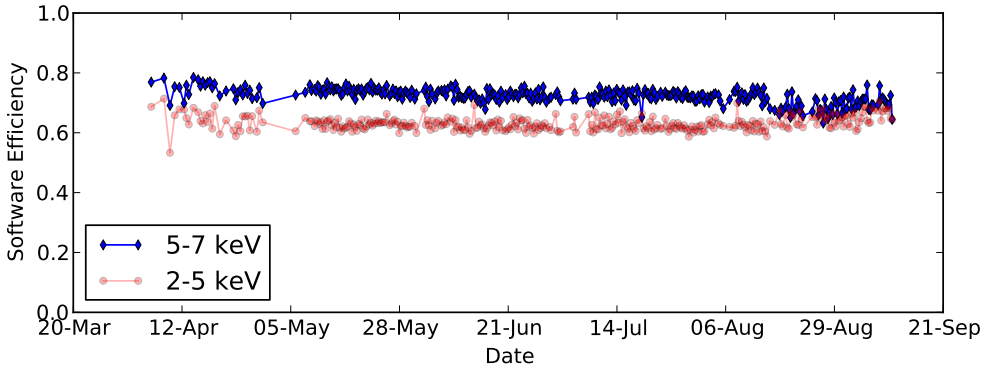


Figure C.16. Evolution of the software efficiency for M6.

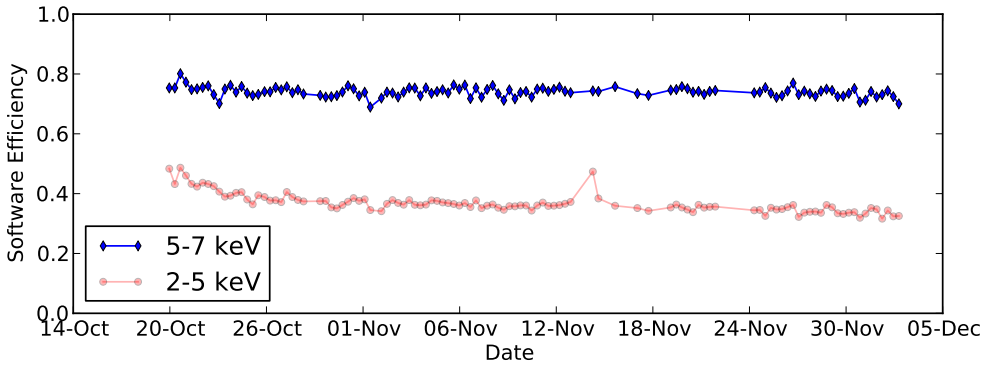


Figure C.17. Evolution of the software efficiency for M9.

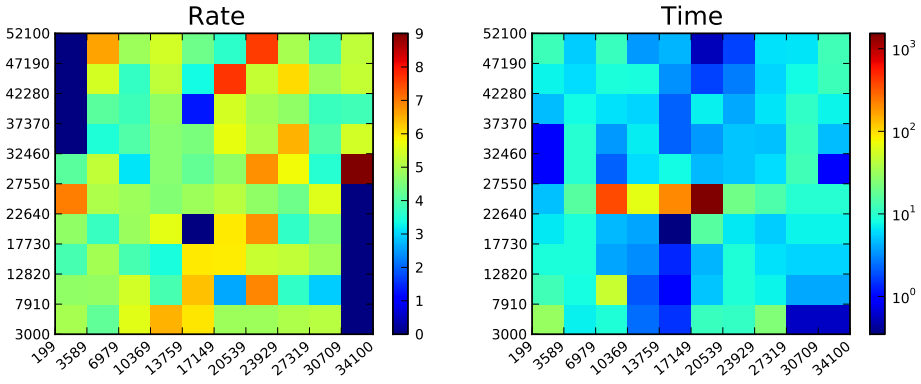


Figure C.18. Background rate in counts/hour at different magnet positions for B3.

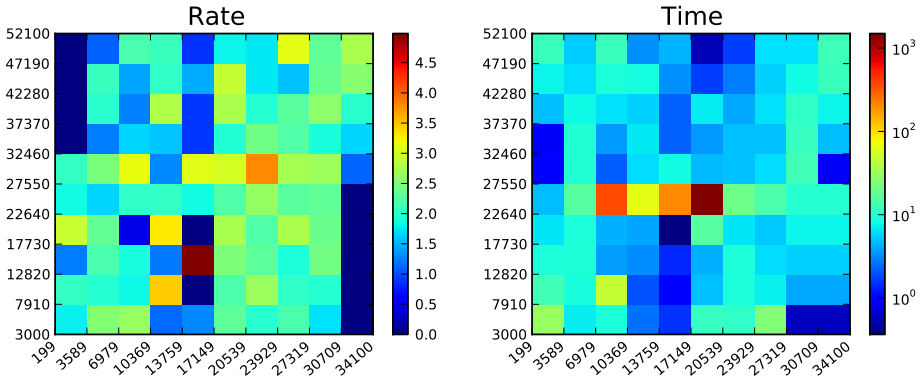


Figure C.19. Background rate in counts/hour at different magnet positions for M6.

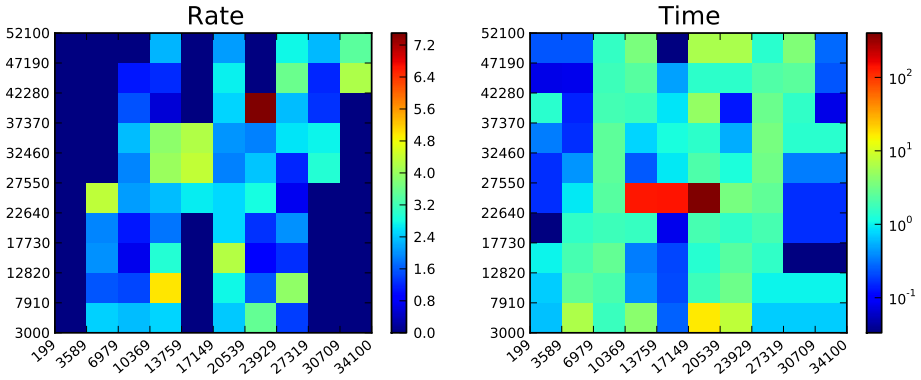


Figure C.20. Background rate in counts/hour at different magnet positions for M9.

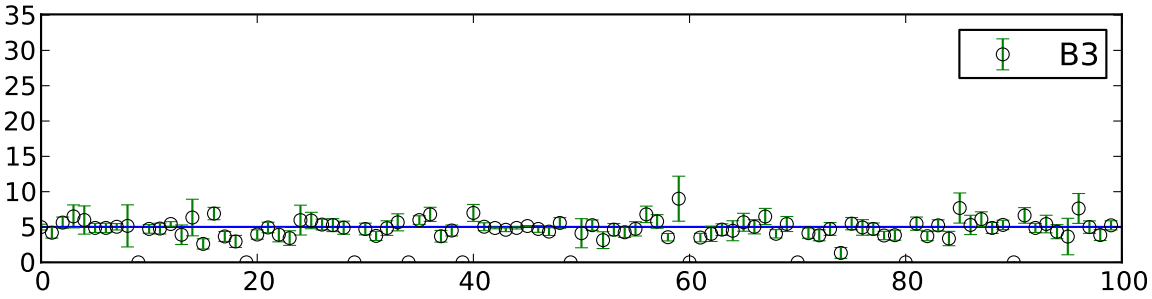


Figure C.21. Background rate and its standard deviation for each bin for B3.

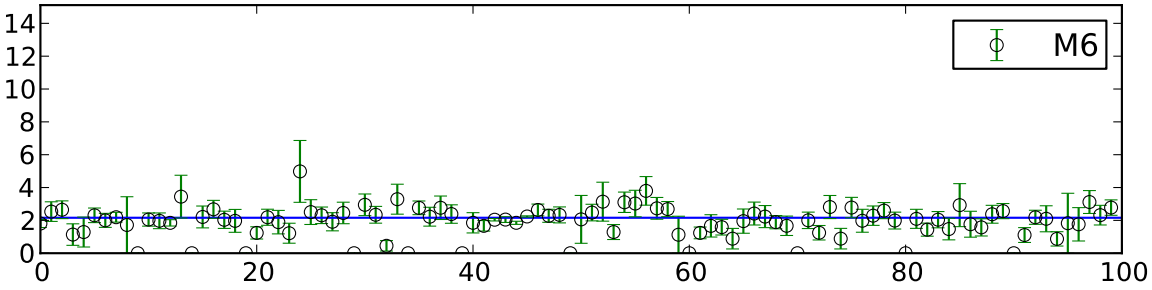


Figure C.22. Background rate and its standard deviation for each bin for M6.

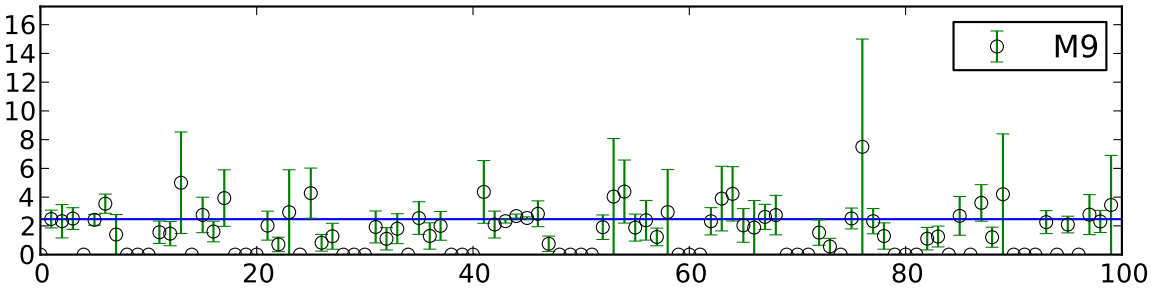


Figure C.23. Background rate and its standard deviation for each bin for M9.

REFERENCES

1. Weinberg, S.,"The U(1) problem", *Physical Review D*, Vol. 11, No. 12, pp. 3583–3593, 1975.

2. 't Hooft, G., "Computation of the Quantum Effects Due to a Four-Dimensional Pseudoparticle", *Physical Review D*, Vol. 14, No. 12, pp. 3432–3450, 1978.

3. Baker, C., D.D. Doyle, P. Geltenbort, K. Green, M. G. D. van der Grinten, P. G. Harris, P. Iaydjiev, S. N. Ivanov, D. J. R. May, J. M. Pendlebury, J. D. Richardson, D. Shiers and K. F. Smith, "Improved Experimental Limit on the Electric Dipole Moment of the Neutron", *Physical Review Letters*, Vol. 97, No. 13, p. 1801, 2006.

4. Peccei, R., "The Strong CP Problem and Axions", *Lecture Notes in Physics*, Vol. 741, No. 1, pp. 3–17, 2008.

5. Leutwyler, H., "The Ratios of the Light Quark Masses", *Physics Letters B*, Vol. 378, No. 1, pp. 313–318, 1996.

6. Primakoff, H., "Photo-Production of Neutral Mesons in Nuclear Electric Fields and the Mean Life of the Neutral Meson", *Physical Review*, Vol. 81, No. 5, p. 899, 1951.

7. Raffelt, G., "Astrophysical methods to constrain axions and other novel particle phenomena", *Physics Reports*, Vol. 198, No. 1, pp. 1–113, 1990.

8. Beringer, J., "Particle Data Group", *Physical Review D*, Vol. 86, No. 1, pp. 1–1528, 2012.

9. Raffelt, G., "Astrophysical Axion Bounds", *Lecture Notes in Physics*, Vol. 741, No. 1, pp. 51–71, 2008.

10. Krauss, L. and F. Wilczek, "A Short Lived Axion Variant", *Physics Letters B*, Vol.

173, No. 2, pp. 189–192, 1986.

11. Peccei, R. D. and H.R. Quinn, "Constraints Imposed By CP Conservation In The Presence Of Pseudoparticles", *Physical Review D*, Vol. 16, No. 4, pp. 1791–1797, 1977.

12. Antoniadis, I. and T. N. Truong, "Lower Bound for Branching Ratio of $K^+ \to \pi^+$ Axion and Non-existence of Peccei-Quinn Axion", *Physics Letters B*, Vol. 109, No. 1, pp. 67–72, 1982.

13. Kim, E.J., "Weak Interaction Singlet and CP Invariance", *Physical Review Letters*, Vol. 43, No. 2, pp. 103–107, 1979.

14. Shifman, M.A., A.I. Vainshtein and V.I. Zakharov, "Can Confinement Ensure Natural CP Invariance Of Strong Interactions", *Nuclear Physics B*, Vol. 166, No. 3, pp. 493–506, 1980.

15. Dine, M., W. Fischlera and M. Srednicki, "A Simple Solution To The Strong CP Problem With A Harmless Axion", *Physics Letters B*, Vol. 104, No. 3, pp. 199–202, 1981.

16. Bertone, G., D. Hooper and J. Silk, "Particle Dark Matter: Evidence, Candidates And Constraints", *Physics Reports*, Vol. 405, No. 5, pp. 279–390, 2005.

17. Komatsu, E., J. Dunkley, M. R. Nolta, C. L. Bennett, B. Gold, G. Hinshaw, N. Jarosik, D. Larson, M. Limon, L. Page, D. N. Spergel, M. Halpern, R. S. Hill, A. Kogut, S. S. Meyer, G. S. Tucker, J. L. Weiland, E. Wollack and E. L. Wright, "Five-Year Wilkinson Microwave Anisotropy Probe (WMAP) Observations: Cosmological Interpretation", *The Astrophysical Journal Supplement Series*, Vol. 180, No. 2, pp. 330–376, 2009.

18. Hannestad, S., A. Mirizzi, G. G. Raffelt and Y. Y. Wong, "Cosmological Constraints On Neutrino Plus Axion Hot Dark Matter: Update After WMAP-5", *Jour-*

nal of Cosmology and Astroparticle Physics, Vol. 2008, No. 4, pp. 1–3, 2008.

19. Abbott, L. and P. Sikivie, "A Cosmological Bound On The Invisible Axion", *Physics Letters B*, Vol. 120, No. 1, pp. 133–136, 1983.

20. Battye, R. and E.P.S. Shellard, "Axion String Constraints", *Physical Review Letters*, Vol. 73, No. 22, pp. 2954–2957, 1994.

21. Chang, S. C. Hagmann and P. Sikivie "Studies Of The Motion And Decay Of Axion Walls Bounded By Strings", *Physical Review D*, Vol. 59, No. 2, pp. 505–526, 1998.

22. Lyth, D., "Estimates Of The Cosmological Axion Density", *Physics Letters B*, Vol. 275, No. 3, pp. 279–283, 1992.

23. Battye, R. and E.P.S. Shellard, "Cosmic Axions", *Proceedings of the 1997 1st International Workshop on Particle Physics and the Early Universe*, 1997.

24. Raffelt, G., "Astrophysics Probes Of Particle Physics", *Physics Reports*, Vol. 333, No. 1, pp. 593–618, 2000.

25. Schlattl, H., A. Weiss and G. Raffelt, "Helioseismological Constraint On Solar Axion Emission", *Astroparticle Physics*, Vol. 10, No. 4, pp. 353–359, 1999.

26. Aharmim, B., "Electron Energy Spectra, Fluxes, And Day-Night Asymmetries Of B-8 Solar Neutrinos From The 391-Day Salt Phase SNO Data Set", *Physical Review C*, Vol. 72, No. 5, pp. 502–559, 2005.

27. Renzini, A. and F. Pecci, "Tests Of Evolutionary Sequences Using Color-Magnitude Diagrams Of Globular Clusters", *Annual Review Of Astronomy And Astrophysics*, Vol. 26, No. 1, pp. 199–244, 1988.

28. Raffelt, G., "Axion Constraints From White Dwarf Cooling Times", *Physics Letters B*, Vol. 176, No. 4, pp. 402–406, 1986.

29. Corsico, A.H., O.G. Benvenuto, L.G. Althaus, J. Isern and E. Garcia-Berro, "The Potential Of The Variable DA White Dwarf G117-B15A As A Tool For Fundamental Physics", *New Astronomy*, Vol. 6, No. 4, pp. 197–214, 2001.

30. Koshiba, M., "Observational Neutrino Astrophysics", *Physics Reports*, Vol. 220, No. 5, pp. 229–381, 1992.

31. Van Bibber, K., N. Dagdeviren, S. Koonin, A. Kerman and H. Nelson, "Proposed Experiment to Produce and Detect Light Pseudoscalars", *Physical Review Letters*, Vol. 59, No. 7, pp. 759–762, 1987.

32. Ruoso, G., R. Cameron, G. Cantatore, A. Melissinos, Y. Semertzidis, H. Halama, D. Lazarus and A. Prodell, "Limits on Light Scalar and Pseudoscalar Particles from a Photon Regeneration Experiment", *Zeitschrift für Physik C*, Vol. 56, No. 4, pp. 505–508, 1992.

33. Cameron, R., G. Cantatore, A. Melissinos, G. Ruoso and Y. Semertzidis, "Search for Nearly Massless, Weakly Coupled Particles by Optical Techniques", *Physical Review D*, Vol. 47, No. 9, pp. 3707–3725, 1993.

34. GammeV Collaboration, "Search For Axionlike Particles Using A Variable-Baseline Photon-Regeneration Technique", *Physical Review Letters*, Vol. 100, No. 8, pp. 402–406, 2008.

35. Ehret, K., M. Frede, S. Ghazaryan, M. Hildebrandt, E. Knabbe, D. Kracht, A. Lindner, J. List, T. Meier, N. Meyer, D. Notz, J. Redondo, A. Ringwald, G. Wiedemann and B. Willke, "Resonant Laser Power Build-Up In ALPS – A "Light-Shining-Through-Walls" Experiment", *Nuclear Instruments and Methods in Physics A*, Vol. 612, No. 1, pp. 83–96, 2009.

36. Pugnat, P., L. Duvillaret, R. Jost, G. Vitrant, D. Romanini, A. Siemko, R. Ballou, B. Barbara, M. Finger, M. Finger, J. Hosek, M. Kral, K. A. Meissner, M. Sulc and J. Zicha, "First Results From The OSQAR Photon Regeneration Experiment: No

Light Shining Through A Wall", *Physical Review D*, Vol. 78, No. 9, p. 2003, 2008.

37. Sikivie, P., D.B. Tanner and K. van Bibber, "Resonantly Enhanced Axion-Photon Regeneration", *Physical Review Letters*, Vol. 98, No. 17, pp. 2–6, 2007.

38. Maiani, L., R. Petronzio and E. Zavattini, "Effects Of Nearly Massless, Spin-Zero Particles On Light Propagation In A Magnetic Field", *Physics Letters*, Vol. 175, No. 1, pp. 359–363, 1986.

39. Semertzidis, Y., R. Cameron, G. Cantatore, A. C. Melissinos, J. Rogers, H. Halama, A. Prodell, F. Nezrick, C. Rizzo and E. Zavattini, "Limits on The Production Of Light Scalar And Pseudoscalar Particles", *Physical Review Letters*, Vol. 64, No. 4, p. 2988, 1990.

40. PVLAS Collaboration,"Experimental Observation of Optical Rotation Generated in Vacuum by a Magnetic Field", *Physical Review Letters*, Vol. 96, No. 11, pp. 406–411, 2006.

41. Bradley, R., J. Clarke, D. Kinion, L.J. Rosenberg, K.Van Bibber, S. Matsuki, M. Mück and P. Sikivie, "Microwave Cavity Searches For Dark-Matter Axions", *Review of Modern Physics*, Vol. 75, No. 3, pp. 777–817, 2003.

42. Wuensch, W.U., S. Panfilis-Wuensch, Y. K. Semertzidis, J. T. Rogers, A. C. Melissinos, H. J. Halama, B. E. Moskowitz, A. G. Prodell, W. B. Fowler and F. A. Nezrick, "Results Of A Laboratory Search For Cosmic Axions And Other Weakly Coupled Light Particles", *Physical Review D*, Vol. 40, No. 1, pp. 3153–3167, 1989.

43. Hagmann, C., P. Sikivie, N. S. Sullivan and D. B. Tanner, "Results from a search for cosmic axions", *Physical Review D*, Vol. 42, No. 4, pp. 1297–1300, 1990.

44. Hagmann, C., D. Kinion, W. Stoeffl, K. van Bibber, E. Daw, H. Peng, J. Rosenberg, J. LaVeigne, P. Sikivie, N. S. Sullivan, D. B. Tanner, F. Nezrick, M. S. Turner, D. M. Moltz, J. Powell and N. A. Golubev, "Results from A High-Sensitivity Search

For Cosmic Axions", *Physical Review Letters*, Vol. 80, No. 1, pp. 2043–2046, 1998.

45. Bradley, R., J. Clarke, D. Kinion, L. Rosenberg, K. Van Bibber, S. Matsuki, M. Mück and P. Sikivie, "Microwave cavity searches for dark-matter axions", *Review of Modern Physics*, Vol. 75, No. 3, pp. 777–817, 2003.

46. Duffy, L. D., P. Sikivie, D. B. Tanner, S. J. Asztalos, C. Hagmann, D. Kinion, L. J. Rosenberg, K. Van Bibber, D. B. Yu and R. F. Bradley, "High Resolution Search For Dark-Matter Axions", *Physical Review D*, Vol. 74, No. 1, pp. 1–11, 2006.

47. Asztalos, S. J., G. Carosi, C. Hagmann, D. Kinion, K. van Bibber, M. Hotz, L. Rosenberg, G. Rybka, J. Hoskins, J. Hwang, P. Sikivie, D. B. Tanner, R. Bradley and J. Clarke, "A SQUID-Based Microwave Cavity Search For Dark-Matter Axions", *Physical Review Letters*, Vol. 104, No. 4, pp. 1301–1305, 2010.

48. Morales, A., F. T. Avignone, R. L. Brodzinski, S. Cebrian, E. Garcia, D. Gonzalez, I. G. Irastorza, H. S. Miley, J. Morales, A. Ortiz de Solorzano, J. Puimedon, J. H. Reeves, M. L. Sarsa, S. Scopel and J. A. Villar, "Particle Dark Matter and Solar Axion Searches With A Small Germanium Detector At The Canfranc Underground Laboratory", *Astroparticle Physics*, Vol. 16, No. 3, pp. 325–332, 2002.

49. Avignone, F., D. Abriola, R. L. Brodzinski, J. I. Collar, R. J. Creswick, D. E. DiGregorio, H. A. Farach, A. O. Gattone, C. K. Guerard, F. Hasenbalg, H. Huck, H. S. Miley, A. Morales, J. Morales, S. Nussinov, A. Ortiz de Solorzano, J. H. Reeves, J. A. Villar and K. Zioutas, "Experimental Search for Solar Axions via Coherent Primakoff Conversion in a Germanium Spectrometer", *Physical Review Letters*, Vol. 81, No. 23, pp. 5068–5071, 1998.

50. Bernabei, R., P. Belli, R. Cerulli, F. Montecchia, F. Nozzoli, A. Incicchitti, D. Prosperi, C.J. Dai, H.L. He, H.H. Kuang, J.M. Ma, S. Scopel, "Search For Solar Axions By Primakoff Effect In NaI Crystals", *Physics Letters*, Vol. 515, No. 1, pp. 6–12, 2001.

51. CDMS Collaboration, "Exclusion Limits On The WIMP-Nucleon Cross Section From The First Run Of The Cryogenic Dark Matter Search In The Soudan Underground Laboratory", *Physical Review D*, Vol. 72, No. 5, pp. 2009–2047, 2005.

52. CDMS Collaboration,"Search for Axions with the CDMS Experiment", *Physical Review Letters*, Vol. 103, No. 14, pp. 1802–1807, 2009.

53. Lazarus D.M, G. C. Smith, R. Cameron, A. C. Melissinos, G. Ruoso, and Y. K. Semertzidis and F. A. Nezrick, "Search For Solar Axions", *Physical Review Letters*, Vol. 69, No. 4, pp. 2333–2336, 1992.

54. Inoue, Y., T. Namba, S. Moriyama, M. Minowa, Y. Takasu, T. Horiuchi and A. Yamamoto, "Search For Sub-Electronvolt Solar Axions Using Coherent Conversion Of Axions Into Photons In Magnetic Field And Gas Helium", *Physics Letters B*, Vol. 536, No. 1, pp. 18–23, 2002.

55. Raffelt, G., "Astrophysical Axion Bounds Diminished By Screening Effects", *Physical Review D*, Vol. 33, No. 4, pp. 897–909, 1986.

56. Raffelt, G., "Plasmon Decay Into Low-Mass Bosons In Stars", *Physical Review D*, Vol. 37, No. 6, pp. 1356–1359, 1988.

57. Bahcall, J., W. Huebner, P. Parker and R. Ulrich, "Standard Solar Models And The Uncertainties In Predicted Capture Rates Of Solar Neutrinos", *Review of Modern Physics*, Vol. 54, No. 4, pp. 767–799, 1982.

58. Di Lella, L., A. Pilaftsis, G. Raffelt and K. Zioutas, "Search For Solar Kaluza-Klein Axions In Theories Of Low-Scale Quantum Gravity", *Physical Review D*, Vol. 62, No. 12, p. 5011, 2000.

59. The CAST Collaboration, "An Improved Limit On The Axion-Photon Coupling From The CAST Experiment", *Journal of Cosmology and Astroparticle Physics*, Vol. 4, No. 10, p. 1475, 2007.

60. Raffelt, G. and L. Stodolsky, "Mixing Of Photon With Low Mass Particles", *Physical Review D*, Vol. 37, No. 5, pp. 1237–1249, 1988.

61. Van Bibber, K., P.M. MaIntyre, D.E. Morris and G. Raffelt, "Design For A Practical Laboratory Detector For Solar Axions", *Physical Review D*, Vol. 39, No. 1, pp. 2089–2099, 1989.

62. Hubbell, J.H., and S. M. Seltzer, *X-Ray Mass Attenuation Coefficients*, 1996, `http://www.nist.gov/pml/data/xraycoef/index.cfm`, accessed at May 2011.

63. Aalseth, C., D. Abriola, F. Avignone, R. Brodzinski, J. Collar, R. Creswick, D. DiGregorio, H. Farach, O. Gattone, Y. Giomataris, S. Gninenko, N. Golubev, C. Guerard, F. Hasenbalg, M. Hasinoff, H. Huck, A. Kovzelev, A. Liolios, V. Matveev, H. Miley, A. Morales, J. Morales, D. Nikas, S. Nussinov, A. Ortiz, G. Polymeris, G. Raffelt, I. Savvidis, S. Scopel, I. Semenyuk, J. Villar and K. Zioutas, "Proposal To The SPSC: A Solar Axion Search Using A Decommissioned LHC Test Magnet", *SPS-PS Experiments Committee*, CERN-SPSC-99-21, 1999.

64. The CAST Collaboration, "Probing eV-Scale Axions With CAST", *Journal of Cosmology and Astroparticle Physics*, Vol. 2009, No. 2, pp. 1–18, 2009.

65. The CAST Collaboration, "Search for Sub-eV Mass Solar Axions By The CERN Axion Solar Telescope With 3He Buffer Gas", *Physics Review Letters*, Vol. 107, No. 26, pp. 1302–1307, 2011.

66. The CAST Collaboration, "CAST Solar Axion Search with ^{3}He Buffer Gas: Closing the Hot Dark Matter Gap", *arXiv Preprints*, arXiv:1307.1985, 2013.

67. K. Barth, D. Delikaris, G. Passardi, M. Pezzetti, O. Pirotte, L. Stewart, B. Vullierme, L Walckiers and K. Zioutas, "Cryogenics for the CERN Solar Axion Telescope (CAST) using a LHC Dipole Prototype Magnet", *Proceedings of 2002 19th International Cryogenic Engineering Conference*, 2002.

68. Spath, H., *Two Dimensional Spline Interpolation Algorithms*, A K Peters, Wellesey, 1993.

69. Yildiz, C., "Comparison of 2011 and 2002 Grids at CAST", *CAST Internal Notes*, 2012.

70. Elias, N., *Conversion and Operation of CAST as a Massive Axion Detector*, PhD Thesis, Universidade Técnica de Lisboa, 2010.

71. Niinikoski, T., B. Bellanger, M. Davenport, N. Elias, S. Aune, J. Franz, "Thin Cryogenic X-ray Windows", *22nd International Cryogenic Engineering Conference and International Cryogenic Materials Conference 2008*, Seoul, 2008.

72. LHCb Collaboration, *PVSS Introduction for Newcomers*, 2008,`http://lhcb-online.web.cern.ch/lhcb-online/ecs/PVSSIntro.htm`, accessed at July 2012.

73. Wolter H, *Glancing Incidence Mirror Systems as Imaging Optics for X-rays*, *Annalen der Physik*, Vol. 10, No. 10, pp. 94-114, 1994.

74. Altmann, J., W. J. Egle, U. Bingel, W. Hafner, B. Gaenswein, H. Schwarz, A. Neugschwender, "Mirror System For The German X-Ray Satellite ABRIXAS: I. Flight Mirror Fabrication, Integration, And Testing", *Proceedings of SPIE, X-Ray Optics, Instruments, and Missions*, Vol. 3444, No. 1, pp. 350–468, 1998.

75. Strüder, L., "The European Photon Imaging Camera on XMM-Newton: The pn-CCD camera", *Astronomy and Astrophysics*, Vol. 365, Number 1, pp. 18–26, 2001.

76. Charpak, G., R. Bouclier, T. Bressani, J. Favier and Č. Zupančič, "The Use Of Multiwire Proportional Counters To Select And Localize Charged Particles", *Nuclear Instruments and Methods in Physics A*, Vol. 62, No. 3, pp. 262–268, 1968.

77. Walenta, A.H., J. Heintze, B. Schürlein, "The Multiwire Drift Chamber A New

Type Of Proportional Wire Chamber", *Nuclear Instruments and Methods in Physics A*, Vol. 92, No. 3, pp. 373–380, 1971.

78. Blum, W., W. Riegler, L. Rolandi, *Particle Detection with Drift Chambers*, 2nd edition, Springer-Verlag, Berlin, 2008.

79. Autiero, D., D Autiero, B. Beltrán, J. Carmona, S. Cebrian, E. Chesi, M. Davenport, M. Delattre, L. Di Lella, F. Formenti, I. Irastorza, H. Gomez, M. Hasinoff, B. Lakic, G. Luzon, J. Morales, L. Musa, A. Ortiz, A. Placci, A. Rodrigurez, J. Ruz, J. Villar and K. Zioutas, "The CAST Time Projection Chamber", *New Journal of Physics*, Vol. 9, No. 6, p. 171, 2007.

80. Ruz, J., *Search for solar axions with the Time Projection Chamber of the CERN Axion Solar Telescope with 4-Helium as buffer gas*, Ph.D. Thesis, University of Zaragoza, 2008.

81. Luzon, G., B. Beltran, J. Carmona, S. Cebrian, H. Gomez, I. Irastorza, J. Morales, A. Ortiz, A. Rodriguez, J. Ruz and J. Villar, "Background Studies And Shielding Effects For The TPC Detector Of The CAST Experiment" *New Journal of Physics*, Vol. 9, No. 1, p. 208, 2007.

82. Y. Giomataris, P. Rebourgeard, J.P. Robert and G. Charpak, "MICROMEGAS A High Granularity Position Sensitive Detector For High Particle Flux Environment" *Nuclear Instruments and Methods in Physics A*, Vol. 376, No. 1, pp. 29–35, 1996.

83. Sauli, F. "Principles of Operation of Multiwire, Proportional and Drift Chambers", *CERN Academic Training Lecture*, Vol. 81, No. 1, pp. 79–188, 1977.

84. Leo, W. R., "Techniques for Nuclear and Particle Physics Experiments", 2nd edition, Springer-Verlag, Heidelberg, 1994.

85. Iguaz F., "Characterization Of Microbulk Detectors In Argon- And Neon-Based Mixtures", *Journal of Instrumentation*, Vol. 7, No. 4, p. 4007, 2012.

86. Charpak, G., J Derré, Y Giomataris and Ph. Rebourgeard, "Micromegas, a multipurpose gaseous detector", *Nuclear Instruments and Methods in Physics A*, Vol. 478, No. 1, pp. 26–36, 2002.

87. Giomataris, I, R. De Oliveira, S. Andriamonje, S. Aune, G. Charpak, P. Colas, G. Fanourakis, E. Ferrer, A. Giganon, Ph. Rebourgeard and P. Salin, "Micromegas in a Bulk", *Nuclear Instruments and Methods in Physics A*, Vol. 560, No. 2, pp. 405–408, 2006.

88. Andriamonje, S., D. Attie, E. Berthoumieux, M. Calviani, P. Colas, T. Dafni, G. Fanourakis, E. Ferrer-Ribas, J. Galan, T. Geralis, A. Giganon, I. Giomataris, A. Gris, C. Sanchez, F. Gunsing, F. J. Iguaz, I. Irastorza, R. De Oliveira, T. Papaevangelou, J. Ruz, I. Savvidis, A. Teixera and A. Tomás, "Development and performance of Microbulk Micromegas Detectors", *Journal of Instrumentation*, Vol. 5, No. 2, p. 2001, 2010.

89. J.C. Santiard, " Gassiplex, a low noise analog signal processor for readout of gaseous detectors", *Physical Review C*, Vol. 52, No. 4, p. 2072, 1995.

90. Cebrian, S., T. Dafni, E. Ferrer-Ribas, J. Galan, I. Giomataris, H. Gomez, F.J. Iguaz, I. Irastorza, G. Luzon, R. De Oliveira, A. Rodriguez, L. Segui, A. Tomas, J.A. Villar, "Radiopurity of Micromegas readout planes", *Astroparticle Physics*, Vol. 34, No. 6, pp. 354–359, 2011.

91. Yildiz, S. C., "Measurements for O2 and H2O concentration in the CAST Sunset MicroMegas Gas", *CAST Internal Notes*, 2012.

92. Agostinelli, S., "Geant4—a simulation toolkit", *Nuclear Instruments and Methods in Physics A*, Vol. 506, No. 3, pp. 250–303, 2003.

93. J. Galan, S. Aune, J. Carmona, T. Dafni, G. Fanourakis, E. Ferrer Ribas, T. Geralis, I. Giomataris, H. Gomez, F.J. Iguaz, I.G. Irastorza, K. Kousouris, G. Luzon, J. Morales, J.P. Mols, T. Papaevangelou, A. Rodriguez, J. Ruz, A. Tomas and T.

Vafeiadis, "Micromegas Detectors In The CAST Experiment", *Journal of Instrumentation*, Vol. 5, No. 6, pp. 1-10, 2010.

94. D. Breton, E. Delagnes and M. Houry, *Very High Dynamic Range and High-Sampling Rate VME Digitizing Boards for Physics Experiments*, *IEEE 2004 Medical Imaging*, Vol. 1, No. 1, p. 23, 2004.

95. CAEN, *V551B Sequencer*, 1999, `http://www.caen.it/jsp/Template2/CaenProd.jsp?paren` accessed at June 2011.

96. Gracia J., "Co-57 source: Simulations and Tests", *Talk given in 47th CAST Collaboration Meeting*, Geneva, 2012.

97. Tomas, A., S. Aune, T. Dafni, G. Fanourakis, E. Ferrer-Ribas, J. Galan, J.A. Garcia, A. Gardikiotis, T. Geralis, I. Giomataris, H. Gomez, J.G. Garza, D.C. Herrera, F.J. Iguaz, I.G. Irastorza, G. Luzon, T. Papaevangelou, A. Rodriguez, J. Ruz, L. Segui, T. Vafeiadis, S.C. Yildiz, "CAST Microbulk Micromegas In the Canfranc Underground Laboratory", *Proceedings of the 2nd International Conference on Technology and Instrumentation in Particle Physics*, Vol. 37, No. 1, pp. 478–482, 2012.

98. Garcia J., "M17 Canfranc Status and M10 Test", *Talk given in 48th CAST Collaboration Meeting*, Geneva, 2012.

99. Brun, R. and F. Rademakers, "ROOT - An Object Oriented Data Analysis Framework", *Nuclear Instruments and Methods in Physics A*, Vol. 389, No. 1, pp. 81–86, 1997.

100. Rencher, A., *Methods of Multivariate Analysis*, Wiley Interscience, New York, USA, 2002.

101. Kousouris, K., "Software for Micromegas in CAST Phase II", *CAST Internal Notes*, 2006.

102. Kousouris, K., *Search for Solar Axions in the CAST Experiment with the Micromegas Detector*, Ph.D. Thesis, University of Athens, 2006.

103. Galan, J., *Probing eV-mass scale Axions with a Micromegas Detector in the CAST Experiment.*, PhD Thesis, Universidad de Zaragoza, 2011.

104. Dafni, T., "Status Report of the CAST Experiment", *SPS-PS Experiments Committee*, 93rd SPSC meeting. CERN-SPSC-2009–030, 2009.

105. Vafeiadis, T., *Contribution to Search on Solar Axion at the CAST Experiment*, Ph.D. Thesis, University of Thessaloniki, 2012.

106. Lyons, L., *Statistics for Nuclear and Particle Physicists*, Cambridge University Press, Cambridge, USA, 1986.

107. Garcia, I., "Some Guidelines for the Analysis of Phase II Data", *CAST Internal Notes*, 2006.

108. Zioutas, K., M. Tsagri, Y. Semertzidis, T. Papaevangelou, T. Dafni and V. Anastassopoulos, "Axion Searches With Helioscopes And Astrophysical Signatures For Axion(-like) Particles", *New Journal of Physics*, Vol. 11, No. 10, pp. 1–27, 2009.

109. Elias, N., B. Lakic, T. Vafeiadis, "Notes on Density Stability Threshold", *CAST Internal Notes*, 2012.

110. Da Riva, E., "CFD Simulations for CAST", *Talk given on CAST 49th CM*, 2012.